UNIVERSITY OF CALIFORNIA

Santa Barbara

Improving Efficiency of III-N Quantum Well Based Optoelectronic Devices through Active Region Design and Growth Techniques

A dissertation submitted in partial satisfaction of the
requirements for the degree of

Doctor of Philosophy

in

Materials

by

Nathan Garrett Young

Committee in charge:

Professor Steven P. DenBaars, Chair

Professor James S. Speck

Professor Claude Weisbuch

Professor Umesh K. Mishra

September 2015

The dissertation of Nathan Garrett Young is approved.

_____

James S. Speck

_____

Claude Weisbuch

_____

Umesh K. Mishra

_____

Steven P. DenBaars, Committee Chair

September 2015

Improving Efficiency of III-N Quantum Well Based Optoelectronic Devices through Active Region Design and Growth Techniques

This dissertation is dedicated to my parents, Jeff and Melinda,

for their unwavering love and support.

ACKNOWLEDGEMENTS

Through my years at UCSB I have been privileged to have the opportunity to interact with, learn from, and build friendships with an incredible group of people. The knowledge I have gained and the relationships I have built here will carry through the rest of my professional and personal life. It was not always my intension to pursue a doctorate degree. In fact, when I look back it seems like it was a relatively last minute and spur of the moment decision to even apply, just as I was starting my first job. Luckily I can now say that was perhaps the best life decision I've made, but I wouldn't feel this way if it wasn't for the exceptional scientists, engineers, colleagues, and friends that have guided me and walked along side me for the last five years.

First and foremost, I must thank my committee for their intellectual guidance and encouragement. Great thanks go to my co-advisor Jim Speck, who directly oversaw my various projects and guided me through the details of my work. Jim showed impressive dedication to his students, and the students of other professors in the SSLEC. He always made a point of finding time to meet even while juggling the organizational demands of his group, the SSLEC, and the Materials department as whole. His work ethic was inspirational, and so was his rigorous approach to science. Meetings with Jim could run the gamut from deep scientific discussion to political and environmental issues to sports (especially cycling) and random trivia. They were always enlightening and I was kept constantly on my toes. I also want to give special thanks to my other co-advisor, Steve DenBaars. Steve was an invaluable source of MOCVD knowledge, and he could be counted on to provide key insights from his academic and industrial experience to solve our growth-related problems. He put in countless hours and airline miles to ensure we always had money for our research. I appreciated his ability to always keep a lighthearted and disarming mood – I'll never forget him jumping across a narrow fissure to a freestanding pillar at the edge of a 1000 foot cliff in the Saudi desert, despite loud protestations from Jim and Shuji. Umesh Mishra was a big proponent of the nitride solar project in my early years, and his support along with Jim's provided a platform for me to learn the ins and outs of graduate research. Umesh was also an unparalleled resource for device physics knowledge. He taught semiconductor device physics from the most basic fundamentals in an intuitive and conversational style that connected with me in a way that no other similar course had. It was the best taught, most useful engineering course I've taken. My committee was completed by Claude Weisbuch, whose immense knowledge of optoelectronic physics perfectly complimented the skill sets of my other committee members. Claude does not settle for anything but the best and most precise scientific approaches and explanations, but he also is generous with his attention in helping his students achieve those goals. By serendipitous chance as much as design, my committee's skills and attributes have aligned to complement each other in an ideal way for

my research efforts. I owe my success as a graduate student and I will certainly owe much of my future success as a scientist to their guidance and inspiration.

There are a small handful of people that have had an outsized impact on my graduate research experience and deserve special thanks here. My first mentor at UCSB was Samantha Cruz. She introduced me to clean room fabrication, solar cell testing, material characterization, and MOCVD growth, and she also showed me how to balance my life and enjoy myself in grad school. Carl Neufeld was also instrumental in teaching me about the tricks of the solar cell process. He had an incredibly deep working knowledge of nitride solar cells and device fabrication that I mined regularly over my first two years. Bob Farrell had recently finished his own PhD when I joined the nitrides group, and he was leading the solar project as a post-doc. At that time the nitrides solar project was a large and well-funded effort. Despite his large and simultaneous responsibilities as a project manager and researcher in the lab trying to get a batch of devices through fabrication and testing every week, Bob took me under his wing. He taught me the value of a meticulous and rigorous approach to research in the lab and when writing papers, and I also count him as a good friend. Even after he left the solar project and took on even more responsibility in running the LED group, we met often to discuss my work. He constantly went out of his way to pass down knowledge to me, particularly in the surprisingly intricate process of making figures and submitting articles. Finally, Stacia Keller was a huge help to me in understanding the science of MOCVD growth. She helped me quite a bit with proper recipe writing and learning which of the various MOCVD knobs to turn.

Many, many members of support and technical staff have contributed greatly to my ability to do research and progress through the Materials PhD program. First I want to thank the MOCVD lab support staff, Mike Iza, David Whitlatch, and Brian Carralejo. Without their effort in troubleshooting and fixing our often troubled reactors none of the work in this dissertation would have been possible. I also want to thank the cleanroom staff for their constant and competent vigilance in maintaining the tools that I used to fabricate solar cells and LEDs. Special thanks to Aidan Hopkins for his help with my many dicing saw problems. Also, many thanks to Mark Cornish for maintaining and training on the AFMs and microscopes in CNSI; to Tom Mates for his comprehensive help running the SIMS tool; to the MRL TEMPO Lab staff for maintaining the UV-VIS spectrometer; and to Youli Li for maintaining the XRD diffractometers. On the administrative side, I want to thank the SSLEC staff: Yukina, Tara, Sheryl, and Aldir, and the Materials Department staff for doing such an excellent job handling the various administrative and financial duties necessary to run a large lab group and department. They allow the students to focus on science and be so much more productive as a result.

I've made many personal relationships in and out of the lab during my time in Santa Barbara that greatly enriched my research experience and my life in general. My excellent officemates over the years have been sounding boards for ideas, partners in commiseration, and good friends: Samantha Cruz, Arthur Reading, Chris Pynn, Anisa Mysaferi, and the rest

Nathan G. Young

7382A Davenport Rd.   (404) 274-5248
Goleta, CA 93117   ngyoung@engineering.ucsb.edu

EDUCATION

University of California, Santa Barbara   *Santa Barbara, CA*
Ph.D. in Materials Engineering   June 2015
Advisors: Jim Speck, Steve DenBaars   (expected)
Dissertation Title: *Efficiency Improvements through Active Region Design and Growth of III-N Quantum Well Based Optoelectronic Devices*

Stanford University   *Stanford, CA*
M.S. in Electrical Engineering   June, 2009

Stanford University   *Stanford, CA*
B.S. in Electrical Engineering   June, 2009

RESEARCH EXPERIENCE

University of California, Santa   *Santa Barbara, CA*
Barbara   September 2010-Present
Graduate Researcher
- MOCVD growth and material characterization of III-nitride thin films for solar cell and LED devices.
- Fabrication and testing of III-nitride devices including solar cells and LEDs.
- Fabricated and tested InGaN-based photovoltaic devices on c-plane, m-plane, and semipolar planes of GaN to determine the polarization-related effects on device performance.
- Employed high temperature measurements in order to understand carrier transport in nitride quantum well devices.
- Developed thin quantum barrier InGaN solar cells for improved current transport and achieved world record performance.
- Implemented a broad-spectrum anti-reflection coating and dichroic mirror to improve efficiency in InGaN solar cells.
- Developed first III-nitride LED with germanium doping for polarization field screening.

- Growth of novel structures for improved understanding of Auger recombination in III-nitride LEDs.
- Growth of novel structures for improved understanding of etch damage in InGaN quantum wells.
- Growth of novel structures for PEC liftoff of III-nitride LEDs.

Stanford University   *Stanford, CA*
Summer Undergraduate Researcher   June-August 2006
- Research assistant in the lab of Peter Peumans. Designed and programmed a user interface for a servomotor cluster tool using LabVIEW. Designed and constructed a spray-coat deposition system for thin films of organic solar cells.

PROFESSIONAL EXPERIENCE

Solexant Corporation (Siva Power)   *San Jose, CA*
Test and Characterization Engineer   June 2009-August 2010
- Owner of all company module-level test equipment. Responsible for maintaining and upgrading existing tools, designing new tools, designing test procedures, and programming user interfaces. Developed process to print top contact conductive grids. Helped develop a grid model to optimize printed grid parameters and minimize power loss.

SunPower Corporation   *San Jose, CA*
R&D Intern   June-August 2007
- Upgraded software on the cell IV measurements and spectral response measurements using LabVIEW. Characterized defects in modules using electroluminescence imaging. Implemented project to measure the effects of polarization in modules over time in various bias configurations.

PATENTS

Nathan G. Young, Tal Margalith, Steven P. DenBaars, James S. Speck, Shuji Nakamura. Germanium doping in III-Nitride LED's. Filed January 2015. Patent Pending.

Nathan G. Young, Steven P. DenBaars, James S. Speck, Shuji Nakamura, Umesh K. Mishra. Doped III-Nitride Electronic Devices. Filed November 2014. Patent Pending.

David Hwang, **Nathan G. Young**, Ben Yonkee, Burhan Saifaddin, Steven P. DenBaars, James S. Speck, Shuji Nakamura. Flexible Arrays of MicroLEDs using the Photoelectrochemical (PEC) Liftoff Technique. Filed October 2014. Patent Pending.

Nathan G. Young, Robert M. Farrell, Steven P. DenBaars, James S. Speck, Shuji Nakamura. Doping in (0001) III-Nitride Light-Emitting Devices for Effective Polarization Field Screening. Filed May 2014. Patent Pending.

AWARDS

Outstanding Graduate Student Research Achievement Award, Solid State Lighting and Energy Electronics Center, (2014).

PUBLICATIONS

N. G. Young, R. M. Farrell, M. Iza, S. Nakamura, S. P. DenBaars, C. Weisbuch, J. S. Speck. "Germanium doping of GaN for Polarization Screening Applications," to be submitted to *Journal of Crystal Growth*.

N. G. Young, R. M. Farrell, S. Oh, M. Cantore, F. Wu, S. Nakamura, S. P. DenBaars, C. Weisbuch, J. S. Speck. "Polarization Field Screening in Thick (0001) Single Quantum Well Light-Emitting Diodes," to be submitted to *Applied Physics Letters*.

Nedy, J., **N. G. Young**, K. Kelchner, Y. Hu, R. M. Farrell, S. Nakamura, S. P. DenBaars, C. Weisbuch, J. S. Speck. "Low damage dry etch for III-nitride light emitters," submitted to *Semiconductor Science and Technology*.

Piccardo, M., L. Martinelli, J. Iveland, **N. G. Young**, S. P. DenBaars, S. Nakamura, J. S. Speck, C. Weisbuch, and J. Peretti. "Determination of the First Satellite Valley Energy in the Conduction Band of Wurtzite GaN by near-Band-Gap Photoemission Spectroscopy." *Physical Review B* 89, 235124 (2014).

Iveland, J., M. Piccardo, L. Martinelli, J. Peretti, J. W. Choi, **N. G. Young**, S. Nakamura, J. S. Speck, and C. Weisbuch. "Origin of Electrons Emitted into Vacuum from InGaN Light Emitting Diodes." *Applied Physics Letters* 105, 052103 (2014).

N. G. Young, E. E. Perl, R. M. Farrell, M. Iza, S. Keller, J. E. Bowers, S. Nakamura, S. P. DenBaars, and J. S. Speck. "High-Performance Broadband Optical Coatings on InGaN/GaN Solar Cells for Multijunction Device Integration." *Applied Physics Letters* 104, 163902 (2014).

N. G. Young, R. M. Farrell, Y. L. Hu, Y. Terao, M. Iza, S. Keller, S. P. Denbaars, S. Nakamura, and J. S. Speck. "High Performance Thin Quantum Barrier InGaN/GaN Solar Cells on Sapphire and Bulk (0001) GaN Substrates." *Applied Physics Letters* 103, 173903 (2013).

Das, N. C., M. L. Reed, A. V. Sampath, H. Shen, M. Wraback, R. M. Farrell, M. Iza, S. C. Cruz, J. R. Lang, **N. G. Young**, Y. Terao, C. J. Neufeld, S. Keller, S. Nakamura, S. P. DenBaars, U. K. Mishra, and J. S. Speck. "Optimization of Annealing Process for Improved InGaN Solar Cell Performance." *Journal of Electronic Materials* 42, 3467 (2013).

Keller, S., R. M. Farrell, M. Iza, Y. Terao, **N. G. Young**, U. K. Mishra, S. Nakamura, S. P. Denbaars, and J. S. Speck. "Influence of the Structure Parameters on the Relaxation of Semipolar InGaN/GaN Multi Quantum Wells." *Japanese Journal of Applied Physics* 52, 08JC10 (2013).

Lang, J. R., **N. G. Young**, R. M. Farrell, Y.-R. Wu, and J. S. Speck. "Carrier Escape Mechanism Dependence on Barrier Thickness and Temperature in InGaN Quantum Well Solar Cells." *Applied Physics Letters* 101, 181105 (2012).

CONTRIBUTED PRESENTATIONS

N. G. Young, L. Alanazi, M. Cantore, S. H. Oh, C. Pynn, D. Becerra, M. Iza, S. Nakamura, S. P. DenBaars, and J. S. Speck. "Germanium Doping for Low Droop (0001) GaN LEDs." Paper presented at the Solid State Lighting and Energy Electronics Center Annual Review, Santa Barbara, California (November 2014).

N. G. Young, R. M. Farrell, Y. L. Hu, Y. Terao, M. Iza, S. Keller, S. Nakamura, S. P. DenBaars, and J. S. Speck. "Development of High Performance Thin Quantum Barrier InGaN Solar Cells on Sapphire and Bulk (0001) GaN Grown by MOCVD." Paper presented at the 56th Electronic Materials Conference, Santa Barbara, California (June 2014).

N. G. Young, E. E. Perl, R. M. Farrell, M. Iza, S. Keller, S. Nakamura, S. P. DenBaars, and J. S. Speck. "Thin Barrier InGaN/GaN MQW Solar Cells with Dielectric Optical Coatings." Paper presented at the Solid State Lighting and Energy Center Annual Review, Santa Barbara, California (November 2013).

N. G. Young, R. M. Farrell, Y. L. Hu, Y. Terao, M. Iza, S. Keller, S. P. DenBaars, and J. S. Speck. "Development of High Performance Thin Barrier InGaN Solar Cells on Sapphire and Bulk (0001) GaN by MOCVD." Paper presented at the UCSB Nitrides Seminar, Santa Barbara, California (May 2013).

N. G. Young, J. R. Lang, Y. Terao, R. M. Farrell, S. P. DenBaars, and J. S. Speck. "Thin Quantum Barrier InGaN Solar Cells on (0001) Bulk GaN Substrates by MOCVD." Poster presented at the Center for Energy Efficient Materials Review, Santa Barbara, California (January, 2013).

N. G. Young, J. R. Lang, R. M. Farrell, C. J. Neufeld, M. Iza, S. C. Cruz, S. Keller, Y. R. Wu, U. K. Mishra, S. Nakamura, S. P. DenBaars, and J. S. Speck. "Influence of Barrier Thickness in InGaN Quantum Well Solar Cells." Paper presented at the Solid State Lighting and Energy Center Annual Review, University of California, Santa Barbara (November 2012).

ABSTRACT

Improving Efficiency of III-N Quantum Well Based Optoelectronic Devices
through Active Region Design and Growth Techniques

by

Nathan Garrett Young

The III-Nitride materials system provides a fascinating platform for developing optoelectronic devices, such as solar cells and LEDs, which have the power to dramatically improve the efficiency of our power consumption and reduce our environmental footprint. Finding ways to make these devices more efficient is key to driving their widespread adoption. This dissertation focuses on the intersection of challenges in physics and metalorganic chemical vapor deposition (MOCVD) growth at the nanoscale when designing for device efficiency.

In order to create the best possible InGaN solar cell, a multiple quantum well (MQW) active region design had to be employed to prevent strain relaxation related degradation. There were two competing challenges for MQW active region design and growth. First, it was observed current collection efficiency improved with thinner quantum barriers, which promoted efficient tunneling transport instead of inefficiency thermally activated escape. Second, GaN barriers could planarize surface defects in the MQW region under the right conditions and when grown thick enough. A two-step growth method for thinner quantum barriers was developed that simultaneously allowed for tunneling transport

and planarized V-defects. Barriers as thin as 4 nm were employed in MQW active regions with up to 30 periods without structural or electrical degradation, leading to record performance. Application of dielectric optical coatings greatly reduced surface reflections and allowed a second pass of light through the device. This both demonstrated the feasibility of multijunction solar integration and boosted conversion efficiency to record levels for an InGaN solar cell.

III-N LEDs have achieved state-of-the-art performance for decades, but still suffer from the phenomena of efficiency droop, where device efficiency drops dramatically at high power operation. Droop is exacerbated by the polarization-induced electric fields in InGaN quantum wells, which originate from a lack of inversion symmetry in GaN's wurtzite crystal structure. These fields can be screened by using highly doped layers, but the extreme dopant densities predicted by simulation for complete screening may require using Ge as an alternative n-type dopant to Si. GaN:Ge layers with excellent electrical characteristics were grown by MOCVD with doping densities exceeding 10^{20} cm^{-3}. However, their surface morphologies were very poor and they proved a poor screening dopant in LED structures. Using Si as the n-type screening dopant, LEDs with single QW active regions were grown, packaged, and tested. Biased photoluminescence showed strong evidence of complete polarization screening. The LEDs had low droop, but also low peak efficiencies. Possible explanations for trends in efficiency with varying QW width and field screening will be discussed.

CONTENTS

1

Introduction

1.1 III-N Material Background

1.1.1 GaN Crystal Structure

(Ga,Al,In)N can have either a wurtzite or zinc blende crystal structure (Fig. 1.1), but the wurtzite form is more thermodynamically stable and thus much more common – it will be the only structure considered in this dissertation. In the wurtzite crystal structure, each group-III atom is tetrahedrally coordinate with 4 nitrogen atoms. The stacking sequence is ABABAB, where A and B each refer to III-N bilayers. Wurtzite is a hexagonal crystal system and can be thought of as interlaced hexagonal close-packed (HCP) sublattices of the individual constituent atom types. The wurtzite space group, $P6_3mc$, is non-centrosymmetric (it lacks inversion symmetry), meaning that wurtzite GaN possesses internal polarization, not present in zinc blende GaN, which gives it many unique properties, the effects of which will be discussed throughout this dissertation. The crystal can be oriented either in the Ga-polar sense (0001) or N-polar sense (000-1). The (0001) c-plane is the normal growth direction of GaN, but by utilizing different substrates, other orientations of GaN can be
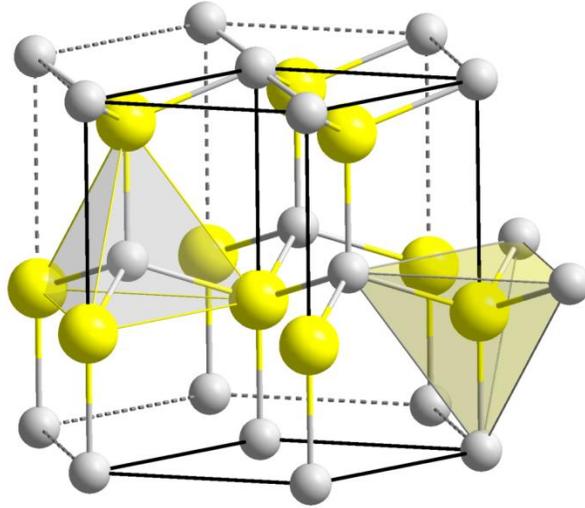
Figure 1.1: Crystal structure of wurtzite III-N compounds with coordination polyhedra. Larger yellow atoms are group-III atoms and smaller grey atoms are nitrogen.

grown, such as nonpolar (11-20) *a*-plane and (1-100) *m*-plane, which are perpendicular to the *c*- growth direction, and a whole host of semipolar planes oriented at angles between 0 and 90 degrees.

1.1.2 Polarization

Current state-of-the-art III-nitride thin films, heterostructures, and devices are grown along the [0001] axis. The total polarization of such films consists of spontaneous (P_{sp}) and piezoelectric (P_{pz}) polarization contributions, both of which originate from the single polar [0001] axis of the wurtzite III-nitride crystal structure. When III-nitride heterostructures are grown pseudomorphically, polarization discontinuities are formed at surfaces and interfaces within the crystal. These discontinuities lead to the accumulation or depletion of carriers at surfaces and interfaces, which in turn produces an electric field. Since the direction of the

Spontaneous polarization		Piezoelectric polarization, Ga face		Piezoelectric polarization, N face	
Ga face	N face	compressive	tensile	compressive	tensile
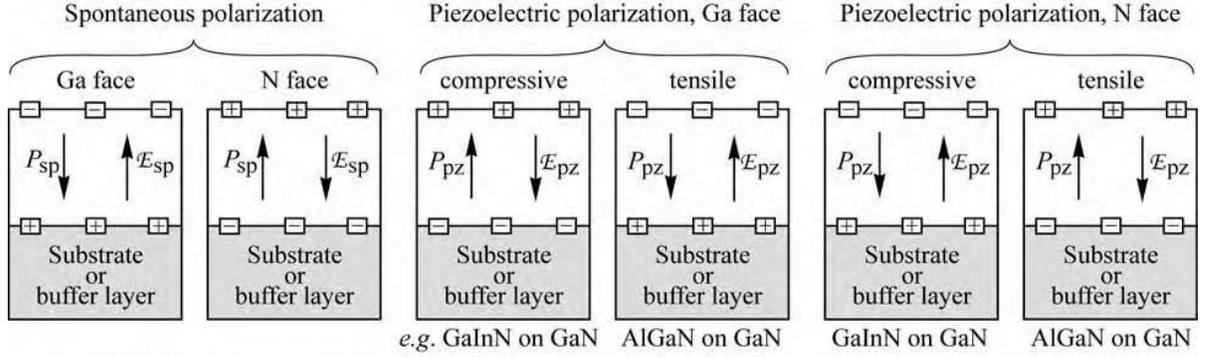
Figure 1.2: Surface charges and direction of electric field and polarization field for spontaneous and piezoelectric polarization in III-nitrides for Ga- and N-face orientations.[1]

polarization-induced electric field coincides with the typical [0001] growth direction of III-nitride thin films and heterostructures, it has the effect of "tilting" the energy bands of III-nitride devices. Certain III-N devices have harnessed polarization effects to great effect. For example, AlGaN/GaN high electron mobility transistors (HEMTs) have a polarization-induced two dimensional electron gas (2DEG) channel that enables very high performance.[2]

As mentioned above there are two separate components of the total in a thin film layer of III-N material. Spontaneous polarization arises from the lack of inversion symmetry in the wurtzite crystal structure, while piezoelectric polarization is caused by strain in the lattice. In III-N materials such as GaN, AlN, and InN, P_{sp} is the result of cation and anion positions deviating from the ideal wurtzite lattice positions. If one knows the strain perpendicular (ϵ_{xx}) and normal (ϵ_{zz}) to the surface (an easy conversion using the elastic constants of the material) then P_{pz} can be calculated:

$$P_{pz} = e_{33}\epsilon_{zz} + 2e_{31}\epsilon_{xx}, \tag{1.1}$$

where e_{31} and e_{33} are piezoelectric constants. The total polarization, **P**, then, is simply P_{pz} + P_{sp}. Spatial variation of **P** leads to a volume charge density:

E_{bi} ⟵

E_P ⟶
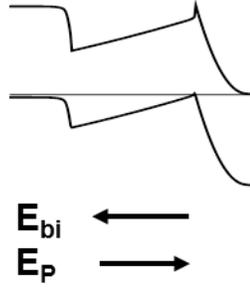
Figure 1.3: Band diagram of GaN/InGaN/GaN showing the polarization field E_p acting in the opposite direction as the built-in field E_{bi}.

$$\rho_{PE} = -\nabla \cdot \mathbf{P}, \qquad (1.2)$$

but at an abrupt heterointerface, $\mathbf{P}$ has a step function change, both due to the difference in P_{sp} between the two materials and the difference in strain, giving rise to an interface sheet charge density:

$$\sigma_{PE} = -\mathbf{n} \cdot \Delta\mathbf{P}, \qquad (1.3)$$

where n is the unit vector normal to the interface.

As shown in Fig. 1.2, P_{sp} and P_{pz} can act in the same direction or opposite directions depending on whether the strain in the layer is compressive or tensile, and whether the material is Ga- or N-face. In the case of Ga-face InGaN on GaN, which will be the heterostructure studied in detail in this dissertation in the context of solar cells and LEDs, the strain in the InGaN layer is compressive and P_{sp} and P_{pz} are opposite each other. In the blue-emitting regime with indium compositions near 20%, P_{pz} dominates, and the resulting interfacial sheet charge density is very large, approximately 2 x 10^{13} cm^{-2}.[3] In a GaN/InGaN/GaN quantum well (QW) the resulting calculated electric field is enormous: 3.25 MV/cm. This electric field acts in the opposite direction of the built-in electric field of

a GaN/InGaN/GaN p-i-n (top down) junction (Fig. 1.3), which has very important consequences in InGaN device design that will be discussed throughout the dissertation.

1.2 Solar Cells

1.2.1 The Solar Resource

The sun is the primary source of energy used to create and sustain life on our planet. It is also involved in the creation of most sources of human power. The sun provided the energy to form organic biomass, which, over millions of years in the heat and pressure beneath the earth's surface, forms hydrocarbon fossil fuels: coal, oil, and natural gas. Nuclear power from the fission of plutonium and uranium is also the result of another star's violent death. All elements in the universe heavier than iron originated from supernovae. As the world's population continues to grow at increasing rates, and with large developing countries just reaching the point of rapid industrial growth, the world's energy demand has been increasing dramatically. In 2012, the total world energy consumption equaled the equivalent of about 9 billion tons of oil.[4] That number is expected to increase to 12 billion tons of oil by 2035, even with new energy policies still under consideration. One of the greatest challenges of the 21st century will be to meet this energy demand without further harming the environment through the burning of fossil fuels.

Direct conversion of solar to electrical energy using photovoltaic (PV) systems promises to play a significant role in replacing fossil fuels with renewable energy sources. Since the turn of the century, the adoption of PV power in the US and worldwide has increased rapidly. The total installed PV capacity in 2014 alone was 40 GW, bringing the total to 177 GW worldwide.[5] As PV technology improves, increasing efficiency and

decreasing costs, it will soon reach grid parity, where it becomes economically preferable to coal and natural gas as a way to generate electrical power for the grid. One way to enable a large jump in PV efficiency is to concentrate the incident light using a relatively inexpensive optical system onto a smaller area, but highly efficient PV device. Concentrated photovoltaic (CPV) technology is a particular area where III-N materials could have a significant impact.

1.2.2 The Electromagnetic Spectrum

The sun acts as a nearly ideal blackbody radiator with an equivalent temperature of ~5800 K, emitting electromagnetic radiation over a wide range of wavelengths. The power in the emission spectrum peaks in the visible wavelengths, between 400 and 700 nm (Fig. 1.4). Just above the earth's atmosphere, the total integrated solar power density is 1353 W/m^2. The actual photon flux spectrum is shifted to longer wavelengths (there are many photons more available in the IR than in the UV) but the energy per photon drops with increasing wavelength:

$$E_{photon} = \frac{hc}{\lambda} \approx \frac{1240}{\lambda} \left(\frac{eV}{nm} \right), \qquad (1.4)$$

where h is Planck's constant, c is the speed of light, and λ is the wavelength of light in nanometers.

As light travels through the atmosphere to the earth's surface, some is reflected back into space and some is absorbed by gasses in the atmosphere. Ultraviolet (UV) light below 300 nm is absorbed by oxygen, nitrogen, and ozone, while H_2O and CO_2 absorb specific bands of the infrared (IR) spectrum. The attenuation of solar power in the atmosphere is
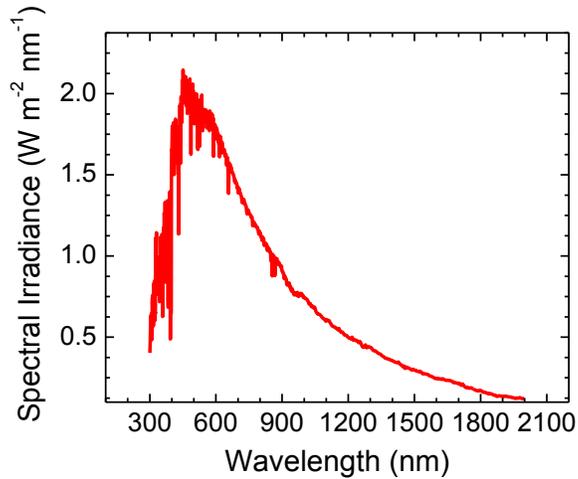
Figure 1.4: Solar spectral irradiance outside the earth's atmosphere as a function of the wavelength of light.

described by the "Air Mass" (AM) standard, which is related to the distance light travels through the atmosphere to reach the earth's surface. The AM factor can be calculated as:

$$AM = \frac{L}{L_0} = \frac{1}{\cos\vartheta},$$

(1.5)

where L is the length of the path light takes through the atmosphere, L_0 is the minimum thickness of the atmosphere form sea level (normal to the surface), and ϑ is the zenith angle of the sun above the ground. It is easy to see that Air Mass will vary with time of day, season, and latitude.

There are some common AM spectra[i] used for standardization of solar cell efficiency measurements. AM0 is the solar spectrum just outside the atmosphere, and is used for spaced based applications. AM1 is the yearly averaged solar spectrum at the equator, while AM1.5 is the solar spectrum at a zenith angle of 48.2°, corresponding to the northern US and most of Europe and commonly used as a testing standard by the solar industry. The

---

[i] The standard spectrum is the yearly average of the spectra at solar noon.
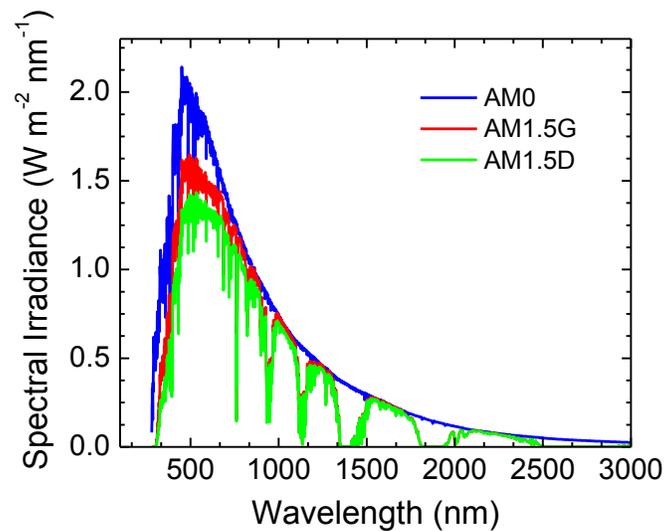
Figure 1.5: Solar spectral irradiance of the AM0, AM1.5 global, and AM1.5 direct spectra.

standardized power density of the AM1.5 spectrum is 1000 W/m^2, decreased by atmospheric effects by 26% from the AM0 power density. There are two variants of the AM1.5 spectrum: AM1.5G (global) and AM1.5D (direct). AM1.5G includes diffusely scattered light, while AM1.5D only includes directly incident light from the sun. CPV systems use the AM1.5D spectrum as a standard because the angle of acceptance of the concentrating optics is very small. The power density of the AM1.5D spectrum is only 768 W/m^2. Figure 1.5 plots the AM0, AM1.5G, and AM1.5D spectra against one another for comparison.

1.2.3 Photovoltaic Operation

At the simplest level, a solar cell is a device that converts light into electrical power. This process is known as the photovoltaic effect, which was first discovered A. E. Becquerel in 1839,[6] and it requires the creation of both a voltage and electrical current in a material that is exposed to light. Solar cells come in many different types, including organic bulk
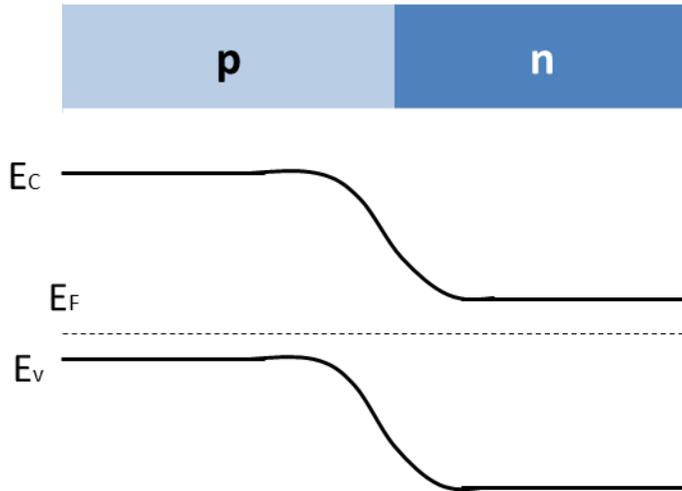
Figure 1.6: Band diagram of a p-n junction in equilibrium.

heterojunctions and dye-sensitized cells, but by far the most common form is the p-n junction diode solar cell.

A p-n junction occurs when a p-type (doped with electron accepting impurity states) and n-type (doped with electron donating impurity states) material are brought into contact (usually through direct epitaxial growth or implantation of dopants into part of a single slab of material). The Fermi level is pinned near the conduction band in the n-type material (excess electrons), near the valence band in p-type material (excess holes), and lies near the center of the bandgap in intrinsic materials. The Fermi level must remain constant at equilibrium, so near the junction, the energy bands bend (Fig. 1.6). The bending of the bands creates a voltage drop (the built in voltage, V_{BI}) in the junction region, which is depleted of charge carriers and is thus called the depletion region or space charge region. In the depletion approximation, this region begins and ends abruptly at the edges of the quasi-neutral regions on either side of the junction. It has a width of W_D given by:

$$W_D = \frac{V_{BI}}{E_{BI}} = \sqrt{\frac{2\epsilon}{q} V_{BI}(N_A + N_D)}, \qquad (1.6)$$

where ϵ is the dielectric constant, q is the charge of an electron, N_A is the concentration of acceptors, N_D is the concentration of donors, and E_{BI} is the electric field produced by ionized dopants in the space charge region.

There is a diffusion current (positive) cause by the electron concentration gradient, which is counteracted by the drift current (negative) of electrons in the electric field of the depletion region. At equilibrium these currents exactly balance and no current flows. The diffusion current increases exponentially as the potential barrier of the junction is lowered by applying a positive external voltage. The drift current from minority carriers (electrons on the p-side, for instance) reaching the edge of the depletion region is largely bias independent. The net I-V characteristics of the diode look as follows:

$$I_D = I_{diffusion} - I_{drift} = I_s \left(\exp\left(\frac{qV}{kT}\right) - 1 \right), \qquad (1.7)$$

where V is the applied voltage, T is the temperature, k is Boltzman's constant, and I_s is the reverse saturation current. I_s is thermally generated, and thus is independent of bias. In the ideal case, the current at reverse bias will be constant. Deviations from the ideal case result from additional recombination current and will affect the slope of the curve.

Under illumination, there is a constant reverse current from photogenerated carriers in the depletion region and within a diffusion length of the depletion region (as long as the p- and n- terminals are connected in a circuit). If the illuminated diode is disconnected from a circuit (open circuit) then no current can flow, but a forward voltage (photovoltage) builds across the junction to balance the generation current with the diffusion current. If the illuminated diode is connected to a circuit with a load, then reverse current will flow

(a)   **(b)**
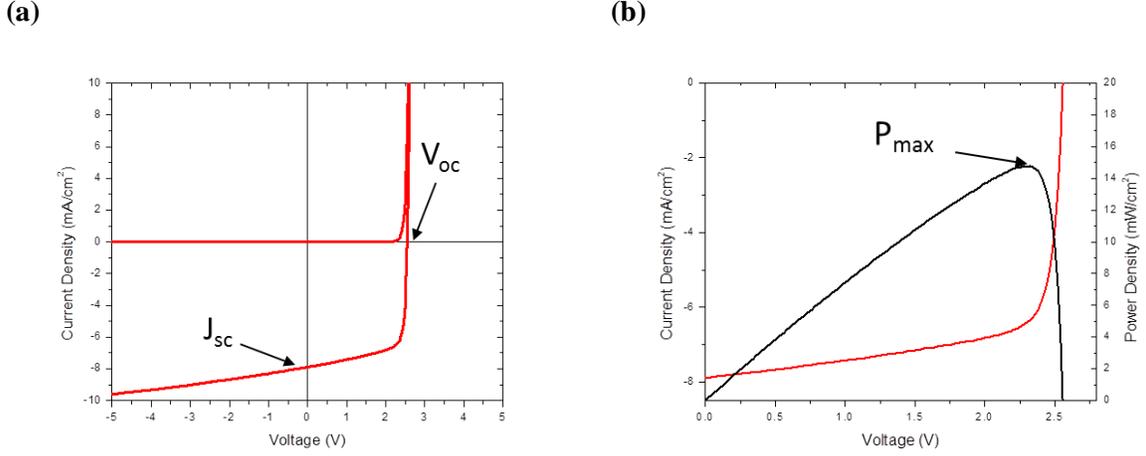
Figure 1.7: (a) J-V curve of a solar cell in the dark and under illumination. (b) P-V curve (black) and J-V curve (red) of an illuminated solar cell.

through the diode while a photovoltage drives the charges through the external circuit, thus delivering electric power. The diode electrical characteristics under illumination are very similar to Eq. (1.7) with the addition of a term for the photogenerated current, I_L:

$$I_{ill} = I_D - I_L = I_s \left(\exp\left(\frac{qV}{kT}\right) - 1 \right) - I_L \,. \tag{1.8}$$

Equation (1.8) is the governing characteristic of a solar cell, and many figures of merit can be derived from it. Three important bias points for a solar cell are the open circuit voltage ($V = V_{oc}$), short circuit ($V = 0$) and maximum power ($V = V_{mp}$). V_{oc} is defined as the voltage at which no net current flows, and V_{mp} is defined as the voltage at which the current*voltage product is a maximum. At short circuit, the current that flows is called the short circuit current, I_{sc}, which in the ideal case of Eq. (1.8) is equal to I_L. Solving Eq. (1.8) for voltage at open circuit gives us:

$$V_{oc} = \frac{kT}{q} \ln\left(\frac{I_L}{I_s} + 1\right) \approx \frac{kT}{q} \ln\left(\frac{I_{sc}}{I_s}\right). \tag{1.9}$$

11
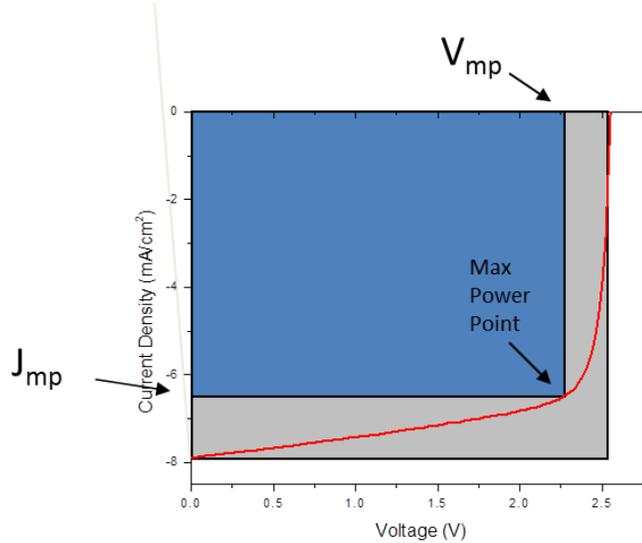
Figure 1.8: J-V curve of an illuminated solar cell with shaded areas showing the maximum power and the ideal maximum power bracketed by V_{oc} and J_{sc}. The ratio of the darker shaded area to the lighter shaded area is the fill factor.

It is important to note that V_{oc} will increase with I_{sc}, a factor in the increased efficiency with higher solar concentration. Figure 1.7(a) shows an example solar cell J-V curve with and without illumination, pointing out the open circuit voltage and short circuit current. Figure 1.7(b) shows the power-voltage curve for the same device, pointing out the maximum power point.

Another important figure of merit from the *I-V* characteristic is the fill factor (FF), a measure of the "squareness" of the *I-V* curve. A solar cell with a perfectly square *I-V* curve would have a FF of 100% and a maximum power operating point at V_{oc} and I_{sc}. The FF is defined as follows:

$$FF = \frac{V_{mp}I_{mp}}{V_{oc}I_{sc}}. \tag{1.10}$$

Figure 1.8 shows a graphical illustration of the FF on an illuminated *J-V* curve. In reality, the FF can never reach 100% because of Eq. (1.8): current has an exponential dependence

on voltage and the "squareness" of the knee of the curve depends on the magnitude of the exponential, which in turn depends on the voltage. Therefore, devices with higher V_{oc} will generally have high FF. The power conversion efficiency of a solar cell is related to its figures of merit in the following way:

$$\eta_{conv} = \frac{FFV_{oc}I_{sc}}{P_{in}}. \tag{1.11}$$

where P_{in} is the total power of the solar irradiance incident on the solar cell.

So far the discussion has been limited to ideal solar cells. Real solar cells have non-idealities, such as electrical leakage, excess recombination, and imperfect contacts. These non-idealities can be described using two parasitic resistance terms: the series resistance, R_s, and the shunt resistance, R_{sh}, as well as a diode ideality factor, n. In an ideal device, $R_s = 0$ and $R_{sh} = $ infinity. In the *I-V* curve, shunt resistance is seen as a slope at or near short circuit, and series resistance is seen as a slope at or near open circuit. The ideality factor becomes more than one when there is excess recombination in the diode. When these terms are incorporated into the solar cell equation (Eq. (1.8)), the more general form can be written as follows:

$$I_{ill} = I_s \left(\exp \left(q \frac{V + IR_s}{nkT} \right) - 1 \right) + \frac{V + IR_s}{R_{sh}} - I_L. \tag{1.12}$$

The presence of the non-ideal terms results in a reduction of FF.

The final figure of merit for a solar cell is the external quantum efficiency (EQE). The EQE is a measure of the number of electrons collected as current per incident photon at a given wavelength. Any photons that are not absorbed will not contribute to the current, so EQE at those wavelengths is zero (below the bandgap energy, for example). For photons that are absorbed, there is another efficiency term, the internal quantum efficiency (IQE),

that measures the efficiency of the conversion of generated electron-hole pairs to collected current.

$$EQE = IQE * Abs \tag{1.13}$$

A measurement of EQE is spectrally resolved − each specific wavelength has a unique EQE value. Often the peak value of the EQE spectrum is quoted. EQE falls off near the bandgap of the solar cell material, as its absorption spectrum falls off. Absorption in solar cells with different architectures will be discussed in Chapter 3. Integrating the product of EQE and spectral irradiance over all wavelengths will yield the J_{sc} of the solar cell. Knowledge of the EQE and *I-V* figures of merit gives a full understanding of the performance of a solar cell.

1.2.4 Solar Cell Efficiency Limit

The efficiency of a single junction solar cell is limited to about 30% under one sun illumination.[7] This is known as the *detailed balance limit* and was derived by Shockley and Quiesser in 1961. Detailed balance uses only thermodynamic principles and no assumptions about the material itself to arrive at a limiting efficiency. It assumes that the solar cell is a perfect black body (at 300K) in radiative contact with the sun, also a black body (at 6000K). At equilibrium the radiation from the sun incident on the solar cell must be equal to the radiation of the solar cell itself. The efficiency reaches its limit when there is perfect radiative coupling between the black bodies and no nonradiative recombination within the solar cell. Thermodynamically speaking, the mechanism by which efficiency is limited is the fact that the solid angle subtended by the sun in the sky is very small. Using optics to concentrate sunlight effectively increases this angle. Even with arbitrarily large concentration, however, the maximum achievable efficiency is 44% because below-bandgap

light is not absorbed (and a zero bandgap material that absorbed all the light would generate no voltage). The maximum achievable efficiency depends on bandgap, and without concentration, it peaks at about 30% at a bandgap of about 1.1 eV.

1.2.5 Multijunction Solar Cells

The efficiency of a single junction solar cell is limited to 30% mainly due to the energy lost to thermalization after the absorption of photons with energies greater than the bandgap. The only way to increase the efficiency of a photovoltaic device at the same light concentration factor is to add more junctions that can more efficiently convert smaller sections of the solar spectrum. This type of device is known as a multijunction solar cell (MJSC). Figure 1.9 shows a schematic of a triple junction solar cell made up of three material junctions of descending bandgap connected optically and electrically in series. Each junction absorbed the slice of the solar irradiance spectrum above its bandgap, and below the bandgap of the junction above it. These slices of the solar spectrum have been color coded in Fig. 1.9. Long wavelength light below the bandgap of the bottom junction material passes through the device unabsorbed.

The reason an MJSC is more efficient than a single junction device that absorbs the same amount of the solar spectrum (for example, a single junction made up of the material that forms the bottom junction in the MJSC) is thermalization losses. No matter the energy of an absorbed photon, the generated electron and hole will almost instantaneously thermalize, or lose energy to lattice vibrations, down to the lowest available state at the conduction and valence band edges. By stacking materials in descending order of bandgap, the solar
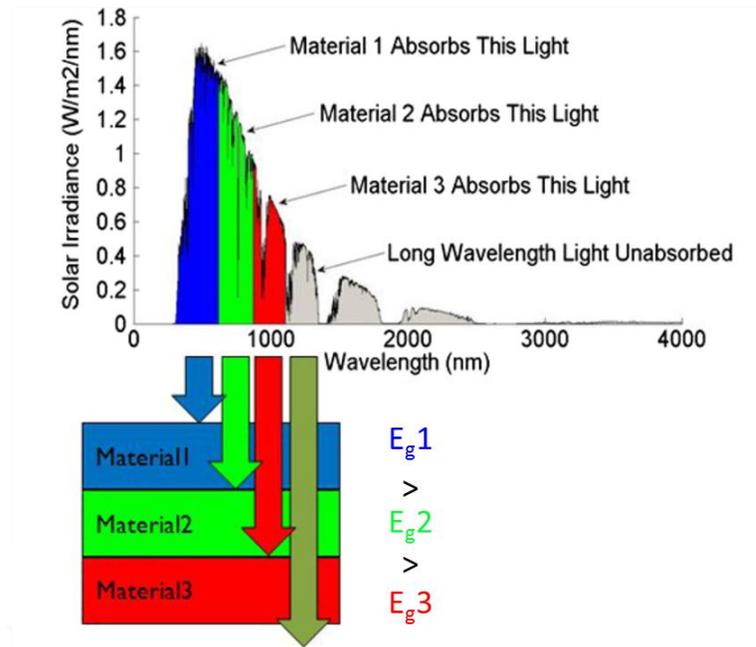
Figure 1.9: A schematic cross section of a triple junction solar cell with three materials of descending bandgap energy that absorb different slices of the solar irradiance spectrum, color coded to match each material. Long wavelength light below the bandgap of Material 3 passes through the structure unabsorbed.

spectrum gets absorbed in slices. Each slice that is absorbed by a higher bandgap than the bottom junction converts more of its energy to power in the device.

Theoretically, with an infinite number of junctions, a solar cell could reach 86% conversion efficiency.[8] In practice, the highest performance MJSCs are 4 junction devices that have reached above 45% efficiency.[9] There are many practical limitations to approaching the theoretical limit, or even to increasing efficiencies to 50%. Since the junctions are most often connected electrically in series, they must be current matched or the lowest current producing junction will limit the current of the other junctions and drive down overall efficiency. Achieving current matching involves carefully choosing the exact bandgap values and absorber thicknesses for each junction so that the photons absorbed for each slice of the spectrum (Fig. 1.9) are equal. However, arbitrary bandgaps are not easily

achievable over a wide range of energies. The easiest way to connect junctions in series is by growing a single epitaxial stack with many different materials and tunnel junctions between each junction. These designs usually begin with either a GaAs or Ge substrate. Materials that make up other junctions in the device are often InGaAs (for lower bandgaps) and InGaP (for higher bandgaps). While it is possible to grow multiple junctions with the same lattice constant and avoid strain relaxation, that approach limits the available bandgaps and the maximum possible efficiency. The most efficient MJSC devices are based on an inverted metamorphic (IMM) structure.[10–12] An example of an IMM growth begins with a GaAs substrate, which forms the middle junction. Then a lattice matched top junction of InGaP is grown on one side (lattice matching maintains material quality, which is most important in the widest bandgap junction that produces the most power), and a metamorphic InGaAs junction is grown on the other side with a compositionally graded buffer in between. The growth of IMM cells, and any MJSC for that matter, is extremely time consuming, complex, and expensive. That is why the dominant current market for these devices is in space, where power per area or weight is a far more important metric than cost. Terrestrially, MJSCs are employed in CPV systems with complicated optics and solar tracking equipment.

CPV systems using MJSCs can achieve efficiencies far exceeding those of systems that use conventional single junction solar cells.[7,13] One of the most effective ways of reducing the system cost is to increase the efficiency of the MJSC. However, the number of junctions must be increased to significantly improve MJSC efficiency. Current state-of-the-art MJSCs with 3 or 4 junctions achieve greater than 40% power conversion efficiency under concentrations up to 1000 suns, but the top junction bandgap energy is limited to

below 2 eV in these designs due to inherent materials limitations in arsenide and phosphide-based III-V semiconductors.[10,11,14] Efficient utilization of higher energy photons requires an additional junction with a wider bandgap, preferably near 2.6 eV for a 5th junction.[15] InGaN is a viable candidate material for this additional junction because of its tunable direct bandgap, high absorption coefficient, radiation resistance, and extensive development for use in high-performance light-emitting diodes, which have very similar structures to InGaN-based solar cells.[16–18] The details of how a nitride-integrated MJSC could be achieve will be discussed in Chapter 4.

1.3 Light-Emitting Diodes

1.3.1 Basic LED Operation

An LED is in many ways identical to a solar cell that is operated in reverse: current flows into it instead of out of it, using power to generate light instead of using light to generate power. The internal structure of an LED is very similar to that of a solar cell. Both rely on a P-N junction diode structure. During operation, current flows from the P and N contacts into the active layers of the LED, where electrons and holes recombine. In a well-designed LED, most of that recombination will be radiative, emitting light at the wavelength corresponding to the recombination transition energy (see Eq. (1.4)). The recombination transition energy is the bandgap of the active material in a homojunction or double heterojunction structure with no quantum confinement or electric field. The transition energy in a QW is larger than the bandgap by the energy separation of the ground electron and hole states. The need for efficient radiative recombination means that LEDs must be

made from direct bandgap materials, a constraint not placed on solar cells, which treat any type of recombination as a loss.[i]

Whereas a solar cell operates at voltages below diode turn on (below the bandgap of the active material), an LED operates at voltages that are generally above the bandgap of the active material. The LED's voltage during operation is known as the forward voltage (V_f). The light output power (LOP) of an LED is the cumulative energy of each photon emitted per second. Often a single wavelength approximation is made when calculating LOP, but real LEDs have a somewhat broad, approximately Gaussian, distribution of wavelengths around the peak wavelength. A figure of merit for the broadness of LED emission is called the full width at half maximum (FWHM), which is the width of the emission spectrum in nm at half the peak intensity. The input electrical power to the LED is V_f times the injected current density, J, and the electrical efficiency of an LED is known as the wall-plug efficiency (WPE), which has the following relationship:

$$WPE = \frac{LOP}{V_f \times J}. \tag{1.14}$$

Another way to look at the performance of an LED is through quantum efficiency. There are two types of quantum efficiency, much like in solar cells: IQE and EQE. The definitions differ slightly from solar cells, however. IQE in an LED is defined as the ratio of photons created to electrons injected into the active region. It can also be called the radiative efficiency. It is useful to look at IQE in terms of recombination rates, since all injected electrons must recombine with holes by either a radiative or nonradiative process. There are three types of recombination processes with rates that depend to varying degrees on the

---

[i] This assumes no photon recycling, where radiatively emitted photons are re-absorbed. Photon recycling is a minor contribution to most solar cells, but is an essential consideration in devices that approach the thermodynamic efficiency limit. Nitride LEDs have minimal self-absorption due to a large Stokes shift.

active carrier density n: Shockley-Read-Hall (SRH) non-radiative recombination (proportional to n), bimolecular radiative recombination (proportional to n^2), and Auger non-radiative recombination (proportional to n^3). The injected current density J can be written as the sum of these rates:

$$J = An + Bn^2 + Cn^3,$$ (1.15)

where A, B, and C are proportionality coefficients for SRH, radiative, and Auger recombination, respectively. IQE is simply the ratio of radiative recombination to total recombination:

$$IQE = \frac{Bn^2}{An + Bn^2 + Cn^3}.$$ (1.16)

EQE, on the other hand, is the ratio of emitted photons to injected electrons. The difference between EQE and IQE lies in the extraction efficiency of the device (η_{ext}).

$$EQE = IQE \times \eta_{ext}$$ (1.17)

Only photons that escape the LED into air contribute to EQE. The details of light extraction are beyond the scope of this dissertation, but the significance of its impact is illustrated by the example of a GaN LED with perfectly flat, parallel surfaces and no coatings. Snell's law dictates that the critical angle for total internal reflection between GaN and air is only about 23 degrees. In this case, any photon emitted more than 23 degrees from perpendicular to the surface will not escape. With only one escape cone (light can only escape out of the top surface and does not reflect off of any other surface) η_{ext} is only about 4% in a GaN based LED. If light can escape out of all 6 sides, then there are 6 escape cones and η_{ext} increases to 24%. There are several strategies to improve light extraction, such as chip shaping, surface roughening, and encapsulation. Light extraction is a close relative to light trapping in solar cells, which will be discussed in more detail in chapter 5.

1.3.2 Efficiency Droop

In an ideal LED, light output power should scale linearly with injected current. Real devices, however, suffer from a phenomena called droop in which the LOP is sublinear with current (Fig 1.10(a)). A more formal definition of droop is in terms of efficiency. The quantum efficiency of an LED peaks at a certain current density and decreases at higher current densities, determining the droop:

$$Droop = 1 - \frac{QE_{(J > J_{peak})}}{QE_{(J_{peak})}}, \tag{1.18}$$

where J_{peak} is the current density at peak quantum efficiency (Fig 1.10(b)). The reason that the IQE has a maximum point can be seen from the *ABC* model for efficiency in Eq. (1.16). As *J* increases, so does *n*. At low carrier density, IQE is dominated by the *A* term. As *n* increases, the *B* term begins to take over, which causes IQE to increase. At high carrier density, the *C* term takes over from the *B* term, causing a drop in IQE. From this simple ABC model, it appears that Auger recombination is the clear cause of droop; however, this has been the topic of intense debate for years.

A few different potential mechanisms for efficiency droop have been proposed. It was initially thought that the Auger coefficient in GaN would be far too low for Auger to be responsible for droop.[19] When theorists took into account higher order conduction bands[20] and phonon scattering,[21] they saw Auger scattering become a realistic possibility. Besides Auger, many have hypothesized that carrier overflow from the active region at high currents was responsible for droop.[22] Others blamed carrier delocalization at high injection from quantum dot-like regions of high indium content.[23] When droop was observed by PL and in

(a)

Flux

sublinear increase

au

current density (A/cm²)

(b)

External Quantum Efficiency

droop

onset ~10A/cm²

au

EQE
droop

current density (A/cm²)
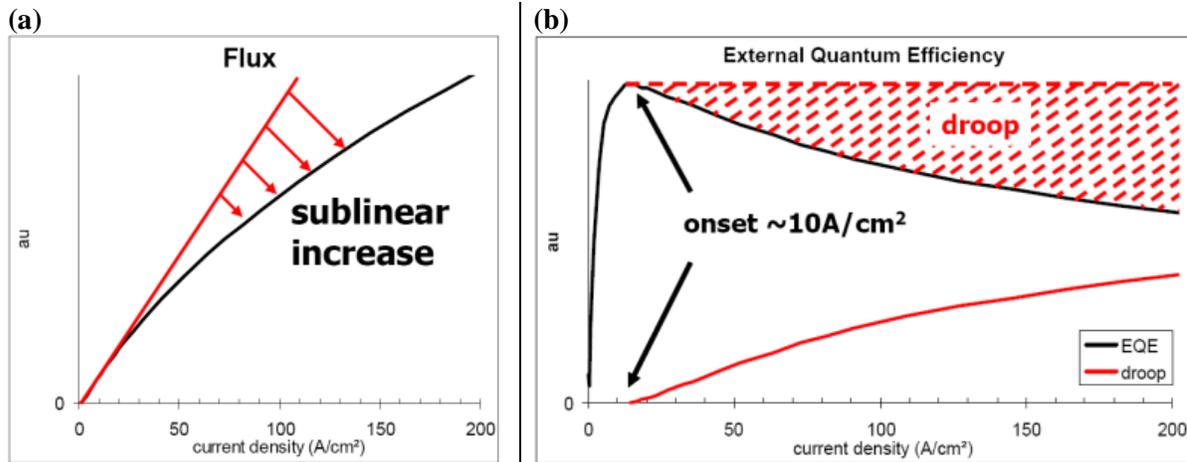
Figure 1.10: LED droop is seen in (a) the sublinear increase of LOP with current, and (b) the drop in efficiency after a peak at lower current density.

bulk GaN homojunctions, the theories of carrier injection effects and indium segregation effects were disproven.[24] Still, until recently, no one had observed direct evidence of Auger recombination in III-N LEDs. That changed when Iveland, *et al*. performed electron emission spectroscopy measurements on InGaN QW-based LEDs.[25] They observed a high energy electron peak simultaneously with a drop in radiative efficiency. The fact that there was a linear correlation between the high energy electron current and the "droop current" was convincing evidence that an Auger process was the dominant mechanism responsible for LED droop.

1.4 Preview of the Dissertation

This dissertation focuses on the growth and characterization of InGaN/GaN quantum well-based optoelectronic structures. Specifically, this work examines novel methods in MOCVD growth and active region design for increasing the efficiency of III-N solar cells and LEDs. Chapter 2 will focus on the specific background necessary to understand the

challenges faced in growing InGaN/GaN QW structures. Of particular interest are the role of threading dislocations, InGaN compositional fluctuations, and V-defects. Chapter 3 will discuss the details of optical processes in III-N QW structures. Starting from Fermi's Golden Rule, the effects of quantum confinement, excitons, and electric fields on absorption will be examined. Chapter 4 will cover advancements in InGaN based multiple quantum well (MQW) solar cells. After a discussion of carrier transport in MQW structures, results of the optimization of a two-step barrier growth method will be shown. The optimized growth structure is then used in InGaN solar cells with optical coatings that show record performance. Chapter 5 will cover the results of polarization screened single QW LEDs, starting with a discussion of the effects of polarization on droop and continuing with simulations predicting full screening of polarization fields through doping. The electrical and optical results of fully packaged single QW LEDs with and without screening will be discussed in detail to prove the effectiveness of polarization screening and explain remaining sources of inefficiency. Chapter 6 will cover efforts in doping GaN with germanium. Electrical characteristics and structural analysis of GaN:Ge layers will be presented. Finally, Chapter 7 will summarize the overall conclusions from this dissertation, as well as present ideas for future work.

References

1. Schubert, E. F. *Light Emitting Diodes*. (Cambridge University Press, 2006).

2. Mishra, U. K., Parikh, P. & Wu, Y. F. AlGaN/GaN HEMTs - An overview of device operation and applications. *Proc. IEEE* **90,** 1022–1031 (2002).

3. Della Sala, F. *et al.* Free-carrier screening of polarization fields in wurtzite GaN/InGaN laser structures. *Appl. Phys. Lett.* **74,** 2002 (1999).

4. http://www.worldenergyoutlook.org/publications/weo-2014/.

5. http://www.ren21.net/status-of-renewables/global-status-report/.

6. https://en.wikipedia.org/wiki/Photovoltaic_effect.

7. Shockley, W. & Queisser, H. J. Detailed Balance Limit of Efficiency of p-n Junction Solar Cells. *J. Appl. Phys.* **32,** 510 (1961).

8. Würfel, P. Thermodynamic limitations to solar energy conversion. *Phys. E Low-Dimensional Syst. Nanostructures* **14,** 18–26 (2002).

9. Green, M. A., Emery, K., Hishikawa, Y., Warta, W. & Dunlop, E. D. Solar cell efficiency tables (Version 45). *Prog. Photovoltaics Res. Appl.* **23,** 1–9 (2015).

10. Stan, M. *et al.* High-efficiency quadruple junction solar cells using OMVPE with inverted metamorphic device structures. *J. Cryst. Growth* **312,** 1370–1374 (2010).

11. Geisz, J. F. *et al.* 40.8% Efficient Inverted Triple-Junction Solar Cell With Two Independently Metamorphic Junctions. *Appl. Phys. Lett.* **93,** 123505 (2008).

12. Geisz, J. F. *et al.* High-efficiency GaInP∕GaAs∕InGaAs triple-junction solar cells grown inverted with a metamorphic bottom junction. *Appl. Phys. Lett.* **91,** 023502 (2007).

13. Henry, C. H. Limiting efficiencies of ideal single and multiple energy gap terrestrial solar cells. *J. Appl. Phys.* **51,** 4494 (1980).

14. King, R. R. *et al.* 40% efficient metamorphic GaInP∕GaInAs∕Ge multijunction solar cells. *Appl. Phys. Lett.* **90,** 183516 (2007).

15. McMahon, W. E. *et al.* Metal Pillar Interconnection Topology for Bonded Two-Terminal Multijunction III–V Solar Cells. *IEEE J. Photovoltaics* **3,** 868–872 (2013).

16. David, A. & Grundmann, M. J. Influence of polarization fields on carrier lifetime and recombination rates in InGaN-based light-emitting diodes. *Appl. Phys. Lett.* **97,** 033501 (2010).

17. Wu, J. *et al.* Superior radiation resistance of In 1-xGa xN alloys: Full-solar-spectrum photovoltaic material system. *J. Appl. Phys.* **94,** 6477–6482 (2003).

18. Krames, M. R. *et al.* Status and Future of High-Power Light-Emitting Diodes for Solid-State Lighting. *J. Disp. Technol.* **3,** 160–175 (2007).

19. Hader, J. *et al.* On the importance of radiative and Auger losses in GaN-based quantum wells. *Appl. Phys. Lett.* **92,** 0–3 (2008).

20. Delaney, K. T., Rinke, P. & Van De Walle, C. G. Auger recombination rates in nitrides from first principles. *Appl. Phys. Lett.* **94,** 92–95 (2009).

21. Pasenow, B. *et al.* Auger losses in GaN-based quantum wells: Microscopic theory. *Phys. Status Solidi Curr. Top. Solid State Phys.* **6,** (2009).

22. Schubert, M. F. *et al.* Polarization-matched GaInNAlGaInN multi-quantum-well light-emitting diodes with reduced efficiency droop. *Appl. Phys. Lett.* **93,** 2006–2009 (2008).

23. Chichibu, S. F. *et al.* Origin of defect-insensitive emission probability in In-containing (Al,In,Ga)N alloy semiconductors. *Nat. Mater.* **5,** 810–6 (2006).

24. David, A. & Gardner, N. F. Droop in III-nitrides: Comparison of bulk and injection contributions. *Appl. Phys. Lett.* **97,** 4–7 (2010).

25. Iveland, J., Martinelli, L., Peretti, J., Speck, J. S. & Weisbuch, C. Direct Measurement of Auger Electrons Emitted from a Semiconductor Light-Emitting Diode under Electrical Injection: Identification of the Dominant Mechanism for Efficiency Droop. *Phys. Rev. Lett.* **110,** 177406 (2013).

2

MOCVD Growth of InGaN/GaN Quantum Well Structures

2.1 MOCVD growth of GaN

All devices and thin films described in this dissertation are grown by metal organic chemical vapor deposition (MOCVD). MOCVD growth of GaN requires gallium and nitrogen precursors: typically tri-methyl gallium (TMGa) or tri-ethyl gallium (TEGa) and ammonia (NH_3). TEGa is often used in active regions of solar cells, LEDs, and laser diodes because of its lower carbon impurity incorporation compared to TMGa. The ethyl groups have a C-C double bond that makes them more stable and results in less free carbon in the reactor that can be incorporated onto the substrate. Growth of InGaN or AlGaN alloys requires indium and aluminum precursors: typically tri-methyl indium (TMIn) and tri-methyl aluminum (TMAl). N_2 and/or H_2 carrier gas flows through these metal-organic (MO) sources either bubbling through a liquid or flowing over a solid surface. The vapor pressure of the MO, controlled by temperature, allows some to be picked up in the vapor phase and carried into the reactor by the carrier gasses. Since nitride optoelectronics are p-n diode-based devices, n- and p-type dopant sources must also be present. Typically disilane (Si_2H6)
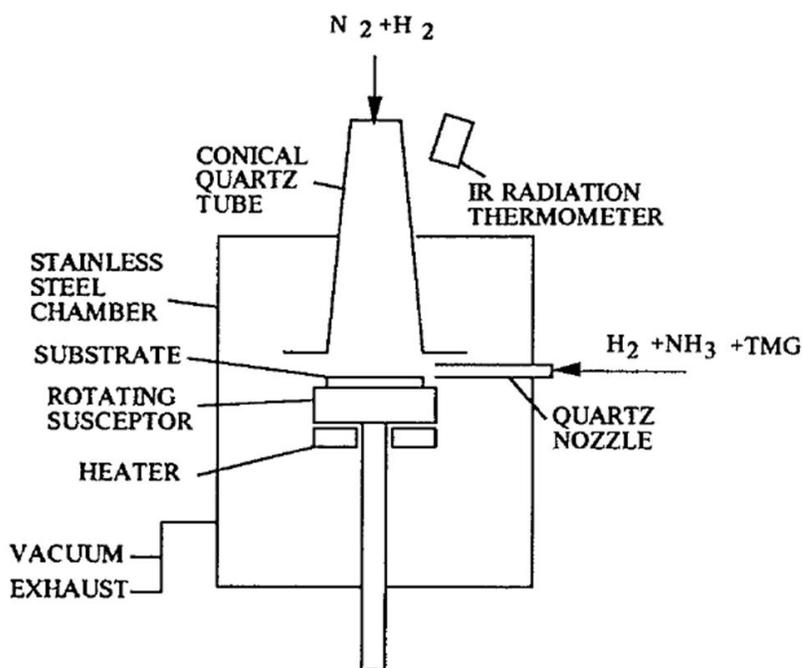
Figure 2.1: Schematic of a novel two-flow MOCVD reactor for GaN growth.[1]

and bis(cyclopentadienyl)magnesium (Cp$_2$Mg) as silicon (n-type) and magnesium (p-type) sources. Disilane is a direct gas source, while Cp$_2$Mg is a bubbler. Generally with these doping sources, the flow rate is proportional to the dopant incorporation.

The reactor used for growths in this dissertation was a horizontal flow design with a vertical subflow, designed by Nakamura (Fig. 2.1).[1] Flows of MO gasses and NH3, pushed by carrier gasses, combine is a nozzle and then flow into the reactor chamber and over the substrate. The substrate sits on a graphite puck, which rests on a SiC susceptor, which is indirectly heated during growth. Susceptor temperatures for (In,Al)GaN growth range from 600°C to 1200°C, though the temperature at the growth surface is slightly lower. High temperatures are necessary to crack MO source molecules, separating the group III metal from its organic side groups (and separating N from NH$_3$). The presence of the vertical subflow helps depress the thermal boundary layer, which is the characteristic region of

27

concentration gradients in which reactants are depleted. Essentially, only MOs that enter the boundary layer contribute to epitaxial growth, and the thinner the boundary layer, the higher and more controllable the growth rate. Carrier flow rates and subflow rates must be chosen carefully to ensure laminar flow of gasses over the substrate for a consistent growth rate. The susceptor also rotates during growth to ensure uniformity over the substrate.

2.2 Substrates and Threading Dislocations

An early difficult for GaN epitaxy was the lack of a native GaN substrate. Several non-native substrates were explored, such as spinel ($MgAl_2O_4$), SiC, and sapphire (Al_2O_3), which turned out to be the most common and is the substrate used for most growths described in this thesis. The lattice mismatch between sapphire, with a corundum crystal structure, and GaN is about 13%. Therefore, when GaN is grown metamorphically on sapphire, a low temperature nucleation layer of GaN or AlN must first be grown. This layer is highly dislocated. Then during high temperature GaN growth dislocations undergo self-annihilations and the film coalesces. The threading dislocation density (TDD) of early GaN on sapphire was well over 10^{10} cm^{-2}. Improved nucleation layers and thicker buffer templates have improved the TDD of GaN on sapphire to near 10^{8} cm^{-2}. Much more in depth information on nucleation layer evolution can be found in a review article by Koleske *et al.*[2] This is still many orders of magnitude higher than defect densities seen in other optoelectronic materials, such as GaAs. It is nothing short of miraculous that GaN can produce such efficient devices with so many defects.

Threading dislocations are electrically charged. They therefore attract carriers, which then recombined nonradiatively at defect states in the bandgap at the dislocation. From a

device perspective, TDs act as nonradiative centers and leakage pathways.[3,4] The largely accepted theory for why radiative recombination remains efficient in GaN based devices with large TDD is that alloy fluctuations lead to carrier localization at potential minima where the majority of recombination takes place, away from the dislocations.[5]

We may be reaching the limits of how efficient devices can be made on foreign substrates with high defect densities. The path to higher efficiencies may lie in bulk freestanding GaN substrates that are much more expensive than sapphire at the moment, but can achieve TDDs of 10^3 cm^{-2} and possibly below.[6] There are three main techniques used to grow bulk GaN. Hydride vapor phase epitaxy (HVPE) has high growth rates but only marginally improved TDD. It is the main method used to create commercial bulk GaN wafer today, up to 6" in diameter. The ammonothermal method uses ammonia as a solvent, and grows GaN crystals at relatively low temperatures around 600°C, but very high pressures of hundreds of MPa.[7] The sodium flux method involves adding Na to a Ga melt to increase the N concentration in solution. It involves a slightly higher temperature, but much lower pressure than ammonothermal growth.[8]

2.3 InGaN Quantum Well Growth

2.3.1 Indium Segregation and Phase Separation

InGaN must be grown at significantly lower temperatures than GaN because of indium's tendency to desorb from the surface at higher temperatures and lower growth rates. One part of the challenge in growing InGaN layers with relatively high indium content is compositional instability that occurs at low growth temperatures. A large miscibility gap is predicted between GaN and InN that originates from the lattice mismatch.[9,10] Phase
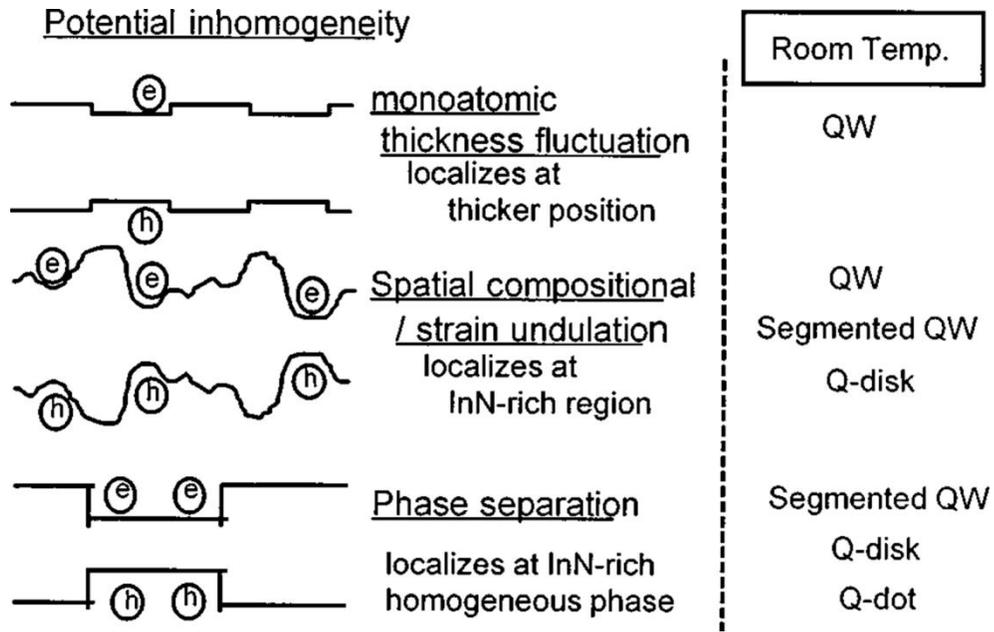
Figure 2.2: Schematic illustration of carrier localization in InGaN. Each structure may act as a QW, segmented QW, Q disk, or Q dot depending on the lateral size and the degree of the potential inhomogeneity at room temperature.[11]

separation depends on growth temperature and composition, but models predict it should occur at lower compositions than those for which it is observed. Biaxial strain present in InGaN epitaxial films helps suppress phase separation by lowering the critical temperature for spinodal decomposition.[12] Phase separation remains an issue for In compositions over 40%, but studies have also demonstrated single phase InGaN over the entire composition range by MOCVD.[13] Phase separation decreases the efficiency of a solar cell because the lowest bandgap phase will dominate the V_{oc}.

Large scale phase separation is rarely observed except in extremes of InGaN composition and thickness, but smaller scale compositional fluctuations are present in most InGaN films. These fluctuations in composition are consistent with a random alloy[14] and are suspected to be responsible for defect-insensitive light emission in nitride LEDs and LDs.[5] Figure 2.2 shows a schematic of the different scales of compositional inhomogeneity in InGaN layers. In solar cells, the resulting potential inhomogeneity in the absorbing InGaN

layers can act as shallow traps and potentially reduce device performance.[15] The scale of the fluctuation also increases with increasing indium content.[16] Simulations of LED performance are greatly improved by including random indium fluctuations in line with observations in atom probe tomography.[14] These simulations show that indium fluctuations are responsible for emission broadening, for much lower than expected operating voltage, and possibly for the Auger recombination dominance of efficiency droop.

2.3.2 Strain and Relaxation

While strain may help InGaN solar cells by suppressing phase separation, it also has significant drawbacks. InN and GaN have a lattice mismatch of about 11%. Blue-emitting QWs with a composition of $In_{0.18}Ga_{0.82}N$ have a mismatch of about 1.8%. As InGaN grows pseudomorphically on GaN, strain builds up in the InGaN layer because of the large lattice mismatch. At a thickness defined as the Matthews-Blakeslee critical thickness, the strain builds to a point where the film starts to relax by either through three-dimensional growth followed by dislocation mediated relaxation, or by direct formation of misfit dislocations.[17] The (0001) plane is the basal slip plane in GaN, on which misfit dislocations could glide and relieve strain via plastic deformation. Semipolar planes oriented at angles from c-plane relax in this manner. However, growth on c-plane means that there is no resolved shear stress on the (0001) plane and consequently no misfit glide. InGaN relaxation on c-plane likely occurs due to local shear stresses around three dimensional growth features such as V-defects.[18] In essence, existing threading dislocations open up into inverted hexagonal pyramidal pits, relieving strain elastically. On bulk GaN substrates with a very low TDD, however, there are few nucleation sites for these kinds of three-dimensional features. In

31
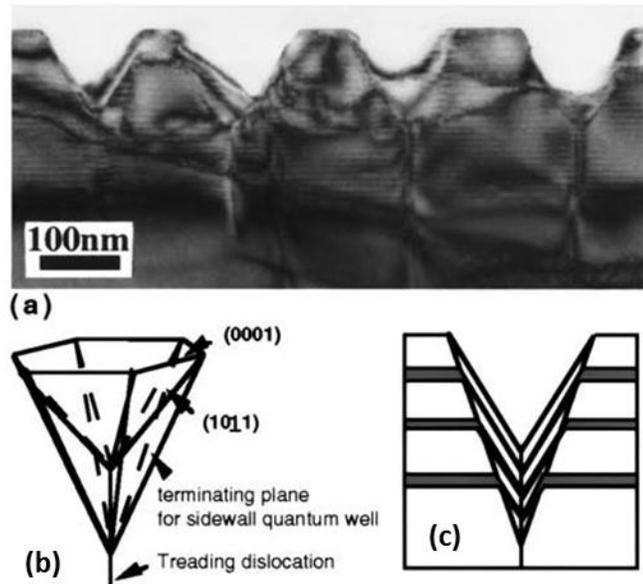
Figure 2.3: a) A TEM image of V-defects in (0001) GaN. b) (10-11) planes terminate the inner sidewalls and nucleation occurs on TDs. c) QWs thickness and spacing changes on v-defect sidewalls.[19]

these situations and with indium compositions greater than 11% and thicknesses greater than 100 nm, it has been found that relaxation occurs via misfit dislocation formation and glide on the secondary (11-22) slip system.[20]

2.4 V-Defects

As discussed in the previous section, V-defects are inverted hexagonal pyramidal pits that nucleate on existing threading dislocations during MOCVD growth of *c*-plane InGaN and GaN. Figure 2.3 shows a cross sectional TEM of V-defects along with schematics of their structure and their effect on an MQW. V-defects may play a role in relieving stress during InGaN layer growth, but their development is not primarily driven by strain in the crystal lattice. Instead they form due to kinetically limited growth on the {10-11} sidewall facets.[19] The low temperatures associated with InGaN QW and GaN barrier

growth (generally 700 – 900°C) reduce the surface diffusivity of Ga atoms. The {10-11} sidewalls become depleted of Ga since less can diffuse there, and the growth rate of the sidewalls decreases relative to the surface. V-defects will continue propagating and growing in surface area during low temperature GaN growth. In layers of very high indium content or on substrates with low TDD, V-defects do not always nucleate on pre-existing threads. They have been found to also form at stacking faults and misfits, which generate new threads within the highly stressed layer.[21,22]

V-defects have been shown to act as nonradiative recombination centers and leakage pathways that severely degrade the V_{oc} of InGaN solar cells,[23,24] and increase efficiency droop in InGaN LEDs.[25] They also cause QW disorder, which can negatively impact the J_{sc} of InGaN solar cells. On the other hand, it has been suggested that V-defects may create a potential barrier that shields injected carriers from dislocation cores in InGaN LEDs, thus reducing nonradiative recombination and improving their efficiency.[26] This beneficial effect has been corroborated by some experimental data,[27] but it may be the effect of other changing variables that improves efficiency. For instance, V-defects increase surface roughness, which in turn improves light extraction.[28] While it is an interesting theory, there is not strong evidence to support V-defects as a means of improving LED performance.

2.5 Conclusion

MOCVD growth of III-nitrides involves flows of metalorganic precursors flowing over a heated substrate, decomposing to release the group-III and N atoms, and the arrangement of the group-III and N atoms on the surface to form a crystal lattice. Nakamura's vertical subflow design greatly improved nitride growth quality by suppressing

the thermal boundary layer. There is no natural native substrate for GaN growth, and creating large area bulk GaN substrates is difficult and expensive. Most GaN is grown on sapphire substrates using a low temperature nucleation layer. The large lattice mismatch between sapphire and GaN leads to a highly dislocated growth. Even with larger densities of dislocations that can act as leakage paths and recombination centers, nitride optoelectronic devices are able to operate efficiently.

When InGaN is grown at low temperature and high InN percent it has a tendency to phase separate. At moderate InN percentages common in blue LEDs, compositional fluctuations are present without complete phase separation, and they cause potential inhomogeneities that have been theorized as the cause of efficient radiative recombination in InGaN QWs. InGaN even at moderate compositions has a significant lattice mismatch to GaN. Growing a bulk layer or more than a few QWs can lead to relaxation via stacking faults, misfit dislocation formation, or v-defect formation. V-defects are inverted hexagonal pyramidal pits that nucleate on threading dislocations and act as nonradiative recombination sites. Their growth is kinetically controlled, so they usually form during low temperature InGaN growth. Despite the challenges faced when growing InGaN QW structures by MOCVD, very efficient optoelectronic devices can be grown, as will be discussed in the coming chapters.

References

1. Nakamura, S., Harada, Y. & Seno, M. Novel metalorganic chemical vapor deposition system for GaN growth. *Appl. Phys. Lett.* **58,** 2021–2023 (1991).

2. Koleske, D. D., Coltrin, M. E., Cross, K. C., Mitchell, C. C. & Allerman, a. a. Understanding GaN nucleation layer evolution on sapphire. *J. Cryst. Growth* **273,** 86–99 (2004).

3. Dai, Q. *et al.* Internal quantum efficiency and nonradiative recombination coefficient of GaInN/GaN multiple quantum wells with different dislocation densities. *Appl. Phys. Lett.* **94,** 111109 (2009).

4. Kozodoy, P. *et al.* Electrical characterization of GaN p-n junctions with and without threading dislocations. *Appl. Phys. Lett.* **73,** 975 (1998).

5. Chichibu, S. F. *et al.* Origin of defect-insensitive emission probability in In-containing (Al,In,Ga)N alloy semiconductors. *Nat. Mater.* **5,** 810–6 (2006).

6. Xu, K., Wang, J.-F. & Ren, G.-Q. Progress in bulk GaN growth. *Chinese Phys. B* **24,** 066105 (2015).

7. Hashimoto, T., Wu, F., Speck, J. S. & Nakamura, S. A GaN bulk crystal with improved structural quality grown by the ammonothermal method. *Nat. Mater.* **6,** 568–71 (2007).

8. Mori, Y. *et al.* Growth of bulk GaN crystal by Na flux method under various conditions. *J. Cryst. Growth* **350,** 72–74 (2012).

9. Ho, I. & Stringfellow, G. Solid phase immiscibility in GaInN. *Appl. Phys. Lett.* **69,** 2701 (1996).

10. Walukiewicz, W. *et al.* Structure and electronic properties of InN and In-rich group III-nitride alloys. *J. Phys. D. Appl. Phys.* **83,** R83–R99 (2006).

11. Chichibu, S., Sota, T., Wada, K. & Nakamura, S. Exciton localization in InGaN quantum well devices. *J. Vac. Sci. Technol. B Microelectron. Nanom. Struct.* **16,** 2204 (1998).

12. Tabata, A. *et al.* Phase separation suppression in InGaN epitaxial layers due to biaxial strain. *Appl. Phys. Lett.* **80,** 769 (2002).

13. Pantha, B. N., Li, J., Lin, J. Y. & Jiang, H. X. Single phase In[sub x]Ga[sub 1−x]N (0.25≤x≤0.63) alloys synthesized by metal organic chemical vapor deposition. *Appl. Phys. Lett.* **93,** 182107 (2008).

14. Yang, T.-J., Shivaraman, R., Speck, J. S. & Wu, Y.-R. The influence of random indium alloy fluctuations in indium gallium nitride quantum wells on the device behavior. *J. Appl. Phys.* **116,** 113104 (2014).

15. Lai, K. Y., Lin, G. J., Lai, Y.-L., Chen, Y. F. & He, J. H. Effect of indium fluctuation on the photovoltaic characteristics of InGaN/GaN multiple quantum well solar cells. *Appl. Phys. Lett.* **96,** 081103 (2010).

16. Ko, S.-M. *et al.* Strong carrier localization and diminished quantum-confined Stark effect in ultra-thin high-indium-content InGaN quantum wells with violet light emission. *Appl. Phys. Lett.* **103,** 222104 (2013).

17. Holec, D. *et al.* Equilibrium critical thickness for misfit dislocations in III-nitrides. *J. Appl. Phys.* **104,** 123514 (2008).

18. Srinivasan, S. *et al.* Slip systems and misfit dislocations in InGaN epilayers. *Appl. Phys. Lett.* **83,** 5187 (2003).

19. Wu, X. H. X. *et al.* Structural origin of V-defects and correlation with localized excitonic centers in InGaN/GaN multiple quantum wells. *Appl. Phys. Lett.* **72,** 692 (1998).

20. Liu, R. *et al.* Misfit Dislocation Generation in InGaN Epilayers on Free-Standing GaN. *Jpn. J. Appl. Phys.* **45,** L549–L551 (2006).

21. Cho, H. K., Lee, J. Y., Yang, G. M. & Kim, C. S. Formation mechanism of V defects in the InGaN/GaN multiple quantum wells grown on GaN layers with low threading dislocation density. *Appl. Phys. Lett.* **79,** 215–217 (2001).

22. Liu, F. *et al.* Site-specific comparisons of V-defects and threading dislocations in InGaN/GaN multi-quantum-wells grown on SiC and GaN substrates. *J. Cryst. Growth* **387,** 16–22 (2014).

23. Le, L. C. *et al.* Carriers capturing of V-defect and its effect on leakage current and electroluminescence in InGaN-based light-emitting diodes. *Appl. Phys. Lett.* **101,** 252110 (2012).

24. Mori, M. *et al.* Correlation between Device Performance and Defects in GaInN-Based Solar Cells. *Appl. Phys. Express* **5,** 082301 (2012).

25. Le, L. C. *et al.* Effect of V-defects on the performance deterioration of InGaN/GaN multiple-quantum-well light-emitting diodes with varying barrier layer thickness. *J. Appl. Phys.* **114,** 143706 (2013).

26. Hangleiter, a. *et al.* Suppression of nonradiative recombination by V-shaped pits in GaInN/GaN quantum wells produces a large increase in the light emission efficiency. *Phys. Rev. Lett.* **95,** 1–4 (2005).

27. Han, S.-H. *et al.* Improvement of efficiency and electrical properties using intentionally formed V-shaped pits in InGaN/GaN multiple quantum well light-emitting diodes. *Appl. Phys. Lett.* **102,** 251123 (2013).

28. Getty, A., Matioli, E., Iza, M., Weisbuch, C. & Speck, J. S. Electroluminescent measurement of the internal quantum efficiency of light emitting diodes. *Appl. Phys. Lett.* **94,** 2007–2010 (2009).

3

Optical Processes in Semiconductors

3.1 Fermi's Golden Rule

Absorption and emission rates in direct band gap semiconductors can be calculated using Fermi's Golden Rule, an important result of time-dependent perturbation theory. If the initial (i) and final (f) states of an electron in the presence of a perturbing electromagnetic field (light) are known, Fermi's Golden Rule gives the rate of transition between those states.[1]

$$W_{if} = \frac{2\pi}{\hbar} \left| \hat{H}_{fi} \right|^2 \delta\left(E_f - E_i - \hbar\omega \right) \tag{3.1}$$

In Eq. 3.1, E_f is the energy of the final state, E_i is the energy of the initial state, $\hbar\omega$ is the energy of the photon being emitted or absorbed, and $\hat{H}_{fi}$ is the transition matrix element:

$$\hat{H}_{fi} = \langle \psi_f | \hat{H}_{po}(\mathbf{r}) | \psi_i \rangle, \tag{3.2}$$

ψ_i and ψ_f are the wavefunctions of the initial and final states, and $\hat{H}_{po}(\mathbf{r})$ is the time-independent perturbing Hamiltonian. The transition matrix element can be written explicitly as:

$$\langle \psi_f | \widehat{H}_{po}(\mathbf{r}) | \psi_i \rangle = \int \psi_f^*(\mathbf{r}) \, \widehat{H}_{po}(\mathbf{r}) \psi_i(\mathbf{r}) d^3 \mathbf{r}, \tag{3.3}$$

which shows the dependence of the transition rate of the spatial overlap of initial and final state wavefunctions. If the transition takes place between the valence and conduction bands, as in absorption and spontaneous emission in a semiconductor, the wavefunction overlap term has the form:

$$F_{cv} = \int \psi_c^*(\mathbf{r}) \, \psi_v(\mathbf{r}) d^3 \mathbf{r}. \tag{3.4}$$

Taking a step back, the full expression for the perturbing Hamiltonian is:

$$\widehat{H}_p(\mathbf{r}, t) = \widehat{H}_{po}(\mathbf{r})[\exp(-i\omega t) + \exp(i\omega t)], \tag{3.5}$$

but only the $\exp(-i\omega t)$ is retained when restricting discussion to absorption processes, and it is necessary in order to continue with this semiclassical description.[i] The perturbing Hamiltonian can also be written as the following:

$$\widehat{H}_p(\mathbf{r}, t) \cong \frac{e}{m_0} \mathbf{A} \cdot \widehat{\mathbf{p}}, \tag{3.6}$$

where $\mathbf{A}$ is the electromagnetic vector potential, $\widehat{\mathbf{p}}$ is the momentum operator, and m_0 is the free electron mass. Treating the wavefunctions as Bloch states, assuming that momentum is conserved, and assuming that the wavelength of the perturbing light is much greater than the crystal lattice spacing, then the transition matrix element can be rewritten in terms of a momentum matrix element, p_{cv}:

$$\widehat{H}_{fi} = -\frac{eA_0}{2m_0} p_{cv}, \tag{3.7}$$

where $\widehat{\mathbf{p}}$ operates on conduction and valence band Bloch states. The momentum matrix element retains the dependence on wavefunction overlap. Now the absorption transition rate between two states can be written as:

---

[i] The second term describes stimulated emission.

$$W_{abs} = \frac{2\pi}{\hbar}\left(\frac{eA_0}{2m_0}\right)^2 |p_{cv}|^2 \delta(E_f - E_i - \hbar\omega) \tag{3.8}$$

Since Eq. 3.8 only represents the transition rate between a particular valence band and conduction band state, in order to calculate the absorption coefficient, for instance, we must know the total transition rate, W_{TOT}:

$$W_{TOT} = \frac{2\pi}{\hbar}\left(\frac{eA_0}{2m_0}\right)^2 \sum_{i,f} |p_{cv}|^2 \delta(E_f - E_i - \hbar\omega). \tag{3.9}$$

Next we convert the sum over all possible transitions to an integral using the 3-dimensional joint density of states, $g_J(E_J)$:

$$g_J(E_J) = \frac{1}{2\pi^2}\left(\frac{2m_{eff}}{\hbar^2}\right)^{3/2}(E_J - E_g)^{1/2} \tag{3.10}$$

where m_{eff} is the electron effective mass and E_J is E_c - E_k. So by combining Eqs. (3.9) and (3.10) and integrating over E_J we arrive at the expression:

$$W_{TOT} = \frac{2\pi}{\hbar}\left(\frac{eA_0}{2m_0}\right)^2 |p_{cv}|^2 \frac{1}{2\pi^2}\left(\frac{2m_{eff}}{\hbar^2}\right)^{3/2}(\hbar\omega - E_g)^{1/2} \tag{3.11}$$

W_{TOT} can then be used to find α, the probability of absorbing a photon per unit length, known as the absorption coefficient.

$$\alpha = \frac{W_{TOT}}{n_p} = \frac{\hbar\omega W_{TOT}}{I} \tag{3.12}$$

Here n_p is the number of incident photons per unit area and I is the optical intensity, which can be written:

$$I = \frac{n_r c\varepsilon_0 \omega^2 A_0^2}{2}, \tag{3.13}$$

where n_r is the refractive index, c is the speed of light, and ε_0 is the permittivity of free space. Another parameter can be defined with units of energy that is often used in actual calculations:

$$E_p = \frac{2}{m_0}|p_{cv}|^2. \tag{3.14}$$

Finally, combining Eqs. (3.10) − (3.14) we arrive at an expression for the absorption coefficient as a function of incident photon energy:

$$\alpha(\hbar\omega) = \frac{\pi\hbar e^2}{2m_0 c\varepsilon_0}\frac{1}{n_r}\frac{E_p}{\hbar\omega}g_J(\hbar\omega) \tag{3.15}$$

Since $\alpha(\hbar\omega)$ is proportional to E_p, a parameter that depends on the squared modulus of the p_{cv}, the strength of absorption in any system will depend on the overlap of the electron and hole wavefunctions.

Incidentally, while optical absorption can be explained within the framework of the Schrödinger Equation, spontaneous emission cannot. That is because, while electronic energy levels were considered to be quantized, electric field was not. Considering an atomic system, the excited states and ground state have no spatial overlap, so the excited state cannot spontaneously decay to the ground state in the presence of a classical electromagnetic field. It was not until the advent of quantum field theory and quantum electrodynamics that spontaneous emission could be completely explained.

3.2 Electroabsorption: The Franz-Keldysh Effect

In bulk semiconductors, the presence of an electric field causes a weak tail of below-gap absorption. Introducing a constant field into the Hamiltonian for the system leads to electron and hole wavefunctions represented by Airy functions, which decay exponentially

into the band gap. The presence of electron and hole wavefunctions in the gap decreases the effective band gap, but since the wavefunctions decrease exponentially in this regions, optical transitions (which depend on wavefunction overlap) will also decrease exponentially in strength. This exponential tail of below-gap absorption is known as the Urbach edge. Dampened oscillations in the bulk absorption spectrum are also seen above the band edge. They are caused by the change the relative phases of overlapping wavefunctions due to the electric field. The combination of a significant below-gap absorption tail and above-gap oscillations in the presence of an electric field is known as the Franz-Keldysh Effect.[2]

To complete the picture of semiconductor absorption, excitons must also be considered. Excitons represent a bound electron and hole with a Coulombic interaction similar to a hydrogen atom. The dominant exciton in III-V materials is the Wannier type exciton, which is spread over many unit cells. Excitons are responsible for a characteristic peak in absorption spectra slightly below the band gap energy. At 0K, excitons have discrete states for negative binding energies, given by the Bohr model,

$$E_{bn} = \frac{\hbar^2}{2\mu a_B^2 n^2} \tag{3.16}$$

where μ is the reduced mass, a_B is the Bohr radius, and n is the quantum number.[2] The optical transition energies for these states are given by $E_g - E_{bn}$. These discrete sub-band gap absorption lines broaden and merge with each other and the continuum by means of scattering due to impurities, defects, and phonons. Excitonic absorption above E_g is accounted for by the Sommerfeld factor, or Coulomb enhancement factor, which substantially increases absorption near the band edge relative exciton-free calculations.[2] At room temperature, bulk excitonic features are almost completely washed out, limited to a
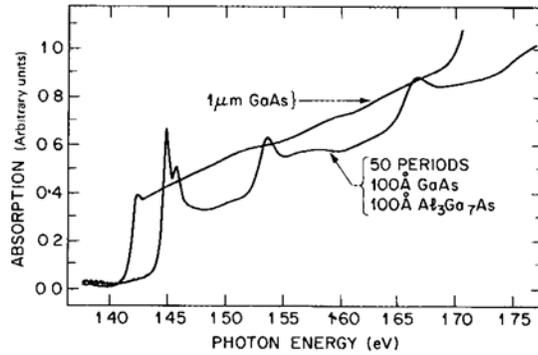
Figure 3.1: Absorption spectra of bulk GaAs and 50x10 nm GaAs MQW.[3]

slight bump near the absorption edge in GaAs (Fig. 3.1).[3] In the presence of an electric field,

the symmetry of the Coulomb potential well is broken, and there is a Stark shift of excitonic

energy levels to lower energies. However, increasing field also decreases the ionization

potential of the exciton, making it easier for electrons and holes to escape from the potential

well. The exciton peak broadens and disappears completely above the ionization field.

Therefore, the maximum shift of the exciton resonance is limited to about 10% of the

binding energy in the bulk.[4]

3.3 Absorption and Recombination in Quantum Wells: The Quantum-Confined Stark Effect

Whereas there are a continuum of states below and above the band gap in bulk

semiconductors, quantum wells contain discrete energy levels. Absorption will only take

place between occupied states in the valence band and unoccupied states in the conduction

band. This leads to an increase in the absorption edge in quantum wells because of the finite

energy of the ground state above the conduction band and below the valence band. Because

of the inverse square dependence of subband energies on well width, the absorption edge

43

will increase in energy as the well becomes narrower. Wavefunction overlap must also be considered in a confined system. In an infinite potential well, which is a decent approximation for many real-life systems, the overlap integral is nonzero only for electron and hole subbands of equal quantum number ($n_e = n_h$). All other transitions are "forbidden". Quantum confinement also splits the hole band into heavy hole (hh) and light hole (lh) bands, which both contribute to $n_h = 1$ absorption. The density of states in a quantum well is step-like, which leads to a step-like absorption spectrum in the ideal case, when excitons are neglected. In finite wells, the wavefunctions penetrate into the barriers, decreasing overlap. Furthermore, since the heights of the electron and hole barriers is often not the same, and their effective masses are different, selection rules no longer strongly apply, and forbidden transitions become possible.[2]

A full picture of absorption in quantum wells must include excitons, which are much more important in a 2D confined system than in bulk. While in the bulk, excitons tend to dissociate at room temperature due to a binding energy that is less than kT (26 meV), in quantum wells they are apparent even at room temperature. Fig. 3.1 compares the absorption spectra of bulk GaAs with 10 nm GaAs quantum wells. The first notable difference is that the absorption edge in the MQW sample is blue-shifted significantly because of energy level quantization. Secondly, multiple excitonic peaks are clearly resolved in the MQW sample, and they exhibit stronger absorption than a bulk layer of twice the total absorber thickness. Peaks are visible for the n = 1, 2, and 3 transitions, as well as the hh and lh transitions for n=1. Quantum confinement increases the electron and hole Coulomb interaction, and thus the exciton binding energy. Coulomb potential changes as 1/L, while confinement potential changes as $1/L^2$, where L is the thickness of the well. Therefore, for wells narrower than the
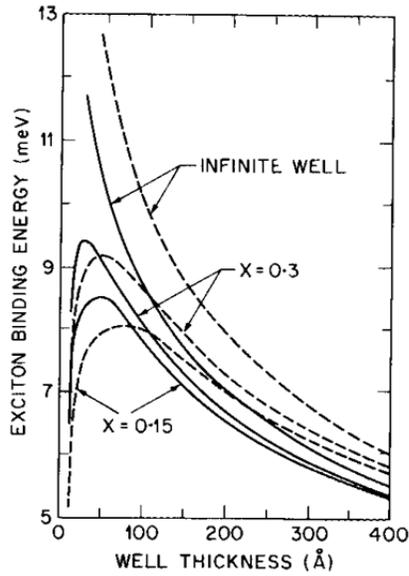
Figure 3.2: Variation of exciton binding energy with well thickness for infinite and GaAs/AlxGa1-xAs finite wells. Solid lines represent heavy hole excitons and dashed lines represent light hole excitons.[3]

exciton's Bohr radius, confinement will dominate in the direction perpendicular to the well. Theory predicts a maximum 4-fold increase in binding energy for the 1s exciton in an infinite well, as well as a 16-fold increase in oscillator strength, which explains increased peak resolution and absorption enhancement compared to the bulk.[2,3] In real finite wells, the maximum binding energy increase is limited by about 2 times. Fig. 3.2 compares calculations of infinite well and finite well binding energy as a function of well thickness. E_{bn} will increase as L decreases until wavefunction penetration into the barriers overcomes enhanced confinement. Above the bandgap, the 2D Sommerfeld factor leads to a factor of 2 increase in absorption over the bulk.[6]

Application of an electric field to a quantum well gives rise to QCSE and QCFK effects. Miller *et al.* defined QCFK in purely numerical terms as a special case of the Franz-Keldysh effect in a quantum confined system without consideration of excitons.[5] An electric field creates a sloped quantum well potential, and the resulting triangular wells localize the
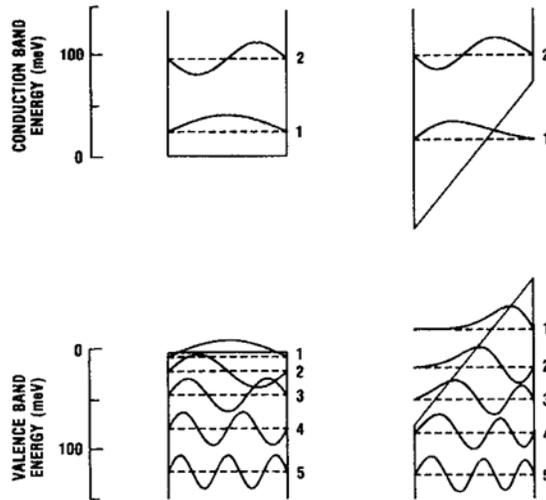
Figure 3.3: Valence and conduction band energy levels and wavefunctions at 0 and 10^5 V/cm.[5]

electron and hole wavefunctions on opposite sides of the well, as depicted in Fig. 3.3. The energies of the lowest subbands in the conduction and valence band decrease quadratically with field, red-shifting the absorption edge, but higher order transitions hardly change in energy. Energy levels in the valence band shift more because holes are heavier and less confined than electrons. The electric field breaks the symmetry of the well, allowing forbidden transitions even in the infinite well case. In many cases those forbidden transitions are actually stronger than the allowed transitions. Fig. 3.4 compares theoretical bulk GaAs absorption to 10nm and 30nm quantum wells, neglecting excitons, at 0 field and 10^5 V/cm. The 0 field quantum wells have quadratically spaced steps that are spaced closer in the thicker well. At 10^5 V/cm, the 10nm well clearly shows a red-shift of the first transition and shows a couple of forbidden transitions, but the 30nm well exhibits many forbidden transitions, and much more closely mirrors the bulk spectrum, including Franz-Keldysh oscillations above the band gap.

It is worth pointing out that, while an electric field allows many previously forbidden transitions, it does not cause a net change in the total absorption due to the sum rule.[3] For
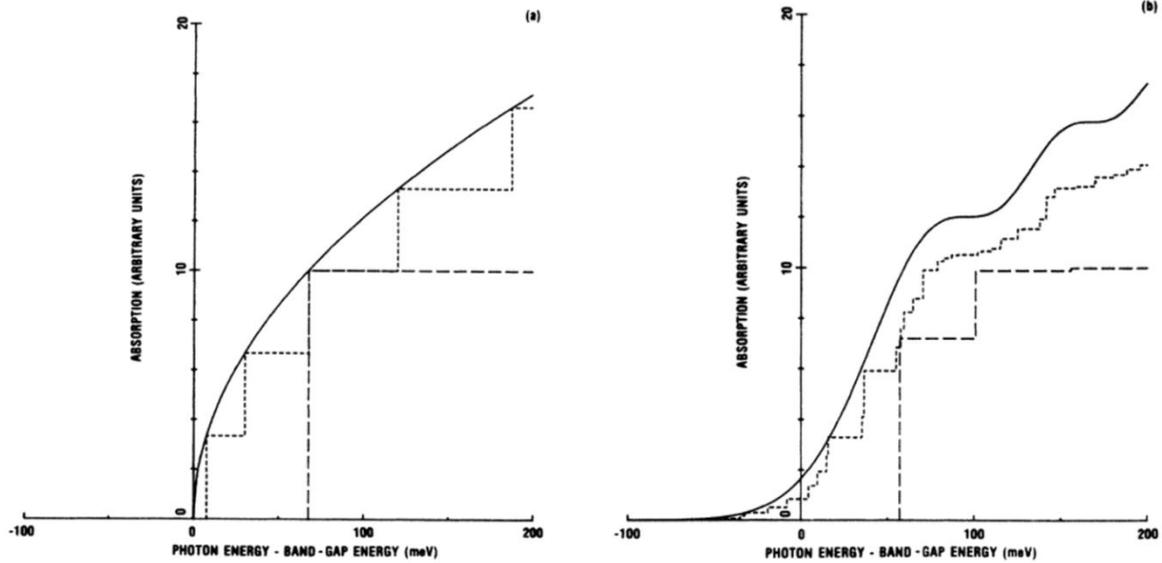
Figure 3.4: Calculated absorption in a 10 nm (large dash) 30 nm (small dash) and infinite thickness (solid) slab with (a) 0 field and (b) 10^5 V/cm.[5]

every gain in strength of a forbidden transition, allowed transitions lose strength so that the sum of step heights in absorption due to all transitions is conserved. This occurs physically because the electron and hole are separated in the well by sloped potential, and their overlap decreases. As well width increases, steps become shorter and more numerous, and the spectrum more closely matches the bulk.

Miller *et al.* defined the quantum confined Stark effect as the large shift in absorption edge that occurs when an electric field is applied perpendicular to a quantum well.[4] The electric field moves the electrons and holes apart in the z direction, but brings them closer in potential, creating a Stark shift in the exciton absorption. Meanwhile, for wells thinner than the 3D exciton diameter, the barriers contain carriers and prevent field ionization. This explains why exciton peaks are resolved at up to 50x the bulk ionization field. The exciton binding energy decreases with increasing field as electron and hole are pulled apart, but the effect of binding energy change is dominated by the shift in single
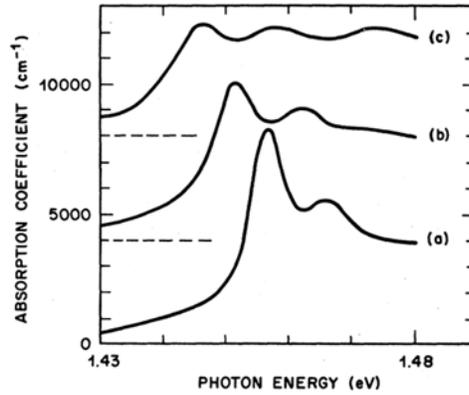
47

Figure 3.5: Absorption spectra with perpendicular field (a) 1E4 V/cm (b) 4.7E4 V/cm (c) 7.3E4 V/cm.[7]

particle states. Miller compared two theoretical models to calculate the change in single particle energy levels and the exciton peak shift. The first was a tunneling resonance method, where the resonant energies of tunneling current out of a well correspond to energy levels. The second was an effective width infinite well model based on variational calculations, where an effective well width was used that matched an infinite well's ground states with those of the finite well at zero field. The two models agreed well with each other and with experiment.[4]

QCSE has been observed experimentally by optical absorption spectroscopy, photocurrent spectroscopy, photoluminescence, electroluminescence, and electroreflectance.[3] Miller *et al.* prepared novel device structures and investigated absorption under bias in GaAs/AlGaAs MQWs with 60 periods grown by MBE.[7] To test perpendicular field, the MQW was imbedded in the intrinsic region of the device, where there would ideally be a constant electric field. The results of the experiment clearly show the band edge shifting to lower energies with increasing reverse bias (Fig. 3.5). Excitonic peaks were resolved up to a field of 10^5 V/cm. They also observed that the shift in
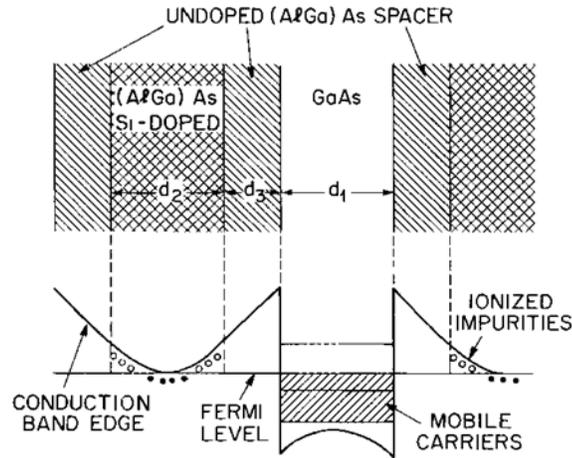
Figure 3.6: Band diagram and corresponding structure for a modulation-doped quantum well.[3]

absorption edge was nonlinear with field, shifting relatively less at low fields. They also performed a separate experiment with the electric field applied parallel to the quantum wells, which produced markedly different results. At low field, the excitonic resonances for light and heavy holes are still resolved, but even moderate fields destroy those resonances. In the parallel field case, electrons and holes are still confined in the z-direction, creating strong room temperature excitonic feature, but when a field is applied in the plane of the well, where wavefunctions can be treated more like plane waves, excitons broaden due to field ionization much like they do in the bulk. However, the ionization field in still higher than it is in the bulk.

A large population of free carriers in a quantum well, either from ionized donors or photogeneration, can change its absorption spectrum. One strategy for injecting free carriers into a quantum well is modulation doping of the barriers. A representative device structure is shown in Fig. 3.6.[3] Only the barriers are doped, but the ionized carriers diffuse into the well and become trapped. The presence of a carrier gas causes the band gap to decrease slightly due to band gap renormalization. Fig. 3.7 shows experimental absorption spectra of
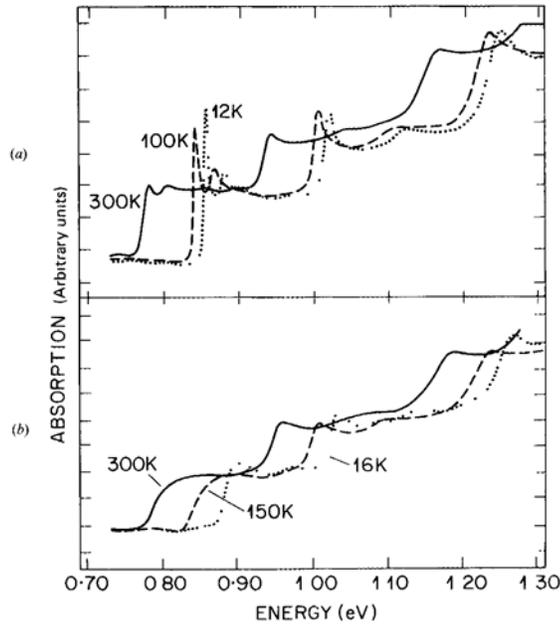
Figure 3.7: Absorption spectra of (a) undoped and (b) modulation doped MQW structures.[3]

undoped and doped MQW structures at different temperatures. The absorption edge red shifts with temperature because of the decrease in band gap, however the absorption edge is at a slightly higher energy in the doped case at each temperature. Also of note is that the n = 1 exciton peaks completely disappear in the doped case, even at low temperature, while the n = 2, 3 peaks are much less affected by the doping. A large population of free carriers has several effects on absorption physics that explain these results. Excitons broaden because their coulomb interaction is screened by the carrier gas. Also, phase space filling (PSF) causes a blue shift of the absorption edge. The blue shift occurs because an empty state in the valence band and a full state in the conduction band will be further separated in the presence of electron and hole gasses. This also explains one origin of the Stokes shift, because emission generally occurs between the bottom of the conduction band and the top of the valence band. PSF is also responsible for eliminating excitons when the Fermi energy
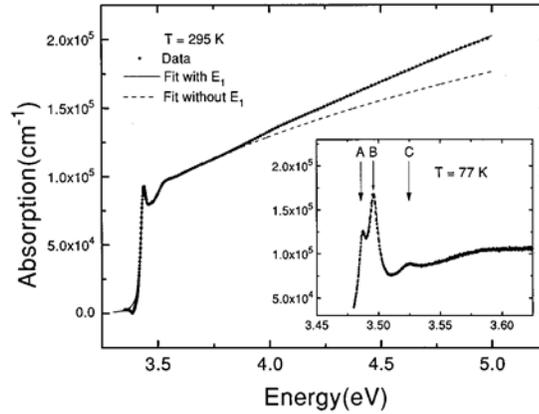
Figure 3.8: Absorption spectrum of GaN at room temperature and 77K.[8]

reaches the exciton resonance energy, since excitons and electrons cannot occupy the same space.[3]

3.4 Electroabsorption in the III-Nitrides

The absorption coefficient of high quality bulk GaN layers in on the order of 10^5 cm^{-1}.[8] Figure 3.8 shows the GaN absorption spectrum with an excitonic peak visible at room temperature, and clear peak resolution at 77K. It is unusual for excitonic peaks to be so well resolved at room temperature in bulk materials, but in GaN, there are few active LO phonons at room temperature available to broaden the peak. GaN excitons also have a large binding energy (26 meV), comparable to kT at room temperature.[10]

When an electric field is applied to bulk GaN, the Franz-Keldysh effect causes the below-gap absorption tail to increase. Jacobson and colleagues found that the Urbach slope of logarithmic sub-E_g absorption increases linearly with electric field (Fig. 3.9).[9] The effect of an electric field on excitons in GaN was measured by absorption and photocurrent response.[11] Room temperature absorption data shows a Stark shift, broadening, and slight

51
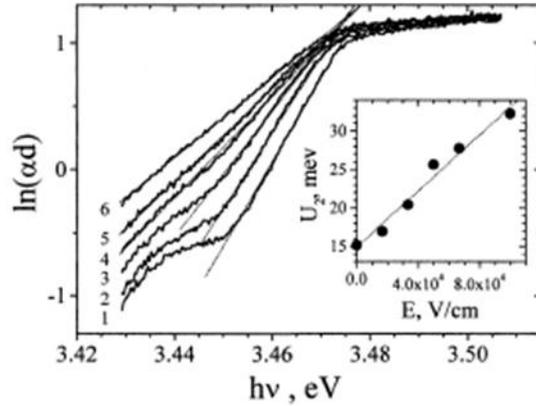
Figure 3.9: Dependence of sub-band gap GaN absorption spectra on electric field.[9]

quenching of the peaks. Photoresponse data at room temperature shows similar quenching and a peak shift to lower energy, but at 80K, the peak amplitude actually increases with field, contrary to the result at room temperature. The transition from an increase to a decrease in peak amplitude with field when going from low to higher temperature is due to interplay between changes in binding energy, ionization probability, and thermal energy.

The large electric fields in InGaN quantum wells, induced by the piezoelectric effect, have a significant effect on optical processes of absorption and emission. Observing the shifts caused by the QCSE in PL measurements and electroabsorption spectroscopy (EA) has allowed researchers to quantify F_{pz} in InGaN quantum wells, which is in excess of 1 MV/cm for even moderate indium concentrations.[12,13] When a reverse bias was applied to a 20nm InGaN/GaN DH, the resulting change in absorption was plotted for each applied field (Fig. 3.10). In this case, the well is too wide for confinement to produce a strong QCSE, but there is a noticeable FK effect on the below gap absorption. The structure is such that the constant built-in depletion field is opposite F_{pz} in the well, so applying an increasing reverse
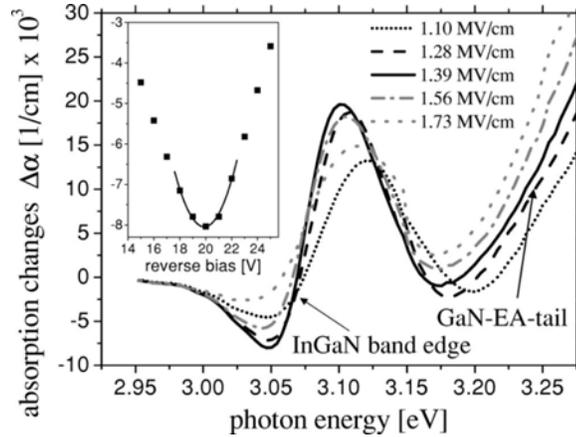
Figure 3.10: Measured absorption changes in 20 nm InGaN layer for various fields. Inset shows absorption change at first minimum vs. reverse bias.[12]

bias will gradually decrease the net field in the well until it is completely compensated. Since an electric field causes increased below-gap absorption, the bias for which the below-gap absorption change is the most negative corresponds to the compensating field (see inset in Fig. 3.10). Knowing the compensating field, the strength of the intrinsic electric field due to piezoelectric polarization can be calculated. Figure 3.11 plots the relationship between F_{pz} and In content. The field is above 1 MV/cm for concentrations above about 7%, which is higher than previous assumptions. Takeuchi, for example, calculated only 1.08 MV/cm for 13% In.[13]

Interpreting the effects of electric field on absorption and emission from quantum wells is also necessary to investigate screening of the piezoelectric field. The addition of a large number of free carriers in a well with an electric field will lead to a carrier distribution that will counteract the existing field. Takeuchi showed a blue-shift of low temperature PL peaks with increasing excitation intensity in a MQW sample, while in a strained bulk layer there was no change in peak position.[13] QCSE should cause a blue-shift of emission when field decreases. A comparison of high and low excitation PL at different well widths
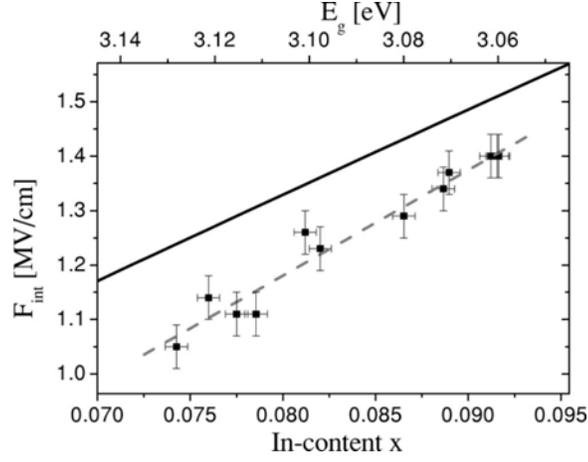
Figure 3.11: Polarization field strength vs indium content in an InGaN/GaN double heterostructure. Solid line is calculated, and squares are experimental data points.[12]

revealed that an intensity of 200 kW/cm^2 completely screened F_{pz}, since its peak transition energy approached the bulk value (Fig. 3.12). Similar results are found when increasing the drive current in electroluminescence measurements (EL). For F_{pz} on the order of a MV/cm, the total shift due to QCSE will be on the order of 100 meV.[10]

Screening of F_{pz} can also be accomplished by doping of the wells and/or barriers.[14–17] Either well doping or modulation doping of barriers will produce a large density of free carriers in the wells, with the same screening effects as high intensity optical excitation. A screened field is evidenced by a decreased Stokes shift, decreased PL decay time, and steeper absorption edge.[14] Comparison of PL and photoluminescence excitation (PLE), which is similar to absorption, for doping densities up to 10^{19} cm^{-3} shows a strong blue shift of PL, and a reduction in the broadness of the absorption tail. Deguchi *et al*. showed that it is possible to dope heavily enough (10^{19} cm^{-3}) to fully screen F_{pz} and eliminate QCSE.[15] Meanwhile, Dalfors *et al*. suggested that the shift in emission energy could only be partially explained by piezoelectric field screening, and that the rest of the shift must be due to the screening of localized potential fluctuations.[16]
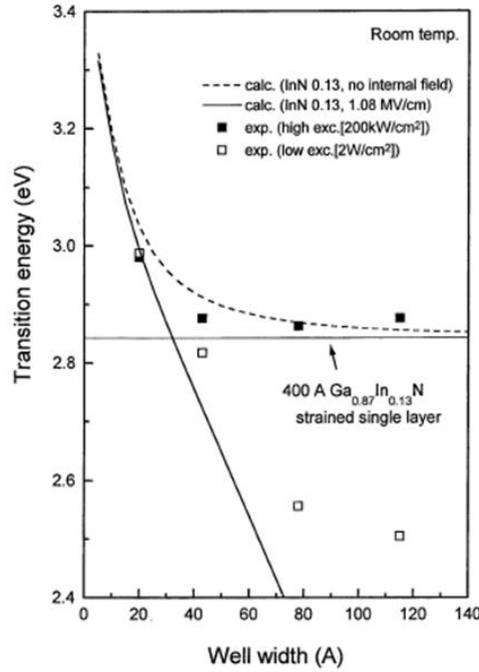
Figure 3.12: PL peak energy of an InGaN MQW under low and high excitation, calculated and experimental.[13]

InGaN epilayers exhibit a Stokes-like shift between emission and absorption in quantum wells. The piezoelectric field in quantum wells is one mechanism that causes Stokes shifts. It separates electron and hole wavefunctions, reducing the oscillator strength of low order absorption, and broadening the absorption edge. On the other hand, emission is dominated by the ground state transition, so its peak will be at a lower energy than the absorption peak. The emission peak is generally located at the end of the absorption tail. Figure 3.13 shows four different cases representing different relationships between well thickness L, internal field F, valence band discontinuity (ΔE_V), and the exciton Bohr radius a_B. In Case 1 when $L < a_B$, and $F*L < \Delta E_V$, the electron and hole are confined with strong overlap, and there is not an appreciable Stoke shift. In Case 2, when $L < a_B$, and $F*L > \Delta E_V$ the hole wavefunction is confined to the triangular well, with continuum states above. In Cases 3 and 4, $L > a_B$, the wavefunctions are fully separated, excitons are broadened, and

55

	$L < a_B$	$a_B < L \ll 3D$
$F \times L < \Delta E_V$	CASE I — QW exciton QCSE — zero Stokes-like shift	CASE III — e-h tunneling (separate weak confine) QCSE+QCFK — Stokes-like shift (vertical+FK)
$F \times L > \Delta E_V$	CASE II — QW e-h pair <exciton?> (vertical hole localization) QCSE+QCFK — Stokes-like shift (vertical)	CASE IV — e-h tunneling (separately confined) QCSE+QCFK — Stokes-like shift (ver.+FK)
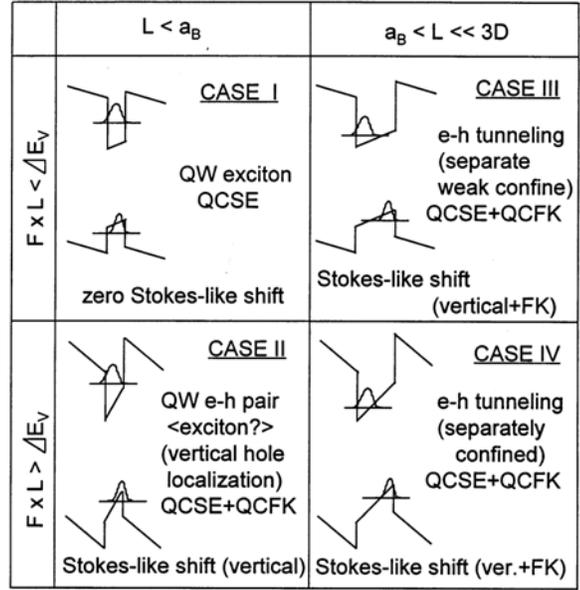
Figure 3.13: Schematic band diagrams of InGaN QWs with width L, under field F, with Bohr radius a_B, and valence band discontinuity ΔE_V.[14]

both QCSE and QCFK play a role in absorption. Stokes shift is present for cases 2-4 because of a loss of strength of the lowest energy absorption transitions.[14] As expected, there is an increase in Stokes shift as L increases. However, the change is not linear; a sharp increase in Stokes shift occurs at 3.6 nm, or about the exciton Bohr radius in GaN, which corresponds to the transition from Case 2 to Case 4. Similarly, as indium content increases, F_{pz} increases, and Stokes shift increases as a result. There is a critical value of composition (x = 0.1) where the Stokes shift begins to increase more rapidly, which corresponds to a transition between Cases 1 and 2.

The other potential cause of Stokes shift is potential inhomogeneity and exciton localization.[10,14,19] Chichibu *et al.* blamed the observed Stokes shift in Case 1 wells on these localization potentials.[14] Potential fluctuations may be caused by monolayer thickness fluctuations, compositional or strain undulations, or small scale phase separation.[10] They result in regions of different band gap, termed quantum disks or segmented quantum wells,
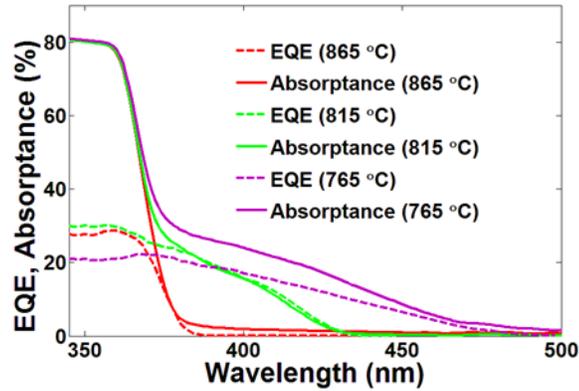
Figure 3.14: Measured absorptance and EQE curves for an InGaN MQW solar cell at different growth temperatures, corresponding to different In-contents and polarization fields.[18]

which are visible through cathodoluminescence. The Stokes shift arises because carriers fall into regions of lower band gap before recombining. The blue shift of emission with excitation would be attributed to band filling of these localized potential wells. While there is strong support for the relation of the Stokes shift to localization potentials, some believe it can be fully explained by QCSE due to piezoelectric fields.[20]

The effects of electroabsorption on nitride solar cells have not been directly investigated, but evidence of electric field effects are present in some published EQE and absorption data.[21–25] Absorption data for a thick layer of c-plane InGaN exhibits a long absorption tail due to the Franz-Keldysh effect. Subtracting measured EQE from absorption yields IQE values of over 90%.[22,23] Long absorption tails are also apparent for high In content MQW devices.[21] There is also evidence from EL measurements that In fluctuations in solar cell active layers cause a substantial Stokes shift when compared to EQE.[24,25] Recent EQE data from UCSB clearly shows the effects of QCSE in c-plane MQW devices. The absorption edge pushes out to longer wavelengths and becomes less steep as the growth temperature of InGaN decreases, which corresponds to an increase in indium content and higher polarization field. Absorption data matches the trend of EQE (Fig. 3.14). Bias-
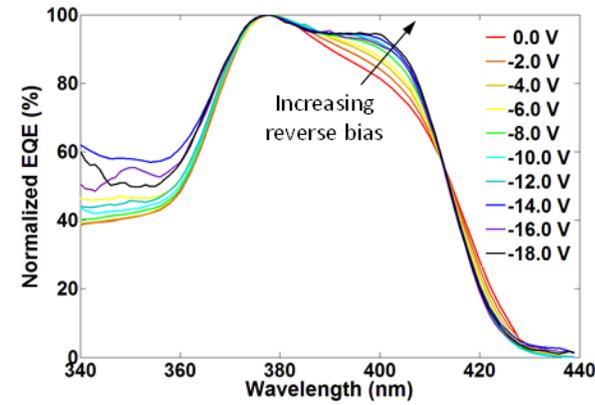
Figure 3.15: Normalized EQE curves for an InGaN MQW solar cell under increasing reverse bias.[18]

dependent EQE measurements show that as reverse bias increases and the field in the wells decreases, the absorption edge blue-shifts, EQE becomes steeper, and EQE just above the band gap increases (Fig. 3.15). This should be reflected in the absorption spectrum due to QCSE and sum rules, which require an increase in absorption at longer wavelengths to be coupled with a decrease at shorter wavelengths. Due to the relative scarcity of absorption data for nitride MQW solar cells, there is a strong opportunity for future research in this area.

3.5 Conclusions

Optical absorption and spontaneous emission are key processes to the operation of solar cells and LEDs. Fermi's Golden Rule gives the rate of absorption and spontaneous emission transitions that leads to an expression for the absorption coefficient. Electric fields in bulk semiconductors lead to a broadening of the absorption edge due to the Franz-Keldysh effect. In quantum wells, confinement leads to quantized energy levels, and excitons become relevant at room temperature. When an electric field exists in a QW, as is the case in strained InGaN wells due to piezoelectric polarization, energy levels change

significantly. QCFK and QCSE result in a red-shifted and broadened absorption edge or emission peak with strong forbidden transitions, and above-gap oscillations in absorption spectra. Increased free carrier concentration in wells screen existing fields and increase the absorption edge energy. Broad absorption edges due to fields or potential inhomogeneity in nitrides lead to a Stokes-like shift between the peaks of absorption and longer wavelength emission. Electroabsorption in nitride solar cells has not been investigated in depth, although absorption spectra and EQE characteristics display evidence of QCSE. There remain many promising experiments involving electroabsorption that can be performed to further investigate material and device properties in nitride solar cells.

References

1. Miller, D. A. B. *Quantum Mechanics for Scientists and Engineers*. (Cambirdge University Press, 2008).

2. Basu, P. K. *Theory of Optical Processes in Semiconductors: Bulk and Microstructures*. (Oxford University Press, 1997).

3. Schmitt-Rink, S., Chemla, D. & Miller, D. Linear and nonlinear optical properties of semiconductor quantum wells. *Adv. Phys.* **38,** 89–188 (1989).

4. Miller, D. A. B. *et al.* Band-edge electroabsorption in quantum well structures: The quantum-confined Stark effect. *Phys. Rev. Lett.* **53,** 2173–2176 (1984).

5. Miller, D., Chemla, D. & Schmitt-Rink, S. Relation between electroabsorption in bulk semiconductors and in quantum wells: The quantum-confined Franz-Keldysh effect. *Phys. Rev. B. Condens. Matter* **33,** 6976–6982 (1986).

6. Davies, J. H. *The Physics of Low-Dimensional Semiconductors: An Introduction*. (Cambridge University Press, 1998).

7. Miller, D. A. B. *et al.* Electric field dependence of optical absorption near the band gap of quantum-well structures. *Phys. Rev. B* **32,** 1043 (1985).

8. Muth, J. *et al.* Absorption coefficient, energy gap, exciton binding energy, and recombination lifetime of GaN obtained from transmission measurements. *Appl. Phys. Lett.* **71,** 2572–2574 (1997).

9. Jacobson, M., Konstantinov, O., Nelson, D., Romanovskii, S. & Hatzopoulos, Z. Absorption spectra of GaN: film characterization by Urbach spectral tail and the effect of electric field. *J. Cryst. Growth* **230,** 459–461 (2001).

10. Chichibu, S., Sota, T., Wada, K. & Nakamura, S. Exciton localization in InGaN quantum well devices. *J. Vac. Sci. Technol. B Microelectron. Nanom. Struct.* **16,** 2204 (1998).

11. Binet, F., Duboz, J., Rosencher, E., Scholz, F. & Härle, V. Electric field effects on excitons in gallium nitride. *Phys. Rev. B. Condens. Matter* **54,** 8116–8121 (1996).

12. Renner, F. *et al.* Quantitative analysis of the polarization fields and absorption changes in InGaN/GaN quantum wells with electroabsorption spectroscopy. *Appl. Phys. Lett.* **81,** 490 (2002).

13. Takeuchi, T., Sota, S., Katsuragawa, M. & Komori, M. Quantum-confined Stark effect due to piezoelectric fields in GaInN strained quantum wells. *Jpn. J. Appl.* (1997). at <http://jjap.jsap.jp/link?JJAP/36/L382/>

14. Chichibu, S. *et al.* Optical properties of InGaN quantum wells. *Mater. Sci. Eng. B* **59,** 298–306 (1999).

15. Deguchi, T. *et al.* Luminescence spectra from InGaN multiquantum wells heavily doped with Si. *Appl. Phys. Lett.* **72,** 3329 (1998).

16. Dalfors, J. *et al.* Optical properties of doped InGaN/GaN multiquantum-well structures. *Appl. Phys. Lett.* **74,** 3299 (1999).

17. Im, J., Kollmer, H. & Off, J. Piezoelectric Field Effect on Optical Properties of GaN/GaInN/AlGaN Quantum Wells. *MRS* **537,** 2–7 (1998).

18. Courtesy of R. M. Farrell. .

19. Chichibu, S. F. *et al.* Origin of defect-insensitive emission probability in In-containing (Al,In,Ga)N alloy semiconductors. *Nat. Mater.* **5,** 810–6 (2006).

20. Hangleiter, A., Im, J. S., Off, J. & Scholz, F. Optical Properties of Nitride Quantum Wells: How to Separate Fluctuations and Polarization Field Effects. *Phys. Status Solidi* **216,** 427–430 (1999).

21. Neufeld, C. J. *et al.* Effect of doping and polarization on carrier collection in InGaN quantum well solar cells. *Appl. Phys. Lett.* **98,** 243507 (2011).

22. Matioli, E. *et al.* High internal and external quantum efficiency InGaN/GaN solar cells. *Appl. Phys. Lett.* **98,** 021102 (2011).

23. Lang, J. R. *et al.* High external quantum efficiency and fill-factor InGaN/GaN heterojunction solar cells grown by NH[sub 3]-based molecular beam epitaxy. *Appl. Phys. Lett.* **98,** 131115 (2011).

24. Fujiyama, Y. *et al.* GaInN/GaN p-i-n light-emitting solar cells. *Phys. Status Solidi* **7,** 2382–2385 (2010).

25. Lai, K. Y., Lin, G. J., Lai, Y.-L., Chen, Y. F. & He, J. H. Effect of indium fluctuation on the photovoltaic characteristics of InGaN/GaN multiple quantum well solar cells. *Appl. Phys. Lett.* **96,** 081103 (2010).

4

InGaN Based Multiple Quantum Well Solar Cells

4.1 Motivation and Background

4.1.1 Nitride Solar Cells

The III-nitrides have several important advantages over the far more popular silicon for photovoltaic applications. The InGaN ternary system has a wide band gap range from 0.7 to 3.4 eV,[1] which covers most of the usable solar spectrum (Fig. 4.1).[2] GaN is a direct band gap material with a high absorption coefficient ,[3] and requires roughly 1000 times less material than silicon to absorb the same amount of light. Nitrides are also highly radiation resistant, making them suitable for space applications.[4] Finally, nitride solar cells are drift-based devices, where high electric fields in the intrinsic region negate poor diffusion length in GaN and allow very high collection efficiency.[5]

In order to absorb a significant amount of the solar irradiance, InGaN must be grown with a composition of indium above 20%, with a bandgap below 2.7eV. Unfortunately, there are significant problems associated with the growth and operation of high composition
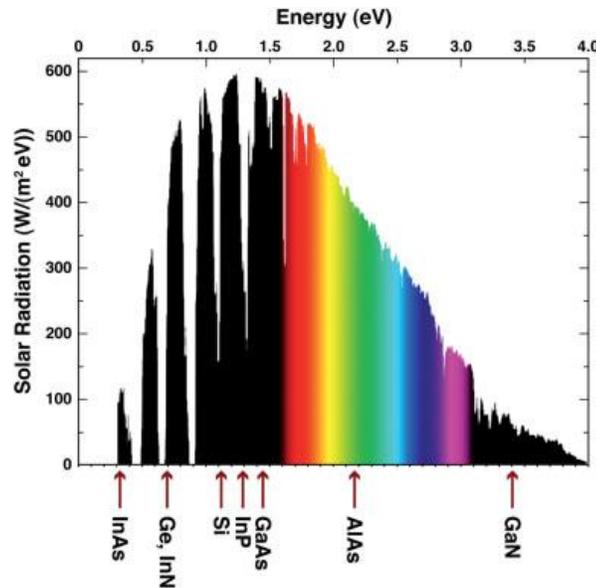
Figure 4.1: A plot of solar spectral power density, along with indicated bandgaps of many common semiconductor materials. Almost the entire solar spectrum falls between the band gaps of GaN and InN.[2]

devices. One problem is phase separation caused by a miscibility gap between GaN and InN that originates because of large lattice mismatch.[6,7] Phase separation or compositional fluctuations reduce the open circuit voltage (V_{oc}) of solar cells and act as shallow quantum wells that trap carriers.[8] Additionally, lattice mismatch between the GaN bulk and InGaN epitaxial layers (Fig. 4.2)[9] builds strain, which past a critical thickness, causes the film to start relaxing by forming defects like misfit dislocations and v-pits, which in turn increase current leakage.[10,11] The III-Nitrides also possess a low symmetry wurtzite structure that leads to macroscopic spontaneous polarization. As a result, strained layers develop large piezoelectric polarization induced electric fields. In typical InGaN/GaN heterostructures, the piezoelectric field in the InGaN acts opposite the built-in field of the diode, which can result in a net field that opposes carrier collection, severely degrading device performance.[12,13] Research in nitride solar cells has focused on overcoming these basic challenges and achieving efficient conversion at longer wavelengths.[14]
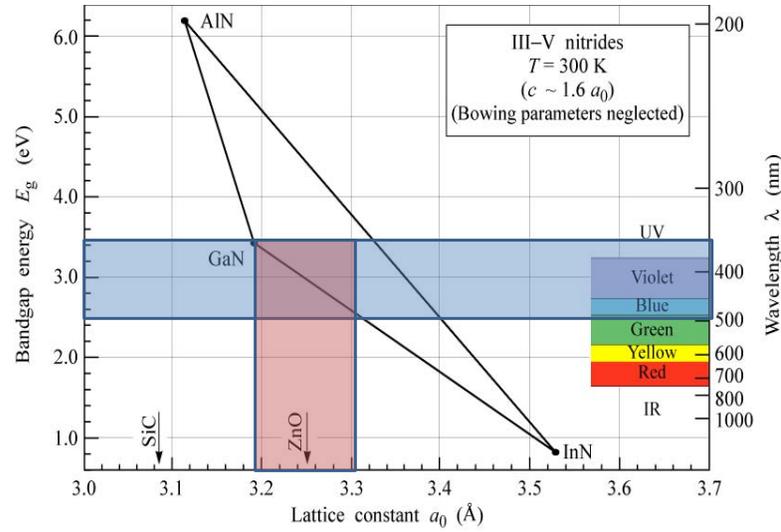
Figure 4.2: E_g and lattice constants for the (Al,In,Ga)N alloy system, highlighting the InGaN composition range applicable to solar cells.[9]

4.1.2 Active Region Evolution

The first published work on nitride solar cells was characterized by p-i-n double heterostructure (DH) devices with poor internal quantum efficiency (IQE < 60%) for indium contents less than 10%, and severe phase separation for higher compositions.[15–17] It was predicted, however, that an all-nitride multi-junction solar cell (MJSC) could achieve 40% efficiency.[18] In 2008, several groups reported improvements in EQE, IQE, and fill factor (FF) at In compositions over 10%.[19–22] Neufeld *et al.* achieved 94% peak IQE (63% EQE) and a FF of 75% with only 200nm of 12% InGaN, while Zheng *et al.* attained an 81% FF with 150nm of 10% InGaN. These improvements were attributed to improved growth conditions and p-GaN contact schemes. Further improvements to DH solar cells were made by growth on bulk GaN and by surface roughening.[23–25] Bulk GaN has a threading dislocation density (TDD) 2 orders of magnitude lower than GaN on sapphire, which reduces leakage current and leads to improvements in V_{oc} and FF. Surface roughening
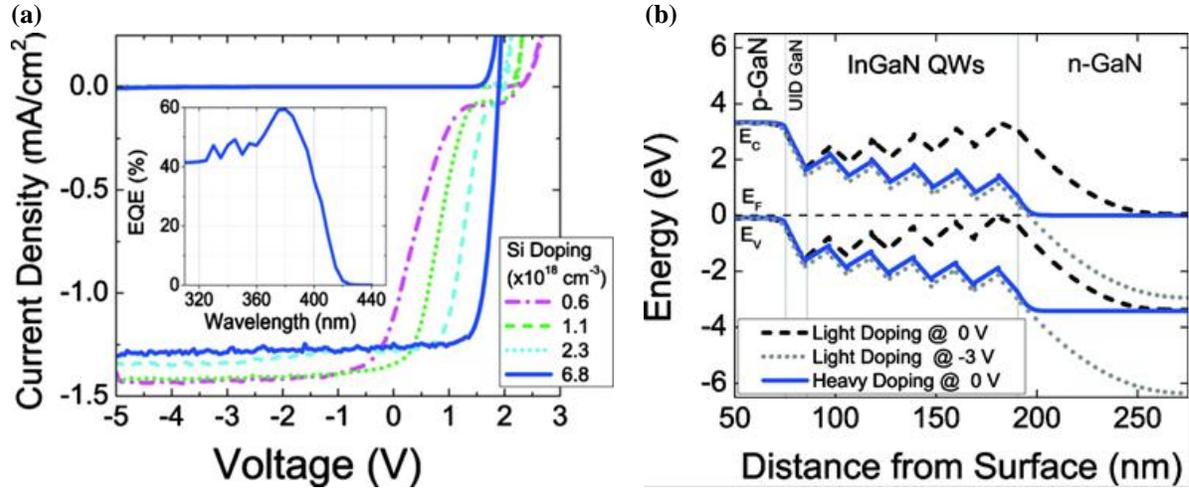
Figure 4.3: (a) *J-V* curves of InGaN MQW solar cell with increasing Si doping. Inset shows high doping EQE curve. (b) Simulated band diagrams for InGaN MQW solar cell with low and high Si doping at zero bias and low doping at -3V. Doping affects net field in the wells.[13]

increases the average optical path length in the active region, increasing absorption and EQE (see Section 4.4.1).

There is an inherent trade-off in growing high performance single junction InGaN solar cells. On one hand, the bandgap of the absorbing layer must be decreased in order to absorb more of the incident power of the solar spectrum. This is accomplished by increasing the amount of indium in the InGaN, and compositions near or above 20% In are generally necessary to make devices with theoretical efficiencies that even approach 10%. On the other hand, hundreds of nanometers of InGaN must be grown to fully absorb that incident light, and at these compositions and thicknesses, catastrophic relaxation will occur in single DH layers. The large lattice mismatch between GaN substrates and InGaN epilayers then necessitates the use of a multiple quantum well (MQW) active region for devices with higher compositions of indium in order to maintain InGaN material quality. In III-nitride solar cells, MQW structures are not used for their potential to boost efficiency theoretical

p-contact grid

| 0-300 nm rough p-GaN |
| 30 nm smooth p-GaN |
| 40 nm smooth p⁺-GaN |
| 10-30X InGaN/GaN MQW |
| 10 nm n⁺-GaN |
| 2 µm n-GaN |
| 1 µm UID GaN   n-contact |
| Sapphire |
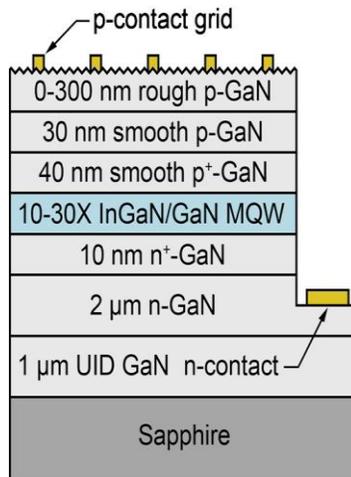
Figure 4.4: Cross-sectional schematic of InGaN MQW solar cell with roughened surface.[26]

efficiency (see Section 4.1.3), but for their ability to alleviate stress built up during thick active region growth.

Performance of bulk P-i-N structure InGaN solar cells have decreased dramatically in the 20% In composition range,[16] while MQW cell performance has remained high with an absorption edge extending beyond 500 nm.[26] Because the critical thickness of epitaxial (0001) InGaN decreases exponentially with increasing indium, many groups have turned to MQW structures, which breaks the absorber thickness up into wells only a few nm thick. MQW structures with In content up to 40% show no phase separation, while 200nm single layers of the same composition show severe phase separation and pit formation.[27,28] Neufeld *et al.* solved the problem of the IV kink in MQW cells by increasing the Si doping on the n-side of the active region (Fig. 4.3(a)), which decreased band bending in the n-GaN, preventing the built-in field in the intrinsic region from being overcome by the polarization-induced field in the QWs (Fig. 4.3(b)).[13] Meanwhile, Farrell *et al.* found that short circuit current (J_{sc}) and peak EQE increase when going from 10 to 30 QW periods with 28% In in the wells.[26] A 30 period cell with an intentionally roughened surface (Fig. 4.4) displayed

66

decent electrical characteristics and absorption out to 520nm, the longest wavelength absorption yet published for a nitride solar cell. More recently, a very high V_{oc} of 2.31V was demonstrated for a MQW device with a 449nm absorption edge, which represents a near ideal bandgap-V_{oc} offset of 0.45V.[29]

In more long-range research, InGaN nanowire array solar cells have also been investigated,[30] and the idea of compositionally graded P-i-N structures has been theoretically explored.[31] An intermediate band nitride solar cell with InGaN quantum dot layers has been proposed with a theoretical efficiency of over 55%.[32] Some are even exploring the use of InGaN MQW solar cells for hydrogen gas production in an artificial photosynthesis system.[33]

4.1.3 Quantum Well Solar Cells

Quantum well solar cells (QWSC) were first proposed and demonstrated by Barnham and colleagues at the Imperial College in London.[34–39] In theory, the addition of quantum wells to a solar cell's active region (intrinsic region of a p-i-n structure) should increase the short circuit current over what is expected from a homojunction device made solely from the barrier material, and simultaneously increase V_{oc} over what is expected from a homojunction device made solely from the well material. The resulting device efficiency was originally proposed to be an enhancement relative to a bulk homojunction cell made from either material.[34] Detailed thermodynamic analysis, however, claimed that no efficiency enhancement over an ideal singe bandgap solar cell is possible.[40] The argument against this analysis and for potential gains in theoretical efficiency rely on the quasi-Fermi level separation in the QWs being reduced compared to the barrier regions (and therefore
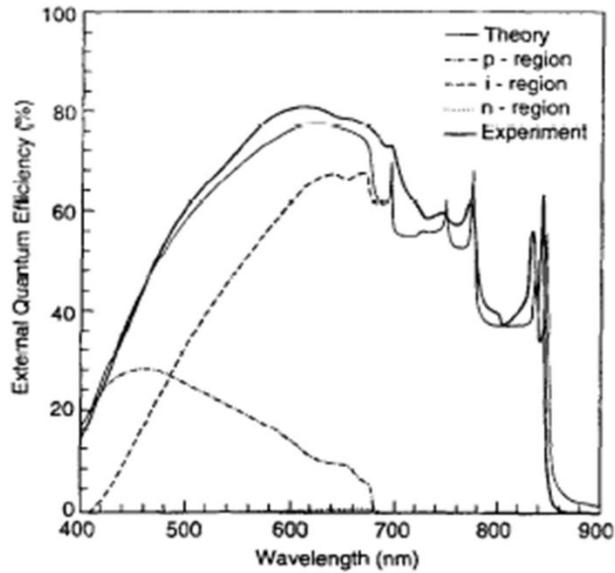
Figure 4.5: Experimental and calculated spectral response of a 50 period AlGaAs/GaAs MQW solar cell showing theoretical absorption in the p- n- and i-regions.[37]

compared to the applied bias), and on the assistance of carrier escape from QWs by phonons instead of only photons, as is assumed in the radiative limit.[39,41,42] In either case, it is expected that any efficiency enhancement will depend strongly on material quality, recombination in the wells and barriers, and the particular choice of bandgaps.[43]

Looking in more detail at the enhancements that are possible in a QWSC, the current enhancement clearly derives from the fact that the lower bandgap QWs extend the absorption edge to longer wavelengths. QWSC spectral response has been accurately modeled,[44] and it show an extended absorption edge compared to the bulk, as well as several quantum well excitonic resonance peaks (Fig. 4.5). The voltage enhancement is a topic of some debate, but it has been shown experimentally and verified theoretically that the open circuit voltage is greater than one would expect given the separation of quantized ground states (seen as the change in absorption edge).[36–38,43] This effect is the result of lower dark current in MQWSCs than that in bulk cells of the same band gap. Figure 4.6 shows

68
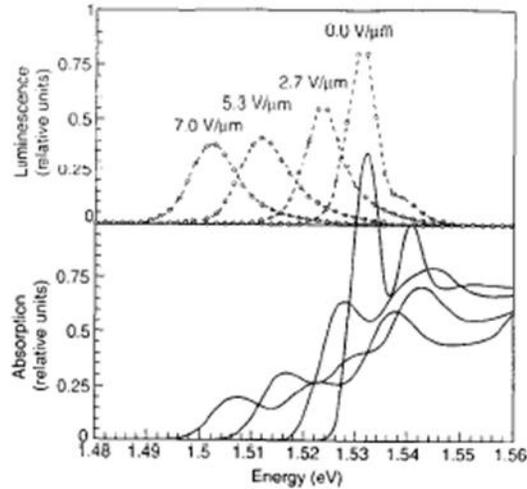
Figure 4.6: Experimental PL spectra and theoretical absorption spectra with electric fields ranging from 0 to 7 V/cm.[37]

experimental photoluminescence (PL) spectra compared with theoretical absorption spectra in an AlGaAs/GaAs single quantum well (SQW) for different electric fields in the well. The effect of QCSE is clearly seen as the peak redshifts and broadens, and there is a noticeable Stokes shift between emission and absorption.

Even if a slight efficiency enhancement was possible in a QWSC design, it would rely so strongly on the specifics of the design and materials involved that it would probably not be worth pursuing on its own. In the nitrides, however, as discussed in the previous section, strain alleviation and the large incremental gains from small increases in the absorption edge give QWSCs a clear advantage over single bandgap designs.

4.2 Carrier Transport in InGaN/GaN Multiple Quantum Wells

4.2.1 Carrier Rate Equations

The processes of carrier escape from quantum wells and carrier collection are essential to the function of MQW solar cells. In order for these devices to operate, generated electrons and holes must escape wells and transit to the contacts before recombining. After a photon has been absorbed, and an electron-hole pair is created in a QW, those charge carriers can either be lost due to recombination or contribute to the photocurrent. Each potential fate for the charge carrier has its own associated characteristic time, and the total carrier lifetime in a QW (τ_{QW}) can be expressed as a competition between recombination and escape mechanisms:

$$\frac{1}{\tau_{QW}} = \frac{1}{\tau_{Rad}} + \frac{1}{\tau_{NR}} + \frac{1}{\tau_T} + \frac{1}{\tau_{TE}}. \tag{4.1}$$

Carriers might recombine radiatively (τ_{Rad}) or nonradiatively (τ_{NR}), which both represent loss from the perspective of a solar cell. One might point out the potential for "photon recycling" following radiative recombination, but due to the large polarization fields intrinsic to the InGaN/GaN system and the resulting Quantum-Confined Stark Effect (QCSE),[45] there is negligible overlap between absorption and emission spectra, especially in MQW devices. Otherwise, the carriers might escape from the well, a process that can happen either by thermionic emission (TE) over the quantum barrier (τ_{TE}), tunneling through the barrier (τ_T). The tunneling rate from any quantum well state n can be estimated through the WKB-approximation as a product an attempt rate ($\frac{v}{L_W}$), which is a function of the carrier velocity, and the tunneling probability from that QW state ($T(E_n)$):[46]

$$\frac{1}{\tau_T} = \frac{v}{L_W} T(E_n) = \frac{n\pi\hbar}{2L_W^2 m^*} \exp \int_0^{L_b} -2\sqrt{\frac{2m^*(E_{C,V}(x) - E_n)}{\hbar^2}} dx. \qquad (4.2)$$

Meanwhile, the rate of thermionic emission depends exponentially on the temperature and on the height of the barrier (found by identifying the maximum potential in the conduction or valence band barrier ($E_{C,V_{max}}$)) relative to the energy level of a confined state:

$$\frac{1}{\tau_{TE}} = \left(\frac{k_B T}{2\pi m^* L_W^2}\right)^{1/2} \exp\left(-\frac{E_{C,V_{max}} - E_n}{k_B T}\right). \qquad (4.3)$$

In both Eqs. (4.2) and (4.3), k_b is Boltzman's constant, T is the absolute temperature, L_w and L_b are the QW and QB thicknesses, respectively, while m* is the effective mass for electrons or holes. The combination of tunneling and thermionic emission time gives us the escape time (τ_{esc}):

$$\tau_{esc} = \left(\frac{1}{\tau_T} + \frac{1}{\tau_{TE}}\right)^{-1}. \qquad (4.4)$$

The thermionic emission rate will increase with increasing temperature or decreasing well depth as the thermal distribution places more carriers above the top of the barrier. Tunneling rate, on the other hand, increases mainly due to decreasing barrier thickness. Once a carrier has made it to the continuum of states above the wells and barriers through either of these methods, it is free to move in the built-in electric field of the diode and will be swept toward the respective contacts. The time it takes for an average carrier to cross the entire intrinsic region is known as the transit time (τ_{trans}). If the effective mobility of the MQW intrinsic region (μ_{MQW}) is known (difficult to estimate in practice, but for the sake of this argument it can be assumed) then the average transit time of a photogenerated carrier is simply half the width of the MQW intrinsic region over the drift velocity:

$$\langle \tau_{trans} \rangle = \frac{L_{MQW}}{2\mu_{MQW}E}, \qquad (4.5)$$

where E is the built-in electric field of the junction. To simplify the expression, it is assumed that carriers drifting in the continuum of states above the QB conduction band maximum do not see the local polarization-induced electric fields in the QW and QB regions. This assumption would be valid if transport of carriers after they escape a QW is primarily ballistic in nature.

Complications arise when the field is weak enough so that the transit time is less than the recapture time, or the time it takes a carrier to thermally relax back into a well. After a recapture event, that carrier will have to go through the same escape and transit process again before recombining in order to contribute to the photocurrent. The total time from generation to collection is called the carrier sweep-out time (τ_{sweep}), which can be simplified by ignoring recapture to the addition of the average transit time and the escape time:

$$\tau_{sweep} = \langle \tau_{trans} \rangle + \tau_{esc}. \qquad (4.6)$$

Another complication to this simplified model arises with the consideration of hot carriers. When photons with energy above the bandgap of the InGaN QW are absorbed, the carriers they generate exist initially in an excited state. From there, it is possible in principle for them to escape the QW before relaxing back to the lowest available energy state in the QW. Escape times for hot carriers should actually be shorter due to field-assisted barrier thinning, and the possibility that a photon of high enough energy could promote a carrier directly into the continuum of states above the QW. Effects of hot carriers on escape, transit, and recapture have been discussed in detail the context of QW infrared photodetectors.[47]

3.2.2 Methods of Extracting Characteristic Times

The carrier extraction model laid out in the previous section is only useful if the various characteristic carrier times are known. Several experimental methods have been demonstrated to extract the relevant carrier lifetimes in quantum well structures. Some of these experiments have been performed on InGaN QWs, while others have only been done in other materials systems, but none have been performed on the specific structure of an InGaN solar cell, where active region thickness and operating bias differ significantly from other types of devices. The experimental lifetimes can then be used to further refine theoretical models, and comparing the lifetimes will reveal where in the device collection efficiency is limited.

Time-resolved photoluminescence (TRPL) is a popular measurement technique for determining the net recombination lifetime τ_R, and it has been previously used for InGaN QWs.[48,49] A femtosecond pulsed laser is required at a wavelength that will resonantly pump the QW, along with a time-resolved high resolution optical measurement system. The characteristic recombination time is extracted from the decay of PL intensity as a function of time after the exciting pulse. Low temperature TRPL (7K) will freeze out non-radiative recombination and yield τ_{Rad}. The escape time, τ_{esc}, is a combination of the tunneling and TE lifetimes from equations (4.2) and (4.3), as well any thermally assisted tunneling or hot carrier escape. It can be measured via time-resolved electroabsorption measurements, where the change in transmission is measured as a function of time after a femtosecond pulse excitation.[50] As carriers transit the active region, they generate a varying space-charge bias, which modulates the electric field in the structure, and causes a shift in transmission. In these pump-probe measurements, the rise time of the differential electroabsorption signal
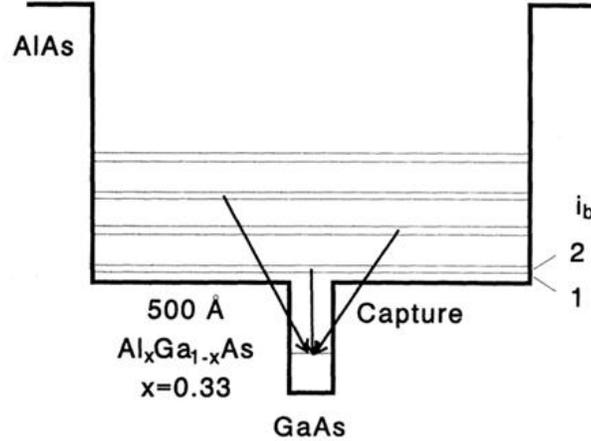
Figure 4.7: Schematic of carrier capture in a AlAs/AlGaAs separate confinement heterostructure with a single GaAs QW used for measuring electron capture rates. Electron energy levels are marked.[54]

corresponds to τ_{esc}. Time from absorption to collection, τ_{sweep}, can be experimentally derived by using time-resolved photocurrent (TRPC) measurements.[51] The difference between τ_{sweep} and τ_{esc} is the active region transit time, τ_{trans}, which would ideally depend only on the drift velocity, and the active region width. Carrier drift velocities can also be measured by the time-resolved electroabsorption method.[52,53] However, carrier recapture events would potentially lengthen this transit time.

The capture time of a carrier into a QW (τ_{recap} in our case) can be measured using a technique similar to experiment of Blom et al.[54] They employed a separate confinement heterostructure with a single quantum well in the center of larger confined region, where the outer barriers are much higher than the inner barriers (AlAs/AlGaAs/GaAs) (Fig. 4.7). Two different methods using this structure resulted in experimental capture times. The first examined the rise time of QW luminescence. Using a short laser pulse and a frequency mixing technique for which the time resolution is comparable to the laser pulse width, the difference in the QW PL rise time between direct (well) and indirect (barrier) excitation

74

gives the capture time. Taking the difference accounts for the time of relaxation to the luminescence level as long as the direct excitation is near the top of the well. The second method examines the decay of barrier excitation. In a pump-probe two pulse setup, the barrier region is excited by the first laser pulse, and after a delay, a second pulse. After the second pulse the luminescence from the barrier is measured. The first pulse will saturate the barrier states with carriers, decreasing the absorption of the second pulse, unless the delay between the pulses is long enough for carriers to be captured by the well. Therefore, the PL signal due to the probe pulse will increase with delay time until all the carriers are captured. In a nitride system, a single InGaN QW with GaN barriers, or a MQW, could be embedded between layers of AlGaN to form the SCH. Another method for measuring τ_{recap} might be the transient differential transmission method.[55]

Another important characteristic time is the hot carrier relaxation time (τ_{relax}). In order to measure τ_{relax}, one can examine the decay in the average energy of the carrier distribution as a function of time after a pulsed photoexcitation.[56] To obtain average distribution energies, the sample is hit by a short laser pulse, and the time-resolved PL signal is measured, then converted to an energy distribution and averaged. The average energies decay on the order of 1 ns, and the distribution becomes thermal. This may not work properly in InGaN QWs because it requires samples of high purity where the acceptor to conduction band luminescence lineshape is clearly distinguished. Another way to measure τ_{relax} is via the transient differential transmission method, as described above for measuring escape time and drift velocity.[57]

4.2.3 The Importance of Electric Fields for Carrier Escape

Electric fields in the wells and barriers also play an important role in carrier escape. For (0001) InGaN/GaN, the field in the wells due to piezoelectric polarization is opposite and much larger than the field due to the built-in voltage drop across the junction ($V_{BI\_GaN} \sim$ 3.3 V). The net field in the wells, assuming complete depletion, heavily doped side regions, and a uniform built-in electric field (F_{BI}), is as follows,

$$F_{QW} = F_{BI} + F_{Pol} + F_{App}$$

$$\cong \frac{V_{BI}}{t_i} + \frac{\sigma_{Pol}}{\epsilon} - \frac{V_{App}}{t_i},$$

(4.7)

where t_i is the thickness of the i-region, σ_{Pol} is the polarization sheet charge density, ϵ is the dielectric permittivity, and V_{App} is the applied bias. Since σ_{Pol} is a material property that only depends on the crystal orientation and composition of InGaN (assuming coherent growth), only variations in t_i and V_{App} will produce changes in F_{QW}. Whereas the net field in the wells will be opposite the direction of carrier collection at zero bias, the polarization field in the barriers is of opposite sense to that in the wells; therefore, the net barrier field (F_{QB}) will be in the same direction as F_{BI}, the direction of carrier collection. Besides locally aiding carrier sweep-out for carriers above the barrier,[i] this field will also effectively thin the barrier because of its triangular potential profile. This will have two effects on carrier escape. First, the TE rate will be weakly field-dependent because of field-assisted barrier lowering.[51] Second, and more importantly, tunneling rates will increase nearly exponentially due to a Fowler-Nordheim type tunneling mechanism as the field effectively lowers and narrows the barrier. Carriers at energies closer to the top of the barrier will escape much

---

[i] It was assumed in section 3.2.1 that the local QW and QB fields do not affect carrier drift. What may happen is that the QB field could give an initial boost in velocity to carriers that have just surmounted the barrier. That boost could be enough to move the carrier into the continuum of states above the wells and barriers, where it will see primarily the built-in field.
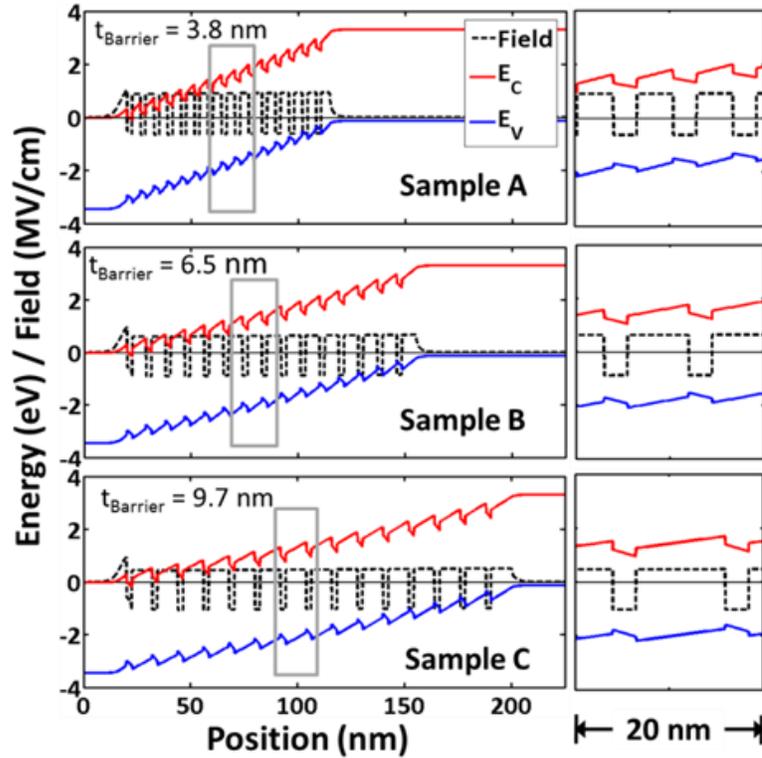
Figure 4.8: Band diagrams for 15X MQW solar cell structures with barrier thicknesses of 3.8nm, 6.5nm, and 9.7nm. Zoomed in sections on the right show QW field increasing and barrier field decreasing with increasing barrier thickness.[46]

more quickly, which would aid hot carrier escape, wherein carriers are initially excited into a higher energy state in the well by an above-gap photon and escape before relaxing via phonon emission.[47]

A study was performed to try and learn more about carrier transport mechanisms in InGaN MQW solar cells.[46] It involved three samples, A, B, and C, with barrier thicknesses of 3.8, 6.5, and 9.7 nm respectively, the same QW thickness (2.5 nm), and the same number of periods (15), grown on sapphire substrates by ammonia molecular beam epitaxy (NH$_3$-MBE). Fig. 4.8 shows band diagrams for the three devices with increasing barrier thickness simulated using SiLENSe version 5.2 software. When zoomed in on the QWs on the right of Fig. 12, it is apparent that there is approximately a 0.4 MV/cm increase in the field in QW
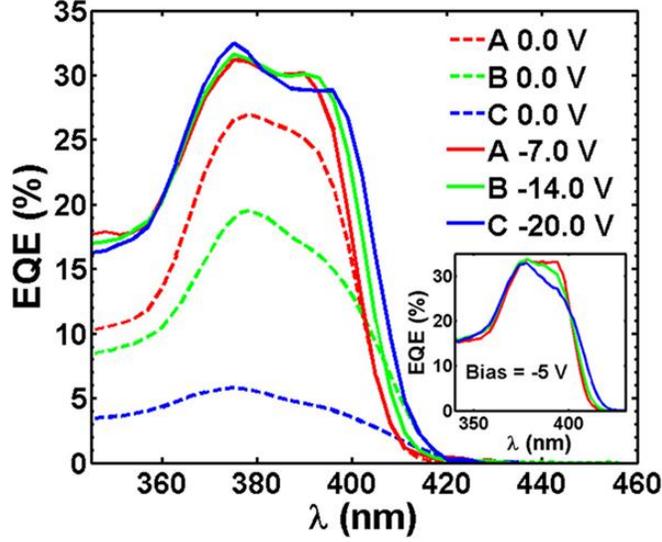
Figure 4.9: External quantum efficiency for samples A, B, and C plotted at 0 applied bias (dotted curve), reverse bias corresponding to calculated flat-band quantum wells (solid curve), and a uniform reverse bias of -5V (inset).[46]

region between samples A and C, and the field in the barrier regions is similarly decreasing. This behavior is expected because the magnitude of F_{BI} is decreasing as the thickness of the structure increases.

The effect should be detrimental to carrier collection for the reasons explained above, and indeed the steady state EQE drops dramatically in thicker barrier samples (Fig. 4.9). Solving Eq. (4.7) for flat band in the wells ($F_{QW} = 0$) gives values ranging from -7 V for the 3.8 nm barrier sample, to -20 V for the 9.7 nm barrier sample. Applying this respective bias to each sample should give a very similar local environment for carrier extraction, and improve extraction efficiency due to effective barrier thinning and creating effectively shallower wells. In fact, as can be seen in Fig. 4.9, at the flat-well bias point of each sample, their EQE spectra lay almost on top of each other. The IQE of the samples at these biases is estimated at near 100% due to the relatively small amount of InGaN (37 nm, less than one quarter of an absorption length) and the ~18% Fresnel surface reflection

78

losses. There are clearly field-dependent carrier extraction issues in InGaN MQW devices that get proportionally worse with increasing barrier thickness, and these the extraction issues dominate device performance. The next section will discuss the identification of the exact mechanism limiting extraction.

4.2.4 Temperature Dependent J-V Measurements

To separate which extraction mechanism, tunneling or thermionic emission (TE), dominates in InGaN MQW solar cells,[i] electrical measurements were performed on the samples described in section 4.2.3 over a range of temperatures from 150 K to 393 K (Fig. 4.10).[46] The tunneling rate should be temperature independent while the TE rate will be strongly temperature dependent.

There is very little change in the *J-V* curves of the thin barrier sample A across the temperature range, and there is only the expected slight decrease in V_{oc} and increase in J_{sc} due to bandgap shrinkage with increasing temperature, which allows the InGaN layers to absorb more photons.[58] On the other hand, the *J-V* curves of the 9.7 nm barrier sample C show a substantial decrease in FF and J_{sc} with decreasing temperature. There is also significant bias dependence of the photocurrent in sample C: at every temperature, the photocurrent recovers to near the same value at -5 V. In fact, the room-temperature photocurrent saturates at the same value of ~0.6 mA/cm^2 in all three samples. As was seen in the reverse-biased EQE spectra in Fig. 4.9, a sufficient reverse bias will increase the carrier collection efficiency to near 100% regardless of barrier thickness.

---

[i] Specifically, which mechanism is dominant when the InGaN composition in the QWs is on the order of 20%, or when the absorption edge or emission peak is beyond 450 nm.
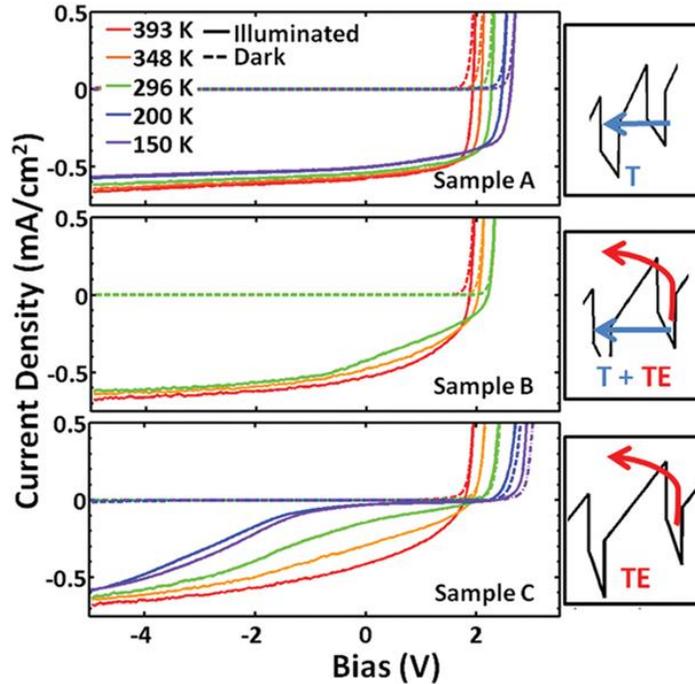
Figure 4.10: (left) Current density vs. bias for samples A, and C having 3.8, and 9.7 nm barriers, respectively, as a function of temperature from 150 to 393K with and without 1-sun intensity illumination. Data for sample B, with 6.5 nm barriers, is also shown from 296 to 393 K. (right) Schematics for relevant escape mechanisms for each sample: T = tunneling and TE = thermionic emission.[46]

It is clear that there is no temperature dependent mechanism in play for 3.8 nm barriers, but a strongly temperature dependent mechanism affects the 9.7 nm barriers. The dominant mechanism in the thicker barrier sample is mitigated by a strong reverse bias, which would effectively thin the barriers. Therefore, carrier escape from QWs with thin barriers or at large reverse bias must be dominated by tunneling, while for thick barriers at small reverse bias or forward bias, escape is dominated by TE.

4.2.5 Carrier Extraction Modelling

To confirm the experimental results from section 3.2.4 with a theoretical model, escape lifetimes for the exact structures of samples A, B, and C were calculated at 300 K

and 400 K and as a function of bias from -5 to +3 V using a coupled Schrodinger-Poisson drift-diffusion solver (Fig. 4.11).[46,59] Escape was only considered from the ground state energy levels for electrons and holes, since that is the worst case scenario for carrier escape and a good assumption in the absence of high excitation levels or hot carrier effects.

The calculations show that the hole is the rate limiting carrier for both tunneling and TE, due to its larger effective mass.[i] Tunneling is clearly much faster with thinner barriers, and the lifetimes also decrease with reverse bias, as expected due to barrier lowering/thinning. At room temperature, tunneling remains dominant in sample A at all biases. For sample B, tunneling escape for the rate limiting carrier, holes, becomes faster than τ_{TE}, at positive bias, but below V_{oc}. Finally, for sample C, τ_{TE} for holes remains faster than τ_T until zero bias. When the calculations for τ_{TE} are performed at 400 K,[ii] the thermionic emission lifetime drops and its relation to τ_T changes. Now the voltage at which τ_{TE} drops below τ_T for holes shifts farther toward negative bias. The black lines on Fig. 4.11 represent an assumed aggregate recombination lifetime of 1 ns,[iii] in accordance with measurements on InGaN MQW structures.[60] The limiting carrier escape lifetime must be smaller than this value in order for carriers to be collected efficiently.

Comparing Figures 4.10 and 4.11, it is clear that at -5 V reverse bias, when all devices have reach their saturation current and IQE should be near 100%, that tunneling is dominant in all devices for electrons and holes. The increasing tunneling lifetimes as barrier thickness increases directly correlates to the decrease in FF of these devices. The bias point at which both the electron and hole tunneling lifetimes become shorter than the

---

[i] At steady state, both electrons and holes must escape at the same rate. When one carrier type has a slower escape rate, space charge will build up to the point that the energy bands readjust until steady state is reached.
[ii] Remember that tunneling rates are assumed to be independent of temperature.
[iii] In reality this recombination lifetime will have some bias dependence because the overlap of electron and hole wavefunctions affect both radiative and non-radiative recombination rates.
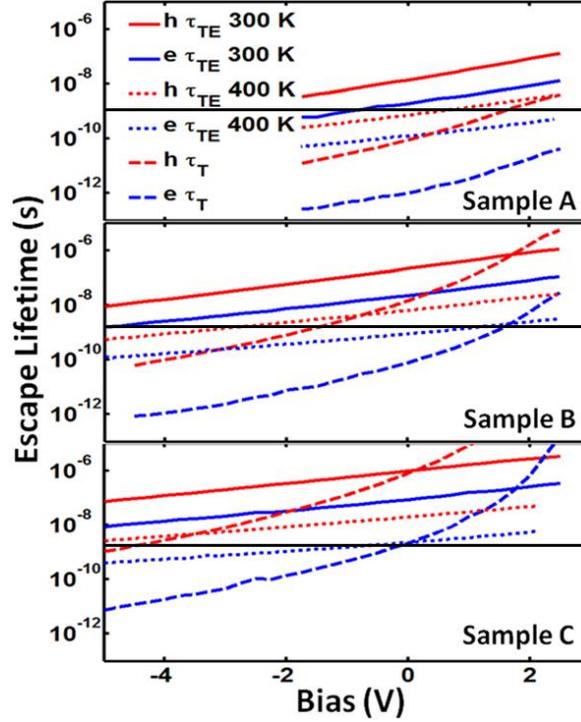
Figure 4.11: Calculated lifetimes for thermionic emission (TE) at 300K and 400K and tunneling (T) at 300K for electrons (e) and holes (h) from the lowest energy bound states of the quantum wells in the three structures. Black horizontal lines represent an assumed aggregate recombination time of 1 ns.[46]

recombination lifetime, corresponds closely to the point in the *J-V* curves at which the photocurrent saturates. These bias points are approximately +1.5 V, -1.8 V, and -5 V for samples A, B, and C respectively. Increasing temperature partially compensates the lack of tunneling efficiency by decreasing τ_{TE}, but does not have much effect on the point of saturation, since τ_{TE} remains above 1 ns when it is also less than τ_T. Therefore, it is clear that tunneling is the more efficient carrier escape mechanism, even at reasonably elevated temperatures that might be experienced during normal operation. This finding has influenced the design of both solar cell and LED active regions by illustrating the importance of decreasing barrier thickness in order to promote tunneling transport.
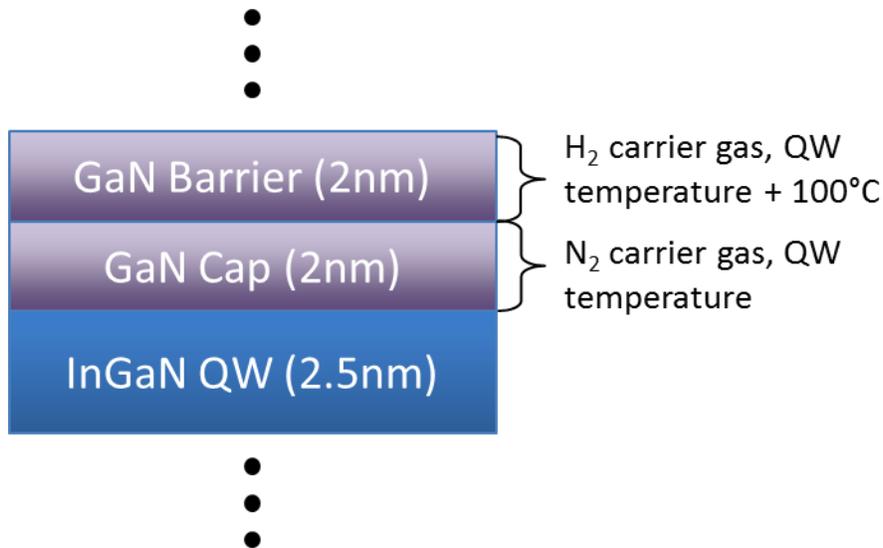
Figure 4.12: Schematic of a single period of a InGaN/GaN MQW solar cell with the optimized two step barrier.

4.3 Optimizing the Multiple Quantum Well Active Region

4.3.1 The Two-Step Barrier Growth Method

The need to decrease QB thickness must be balanced against the need to avoid V-defect formation, which occurs during low temperature *c*-plane GaN or InGaN growth by MOCVD. Refer to Chapter 2 for an in-depth discussion of the properties of V-defects. For the purposes of InGaN solar cells, V-defects act as non-radiative recombination centers and leakage pathways that can severely degrade the open-circuit voltage.[61,62] A two-step QB growth process can be employed to mitigate the propagation of V-defects through an InGaN/GaN MQW stack.[63,64] Figure 4.12 shows a schematic of one period of a MQW employing a two-step barrier. A low temperature GaN capping layer immediately above the InGaN QW protects the integrity of the QW against indium desorption and/or thickness fluctuations, which can be induced during the ramp up to higher temperatures and in the presence of H_2.[65] This GaN cap is grown at the same temperature as the QW and with N_2 as
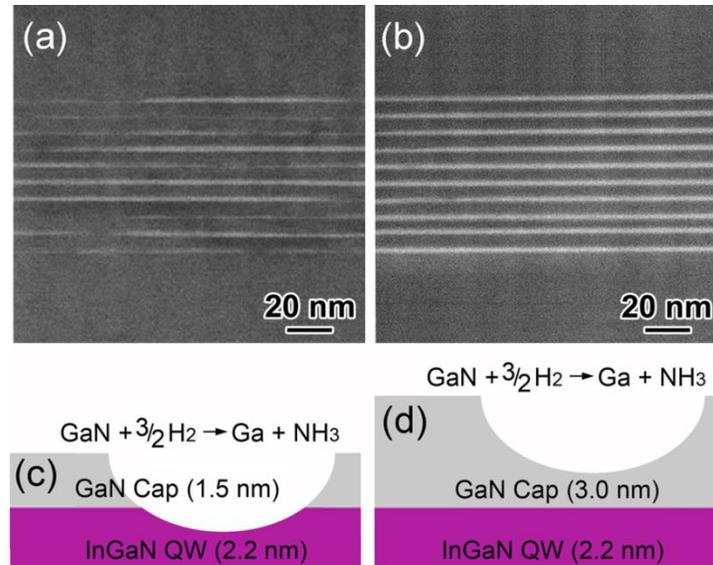
Figure 4.13: (a) HAADF-STEM image showing disordered QWs with 1.5nm GaN cap due to (c) a process of H_2 etching of the InGaN well. (b) Ordered wells with 3.0 nm cap, (d) which is thick enough to prevent well exposure during the etching process.[63]

the carrier gas. The subsequent GaN layer is grown at higher temperature and with H_2 added to the carrier gas mixture in order to improve surface adatom mobility and effectively fill in V-defects before they can grow and propagate.[64,66–68] Growth of barriers at higher temperatures and with the addition of H2 carrier gas without a sufficiently thick protective GaN cap layer have been shown to be detrimental to InGaN/GaN MQW solar cell performance.[69]

Previously, a correlation had been demonstrated between thicker low temperature GaN cap layers and superior microstructure and device performance.[63] Figure 4.13 shows the process by which InGaN QWs are degraded during high temperature barrier growth. High angle annular dark field scanning transmission electron microscopy (HAADF-STEM) of InGaN/GaN MQWs with two-step barriers reveal severe thickness fluctuations when the cap thickness is 1.5 nm (Fig. 4.13(a)), but no evident fluctuations when the cap thickness is 3.0 nm (Fig. 4.13(b)). The origin of the fluctuations was proposed to be hydrogen back-
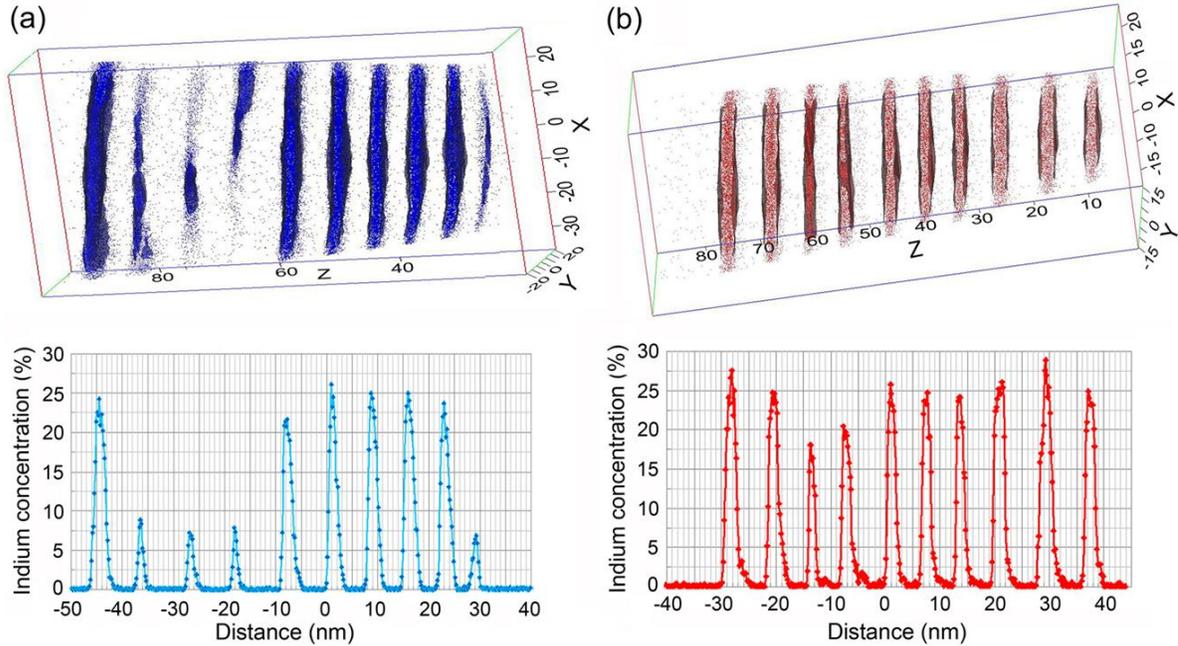
Figure 4.14: APT data from (a) the sample with 1.5 nm GaN cap layers and (b) the sample with 3.0 nm GaN cap layers. 3-D indium atom maps are shown in the upper part of the figure and 1-D profiles of the average indium concentration are shown in the lower part of the figure. The isoconcentration surfaces in the 3-D atom maps identify the locations at which the indium concentration (x in $In_xGa_{1-x}N$) is equal to 5%. [63]

etching of the cap and QW (Fig. 4.13(c)). When the cap is thick enough, the etching does not penetrate the QW during high temperature barrier growth (Fig. 4.13(d)). The erosion of the GaN cap due to the reaction of GaN with H_2 likely occurs at the end of the temperature ramp when H_2 is first introduced at the beginning of the high temperature growth step because there is not already TMIn or TEGa in the reactor driving growth.

Atom probe tomography (APT) confirmed the difference in thickness fluctuations between QWs with 1.5 nm and 3.0 nm cap thicknesses (Fig. 4.14(a) and Fig. 4.14(b), respectively), and also revealed a large difference in average and maximum compositions between the respective InGaN layers. The APT results correlated with electrical characteristics as well as PL and EQE spectra. In the case where the cap layer was too thin and had been eroded to the point where parts of the InGaN QW had been exposed and

decomposed, the amount of InGaN material volume available for absorption of incident photons decreased. Also, the average InGaN composition decreased, so the average bandgap increased, which also would lead to fewer photons being absorbed. These effects caused the decreases in EQE, J_{sc}, and peak PL intensity in the sample with a 1.5 nm cap, as well as the blue-shift in PL peak intensity. The observed differences are characteristic of solar cells that suffer from QW thickness fluctuations and indium desorption. The need to protect the integrity of the QW with a sufficiently thick cap must then be balanced against the need to decrease total GaN barrier thickness in order to promote efficient tunneling transport. Growth optimization around that trade-off will be the subject of the next section. More recently, an AlGaN capping layer has been proposed, which could, if kept thin, preserve fast carrier escape while also of the QW layers and interfaces.[70]

4.3.2 Optimization of Thin Quantum Barriers

Section 4.2 explained the benefit of thinner quantum barriers for carrier transport in the InGaN/GaN MQW solar cell structure, and section 4.3.1 described the benefits and limitations of a two-step barrier growth scheme. The challenge for developing a process for MOCVD growth of a thin barrier MQW InGaN solar cell lies in using a two-step barrier growth method while simultaneously shrinking the barrier thickness as much as possible. There is a three way trade-off between decreasing barrier thickness for improved carrier transport, increasing cap thickness for better well protection, and increasing barrier temperature for better v-defect control. It was necessary to optimize each of these variables sequentially in order to arrive at the best possible (0001) MQW device on sapphire.
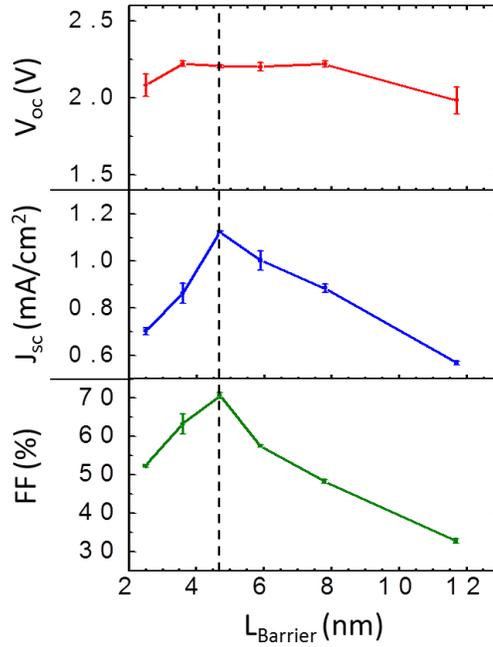
Figure 4.15: Average values of V_{oc}, J_{sc}, and FF for 10X In$_{0.2}$Ga$_{0.8}$N MQW solar cells with 2.5 nm wells plotted as a function of barrier thickness, with optimum thickness of 4.7 nm marked by a dashed line.

For all of the devices described in the optimization series in this section, the active region consisted of a 10 period MQW with ~2.5 nm In$_{0.2}$Ga$_{0.8}$N QWs grown at 800°C, corresponding to an absorption edge between 450 and 460 nm. The low temperature cap layer in all devices was also grown at 800°C, and the cap growth and subsequent temperature ramp prior to the high temperature barrier growth were performed in N$_2$. High temperature barrier growth was performed with a mix of N$_2$ and H$_2$ carrier gases. During temperature ramps either up or down, the temperature was allowed to settle before the growth of the next step proceeded. Samples were grown by MOCVD on double-side-polished (0001) sapphire wafers. After the nucleation seed layer, a 3 μm Si-doped n-GaN ([Si] = 6 x 10^{18} cm^{-3}) template layer was grown followed by a 10 nm highly Si-doped n^{+}-GaN ([Si] = 2 x 10^{19} cm^{-3}) layer. Immediately after the final QW of the active region, 25 nm

(a)　　　　　　　　　　　　　　　　　　　　**(b)**
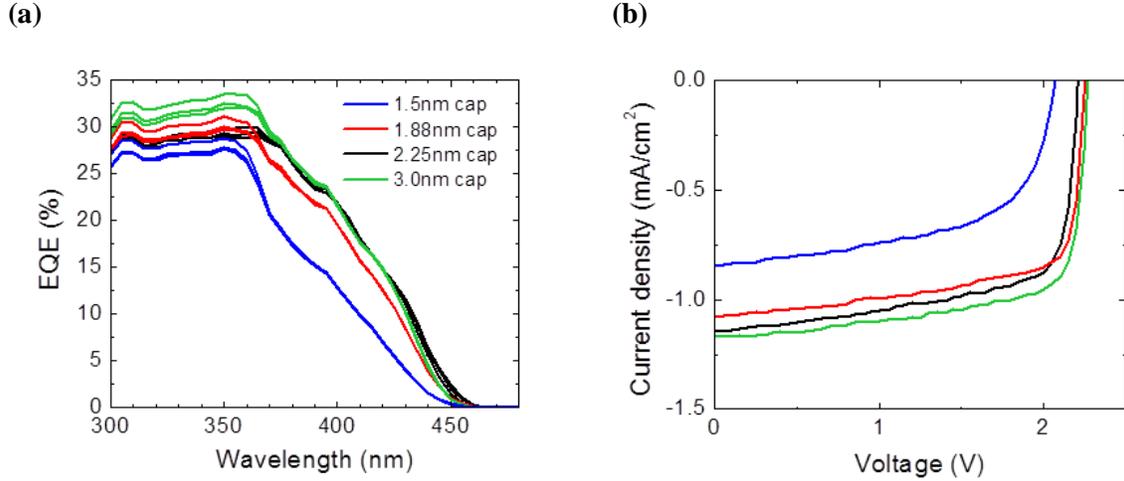
Figure 4.16:　(a) EQE spectra and (b) *J-V* characteristics for 10X $In_{0.2}Ga_{0.8}N$ MQW solar cells with cap thicknesses ranging from 1.5 nm to 3.0 nm.

of highly Mg-doped p^+-GaN ([Mg] = 5 x 10^{19} cm^{-3}), 20 nm moderately Mg-doped p-GaN

([Mg] = 2 x 10^{19} cm^{-3}), and a 10 nm highly Mg-doped p^+-GaN contact layer ([Mg] = 1 x

10^{20} cm^{-3}) were subsequently grown.

Characterization of all samples discussed in this section proceeded as follows. The

sample surfaces were characterized by atomic force microscopy (AFM). The QW and QB

thicknesses and indium composition were measured by x-ray diffraction (XRD). Absorption

spectra were measured using a UV-VIS-NIR spectrophotometer coupled with an integrating

sphere.[24]　The samples were then processed into solar cells using standard contact

lithography. Cl_2-based reactive ion etching was used to define 1 mm by 1 mm mesas. The p-

contact scheme consisted of 30/300 nm Pd/Au electron-beam deposited grids on the top of

each mesa with a grid spacing of 200 μm and a grid width of 5 μm, and the n-contact

scheme consisted of 30/300 nm Al/Au electron-beam deposited rings around the base of

each mesa. After fabrication, dark and illuminated current density versus voltage (*J-V*)

measurements were taken using a Keithley 2632 source meter. An Oriel 300 W Xe lamp

T_b (C)	Voc_{avg} (V)	FF_{avg} (%)	Jsc_{avg} (mA/cm^2)
875	2.24	69.0	0.91
900	2.25	70.0	0.97
925	2.20	69.0	0.95
950	2.16	68.9	0.95

Table 4.1: Average values of V_{oc}, J_{sc}, and FF for 10X In$_{0.2}$Ga$_{0.8}$N MQW solar cells with barrier growth temperatures ranging from 875°C to 950°C.

provided broadband illumination with an unfiltered intensity of 1 sun, as determined by integration of the external quantum efficiency (EQE) spectra over the AM0 solar spectrum. EQE spectra were measured under monochromatic illumination using the same lamp with an Oriel 260 monochromator and were calibrated using a reference Si photodetector.

The initial series of devices examined reducing barrier thickness by reducing the cap and barrier simultaneously, maintaining and 1:1 thickness ratio. Total GaN QB thicknesses ranged from 3.0 to 11.5 nm. The resulting trends for important device figures of merit are shown in Fig. 4.15. The V_{oc} held relatively constant over the full range of barrier thicknesses, always more than 2V, but the J_{sc} and FF decreased substantially on either side of a 4.7 nm total barrier thickness. For thicknesses greater than 4.7 nm, the degradation can be attributed to inefficient tunneling and poor carrier collection. For thicknesses less than 4.7 nm, the degradation is likely due to a loss of well integrity resulting from the reduced cap thickness.

In order to reduce barrier thickness below 4.7 nm without QW degradation, it is necessary to find the thinnest cap that does not result in QW damage. When Hu et. al. performed a similar experiment (described in section 4.3.1), they found that device performance increased with cap thickness up to a 3 nm cap; however, their total barrier was much thicker.[63] A series of devices was grown with a total barrier thickness fixed at of 4.5
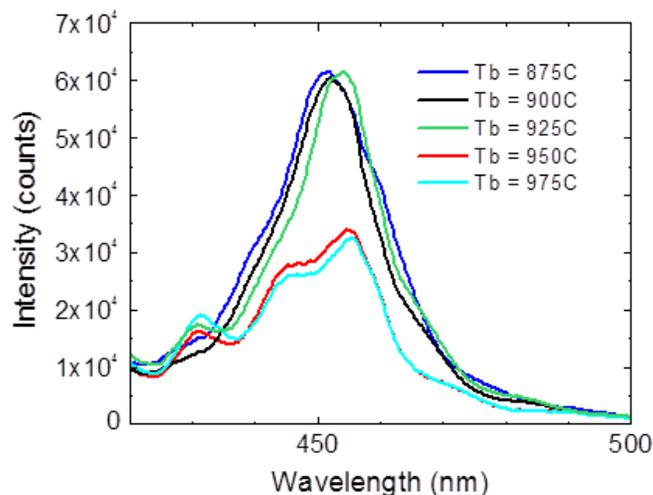
Figure 4.17: Photoluminescence spectra for 10X $In_{0.2}Ga_{0.8}N$ MQW solar cells with barrier growth temperatures ranging from 875°C to 950°C.

nm, while the low temperature cap thickness was varied between 1.5 nm and 3.0 nm. Electrical results (Fig. 4.16) reveal that the EQE and *J-V* curves of devices with a cap thickness greater than 1.5 nm are very similar within normal run-to-run variations, but there is a significant drop in voltage, current, and EQE for the 1.5 nm cap device. The decision was made to move forward in the optimization with a cap thickness of 2.0 nm as it was as thin as possible while being safely above the cutoff for performance drop, which occurred somewhere between 1.5 and 1.9 nm.

Next, the growth temperature of the high temperature barrier step was optimized. Morphology was expected to improve due to improved v-defect filling with increased growth temperature, but there is also an increased chance of QW degradation through thickness fluctuations and indium desorption. Table 4.1 shows that there was very little change in the device metrics between barrier temperatures of 875°C and 950°C, besides a slight drop in V_{oc} above 900°C. Because the goal is to develop a process that will be robust

90
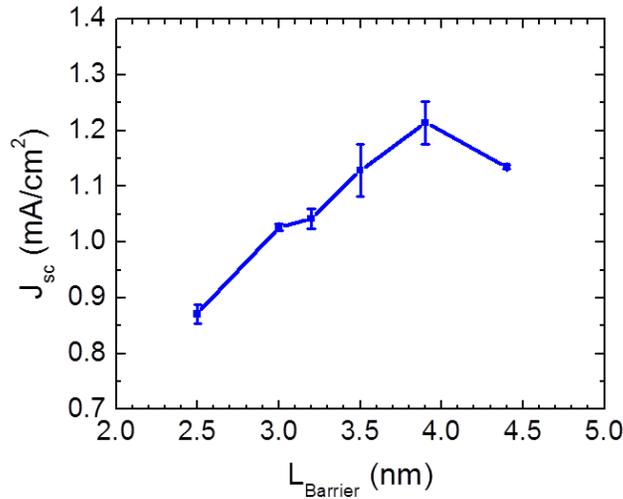
Figure 4.18: Trend of J_{sc} vs. barrier thickness for 10X $In_{0.2}Ga_{0.8}N$ MQW solar cells with 2.5 nm wells.

when increasing the indium content of the wells, which might need to be done in the future to optimize for MJSC integration, a temperature should be chosen that closes v-defects without being close to the limit for well damage. AFM scans of the top barrier in the MQW showed that pits begin filling at 900°C, while PL emission began to show characteristic signs of high temperature QW damage – peak quenching and the formation of a second peak at shorter wavelengths – starting at 925°C (Figure 4.17). Therefore, it was decided that 900°C was the most appropriate barrier temperature.

Finally, another series was grown to further decrease barrier thickness with an optimized cap thickness and barrier temperature. Unfortunately, there was not much improvement over the unoptimized structures. The 10 period MQW samples had barrier thicknesses ranging from 2.5 to 3.4 nm, each with a 2 nm cap, wells grown at 800°C and barriers grown at 900°C. There was not much change in FF or V_{oc}, but the J_{sc} dropped sharply for barriers less than 4 nm thick (Fig. 4.18). The most probable cause for this behavior is that the high temperature portion of the barrier was not grown thick enough to

91

effectively fill pits and mitigate v-defect propagation. Since this effect was seen in the absorption spectra as well, there was most likely a decrease in well integrity with decreasing barrier thickness. Other factors limiting FF increase (expected to occur with thinner barriers and more efficient carrier collection) could be the high TDD on sapphire substrates or other impurities. It was important to examine in the next steps not only higher numbers of MQW periods, but also the effect of lower TDD on free standing GaN substrates.

4.3.3 High Performance Devices with Thin GaN Barriers

After optimizing the two-step GaN barrier for minimal thickness, a series of solar cells were grown using the optimal barrier conditions with increasing numbers of well/barrier periods. MOCVD was used to grow InGaN/GaN MQW solar cells on co-loaded substrates consisting of half of a 50 mm double-side-polished (0001) sapphire wafer with a 2 μm n-GaN ([Si] = 6 x 10^{18} cm^{-3}) template and a 5 mm x 5 mm piece of a hydride vapor phase epitaxy (HVPE) grown bulk (0001) GaN substrate from Furukawa Denshi Co., Ltd. The bulk (0001) GaN substrate had a threading dislocation density (TDD) of less than 3 x 10^6 cm^{-2}, while the TDD of GaN grown on sapphire was at least 2 orders of magnitude higher.[71] As shown in the schematic structure in Figure 4.19, the MOCVD growth consisted of a 2 μm Si-doped n-GaN ([Si] = 6 x 10^{18} cm^{-3}) template layer followed by a 10 nm highly Si-doped n$^+$-GaN ([Si] = 2 x 10^{19} cm^{-3}) layer. The intrinsic active region consisted of an undoped In$_{0.2}$Ga$_{0.8}$N/GaN MQW with 10 to 50 periods, 2.3 nm QWs for samples grown on sapphire, 3.0 nm QWs for samples grown on bulk (0001) GaN, and 4.0 nm QBs for all samples. The final QW was immediately followed by a 25 nm highly Mg-doped p$^+$-GaN
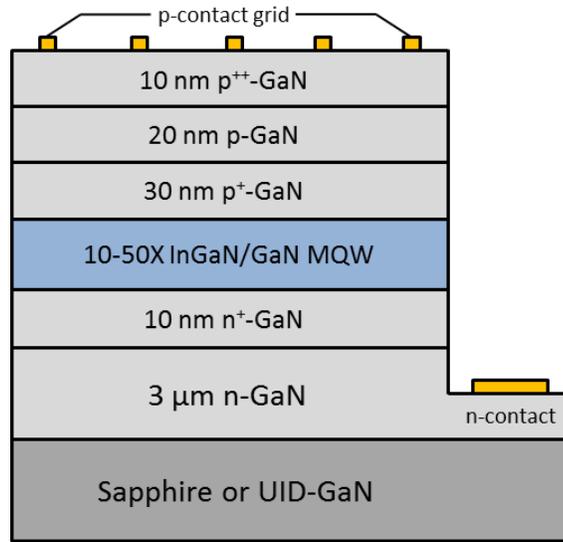
Figure 4.19: Cross sectional schematic of general device structure for a InGaN/GaN MQW solar cell with a varying number of QW periods and optimized thin barriers.

([Mg] = 5 x 10^{19} cm^{-3}) layer, a 20 nm moderately Mg-doped p-GaN ([Mg] = 2 x 10^{19} cm^{-3}) layer, and a 10 nm highly Mg-doped p$^+$-GaN contact layer ([Mg] = 1 x 10^{20} cm^{-3}).

Following the MOCVD growth, the sample surfaces were characterized by atomic force microscopy (AFM) with a Digital Instruments Dimension 3000 AFM, the QW and QB thicknesses and indium composition were measured by x-ray diffraction (XRD) using a PANalytic MRD PRO diffractometer, and the layer thicknesses were confirmed by high angle annular dark field scanning transmission electron microscopy (HAADF-STEM). The absorption spectra of the samples were measured using a Shimadzu UV-3600 UV-VIS-NIR spectrophotometer coupled with an integrating sphere.[24] The samples were then processed into solar cells using standard contact lithography. Cl$_2$-based reactive ion etching was used to define 1 mm by 1 mm mesas. The p-contact scheme consisted of 30/300 nm Pd/Au electron-beam deposited grids on the top of each mesa with a grid spacing of 200 μm and a grid width of 5 μm, and the n-contact scheme consisted of 30/300 nm Al/Au electron-beam deposited rings around the base of each mesa. After fabrication, dark and illuminated current

(a)   **(b)**
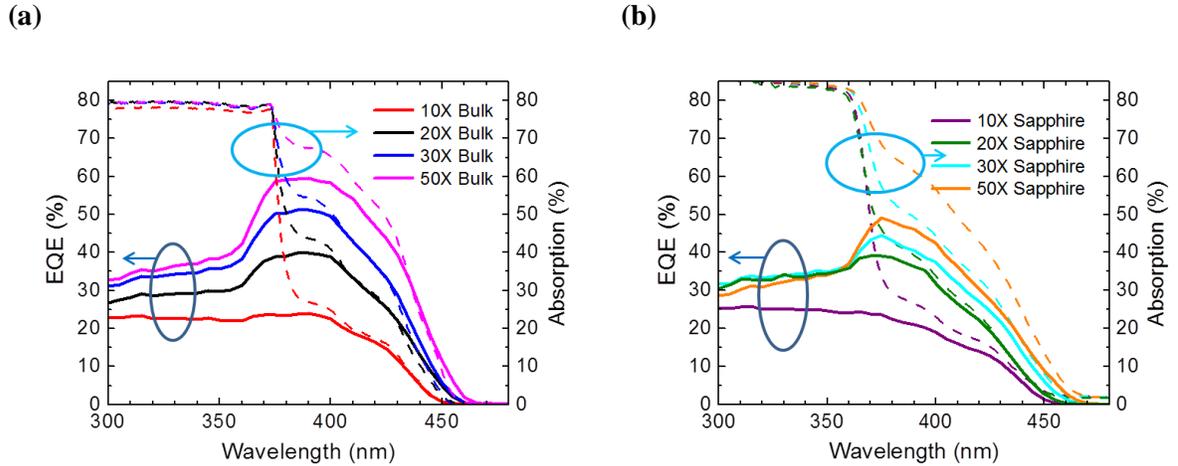
Figure 4.20:   EQE (solid lines) and absorption (dashed lines) measurements for InGaN solar cells with 10–50 QWs. Samples were grown on co-loaded (a) bulk (0001) GaN substrates and (b) sapphire substrates with 2 μm n-GaN templates.[72]

density versus voltage (*J-V*) measurements were taken using a Keithley 2632 source meter. An Oriel 300 W Xe lamp provided broadband illumination with an AM0 intensity of 1 sun, as determined by integration of the external quantum efficiency (EQE) spectra over the AM0 solar spectrum. EQE spectra were measured under monochromatic illumination using the same lamp with an Oriel 260 monochromator and were calibrated using a reference Si photodetector.

Figures 4.20(a) and 4.20(b) show the EQE and absorption spectra of solar cells with 10, 20, 30, and 50 QW periods grown concurrently on bulk (0001) GaN and sapphire, respectively. The bulk (0001) GaN devices increased in EQE across the spectrum with increasing QWs, and reached a peak EQE of 60% with 50 QWs. The sapphire devices, in contrast, showed a similar increase in EQE between 10 and 20 QWs, but diminishing improvement compared to the bulk (0001) GaN devices as the number of QWs increased above 20. In addition, the internal quantum efficiency (IQE), which can be extracted by taking the ratio of the EQE and absorption spectra, was significantly better for the bulk

94

(a)

(b)
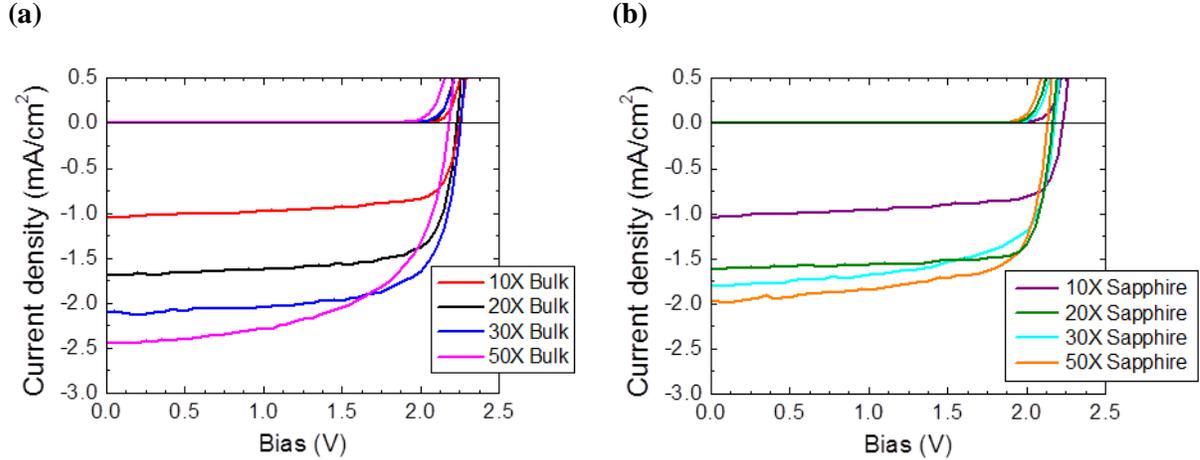
Figure 4.21: *J-V* curves for InGaN solar cells with 10–50 QWs grown on co-loaded (a) bulk (0001) GaN and (b) sapphire substrates.[72]

(0001) GaN devices with more than 20 QWs than for the sapphire devices with more than 20 QWs. IQE, which is a measure of carrier collection efficiency, is very sensitive to non-radiative recombination resulting from TDs and V-defects, so this trend is not surprising. Crossing of the absorption and EQE spectra near the absorption edge in Fig. 4.20(a) is not physical and likely resulted from on wafer wavelength variations between different measurement areas.

Dark and illuminated *J-V* measurements for the solar cells on bulk (0001) GaN are presented in Fig. 4.21(a), while the corresponding measurements for solar cells on sapphire appear in Fig. 4.21(b). These thin barrier devices exhibited very high open circuit voltages (V_{oc}) as a whole, with values up to 2.28 V. Additionally, they demonstrated fill factors (FFs) up to 80%. The best performing device overall was the 30X MQW solar cell on bulk (0001) GaN, with a peak EQE of 51.2%, a V_{oc} of 2.26 V, a FF of 70.4%, a short circuit current density (J_{sc}) of 2.10 mA/cm^2, a maximum power density ($P_{d,max}$) of 3.33 mW/cm^2, and a conversion efficiency of 2.4% compared to the AM0 integrated power density of 1366.1 W/m^2.
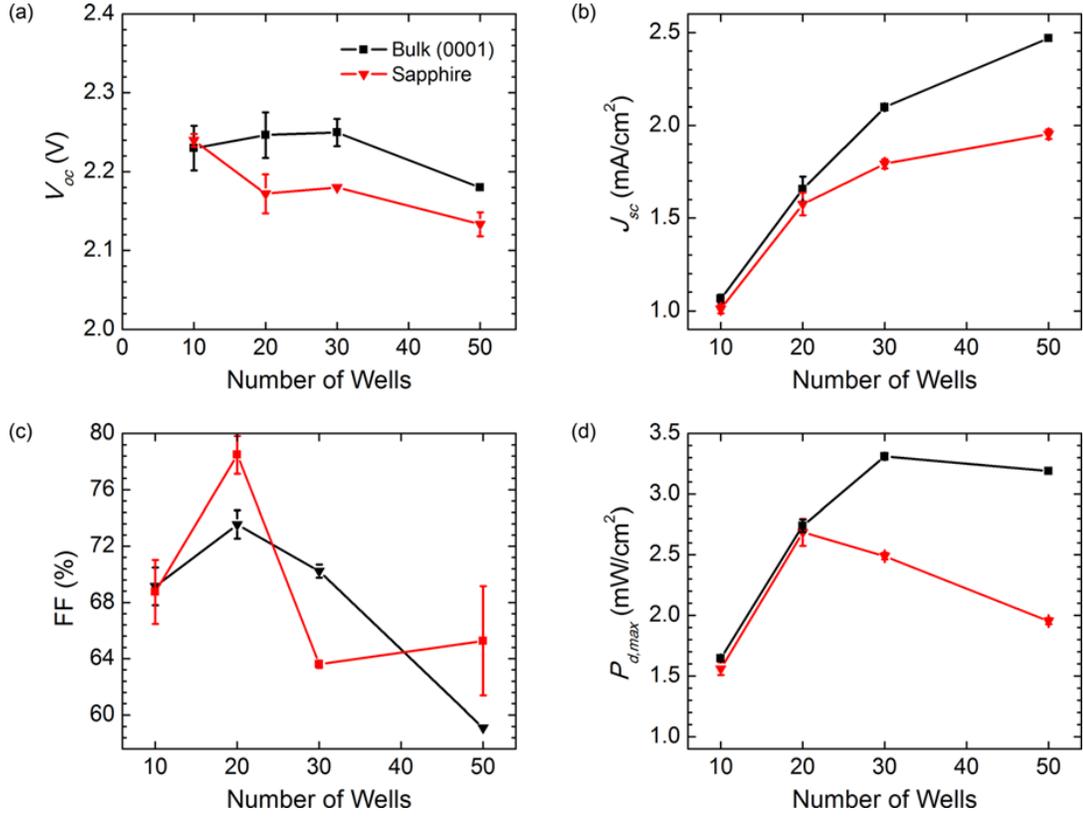
Figure 4.22: Dependence of (a) open circuit voltage, (b) short-circuit current density, (c) fill factor, and (d) maximum power density on number of QWs for InGaN solar cells grown on co-loaded bulk (0001) GaN and sapphire substrates.[72]

The main difference between growth on non-native sapphire and native GaN substrates is the large difference in TDD in the epitaxial layers. Threading dislocations act as non-radiative recombination centers and leakage pathways in GaN-based devices;[11,73] therefore, improved performance on bulk (0001) GaN substrates is expected. A comparison of device performance for growth on sapphire and bulk (0001) GaN substrates can be seen in Figs. 4.22(a)-(d), which show the dependence of V_{oc}, J_{sc}, FF, and $P_{d,max}$ on the number of QWs in the active region, respectively. Each of these values, with the exception of FF, clearly improved on bulk (0001) GaN substrates. On sapphire, the decrease of V_{oc} and FF and the relative drop of J_{sc} compared to bulk (0001) GaN are likely due to the propagation

96

(a)   (b)
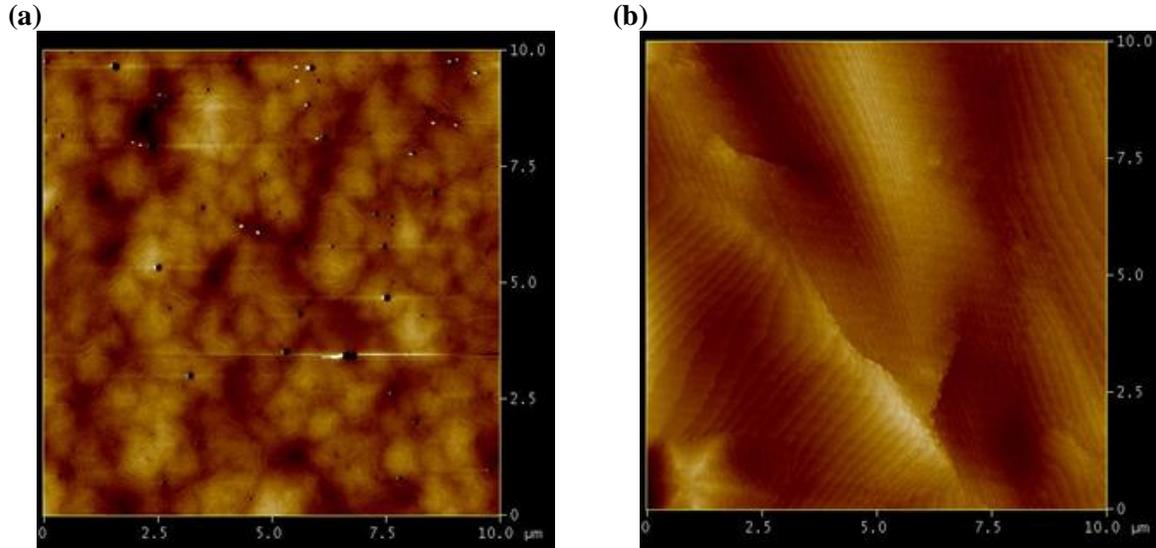
Figure 4.23: AFM micrographs (10 µm scan) of the p-GaN surface of InGaN solar cells with 50 QWs grown on co-loaded (a) bulk (0001) GaN and (b) sapphire substrates.

of V-defects through the MQW stack. AFM images show pits on the surface of the p-GaN on sapphire samples starting with 20 QWs, and the size of the pits increasing monotonically with increasing QW number (Fig. 4.23(a)). Increasing the number of QWs promotes V-defect formation in this case,[74] despite growth conditions designed to prevent them. All samples on bulk GaN, in contrast, were smooth and pit-free, as expected due to the low TDD (Fig. 4.23(b)). Nevertheless, some degradation still occurred between the 30 QW and 50 QW bulk (0001) GaN devices in the absence of V-defects, as indicated by the decrease seen in $P_{d,max}$ in Fig. 4.22(d).

Samples with 50 QWs on both sapphire and bulk (0001) GaN were investigated by HAADF-STEM to verify layer thicknesses and compare structural degradation mechanisms. Figure 4.24(a) shows a cross sectional image of the 50 QW sample on bulk (0001) GaN, with good structural quality through the entire stack, though there were some slight barrier width fluctuations. This contrasts with the image of the 50 QW sample on sapphire (Fig. 4.24(b)), which shows severe QW width fluctuations. In addition, it was noted that the QWs

97
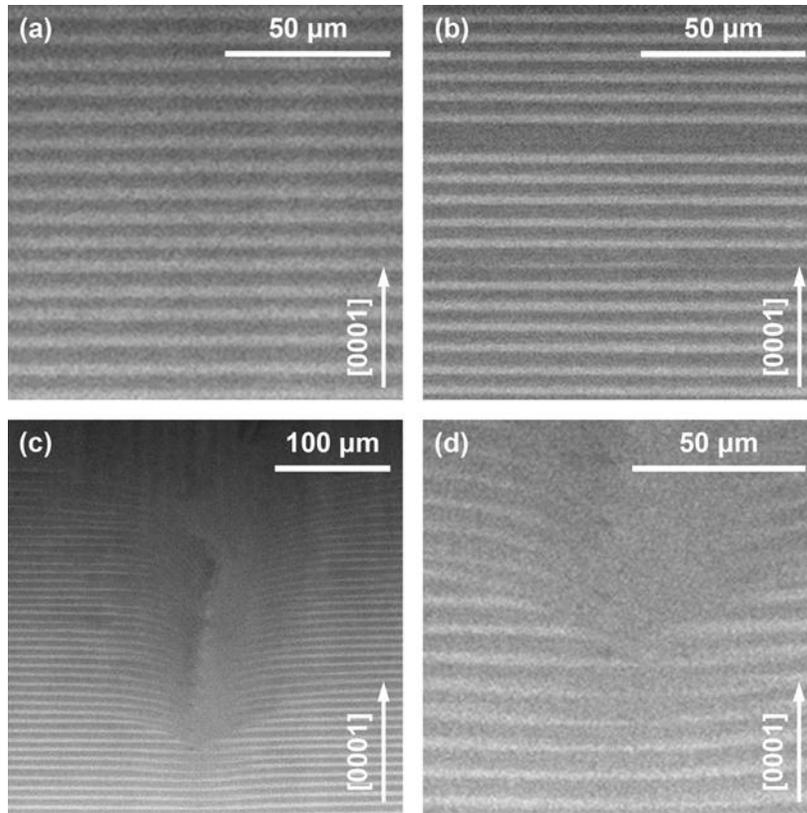
Figure 4.24: HAADF-STEM images of partial MQW stacks for InGaN solar cells with 50 QWs grown on coloaded (a) bulk (0001) GaN and (b) sapphire substrates. Additionally, images of a defect in the (0001) bulk GaN 50 QW sample (c) at low magnification and (d) at higher magnification.[72]

were 30% thicker (3.0 nm vs. 2.3 nm) on the bulk (0001) GaN substrate even though the samples were loaded during the same growth. The difference in InGaN growth rate without a change in GaN QB growth rate or a significant change in InGaN composition is not fully understood at this time and is a subject of further investigation. The resulting larger total thickness of InGaN on bulk (0001) GaN devices than on sapphire explains some of the difference in current and EQE due to higher absorption, but the IQE is also significantly better on bulk (0001) GaN (see Fig. 4.20), indicating the higher material quality on bulk (0001) GaN.

The HAADF-STEM images in Figs. 4.24(c) and 4.24 (d) show one defect originating in the middle of the 50 QW stack and propagating in the [0001] growth

direction. It is unlikely to have been associated with a preexisting TD, since no TD was observed beneath the MQW, and the chance of finding a preexisting TD at this magnification with a TDD of less than 3×10^6 cm^{-2} is very small. This defect is likely a TD initiated by a misfit dislocation generated within the MQW stack due to strain accumulation, which has been previously observed in InGaN QWs on bulk (0001) GaN.[75] This evidence of a structural degradation mechanism on bulk (0001) GaN that occurs without the presence of preexisting TDs would explain the drop in device performance between 30 QWs and 50 QWs.

4.3.4 Comparison to an Ideal Device

Although state-of-the-art at the time of its demonstration, the performance of the 30 QW device on bulk (0001) GaN is still far from that of an ideal InGaN solar cell with perfect growth quality, no defect generation, and enough InGaN to absorb all of the incident light. Table 4.2 compares the actual values of J_{sc}, V_{oc}, FF, and $P_{d,max}$ from the 30 QW device to those of an ideal InGaN/GaN cell with the same bandgap. This ideal device is a p-i-n double heterostructure with 500 nm of In$_{0.2}$Ga$_{0.8}$N in the active region for full absorption. Collection efficiency is assumed to be perfect so that EQE is 100% above the InGaN bandgap of 2.73 eV. Therefore, the ideal J_{sc} is calculated by integrating the AM0 solar irradiance spectrum normalized by photon energy over all wavelengths above the bandgap. Ideal V_{oc} is a function of the minimum effective bandgap-voltage offset $W_{oc,eff}$, defined as the difference between the solar cell's effective bandgap and V_{oc}.[76] The effective bandgap of 454 nm is estimated by extrapolating the linear shoulder of the EQE spectrum to the

Parameter	Measured Value	Theoretical Value	Percent of Ideal
J_{sc} (mA/cm^2)	2.10	6.23	33.7%
$W_{oc,eff}$ (V)	0.47	0.388	78.9%
V_{oc} (V)	2.26	2.343	96.5%
FF (%)	70.4	89.5	78.7%
$P_{d,max}$ (mW/cm^2)	3.33	13.06	25.5%

Table 4.2: Comparison of device parameters between values measured for the 30 QW InGaN/GaN solar cell on bulk (0001) GaN and values for an ideal InGaN-based solar cell with the same bandgap.[72]

wavelength axis. In the ideal case where radiative recombination is the dominant recombination mechanism, $W_{oc,eff}$ is given by:

$$W_{oc,eff} = \frac{kT}{q} \ln\left(\frac{qwBN_CN_V}{J_{ph}}\right), \tag{4.8}$$

where w is the active region thickness.[76] We use a value of 5 x 10^{-11} for B, the InGaN radiative recombination coefficient.[77] N_C and N_V are the conduction and valence band effective density of states for In$_{0.2}$Ga$_{0.8}$N,[9] respectively, and J_{ph} is the photogenerated current density, assumed to be equal to the ideal J_{sc}. Ideal FF can be approximated very closely by the following expression:

$$FF = \frac{v_{oc} - \ln(v_{oc} + 0.72)}{v_{oc} + 1}, \tag{4.9}$$

where v_{oc} is the normalized open circuit voltage, equal to ideal V_{oc} divided by nkT/q.[78] We assume the ideality factor n equals 2 since the active region is fully depleted in an ideal p-i-n structure.

It is clear from Table 4.2 that the J_{sc} shows the largest discrepancy compared to an ideal device, and thus has the largest impact on the maximum output power, which is equal to $P_{d,max} = V_{oc} \times J_{sc} \times FF$. J_{sc} is limited mainly by the thickness of InGaN that can be grown before the onset of structural instabilities due to mismatch stresses, as seen in Fig.

4.24. Likewise, the FF can be improved significantly by limiting non-radiative recombination, while the V_{oc} is already very close to its theoretical value. One possible solution for preventing strain-related degradation is a strain-balanced InGaN/AlGaN MQW active region, though any solution will involve significant materials growth challenges.

3.4 Optical Coatings for Multijunction Integration

3.4.1 Light Trapping in Solar Cells

Idealized solar cell structures generally assume that light passes directly through the device, perpendicular to the top surface, and if it is not absorbed it passes out the other side and is lost. This simple approach ignores the very important contributions of reflections and scattering to the solar cell's efficiency. The idea of light trapping, or having multiple passes of light through an absorbing layer, was first proposed for thin film solar cells in 1974 by Redfield.[79] Of course, putting a perfect planar mirror on the back surface will double the optical

path length in a solar cell. Redfield proposed that if the back surface is not parallel to the front surface (that it is angled or textured) then it is possible to design reflection angles that will be totally internally reflected, allowing multiple passes of unabsorbed light through the film. Statistical-mechanical analysis by Yablonovitch and Cody shows that absorption in a randomly textured (Lambertian) semiconductor film can be enhanced by a factor of up to $4n^2$, where n is the index of refraction of the semiconductor, compared to a planar film (Fig. 4.25).[80] This model relies on the assumption that after a few reflections, light will be completely randomized and fill the entire phase space, increasing the optical density. It was then applied successfully to solar cell devices,[81] and to a better model for solar cell limiting
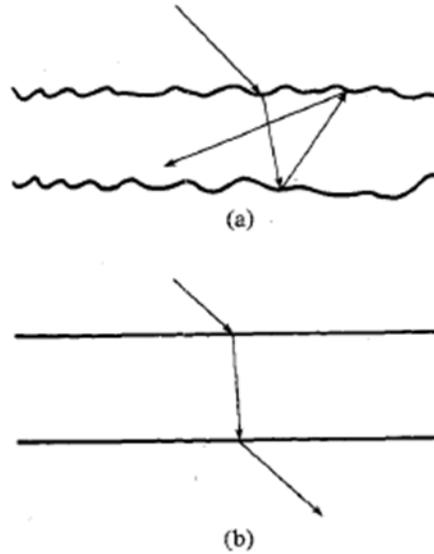
Figure 4.25: Two optical sheets with different surface textures. (a) Randomized angles of reflections in a Lambertian film lead to intensity enhancement. (b) Parallel planar surfaces cause no angular randomization.[80]

efficiency.[82] Controlled repeating patterns have also been proposed as an alternative to Lambertian roughness, but they perform worse unless engineered very precisely.[83] Beyond simple macroscopic surface texturing, another way to trap light in a thin film absorbing layer is by employing surface plasmons.[84–86] Surface plasmon polaritons occur when there is a nanostructured metallic film on the semiconductor surface – they are free electron oscillations at the metal/semiconductor interface. They can confine and guide light into films that are thinner than the wavelength of the light being absorbed, something that cannot be accomplished with traditional surface patterning. Plasmonic enhancement has been successfully applied to photovoltaic devices as well.[87,88]As for light trapping in nitride solar cells, various methods have been applied to InGaN-based devices in order to improve light coupling: such as backside mirrors,[25,89,90] backside roughening,[91,92] p-GaN roughening,[24,93–96] and plasmonic scattering.[97]

4.4.2 Multijunction Integration of Nitride Solar Cells

Efficient utilization of higher energy photons requires an additional junction with a wider bandgap, preferably near 2.65 eV for a 5th junction.[98] Because of the large lattice mismatch between GaN and common multijunction solar cell materials, such as InGaP and GaAs, InGaN-based devices cannot be grown epitaxially on underlying junctions composed of those materials. One way around this problem is to integrate the InGaN/GaN subcell in a bonded configuration. We refer to this configuration as a 3 junction + 1 junction design or a 4 junction + 1 junction design, where the number of the junctions in the first term depends on the design of the underlying MJSC. Due to the relatively small current that would be produced by an InGaN-based solar cell with an absorption edge near 2.65 eV,[72] efficient current matching with underlying junctions would not be possible, and the InGaN/GaN subcell must be electrically isolated from the underlying MJSC in a three or four terminal design.[98] The bonding layer therefore does not need to be electrically conductive, and the bonding process can be simplified by using a transparent polymer such as benzocyclobutene (BCB). A schematic of a potential 4 junction + 1 junction device is shown in Fig. 4.26. The 4 junction underlying multijunction device is an inverted metamorphic structure based on a GaAs substrate.[100] Direct bonding of GaAs and InP-based subcells for a five junction solar cell has been successfully demonstrated.[101]

Multijunction solar cells are often operated in concentrating photovoltaic systems with optical concentration factors of 300-1000 suns. This presents extra challenges for device design because of heating and high current density. Usually high temperature operation causes a reduction in efficiency for solar cells because of a drop in V_{oc}. InGaN MQW solar cells, on the other hand, have been shown to have a positive temperature
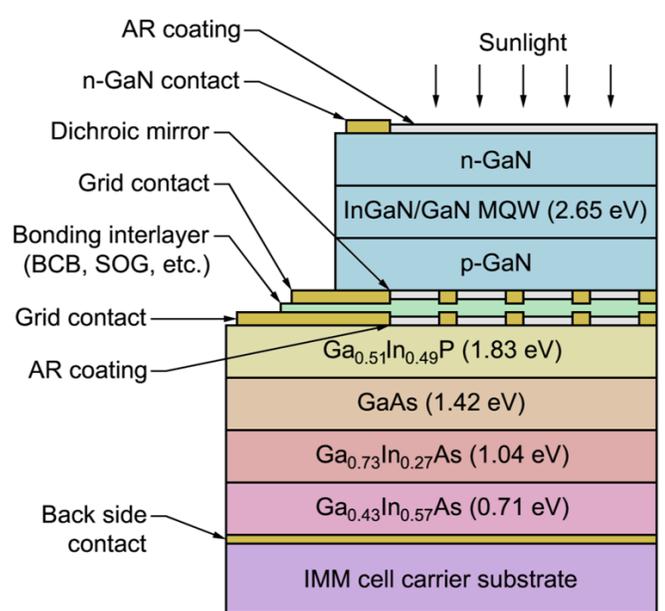
Figure 4.26: Cross-sectional schematic of 1 junction + 4junction MJSC with an InGaN/GaN MQW top cell.[99]

coefficient up to 100°C, due to greater thermionic emission from QWs contributing to higher J_{sc}.[102] InGaN solar cell operation under concentrated illumination has been reported up to 300 suns and 4% efficiency.[29,103] Correct choice of metal contacts and current spreading layers becomes very important under concentration because of the high current density and subsequent larger power loss due to series resistance.

4.4.3 Design and Fabrication of Dielectric Optical Coatings for InGaN/GaN Solar Cells

Careful optical design is essential for successful integration of an InGaN/GaN solar cell with an underlying MJSC. For example, there are two important considerations with the 4 junction + 1 junction design. First, it is necessary to maximize transmission for photons with energies between 0.7 and 3.4 eV through the topside of the InGaN/GaN solar cell. This

is the range of useful absorption between the bandgap of the bottom junction material of a MJSC, which is commonly near 0.7 eV,[104] and the bandgap of GaN, which is 3.4 eV. To accomplish this, a broadband antireflection coating (ARC) needs to be designed and deposited on the topside of the InGaN/GaN solar cell. ARCs have been demonstrated on InGaN/GaN solar cells,[105,106] but have not yet exhibited antireflection properties over wide wavelength ranges.

Second, since the total InGaN thickness must be kept relatively small to avoid strain-induced material degradation,[72] an increase in light coupling for photons with energies between 2.65 eV (the ideal InGaN bandgap) and 3.4 eV is highly beneficial for the InGaN/GaN subcell. However, it is also necessary to maximize transmission for unabsorbed light between 0.7 eV and 2.65 eV at the bonding interface to avoid degrading the performance of the fully integrated device. While the optical path length in the InGaN can be doubled with a well-designed dichroic mirror, it would be possible to increase this factor to $4n^2$, where n is the index of refraction of GaN, with a cleverly designed scattering structure.[80] However, it is important that these structures do not affect the operation of the lower four junctions by scattering light below 2.65 eV. Alternate methods for improving light coupling into InGaN/GaN solar cells such as backside mirrors, and front or backside roughening, are problematic because they result in reflections or scattering of wavelengths of light that are useful to underlying subcells. To increase light coupling to the InGaN absorber layer while avoiding undesired reflections and scattering, a broadband dichroic mirror (DM) needs to be designed and deposited on the backside of the InGaN/GaN solar cell.

Both the ARC and DM coatings were designed using TFCalc by Software Spectra, Inc., an optical coating simulation tool that utilizes the transfer-matrix method. It optimizes the thickness of each layer of SiO_2 and Ta_2O_5 to minimize the difference between a target reflectance spectrum and the simulated reflectance spectrum. The ARC target was 100% transmission for wavelengths from 365 nm (3.4 eV) and 1771 nm (0.7 eV). The DM target was 100% reflectance for wavelengths between 365 and 470 nm (2.65 eV) and 100% transmission between 470 and 1771 nm. It should be noted that this DM was designed for a GaN/air interface rather than the GaN/bonding layer interface that would be present in a 4 junction + 1 junction design. 6 layers were found to be optimal for the ARC. For the DM, additional layers generally provided higher reflectivity from 365 – 470 nm. We chose a 14 layer coating for the DM to balance performance and complexity. In the final design, the 6 layer ARC and 14 layer DM were optimized with layer thicknesses ranging from 9.5 to 148 nm.

Dielectric layers for the optical coatings were deposited using ion-beam deposition. The 6 layer ARC was deposited on the front side of the sample (the 30X MQW solar cell on bulk GaN substrate described in section 4.3.3), with patterned via holes to allow contact to the n-type and p-type electrodes. Then the 14 layer DM was deposited on the back side of the sample. Single side polished bulk GaN substrates were co-loaded during the deposition of the ARC and DM for the purpose of measuring the reflectance of the coatings. The backside of the sample was then coated with black paint to minimize backside reflections, and the reflectance of the topside of the sample was measured using a Cary 500 spectrophotometer.
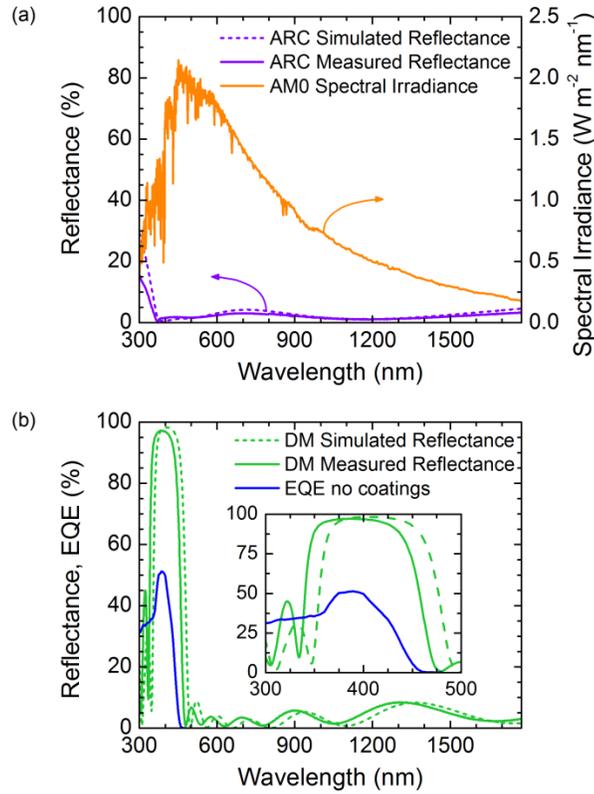
Figure 4.27: Simulated and measured reflectance of (a) the ARC and (b) the DM. ARC reflectance is compared to the spectrum of AM0 solar irradiance. DM reflectance is compared to the uncoated device EQE spectrum. Inset in (b) clearly shows the range of InGaN photoresponse between 365nm and 455 nm. Left axis in the inset in (b) represents the same quantities and is in the same units as the left axis of the main plot.[107]

Figure 4.27 shows the reflectance spectra of the ARC and DM coatings. The simulated and measured spectra of the ARC are in very good agreement (Fig. 4.27(a)). Between 365 and 1771 nm, the average reflectance is 2.4%. This wavelength range corresponds to the vast majority of the power in the AM0 solar spectrum which is plotted in Fig 4.27(a) and should be absorbed by successive layers in a MJSC. In Fig. 4.27(b), the simulated and measured DM reflectance spectra are also in good agreement, aside from a ~15 nm blue-shift of the actual coating, likely caused by a slight drift in the Ta_2O_5 deposition rate. For comparison, the EQE spectrum of the uncoated device is plotted alongside the DM spectra. The highly reflecting portion of the DM spectrum has an average
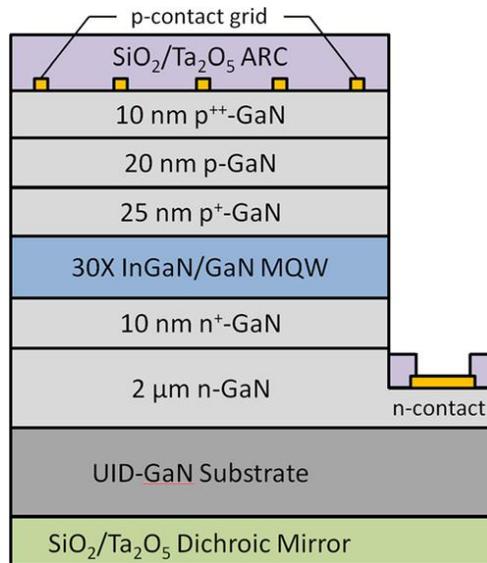
Figure 4.28: Cross sectional schematic of a 30X InGaN/GaN MQW solar cell with deposited anti-reflective coating and dichroic mirror.[107]

reflectance of 89.3% in the region coinciding with the InGaN photoresponse (365 to 460 nm), as seen in the inset of Fig. 4.27(b). At wavelengths beyond 470 nm, the reflectance remains below 10% and averages 3.0%.

4.4.4 InGaN Solar Cells with Optical Coatings

The device used to test the application of optical coatings was the 30X MQW solar cell described in detail in section 4.3.3, which was chosen because it exhibited the highest maximum power density. A cross-sectional schematic of the general structure of the solar cell with optical coatings is shown in Figure 4.28. Electrically characterized was performed at three stages in the process: prior to coating deposition, after the ARC deposition, and after the DM deposition. *J-V* measurements and EQE measurements were performed using the same procedures and equipment described in section 4.3.3.
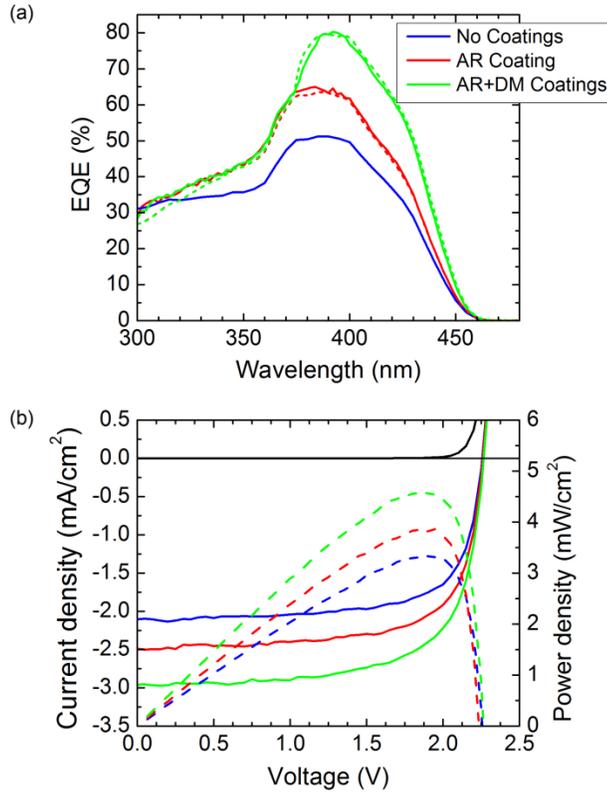
Figure 4.29: Electrical measurements of the 30 QW solar cell device before and after depositing both the ARC and DM. (a) EQE spectra and (b) current density and power density vs. voltage characteristics. Dotted lines in (a) represent calculations of expected EQE after ARC and DM deposition based on uncoated EQE data and optical coating reflectance data presented in Fig. 4.27.[107]

The improved electrical characteristics as a result of the optical coatings are shown in Fig. 4.29. Peak EQE improved by 27% (relative) over the uncoated value after the application of the ARC, and by 56% (relative) after both the ARC and DM were applied. The measured EQE data in Fig. 4.29(a) agree well with the expected EQE values after coating deposition (dotted lines). The expected EQE with the ARC alone was calculated by multiplying the measured EQE for an uncoated device (EQE_0) by $(1 - R_{ARC})/(1 - R_{GaN})$, the ratio of front surface transmission between the coated and uncoated sample, where R_{ARC} is the measured reflectance of the ARC, and R_{GaN} is the reflectance from an air/GaN
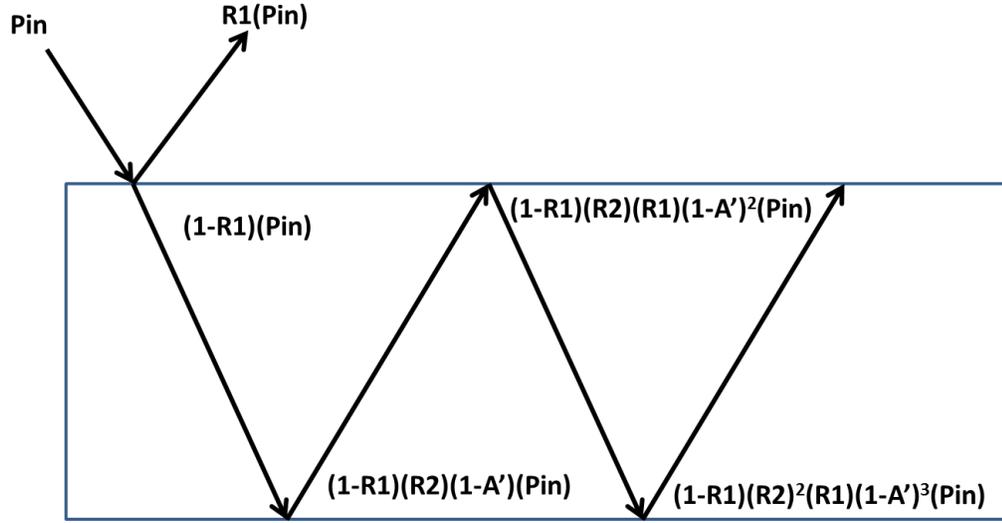
Figure 4.30: Schematic of the evolution of the optical power of radiation incident on an absorbing layer after a series of reflections off of the top and bottom surfaces. The incident power is Pin. The reflectivities of the top and bottom surfaces are R1 and R1, respectively. The absorption that occurs during a single pass of light through the film is A'. The sum of the optical power in the film after each reflection, for an infinite number of reflections, gives the total effective optical power in the film.

interface. With both the ARC and DM, the expected EQE was calculated using the following formula:

$$EQE_{DM+ARC} = EQE_0 \frac{\{1 - R_{ARC}\}\{1 + R_{DM}(1 - A')\}\{1 - R_{GaN}{}^2(1 - A')^2\}}{\{1 - R_{GaN}\}\{1 + R_{GaN}(1 - A')\}\{1 - R_{ARC}R_{DM}(1 - A')^2\}}, \quad (4.10)$$

which was derived by considering an infinite number of internal reflections off the front and back interfaces for both coated and uncoated GaN (Fig. 4.30). EQE_{DM+ARC} is the EQE after deposition of both the ARC and DM, R_{DM} is the measured reflectance of the DM, and A' is single pass absorption of light normalized to its maximum value. A' has been calculated from the normalized measured absorption, A, of the InGaN/GaN MQW sample using the following equation:

$$A' = \frac{A(1 - R_{GaN})}{1 - A \times R_{GaN}}, \quad (4.11)$$

110

Coating	Peak EQE (%)	V_{oc} (V)	FF (%)	J_{sc} (mA/cm^2)	$P_{d,max}$ (mW/cm^2)	Change in power density
No coatings	53.8	2.25	70.2	2.10	3.31	--
ARC	64.8	2.26	69.9	2.46	3.87	+16.9%
ARC + DM	79.8	2.26	67.9	2.97	4.55	+37.5%

Table 4.3: Comparison of average values of device parameters for three devices per data point on the same bulk (0001) GaN substrate before coating deposition, after ARC deposition, and after DM deposition.[107]

which was derived in a way analogous to Eq. (4.11). These calculations assume that no reflections arise at the InGaN/GaN QW interfaces. The close agreement between measured and modeled EQE shown in Fig. 4.29(a) is an indication that this assumption is valid, and that the model discussed above provides a good approximation of the actual performance of the cells.

Significant improvement was also observed in the *J-V* characteristics after deposition of the optical coatings (Fig. 4.29(b)). As expected, the increase in performance was dominated by an increase in the current density, which led to an increase in power density with little change in open circuit voltage (V_{oc}) or fill factor (FF). Table 4.3 shows the average values of device parameters from three devices per data point on the bulk (0001) substrate. The deposition of the ARC and DM led to a substantial 37.5% increase in $P_{d,max}$, which is equivalent to a relative increase in conversion efficiency of the same magnitude. The resulting $P_{d,max}$ of 4.55 mW/cm^2 corresponds to a conversion efficiency of 3.33% for an AM0 integrated spectral power density of 1366 W/m^2.

4.5 Conclusions

The III-N material system has been proposed as a revolutionary photovoltaic technology, with a bandgap that has the potential to span the entire range of the useful solar spectrum. However, several key difficulties have limited the performance of InGaN-based solar cells. Absorbing layers of InGaN must be made thick enough, hundreds of nanometers at least, to absorb most of the incident light. The large lattice mismatch between InN and GaN means that only a small fraction of indium can be incorporated, and the bandgap can only decrease into the blue or green wavelengths, before strain relaxation begins to severely degrade performance. Transitioning from a DH design to an MQW design alleviates the strain to some degree, allowing thicker active regions, more indium incorporation, and improved performance, but high performance devices with an absorption edge beyond 500 nm remain elusive. Polarization-induced electric fields also present problems. They act opposite the direction of the junction field, hampering current collection, and they cause QCSE, weakening absorption near the band edge.

MQW designs have improved efficiencies overall, but present new challenges in carrier transport. Generated carriers must be able to escape QWs and transit the active region before recombining. Many techniques, including time-resolved PL and electroabsorption, have been discussed, which can measure relevant carrier lifetimes within the collection process. Biased dependent EQE measurements demonstrated the electric field dependence on carrier collection in InGaN/GaN MQW solar cells. Increased reverse bias improved extraction efficiency by promoting tunneling transport out of wells through effective barrier lower and thinning. Temperature dependent *I-V* measurements demonstrated the importance of having thinner quantum barriers to promote tunneling

transport over thermionic emission for carrier escape out of QWs. Carrier escape modelling confirmed the temperature dependent results, giving an accurate comparison of tunneling rates, thermionic emission rates, and recombination rates in InGaN MQW devices with varying barrier thickness.

In order to grow high quality InGaN MQW solar cell active regions with thin barriers by MOCVD, a two-step barrier growth processed needed to be optimized. When barriers are grown at the well temperature it allows V-defects to propagate through the active region, severely degrading performance. Elevated growth temperatures and the presence of H_2 carrier gas contribute to the filling in of V-defects, but also cause indium desorption and thickness fluctuations in QWs. A thin low temperature cap layer with only N_2 carrier gas must be grown on top of each QW, followed by a high temperature GaN barrier layer with H_2 carrier gas. After growth and testing of optimization series for cap layer thickness, barrier layer temperature and barrier layer thickness, the final optimized barrier structure consisted of a 2 nm cap layer grown at the QW growth temperature (800°C), and a 2 nm barrier layer grown at 900°C. Thinner barriers were not able to prevent the propagation of V-defects.

High performance InGaN/GaN MQW solar cells have been demonstrated with thin barriers to promote efficient carrier transport. Growth on low TDD bulk (0001) GaN substrates provided improvements in performance compared to sapphire substrates, especially with an increasing number of QWs. Device degradation occurred as MQW thickness increased, with the onset being delayed on bulk (0001) GaN substrates. Results indicate that V-defects form on preexisting TDs during MQW growth on sapphire, while new defects nucleate during MQW growth on bulk (0001) GaN. Thin barrier solar cells

exhibited EQEs up to 60%, V_{oc} as high as 2.28 V, FF up to 80%, and a maximum conversion efficiency of 2.4% under 1 sun AM0 equivalent illumination.

Results of applying optical coatings indicate that well-designed broadband dielectic coatings can enhance the performance of current state-of-the-art InGaN-based solar cells while also allowing for high transparency to underlying junctions. Ion beam deposition of a 6-layer ARC on the front surface and a 14-layer DM on the back surface increased the peak EQE of a 30 QW InGaN/GaN solar cell by 56% (relative). In addition, the AM0 conversion efficiency increased by 37.5% (relative), resulting in a conversion efficiency of 3.33% after deposition of optical coatings. Significant improvements can still be made in ARC transparency as well as DM reflectivity and long wavelength transparency, which should further enhance the performance of InGaN/GaN solar cells with broadband optical coatings.

References

1. Wu, J. *et al.* Unusual properties of the fundamental band gap of InN. *Appl. Phys. Lett.* **80,** 3967 (2002).

2. Brown, G. F. & Wu, J. Third generation photovoltaics. *Laser Photonics Rev.* **3,** 394–405 (2009).

3. Muth, J., Lee, J., Shmagin, I. & Kolbas, R. Absorption coefficient, energy gap, exciton binding energy, and recombination lifetime of GaN obtained from transmission measurements. *Appl. Phys.* **71,** 2572–2574 (1997).

4. Wu, J. *et al.* Superior radiation resistance of In 1-xGa xN alloys: Full-solar-spectrum photovoltaic material system. *J. Appl. Phys.* **94,** 6477–6482 (2003).

5. Bandić, Z. Z., Bridger, P. M., Piquette, E. C. & McGill, T. C. Minority carrier diffusion length and lifetime in GaN. *Appl. Phys. Lett.* **72,** 3166 (1998).

6. Ho, I. & Stringfellow, G. Solid phase immiscibility in GaInN. *Appl. Phys. Lett.* **69,** 2701 (1996).

7. Walukiewicz, W. *et al.* Structure and electronic properties of InN and In-rich group III-nitride alloys. *J. Phys. D. Appl. Phys.* **83,** R83–R99 (2006).

8. Lai, K. Y., Lin, G. J., Lai, Y.-L., Chen, Y. F. & He, J. H. Effect of indium fluctuation on the photovoltaic characteristics of InGaN/GaN multiple quantum well solar cells. *Appl. Phys. Lett.* **96,** 081103 (2010).

9. Schubert, E. F. *Light Emitting Diodes*. (Cambridge University Press, 2006).

10. Holec, D. *et al.* Equilibrium critical thickness for misfit dislocations in III-nitrides. *J. Appl. Phys.* **104,** 123514 (2008).

11. Kozodoy, P. *et al.* Electrical characterization of GaN p-n junctions with and without threading dislocations. *Appl. Phys. Lett.* **73,** 975 (1998).

12. Li, Z. Q., Lestradet, M., Xiao, Y. G. & Li, S. Effects of polarization charge on the photovoltaic properties of InGaN solar cells. *Phys. Status Solidi* **931,** 928–931 (2010).

13. Neufeld, C. J. *et al.* Effect of doping and polarization on carrier collection in InGaN quantum well solar cells. *Appl. Phys. Lett.* **98,** 243507 (2011).

14. Bhuiyan, A. G., Sugita, K., Hashimoto, A. & Yamamoto, A. InGaN Solar Cells: Present State of the Art and Important Challenges. *IEEE J. Photovoltaics* **2,** 276–293 (2012).

15. Jani, O. *et al.* Design, Growth, Fabrication and Characterization of High-Band Gap InGaN/GaN Solar Cells. *2006 IEEE 4th World Conf. Photovolt. Energy Conf.* 20–25 (2006). doi:10.1109/WCPEC.2006.279337

16. Jani, O. *et al.* Characterization and analysis of InGaN photovoltaic devices. in *Photovolt. Spec. Conf. 2005. Conf. Rec. Thirty-first IEEE* 37–42 (IEEE, 2005). at <http://ieeexplore.ieee.org/xpls/abs_all.jsp?arnumber=1488064>

17. Jani, O., Ferguson, I., Honsberg, C. & Kurtz, S. Design and characterization of GaN∕InGaN solar cells. *Appl. Phys. Lett.* **91,** 132117 (2007).

18. Hamzaoui, H., Bouazzi, A. & Rezig, B. Theoretical possibilities of InGaN tandem PV structures. *Sol. Energy Mater. Sol. Cells* **87,** 595–603 (2005).

19. Kuwahara, Y. *et al.* Nitride-based light-emitting solar cell. *Phys. Status Solidi* **7,** 1807–1809 (2010).

20. Fujiyama, Y. *et al.* GaInN/GaN p-i-n light-emitting solar cells. *Phys. Status Solidi* **7,** 2382–2385 (2010).

21. Neufeld, C. J. *et al.* High quantum efficiency InGaN/GaN solar cells with 2.95 eV band gap. *Appl. Phys. Lett.* **93,** 143502 (2008).

22. Zheng, X. *et al.* High-quality InGaN∕GaN heterojunctions and their photovoltaic effects. *Appl. Phys. Lett.* **93,** 261108 (2008).

23. Kuwahara, Y. *et al.* Realization of Nitride-Based Solar Cell on Freestanding GaN Substrate. *Appl. Phys. Express* **3,** 111001 (2010).

24. Matioli, E. *et al.* High internal and external quantum efficiency InGaN/GaN solar cells. *Appl. Phys. Lett.* **98,** 021102 (2011).

25. Horng, R. H. *et al.* Improved conversion efficiency of GaN/InGaN thin-film solar cells. *Electron Device Lett. IEEE* **30,** 724–726 (2009).

26. Farrell, R. M. *et al.* High quantum efficiency InGaN/GaN multiple quantum well solar cells with spectral response extending out to 520 nm. *Appl. Phys. Lett.* **98,** 201107 (2011).

27. Dahal, R., Pantha, B., Li, J., Lin, J. Y. & Jiang, H. X. InGaN/GaN multiple quantum well solar cells with long operating wavelengths. *Appl. Phys. Lett.* **94,** 063505 (2009).

28. Sheu, J. K. *et al.* Demonstration of GaN-based solar cells with GaN/InGaN superlattice absorption layers. *Electron Device Lett. IEEE* **30,** 225–227 (2009).

29. Li, X., Zheng, X., Zhang, D. & Wu, Y. InGaN/GaN Multiple Quantum Well Solar Cells with Good Open-Circuit Voltage and Concentrator Action. *Jpn. J. Appl. Phys.* **51,** 1–4 (2012).

30. Wierer, J. J., Li, Q., Koleske, D. D., Lee, S. R. & Wang, G. T. III-nitride core–shell nanowire arrayed solar cells. *Nanotechnology* **23,** 194007 (2012).

31. Kuo, Y.-K., Chang, J.-Y. & Shih, Y.-H. Numerical Study of the Effects of Hetero-Interfaces, Polarization Charges, and Step-Graded Interlayers on the Photovoltaic Properties of (0001) Face GaN/InGaN p-i-n Solar Cell. *IEEE J. Quantum Electron.* **48,** 367–374 (2012).

32. Tang, H., Liu, B. & Wang, T. Influence of piezoelectric fields on InGaN based intermediate band solar cells. *J. Phys. D. Appl. Phys.* **48,** 025101 (2015).

33. Dahal, R., Pantha, B. N., Li, J., Lin, J. Y. & Jiang, H. X. Realizing InGaN monolithic solar-photoelectrochemical cells for artificial photosynthesis. *Appl. Phys. Lett.* **104,** 143901 (2014).

34. Barnham, K. W. J. & Duggan, G. A new approach to high-efficiency multi-band-gap solar cells. *J. Appl. Phys.* **67,** 3490 (1990).

35. Barnham, K. W. J., Braun, B., Nelson, J. & Paxman, M. Short-circuit current in a low-dimensional and energy efficiency structure photovoltaic enhancement device. *Appl. Phys. Lett.* 135–137 (1991).

36. Barnham, K. *et al.* Voltage enhancement in quantum well solar cells. *J. Appl. Phys.* **80,** 1201 (1996).

37. Barnham, K. *et al.* Quantum well solar cells. *Appl. Surf. Sci.* **113/114,** 722–733 (1997).

38. Barnham, K. *et al.* Quantum well solar cells. *Phys. E Low-dimensional Syst. Nanostructures* **14,** 27–36 (2002).

39. Mazzer, M. *et al.* Progress in quantum well solar cells. *Thin Solid Films* **511-512,** 76–83 (2006).

40. Luque, A., Marti, A. & Cuadra, L. Thermodynamic consistency of sub-bandgap absorbing solar cell proposals. *IEEE Trans. Electron Devices* **48,** 2118–2124 (2001).

41. Barnham, K. W. J. *et al.* Quantum well solar cells. *Phys. E Low-dimensional Syst. Nanostructures* **14,** 27–36 (2002).

42. Anderson, N. On quantum well solar cell efficiencies. *Phys. E Low-dimensional Syst. Nanostructures* **14,** 126–131 (2002).

43. Anderson, N. G. Ideal theory of quantum well solar cells. *J. Appl. Phys.* **78,** 1850 (1995).

44. Paxman, M. *et al.* Modeling the spectral response of the quantum well solar cell. *J. Appl. Phys.* **74,** 614 (1993).

45. Miller, D. A. B. *et al.* Band-edge electroabsorption in quantum well structures: The quantum-confined Stark effect. *Phys. Rev. Lett.* **53,** 2173–2176 (1984).

46. Lang, J. R., Young, N. G., Farrell, R. M., Wu, Y.-R. & Speck, J. S. Carrier escape mechanism dependence on barrier thickness and temperature in InGaN quantum well solar cells. *Appl. Phys. Lett.* **101,** 181105 (2012).

47. Levine, B. *et al.* Photoexcited escape probability, optical gain, and noise in quantum well infrared photodetectors. *J. Appl. Phys.* **72,** 4429–4443 (1992).

48. Sun, C.-K. *et al.* Radiative recombination lifetime measurements of InGaN single quantum well. *Appl. Phys. Lett.* **69,** 1936 (1996).

49. Jho, Y., Yahng, J. & Oh, E. Field-dependent carrier decay dynamics in strained InGaN/GaN quantum wells. *Phys. Rev. B* 1–11 (2002). doi:10.1103/PhysRevB.66.035334

50. Fox, A., Miller, D. & Livescu, G. Quantum well carrier sweep out: Relation to electroabsorption and exciton saturation. *Quantum* **27,** (1991).

51. Schneider, H. & Klitzing, K. Thermionic emission and Gaussian transport of holes in a GaAs/Al_ {x} Ga_ {1-x} As multiple-quantum-well structure. *Phys. Rev. B* **38,** 6160–6165 (1988).

52. Wraback, M. *et al.* Time-resolved electroabsorption measurement of the electron velocity-field characteristic in GaN. *Appl. Phys. Lett.* **76,** 1155 (2000).

53. Yang, C. *et al.* Measurement of Effective Drift Velocities of Electrons and Holes in Shallow Mutliple-Quantum-Well p-i-n Modulators. *Quantum* **33,** 1498–1506 (1997).

54. Blom, P., Smit, C., Haverkort, J. & Wolter, J. Carrier capture into a semiconductor quantum well. *Phys. Rev. B* **47,** 2072 (1993).

55. Özgür, Ü. *et al.* Ultrafast optical characterization of carrier capture times in InGaN multiple quantum wells. *Appl. Phys. Lett.* **77,** 109–111 (2000).

56. Ulbrich, R. Energy relaxation of photoexcited hot electrons in GaAs. *Phys. Rev. B* (1973). at <http://prb.aps.org/abstract/PRB/v8/i12/p5719_1>

57. Sun, C., Vallee, F., Keller, S., Bower, J. & DenBaars, S. Femtosecond studies of carrier dynamics in InGaN. *Appl. Phys. Lett.* **70,** 2004–2006 (1997).

58. Varshni, Y. P. Temperature dependence of the energy gap in semiconductors. *Physica* **34,** 149–154 (1967).

59. Wu, Y. R., Singh, M. & Singh, J. Gate leakage suppression and contact engineering in nitride heterostructures. *J. Appl. Phys.* **94,** 5826–5831 (2003).

60. Schwarz, U. T. *et al.* Interplay of built-in potential and piezoelectric field on carrier recombination in green light emitting InGaN quantum wells. *Appl. Phys. Lett.* **91,** 123503 (2007).

61. Le, L. C. *et al.* Carriers capturing of V-defect and its effect on leakage current and electroluminescence in InGaN-based light-emitting diodes. *Appl. Phys. Lett.* **101,** 252110 (2012).

62. Mori, M. *et al.* Correlation between Device Performance and Defects in GaInN-Based Solar Cells. *Appl. Phys. Express* **5,** 082301 (2012).

63. Hu, Y.-L. *et al.* Effect of quantum well cap layer thickness on the microstructure and performance of InGaN/GaN solar cells. *Appl. Phys. Lett.* **100,** 161101 (2012).

64. Ting, S. M. *et al.* Morphological evolution of InGaN/GaN quantum-well heterostructures grown by metalorganic chemical vapor deposition. *J. Appl. Phys.* **94,** 1461 (2003).

65. Ju, J.-W. *et al.* A well protection layer as a novel pathway to increase indium composition: a route towards green emission from a blue InGaN/GaN multiple quantum well. *Nanotechnology* **18,** 295402 (2007).

66. Kumar, M. S. *et al.* Effect of barrier growth temperature on morphological evolution of green InGaN/GaN multi-quantum well heterostructures. *J. Phys. D. Appl. Phys.* **40,** 5050–5054 (2007).

67. Pendlebury, S. T., Parbrook, P. J., Mowbray, D. J., Wood, D. A. & Lee, K. B. InGaN/GaN quantum wells with low growth temperature GaN cap layers. *J. Cryst. Growth* **307,** 363–366 (2007).

68. Leem, S. J. *et al.* Optimization of InGaN/GaN multiple quantum well layers by a two-step varied-barrier-growth temperature method. *Semicond. Sci. Technol.* **23,** 125039 (2008).

69. Kuwahara, Y. *et al.* GaInN-Based Solar Cells Using Strained-Layer GaInN/GaInN Superlattice Active Layer on a Freestanding GaN Substrate. *Appl. Phys. Express* **4,** 021001 (2011).

70. Koleske, D. D., Fischer, A., Bryant, B. N., Kotula, P. G. & Wierer, J. J. On the increased efficiency in InGaN-based multiple quantum wells emitting at 530–590nm with AlGaN interlayers. *J. Cryst. Growth* **415,** 57–64 (2015).

71. Wu, X. H. *et al.* Defect structure of metal-organic chemical vapor deposition-grown epitxial (0001) GaN/Al2O3. *J. Appl. Phys.* **80,** (1996).

72. Young, N. G. *et al.* High performance thin quantum barrier InGaN/GaN solar cells on sapphire and bulk (0001) GaN substrates. *Appl. Phys. Lett.* **103,** 173903 (2013).

73. Dai, Q. *et al.* Internal quantum efficiency and nonradiative recombination coefficient of GaInN/GaN multiple quantum wells with different dislocation densities. *Appl. Phys. Lett.* **94,** 111109 (2009).

74. Wu, X. H. X. *et al.* Structural origin of V-defects and correlation with localized excitonic centers in InGaN/GaN multiple quantum wells. *Appl. Phys. Lett.* **72,** 692 (1998).

75. Zhu, M. *et al.* Various misfit dislocations in green and yellow GaInN/GaN light emitting diodes. *Phys. Status Solidi* **207,** 1305–1308 (2010).

76. King, R. R. *et al.* Bandgap-Voltage Offset and Energy Production in Next-Generation Multijunction Solar Cells. *5th World Conf. Photovolt. Energy Convers. 25th Eur. Photovolt. Sol. Energy Conf.* 6–10 (2010).

77. Li, X. *et al.* Impact of active layer design on InGaN radiative recombination coefficient and LED performance. *J. Appl. Phys.* **111,** 063112 (2012).

78. Green, M. Accuracy of analytical expressions for solar cell fill factors. *Sol. Cells* **7,** 337–340 (1982).

79. Redfield, D. Multiple-pass thin-film silicon solar cell. *Appl. Phys. Lett.* **25,** 647–648 (1974).

80. Yablonovitch, E. & Cody, G. G. D. Intensity enhancement in textured optical sheets for solar cells. *IEEE Trans. Electron Devices* **29,** 300–305 (1982).

81. Deckman, H. W., Roxlo, C. B. & Yablonovitch, E. Maximum statistical increase of optical absorption in textured semiconductor films. *Opt. Lett.* **8,** 491–493 (1983).

82. Tiedje, T., Yablonovitch, E., Cody, G. D. & Brooks, B. G. Limiting efficiency of silicon solar cells. *IEEE Trans. Electron Devices* **31,** 711–716 (1984).

83. Campbell, P. & Green, M. A. Light trapping properties of pyramidally textured surfaces. *J. Appl. Phys.* **62,** 243–249 (1987).

84. Ferry, V. E., Sweatlock, L. A., Pacifici, D. & Atwater, H. A. Plasmonic nanostructure design for efficient light coupling into solar cells. *Nano Lett.* **8,** 4391–4397 (2008).

85. Catchpole, K. R. & Polman, a. Design principles for particle plasmon enhanced solar cells. *Appl. Phys. Lett.* **93,** 1–4 (2008).

86. Stuart, H. R. & Hall, D. G. Island size effects in nanoparticle-enhanced photodetectors. *Appl. Phys. Lett.* **73,** 3815–3817 (1998).

87. Pillai, S., Catchpole, K. R., Trupke, T. & Green, M. A. Surface plasmon enhanced silicon solar cells. *J. Appl. Phys.* **101,** 0–8 (2007).

88. Derkacs, D., Lim, S. H., Matheu, P., Mar, W. & Yu, E. T. Improved performance of amorphous silicon solar cells via scattering from surface plasmon polaritons in nearby metallic nanoparticles. *Appl. Phys. Lett.* **89,** 109–112 (2006).

89. Tsai, C.-L., Liu, G.-S., Fan, G.-C. & Lee, Y.-S. Substrate-free large gap InGaN solar cells with bottom reflector. *Solid. State. Electron.* **54,** 541–544 (2010).

90. Jeng, M.-J. & Lee, Y.-L. Increasing Solar Efficiency of InGaN∕GaN Multiple Quantum Well Solar Cells with a Reflective Aluminum Layer or a Flip-Chip Structure. *J. Electrochem. Soc.* **159,** H525 (2012).

91. Bae, S.-Y., Shim, J.-P., Lee, D.-S., Jeon, S.-R. & Namkoong, G. Improved Photovoltaic Effects of a Vertical-Type InGaN/GaN Multiple Quantum Well Solar Cell. *Jpn. J. Appl. Phys.* **50,** 092301 (2011).

92. Lin, C.-F. *et al.* InGaN-based solar cells with a tapered GaN structure. *J. Cryst. Growth* **370,** 97–100 (2013).

93. Farrell, R. M. *et al.* Effect of intentional p-GaN surface roughening on the performance of InGaN/GaN solar cells. *Appl. Phys. Lett.* **103,** 241104 (2013).

94. Chen, K.-T., Lin, C.-F., Lin, C.-M., Yang, C.-C. & Jiang, R.-H. InGaN-based light-emitting solar cells with a pattern-nanoporous p-type GaN:Mg layer. *Thin Solid Films* **518,** 7377–7380 (2010).

95. Zhang, D.-Y. *et al.* Photovoltaic Effects of InGaN/GaN Double Heterojunctions With p-GaN Nanorod Arrays. *IEEE Electron Device Lett.* **31,** 1422–1424 (2010).

96. Ho, C.-H. *et al.* Hierarchical structures consisting of SiO2 nanorods and p-GaN microdomes for efficiently harvesting solar energy for InGaN quantum well photovoltaic cells. *Nanoscale* **4,** 7346–9 (2012).

97.   Pryce, I. M., Koleske, D. D., Fischer, A. J. & Atwater, H. a. Plasmonic nanoparticle enhanced photocurrent in GaN/InGaN/GaN quantum well solar cells. *Appl. Phys. Lett.* **96,** 95–98 (2010).

98.   McMahon, W. E. *et al.* Metal Pillar Interconnection Topology for Bonded Two-Terminal Multijunction III–V Solar Cells. *IEEE J. Photovoltaics* **3,** 868–872 (2013).

99.   Courtesy of R. M. Farrell. .

100.   Stan, M. *et al.* High-efficiency quadruple junction solar cells using OMVPE with inverted metamorphic device structures. *J. Cryst. Growth* **312,** 1370–1374 (2010).

101.   Chiu, P. T. *et al.* Direct Semiconductor Bonded 5J Cell for Space and Terrestrial Applications. *IEEE J. Photovoltaics* **4,** 493–497 (2014).

102.   Jeng, M.-J., Lee, Y.-L. & Chang, L.-B. Temperature dependences of In x Ga 1− x N multiple quantum well solar cells. *J. Phys. D. Appl. Phys.* **42,** 105101 (2009).

103.   Mori, M. *et al.* Concentrating Properties of Nitride-Based Solar Cells Using Different Electrodes. *Jpn. J. Appl. Phys.* **52,** 08JH02 (2013).

104.   Friedman, D. J. Progress and challenges for next-generation high-efficiency multijunction solar cells. *Curr. Opin. Solid State Mater. Sci.* **14,** 131–138 (2010).

105.   Lin, G. J., Lai, K. Y., Lin, C. a., Lai, Y.-L. & He, J. H. Efficiency Enhancement of InGaN-Based Multiple Quantum Well Solar Cells Employing Antireflective ZnO Nanorod Arrays. *IEEE Electron Device Lett.* **32,** 1104–1106 (2011).

106.   Cheng Lee, H. *et al.* Discussion on electrical characteristics of i-In0.13Ga0.87N p-i-n photovoltaics by using a single/multi-antireflection layer. *Sol. Energy Mater. Sol. Cells* **94,** 1259–1262 (2010).

107.   Young, N. G. *et al.* High-performance broadband optical coatings on InGaN/GaN solar cells for multijunction device integration. *Appl. Phys. Lett.* **104,** 163902 (2014).

5

Polarization Screening in Single Quantum Well Light-Emitting Diodes

5.1 Polarization Fields and Droop

As was discussed in Chapter 1, polarization discontinuities at heterointerfaces between different compositions of *c*-plane wurtzite III-nitride materials ((Ga,Al,In)N alloys) cause large electric fields to develop. In a strained InGaN/GaN quantum well (QW), the polarization-induced electric field (dominated by piezoelectric polarization) leads to "tilted" energy bands that spatially separate the electron and hole wavefunctions (Fig 5.1). Spatial charge separation reduces the wavefunction overlap (F_{cv}, see Eq. 3.4), which reduces the oscillator strength, and therefore the rate, of all recombination transitions. Every carrier injected into an LED will recombine either radiatively or non-radiatively, and so, as shown in Eq. 1.15, the total current density *J* can be written as the sum of three recombination types that depend to differing degrees on the carrier density, *n*: Shockley-Read-Hall (SRH) non-radiative recombination (An), bimolecular radiative recombination (Bn^2), and Auger non-radiative recombination (Cn^3). It is important, however, to know the dependency of each of
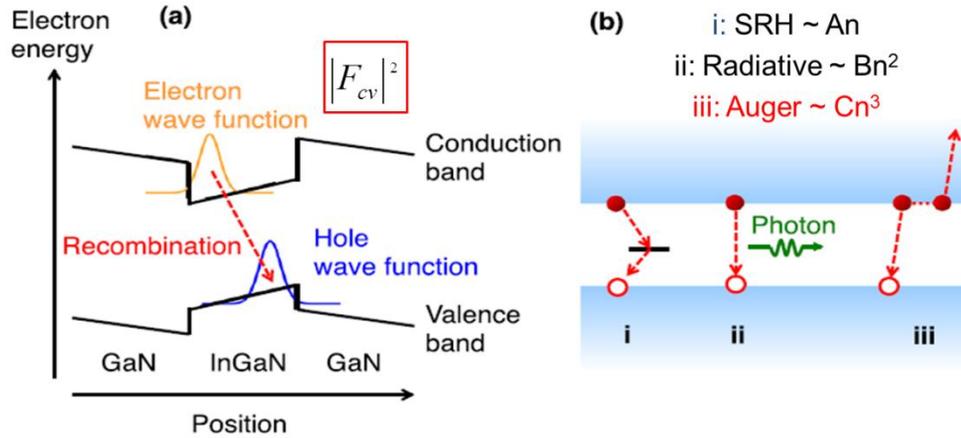
Figure 5.1: (a) Schematic of the enegy bands of a (0001) InGaN/GaN quantum well with separated electron and hole wavefunctions. The piezoelectric field in the QW reduces wavefunction overlap, F_{cv}. (b) The reduction in $|F_{cv}|^2$ affects each type of recombination: (i) Shockly-Read-Hall (SRH, rate An), (ii) radiative (rate Bn^2), (iii) Auger (rate Cn^3, responsible for LED efficiency droop). Figure adapted from Kioupakis *et al.*[1]

the recombination coefficients on the wavefunction overlap so that conclusions about IQE

and droop (see Eq. 1.16) can be drawn.

If the coefficients *A*, *B*, and *C* each have the same functional dependence on F_{cv}, then

Auger recombination will become relatively more influential with higher QW electric field,

since it depends on the cube of the carrier density. Kioupakis *et al.* make a theoretical case

for *A*, *B*, and *C* to each depend on the square of the wavefunction overlap.[1] They note that

$B = B_0|F_{cv}|^2$ because the radiative coefficient is proportional to the square of the matrix

element of the coupling Hamiltonian, which in turn is proportional to the electron-hole

wavefunction overlap (see Chapter 3 for more details). They also argue that $C = C_0|F_{cv}|^2$

because in this three carrier process,[i] the wavefunction the third carrier (excited state)

overlaps completely with its corresponding recombining carrier and so doesn't need to be

considered in the overlap integral. It is an assumption that holds especially well for the *hhe*

---

[i] Electron-electron-hole or hole-hole-electron Auger recombination are both possible, but hhe is more probable in GaN.

Auger process, which dominates in GaN.[2] Finally, they argue that the rate of SRH at a deep level defect should be proportional to the square of the overlaps of each carrier's wavefunction with that defect, and since the extent of a defect is very small compared to a carrier's wavefunction, the rate of SRH is simply given by $A = A_0|F_{cv}|^2$. It is worth noting that this assumption would break down if the capture of one carrier by the defect changed the probability of capture of the other carrier through Coulomb attraction, of if the distribution of defects were not equivalent over the full extent of both the electron and hole wavefunctions.

Interestingly, an increase in wavefunction overlap would increase both radiative and non-radiative recombination rates, so it might not be immediately obvious that something had been gained. Many discussions of polarization fields and wavefunction overlap oversimplify the problem by claiming that only the radiative rate is affected and that IQE is improved as a direct result of increasing overlap. In fact, if the recombination mechanisms all have the same functional dependence on overlap, as described above, the IQE would be independent of F_{cv} at a given n, and the peak IQE will not change. The improvement in LED performance as a result of better overlap can be understood as follows. If all the carrier recombination coefficients are proportional to the square of the wavefunction overlap, then the current density in the device can be written as

$$J = qd \cdot (A_0 n + B_0 n^2 + C_0 n^3)|F_{cv}|^2, \tag{5.1}$$

similar to Eq. 1.15, but with the wavefunction overlap term factored out. From Eq. 5.1, it can be easily seen that at a given injected current density, n will increase when the wavefunction overlap decreases due to increased internal electric field in the QW. This also makes intuitive sense because a decrease in F_{cv} causes slower recombination, leading to a

build-up of higher carrier density. As n increases, the $C_0 n^3$ Auger term should begin to dominate and IQE will decrease at a given J. It has been well-established that Auger recombination is primarily responsible for efficiency droop in III-N LEDs,[2–7] so reducing net field in InGaN QWs should improve droop performance. Indeed, a one-to-one correlation has been found between the net electric field in the active region and the magnitude of efficiency droop for c-plane III-nitride LEDs.[8] The peak IQE of the device should not change, but increasing wavefunction overlap will shift the peak to higher current densities.

In addition to lowering radiative efficiency, internal QW fields also red-shift the emission wavelength. These effects are manifestations of the quantum confined Stark effect (QCSE) and have been thoroughly analyzed for III-nitride QWs (see Chapter 3 for more information on QCSE).[9–14] Under device operation, the large polarization-induced electric fields can be partially screened by injected carriers.[15] While this diminishing of the internal electric field inside the quantum wells increases radiative efficiency, it also causes a significant blue-shift in emission wavelength with increasing injection. The wider the QW, the larger the blue-shift is expected to be because of the additional potential drop in the QW, as long as emission always comes from ground state transitions.[16] QCSE due to polarization fields results in emission spectra that are difficult to engineer accurately.

Rather than reducing QW polarization fields by growing on nonpolar or semipolar planes of GaN,[17–21] which involve using much smaller and more expensive substrates, or by using AlInN /InGaN QWs in a "polarization-matched" active region,[22,23] which would add significant growth complications, it would be preferable to grow InGaN/GaN LEDs on c-plane. The wide single quantum well (SQW) active regions and low droop demonstrated on

semipolar planes such as (20-2-1) and (30-3-1) should also be achievable on (0001) if the polarization field can be effectively eliminated. In LEDs grown on *c*-plane, the polarization field in the InGaN QW is in the opposite sense to the built-in field of the p-n junction. Therefore, the impurity doping profile can be designed so that the built-in field effectively screens the polarization field, resulting in a near zero net field in the active region of a properly doped SQW device. These doping profiles can also be tuned so that there is zero field at the current density of interest for device operation. Using doping to screen polarization fields and suppress QCSE was first proposed by Fiorentini and Bernardini.[24] Because of the large polarization discontinuities on the polar (0001) plane, giving rise to electric fields in excess of a MV/cm, very large dopant concentrations well in excess of 1 x 10^{19} cm^{-3} may be necessary to screen fixed polarization charges at heterointerfaces. Other groups have correlated n-type doping with a reduction in QW electric field and increase in radiative efficiency, though they do not agree on the physical methods involved.[25–28] In nitride solar cells, a similar effect of polarization screening through doping was observed to improve carrier transport out of the active region.[29]

Decreasing the net electric field in the InGaN also allows for the growth of thicker QWs without a loss of wavefunction overlap. Thicker QW designs will also decrease the carrier density and reduce efficiency droop. LEDs with a properly designed doping profile should result in minimal electric field in QW, maximum wavefunction overlap, allowing thicker active volume, and thus droop onset at higher currents. Additionally, a *c*-plane QW with a screened polarization field would behave more like an *m*-plane QW, and should exhibit no droop dependence on indium content, potentially allowing more efficient devices at longer wavelengths.[1]

5.2 Polarization Screened Single Quantum Well Simulations

Before attempting to grow polarization screened SQW LEDs, simulations were performed to find the correct doping level for flattening the electric field and maximizing the wavefunction overlap in the QW and to see the effect of QW thickness on overlap. Figure 5.2 shows a cross-sectional schematic of the (0001) SQW LED structure under consideration. The structure consists of a 120 nm n-GaN layer with $[Si] = 1E18$ cm^{-3}, a 10 nm n-GaN barrier layer with varying doping level, an $In_{0.20}Ga_{0.80}N$ QW of varying thickness with an n-type background doping level of 1E16 cm^{-3}, a 10 nm p-GaN barrier layer with varying doping level, a 15 nm p-$Al_{0.20}Ga_{0.80}N$ electron blocking layer with $[Mg] = 5E19$ cm^{-3}, a 100 nm p-GaN layer with $[Mg] = 1E19$ cm^{-3}, and a 15 nm p-GaN contact layer with $[Mg] = 1E20$ cm^{-3}. Since equal fixed positive and negative sheet charges exist at the top and bottom interfaces of the SQW, respectively, the doping levels in the n-GaN and p-GaN barrier layers were varied equally and concurrently. For the purposes of the simulation, LEDs with four SQW thicknesses of 3, 5, 8, and 12 nm were considered with unintentionally doped (UID) GaN barrier.[i] Additionally, LEDs with four barrier layer doping levels of 1E19 cm^{-3}, 4E19 cm^{-3}, 7E19 cm^{-3}, and 1E20 cm^{-3} were considered with a 12 nm SQW. For the sake of simplicity, only effects on the longitudinal (along (0001)) ground state of the SQW structure are described. While it is an excellent approximation for the thinnest QW structure, an exact rendition would need to model excited states in thicker layer samples, which would add unnecessary complexity without changing the arguments developed below.

---

[i] The UID layers were given an n-type background doping of 1E16 cm^{-3} due to oxygen impurities.

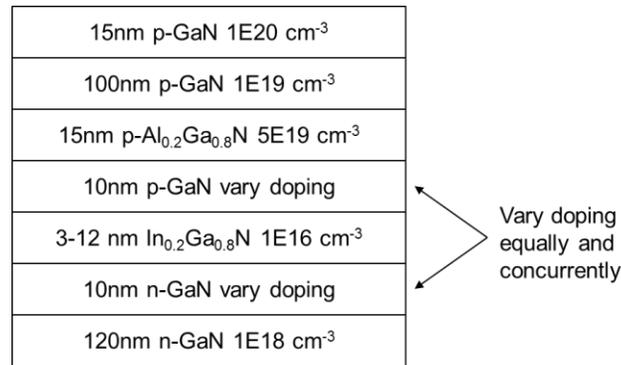| 15nm p-GaN 1E20 cm^{-3} |
| 100nm p-GaN 1E19 cm^{-3} |
| 15nm p-Al$_{0.2}$Ga$_{0.8}$N 5E19 cm^{-3} |
| 10nm p-GaN vary doping |
| 3-12 nm In$_{0.2}$Ga$_{0.8}$N 1E16 cm^{-3} |
| 10nm n-GaN vary doping |
| 120nm n-GaN 1E18 cm^{-3} |

Vary doping equally and concurrently

Figure 5.2: Cross-sectional schematic of a (0001) SQW LED structure.

All simulations were performed using the SiLENSe version 5.4 software.[7] Figure 5.3 shows simulated energy band diagrams and ground state electron and hole wavefunctions under forward bias (at a current density, $J = 100$ A/cm^2) for LEDs with varying QW thicknesses and UID barrier layers. The low background doping in the barrier layers will not screen the polarization fields in the QW. As shown in Fig. 5.3(a), the ground state electron and hole wavefunctions are pressed together by the wide bandgap barrier confinement even though the electric field in the QW is very high. The high degree of confinement in a 3 nm SQW LED maintains a significant carrier wavefunction overlap, about 18% at zero current injection (Fig. 5.4). In Figs. 5.3(b-d), as the QW thickness increases, the separation of the ground state wavefunctions also increases, resulting in decreased wavefunction overlap. The potential remains large in the case of 5, 8, and 12 nm QWs even though the electric field is non-uniform because it has been partially screened at the relatively high injected current density of $J = 100$ A/cm^2. This corresponds to the high excitation regime defined by Della Salla et $al.$[15] In the case of the 12 nm QW, the field is nearly flat in the center, but increases significantly at the right and left edges, causing the electron and hole ground state wavefunctions to be confined at the edges of the well rather
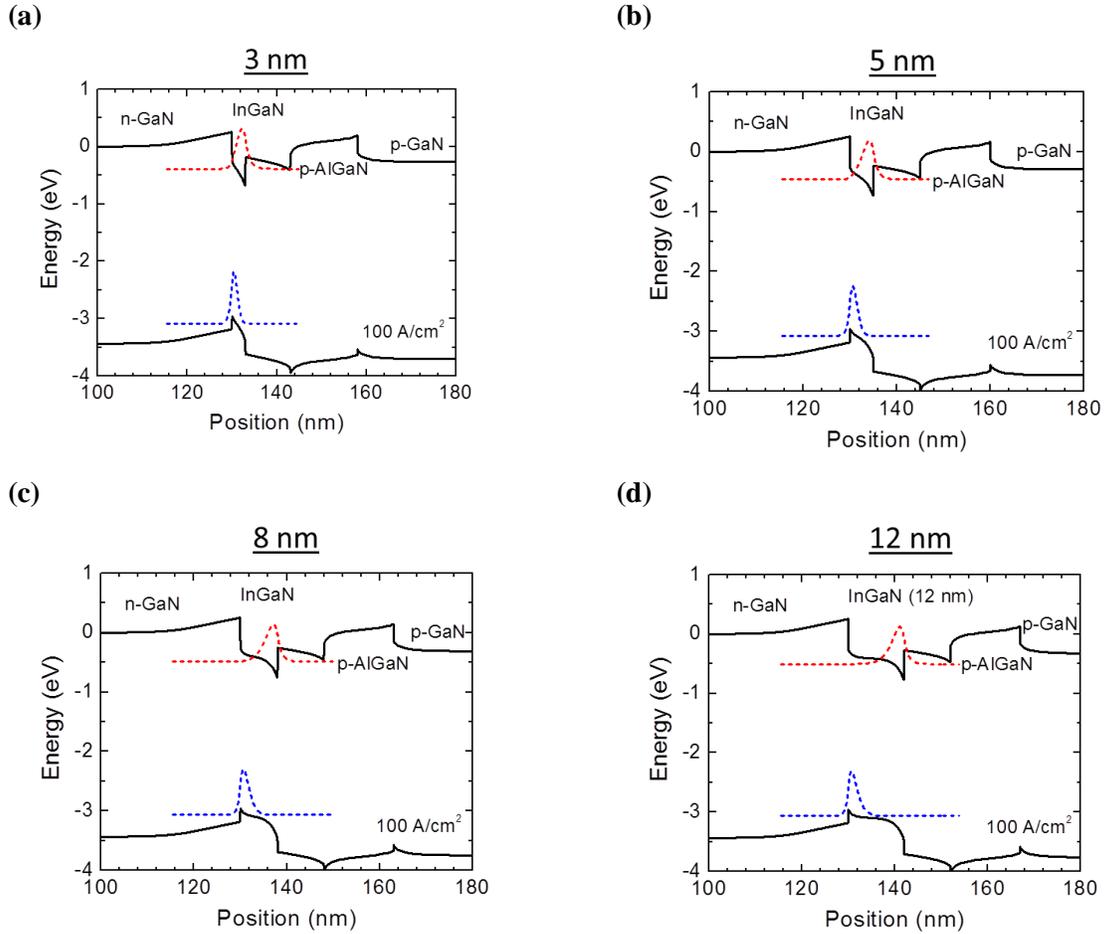
Figure 5.3: Simulated energy band diagrams and ground state electron and hole wavefunctions under forward bias ($J = 100$ A/cm^2) for SQW LEDs with QW thicknesses of (a) 3 nm, (b) 5 nm, (c) 8 nm, and (d) 12 nm.

than spreading across the entire width of the well. Well-designed n-type and p-type barrier layer doping is necessary to fully screen the polarization charges at the QW interfaces and flatten the electric field in the QW, thereby increasing wavefunction overlap.

Figure 5.4 summarizes the simulated dependence of the square of the wavefunction overlap on current density for LEDs with a range of active region thicknesses and no intentional barrier layer doping. As shown in Fig. 5.4, the LEDs with QW thicknesses of 3, 5, and 8 nm exhibited wavefunction overlap that increased monotonically as a function of
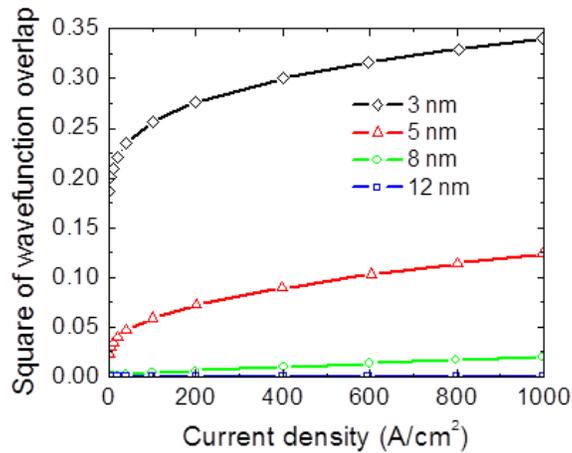
130

Figure 5.4: Simulated dependence of the square of the wavefunction overlap on current density for SQW LEDs with a range of QW thicknesses.

current density. There was, however, a dramatic decrease in the values of wavefunction overlap between the 3 nm QW and the 5 nm QW, and again between the 5 nm QW and the 8 nm QW. The LED with a thickness of 12 nm exhibited nearly zero wavefunction overlap with little dependence on current density. The increase in wavefunction overlap with increasing current density is indicative of the expected partial screening of polarization by injected carriers. Nevertheless, the maximum overlap of all four LEDs with nominally undoped barriers was still less than less than 0.35 at 1 kA/cm^2 due to incomplete screening of the polarization, which becomes worse for the thicker active layers due to their increased separation between the electron and hole ground state wavefunctions.

Larger QW thicknesses are desired, however, in order to reduce efficiency droop by reducing active region carrier density at a given drive current density. This is due to the non-linear dependence of the Auger non radiative process causing droop on the carrier density.[3] Two main effects from the screening of polarization fields to increase electron hole pair overlap for thick active layers are expected: (i) the retention of large overlap even for

131
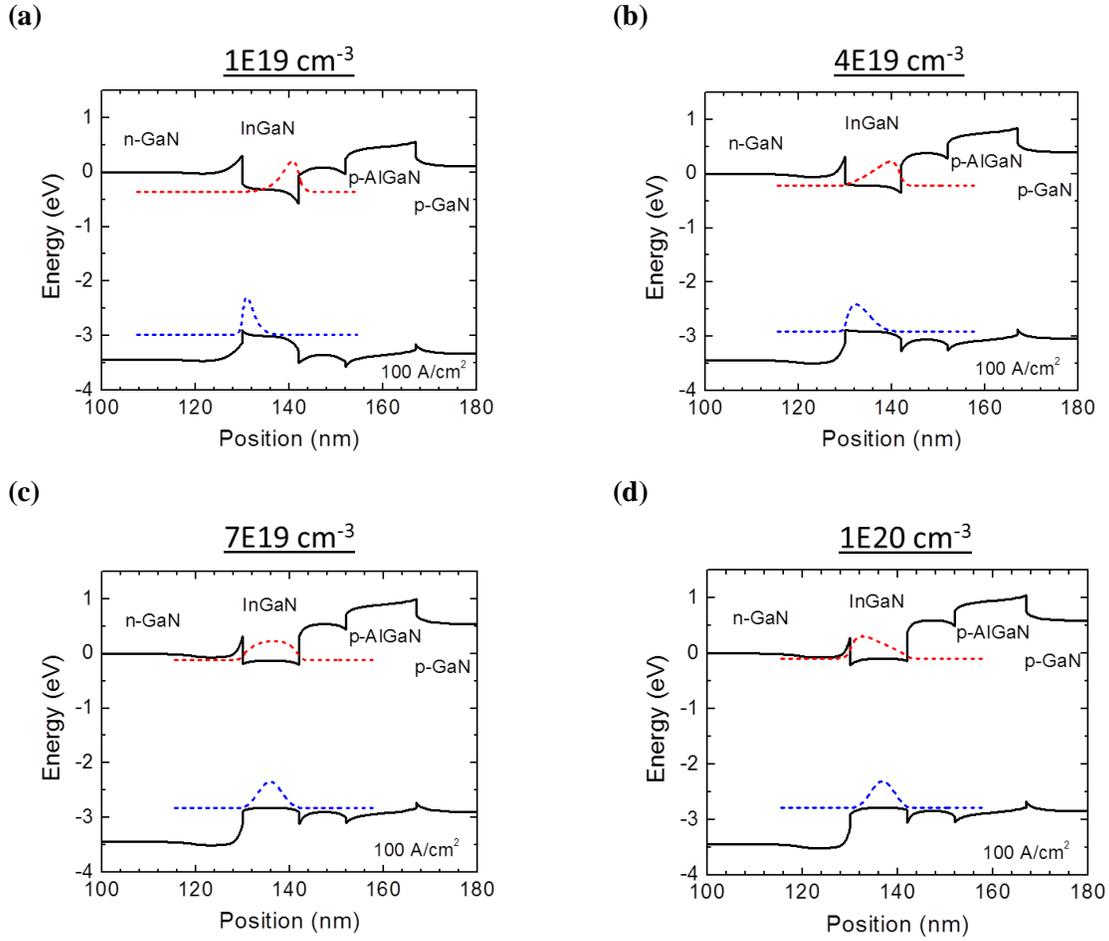
Figure 5.5: Simulated energy band diagrams and ground electron and hole wavefunctions under forward bias (J = 100 A/cm^2) for12 nm SQW LEDs with doping levels of (a) 1E19 cm^{-3}, (b) 4E19 cm^{-3}, (c) 7E19 cm^{-3}, and (d) 1E20 cm^{-3} in the barrier regions on either side of the QW.

thick active layers; (ii) increased overlap compared to the value reached in thin QWs without screening.

Figure 5.5 shows simulated energy band diagrams and ground state electron and hole wavefunctions under forward bias (at J = 100 A/cm^2) for LEDs with concurrently varying n and p barrier doping levels and a thick 12 nm QW. Figure 5.5(a) shows that even with n and p barrier layer doping of 1E19 cm^{-3}, there is little difference from the undoped case (Fig. 5.5(d)): the electric field in the QW is still in the opposite sense to the built-in field since the polarization field remains largely unscreened. This leads to a spatial separation of

the ground state electron and hole wavefunctions, yielding a near zero wavefunction overlap. Figure 5.5(b) shows that upon increasing the doping to 4E19 cm^{-3}, the electric field in the QW begins to decrease and the energy bands begin to flatten, bringing the electron and hole wavefunctions closer together and increasing the overlap, though it is apparent that the wavefunctions are still spatially separated. Increasing the doping slightly more to 7E19 cm^{-3}, as shown in Fig. 5.5(c), results in nearly zero electric field in the QW,[i] indicating that the polarization field in the QW was fully screened. The wavefunction overlap in this case is very high. In contrast, Fig. 5.5(d) once again shows some spatial separation between the electron and hole wavefunctions. The doping level of 1E20 cm^{-3} was high enough to be degenerate on the n-side of the QW and cause an accumulation of electrons. This resulted in a lowering of the bands on the n-side of the well, which lead to a localization of the electron wavefunction nearer to the n-side of the well. The hole wavefunction remained largely unchanged between Figs. 5.5(c) and 5.5(d). According to these simulations, the condition of near zero electric field in the QW is met at a doping level near 7E19 cm^{-3}.

Figure 5.6 summarizes the simulated dependence of the square of the wavefunction overlap on current density for LEDs with a range of doping levels. As shown in Fig. 5.6, the LED with a doping level of 1E19 cm^{-3} exhibited nearly zero wavefunction overlap over a large range of current densities. The LED with a doping of 4E19 cm^{-3} exhibited a relatively low but non-zero wavefunction overlap that increased monotonically with increasing current density. Likewise, the LED with a doping level of 1E20 cm^{-3} showed a similar, albeit much higher, dependence of overlap on current density. In contrast, the LED with a doping level of 7E19 cm^{-3} exhibited a high wavefunction overlap with little

---

[i] There is still some curvature in the bands due to an accumulation of electrons in the QW. The electron Fermi level lies above the conduction band of the QW, which means that the QW is modulation doped.
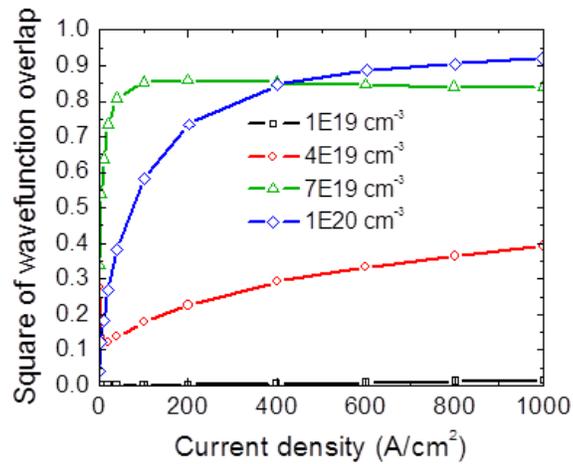
Figure 5.6: Simulated dependence of the square of the wavefunction overlap on current density for SQW LEDs with a range of QW thicknesses.

dependence on current density above $J = 100$ A/cm^2. This behavior is similar to that expected for a nonpolar LED with the same structure and indicates that the polarization field in the QW was fully screened with a doping level of 7E19 cm^{-3}. It should be noted that, in the case of a doping level of 7E19 cm^{-3}, the overlap has a local maximum near $J = 100$ A/cm^2. Increasing the doping further pushes that maximum point to higher overlaps and higher current densities. No maximum is evident in the curve for the case of an LED with a doping level of 1E20 cm^{-3}, but above $J = 400$ A/cm^2, the wavefunction overlap is actually higher than the case of 7E19 cm^{-3} doping. However, it is desirable to design a structure that has high overlap, and therefore high radiative efficiency, at both low and high drive current densities. A structure like the one described above, with a wide active region and high wavefunction overlap over a wide range of drive current densities, is likely to exhibit a minimal amount of efficiency droop.

5.3 Decreasing the Number of Quantum Wells

The first InGaN-based high power LEDs were based on SQW or double heterostructure[i] active regions.[30–32] Eventually the width of the SQW InGaN layer was narrowed and more QWs were added in order to maintain good crystal quality and high power when going to longer wavelengths, and MQW active regions had already been proven for efficient laser diodes.[33,34] Going from today's standard *c*-plane MQW LED to a SQW design with polarization screening is not trivial. Factors such as the wavelength of emission, the active volume, and the wavefunction overlap will change significantly. It has been shown that in a MQW LED, emission is dominated by one or two wells on the p-side of the active region.[35] In this case, the slow diffusion of holes across the quantum barriers of the active region limits current spreading. This limitation leads to higher carrier densities and greater droop than if there were even current spreading and emission over all the QWs. A SQW LED would not suffer from this limitation, and all of its InGaN volume would be active in recombination.

An experiment was performed on LEDs with decreasing number of QWs, but with the nominal InGaN volume remaining constant. The samples were grown by MOCVD on single-side polished (SSP) sapphire substrates and included a ~3 μm GaN template doped at 6×10^{18} cm^{-3}. Below the active region there was a 10 nm n^+ layer of GaN:Ge[ii] doped at 7×10^{19} cm^{-3}, and above the active region there was a 10 nm p^+ layer of GaN:Mg doped at 7×10^{19} cm^{-3}. There was a ~10 nm $Al_{0.12}Ga_{0.88}N$ electron blocking layer (EBL) immediately after the p+ layer. The EBL was followed by ~280 nm p-GaN doped at 5×10^{19} cm^{-3}. In the

---

[i] Many consider a layer of lower bandgap between layers of higher bandgap to be a double heterostructure if its thickness is more than 10 nm because "quantum well" implies significant quantum confinement and layers start to behave more "bulk-like" at around 10 nm.

[ii] Chapter 6 will discuss germanium doping of GaN in detail. For now, the reader can assume it behaves the same as silicon.
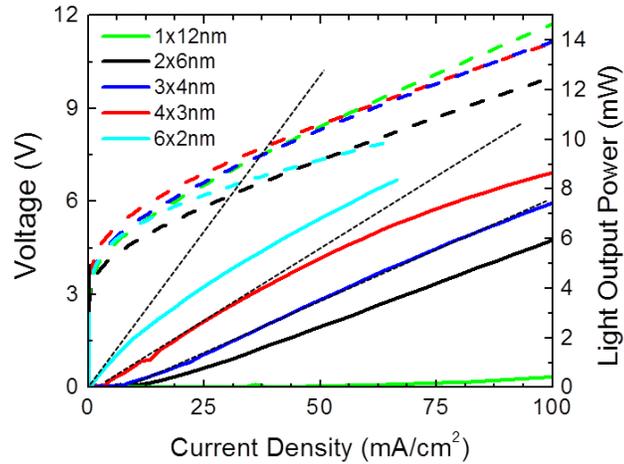
Figure 5.7: Quicktest electrical results of voltage and light output power as a function of injected current density for LEDs with active regions comprised of a varying number of InGaN/GaN QWs, but the same total InGaN thickness, from 1x12 nm to 6x2 nm. The dotted lines are extensions of the maximum slopes of the *L-I* curves, and the difference between the dotted line and the actual power curve represents the droop in device efficiency.

series, the number of QWs and their thicknesses in the active region were 1 x 12 nm, 2 x 6 nm, 3 x 4 nm, 4 x 3 nm, and 6 x 2 nm. The UID GaN barrier thickness between each QW was 20 nm, and the thickness of the UID GaN barriers between the outermost QWs and the doped layers was 10 nm. The QWs contained roughly 17% indium and emitted close to 450 nm.

Figure 5.7 shows the quicktest electrical results, which utilize indium top contacts, a scratched n-contact, and extract light out of the backside of the substrate. There does not seem to be a trend in turn-on voltage with decreasing QW number and increasing QW thickness. There may be a slight increase in series resistance from the 6 x 2 nm sample to the 1 x 12 nm sample, but quicktest is notoriously unreliable for voltage and resistance. The clear trend is in the light output power (L_{op}). As the number of QWs increases and the QW thickness increases, L_{op} decreases dramatically at all measured injection current densities. At the same time, the onset of droop occurs at higher current densities. In the case of an *L-I*

136
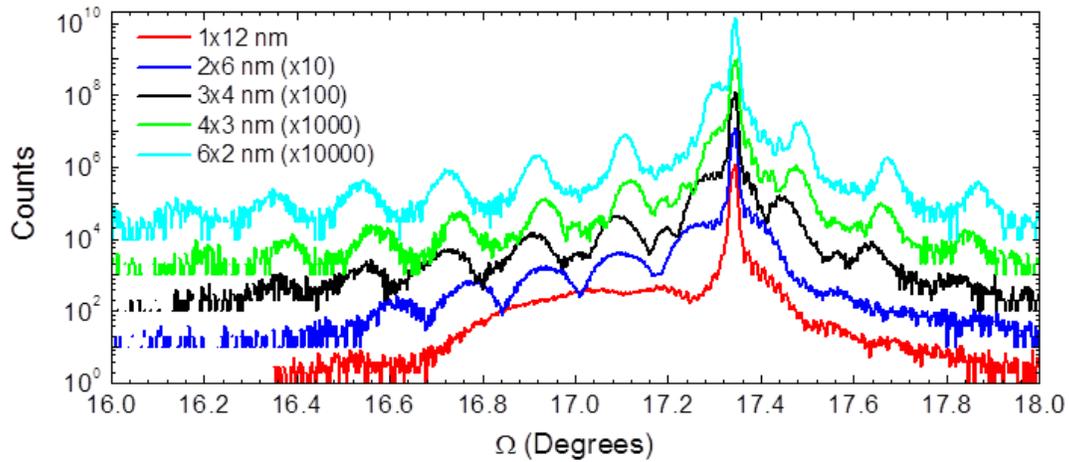
Figure 5.8: High resolution Ω-2Θ XRD scans of LEDs with active regions comprised of a varying number of InGaN/GaN QWs, but the same total InGaN thickness, from 1x12 nm to 6x2 nm.

relationship, the droop is defined as the difference between the actual measured power and the extension of the maximum slope, which is shown on the plot.

There are two explanations for the observed behavior. First, the polarization fields in these QWs are not screened because the heavily doped layers are not immediately adjacent to the QWs. As the QW thickness increases, electron and hole wavefunctions are further separated by the field. Section 5.1 explained in detail how a decrease in wavefunction overlap will result in peak efficiency and droop onset occurring at higher current densities. Another explanation for the large decrease in output power with increasing QW thickness is degradation in material quality caused by the increasing strain in the thick InGaN layers. Figure 5.8 shows high resolution X-ray diffraction (XRD) Ω-2θ scans for each of the different QW number samples. The initial InGaN layer peak on the left shoulder of the GaN substrate peak is in the same position for the MQW samples, but broadens significantly as QW thickness increases. The fringe peaks for the MQW samples also broaden. The 1 x

QW Number	n-side barrier (nm)	n-side doping (cm^{-3})	p-side barrier (nm)	p-side doping (cm^{-3})	Voltage (V)	L_{op} (mW)	λ (nm)	FWHM (nm)
6	10	6e18	10	7e19	4.96	7.05	440	19.9
1	10	6e18	10	7e19	4.78	2.29	423	16.9
1	0	1e19	10	7e19	4.83	3.31	447	26.0
1	0	5e19	0	7e19	4.71	2.39	441	23.0

Table 5.1: Growth parameters and quicktest LED metrics for devices progressing from a standard blue *c*-plane MQW LED to a polarization screened SQW LED. QW thickness for all samples was ~3 nm. Quicktest results were taken at 20 A/cm^2.

12nm SQW sample scan barely has a discernable layer peak severe broadening. The peak broadening is a sign up InGaN layer degradation relaxation and associated defect formation.

Even before the onset of relaxation, thick *c*-plane InGaN QWs behave poorly as LEDs when the polarization field remains unscreened, as was seen in the experiment just described. Moving toward a thick, polarization screened SQW LED like the device simulated in Section 5.2 required a careful step-by-step progression of growths starting with a standard c-plane blue LED structure on a patterned sapphire substrate (PSS), consisting of 6 well/barrier periods of approximately 3 nm and 20 nm, respectively. The n-GaN template, EBL, and p-GaN in the standard blue LED are identical to the devices in the QW number series described above, but it does not include the heavily doped n$^+$ and p$^+$ layers on either side of the active region.

Table 5.1 displays the relevant growth parameters as well as key quicktest LED metrics for devices progression from the standard blue LED to a SQW LED with heavily doped n$^+$ and p$^+$ layers immediately adjacent to the QW. The QW thicknesses for each device in Table 5.1 are ~ 3 nm, and quicktest results were taken at 20 A/cm^2. The first step away from the standard blue 6 QW LED was to eliminate all but one QW, leaving the 10 nm outer barriers. The result was a significant drop in L_{op}, probably because of an increased
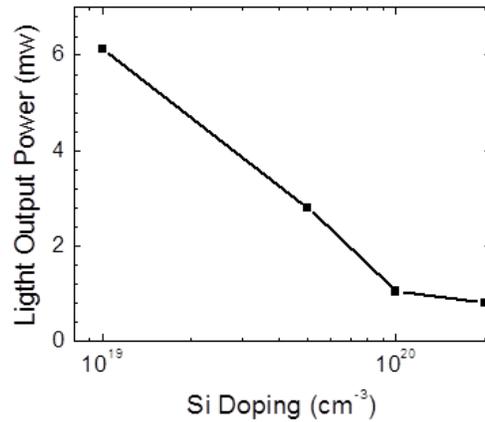
Figure 5.9: Quicktest output powers of SQW LEDs grown on PSS with varying levels of silicon doping in a 10 nm GaN layer immediately below the 3 nm InGaN QW.

A coefficient. There is not a proven explanation for this effect, but it likely has to do with the role that initial InGaN layers, grown at lower temperature than typical n-GaN layers, play in "conditioning" the structure, resulting in fewer point defects higher in the epitaxial stack. It has been demonstrated that an InGaN underlayer or superlattice added below the active region reduces the point defect density in the active region and improves radiative efficiency.[36] That could explain why a MQW, where light is only emitted from the p-side QWs some distance away from the first grown QW on the n-side, would perform better at relatively low current density where *A* plays a large role. The drop in emission wavelength from 440 nm to 423 nm was due to the blue shift resulting from the increase of the built-in field of the p-n junction (because of the decrease in active region thickness) cancelling out some of the polarization field in the QW. In subsequent SQW devices, the InGaN was grown at a colder temperature to incorporate more In and raise the emission wavelength to the blue range (440-460 nm).

The next step shown in Table 5.1 was to dope the 10 nm layer on the n-side of the SQW with a silicon concentration of 1×10^{19} cm^{-3}, which was known to be achievable

without device degradation. Power increased from 2.29 mW to 3.31 mW, perhaps due to an increase in wavefunction overlap, or because of a decreased injection barrier to electrons. The increase in the full width at half maximum (FWHM) of the emission spectrum from 16.9 to 26.0 is likely due to the increased indium content needed to get back to ~ 450 nm. When the doping on the n-side was increased to 5×10^{19} cm^{-3} and the p-side undoped barrier was eliminated, the device approximates the polarization screening device simulated in Section 5.2. The decrease in L_{op} from 3.31 mW to 2.39 mW could be due to an increase in SRH caused by the heavily doped layer in immediate proximity to the QW.

A series of SQW LEDs identical to sample from the last row of Table 5.1 but with varying levels of Si doping from 1×10^{19} cm^{-3} to 2×10^{20} cm^{-3}. The quicktest output powers of the samples in the Si doping series are shown in Fig. 5.9. There is a significant decline in performance when increasing the [Si] below the QW from 1×10^{19} cm^{-3} to 1×10^{20} cm^{-3}, the same trend that was seen in Table 5.1. Again, this is most likely due to an increase in SRH recombination. Heavy silicon doping has been known to add strain to the lattice and cause morphological degradation, so this is not necessarily a surprising result.[37] While this series does not indicate the extent to which the polarization field has been screened, a quicktest power over 2 mW when the doping level is close to what simulations say will fully screen the polarization is high enough to investigate the effects of field screening on thicker SQW LEDs in a more detailed experiment.

5.4 Increasing Single Quantum Well Thickness

5.4.1 Screened vs. Unscreened Wells

In order to properly asses the effects of doping on the QW electric field and LED performance, devices with polarization-screened SQWs of varying thicknesses were compared to equivalent unscreened SQWs. InGaN QWs in which the polarization field is screened by proper doping in the adjacent GaN layers should have greater electron-hole wavefunction overlap than unscreened wells. That increase in overlap should lead to higher efficiencies at higher injection current density and less efficiency droop. The difference between screened and unscreened devices should become even greater with wider SQWs. Additionally, there should be much less emission wavelength shift as a function of injection current in screened devices. Section 5.4.2 will demonstrate conclusive proof of full polarization screening, so until then it can be assumed that there is no polarization field present in the screened devices and that wavefunction overlap is maximized.

Blue SQW LEDs of varying QW thickness were grown by MOCVD on 2" patterned sapphire substrates (PSS) from Precision Micro Optics, with and without doped layers to screen polarization. The grown structures (schematic shown in Fig. 5.10) were very similar to the simulated structures from Section 5.2. The MOCVD growth consisted of a 4 μm Si-doped n-GaN ([Si] = 6 x 10^{18} cm^{-3}) template layer followed by a 10 nm layer that was either highly Si-doped n$^+$-GaN ([Si] = 7 x 10^{19} cm^{-3}) or left undoped. The intrinsic active region consisted of an undoped In$_{0.17}$Ga$_{0.83}$N SQW with thicknesses of 3.8 nm, 5.0 nm, 7.5 nm, and 11.3 nm (confirmed by HAADF-STEM). The SQW was immediately followed by a 10 nm layer that was either highly Mg-doped p$^+$-GaN ([Mg] = 7 x 10^{19} cm^{-3}) or left undoped. There was a 10 nm Mg-doped p-Al$_{0.18}$Ga$_{0.82}$N ([Mg] = 5 x 10^{19} cm^{-3}) EBL immediately after
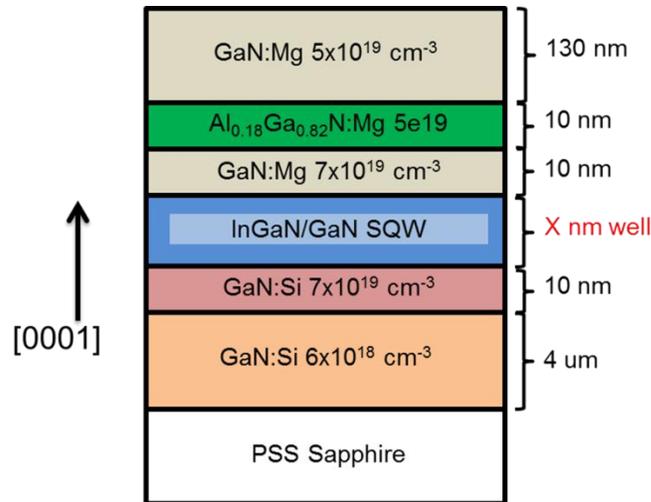
Figure 5.10: A schematic cross-section of the LED structure grown for the screened SQW thickness series.

the p$^+$ layer. The EBL was followed by a ~130 nm Mg-doped p-GaN ([Mg] = 5 x 10^{19} cm^{-3}) layer, and a 15 nm highly Mg-doped p$^+$-GaN contact layer ([Mg] ~ 1 x 10^{20} cm^{-3}).

In addition, a MQW blue LED on PSS was used for comparison against the SQW LEDs. Its structure was identical to the SQW samples described above except for the following differences. It contained an underlying short period superlattice (SPSL) consisting of 50 periods of 2.5 nm In$_{0.035}$Ga$_{0.0965}$N and 2.5 nm GaN layers situated directly beneath the light-emitting active region, for the purpose of improving device efficiency. The underlying superlattice has been suggested as a getter for point defects,[36] or as a prestrain layer that improves strain relaxation and reduces QCSE.[38–40] The active region of the MQW LED contained 6 QWs instead of one. The QWs were approximately 3 nm thick and grown in the exact same conditions as in the SQW samples. The GaN barriers surrounding the QWs were approximately 20 nm thick.

Following the MOCVD growth, an Asylum MFP-3D AFM was used to characterize the sample surfaces. The QW thicknesses and indium composition were measured by XRD

using a PANalytic MRD PRO diffractometer, and the QW layer thicknesses were confirmed by HAADF-STEM. The samples were then processed into LEDs using standard contact lithography. Following a 30 sec dip in 1:1 HCl:H_2O to remove surface oxide, a current spreading layer consisting of 110 nm of tin-doped indium oxide (ITO) was deposited on the p-GaN surface by electron-beam deposition. During deposition, the samples were heated to 300°C using a custom-built resistive heater to improve ITO transparency and conductivity.[41] The ITO deposition rate was measured in-situ using a quartz crystal monitor and the thickness was confirmed ex-situ using a J. Woolam ESM-300 Ellipsometer. Then rectangular mesas (active area of 0.1mm^2) were defined using a methane-hydrogen-argon etch to remove the ITO and a Cl_2-based reactive ion etch to down to the n-GaN below the active region. Finally, Ti/Al/Ni/Au n-contacts and Cr/Ni/Au p- and n-pads were deposited by electron-beam evaporation and a conventional liftoff process. The samples were then thinned and polished from the backside to ~170 μm and devices were singulated using a diamond tip scribing tool. After singulation, devices were bonded to silver headers using Ag-paste, wire bonded with Au wires, and encapsulated in silicone. In contrast, the MQW LED was bonded to a transparent ZnO vertical stand before being encapsulated in silicone.[42]

Packaged LEDs were tested at current densities up to 900 A/cm^2 in an Instrument Systems integrating sphere with a MAS 40 spectrometer, and driven using an Agilent 8114A pulse generator with a 10 μs pulse width and 1% duty cycle to avoid heating. Injected current was calculated by measuring the voltage pulse across a 50Ω resistor in series with the LED on a Tektronix DPO 3014 oscilloscope. *L-I-V* data for the 4 screened and 4 unscreened SQW LEDs with varying QW width are shown in Fig. 5.11(a). The voltage of the screened SQW LEDs is lower than that of the unscreened SQW LEDs at all
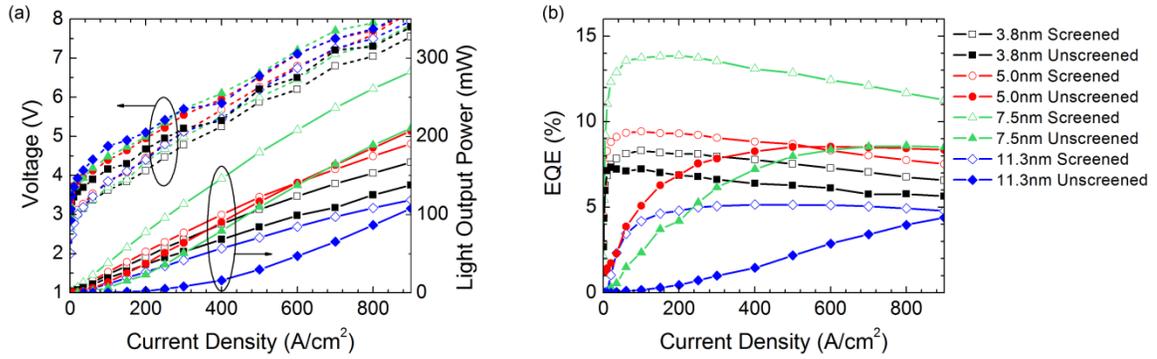
Figure 5.11: Fully packaged *LIV* results (a) and EQE results (b) for screened and unscreened SQW LEDs with QW thickness ranging from 3.8 nm to 11.3 nm at operating current densities up to 900 A/cm^2.

current densities by nearly 1 V. The voltage difference is likely caused by a combination of improved lateral current spreading in the n-GaN due to the highly Si-doped layer, and a lowering of the barriers to electron and hole injection, as seen in Fig. 5.5. Light output powers for the screened LEDs are higher than the unscreened LEDs with the same QW width across the entire range of current densities, except for a crossover at 600 A/cm^2 in the 5.0 nm QW devices. There is also a trend of increasing output power with increasing QW width for the screened SQW LEDs, until the power drops dramatically at a QW width of 11.3 nm.

The trends seen in L_{op} are even more clear in EQE as a function of current density (Fig. 5.11(b)). EQE increases with increasing QW width up to 7.5 nm in the screened LEDs, and EQE of the screened LEDs are higher than for the unscreened LEDs with the same QW width across the entire current density range (except for the same crossover seen in L_{op} for the 5.0 nm QW LEDs). From the EQE curves we can make observations about how the internal electric fields in the screened and unscreened LEDs impact device performance.

In Section 5.1 an argument was put forth about how changes in electron-hole wavefunction overlap should affect LED efficiency. This argument states that if all other

144

factors remain equal, LEDs with greater wavefunction overlap in their QWs will have a lower carrier density at a given current density. Therefore, they should exhibit lower efficiency droop but the *same* value of peak efficiency occurring at a higher current density. A similar argument holds for LEDs with increasing QW width. The data in Fig. 5.11, however, does not support either of those arguments. First, when comparing screened and unscreened LEDs of the same QW width, we do not see similar peak efficiencies, and with the exception of the 3.8 nm QW devices, the peak in the unscreened devices, which have lower wavefunction overlap, occurs at *higher* current density. Second, when comparing screened LEDs of increasing QW width, the peak efficiency does not remain the same, but in fact increases.[i]

Finally, the unscreened devices present a difficult case. They actually hold to the argument based on QW width reasonably well, having similar peak efficiencies and increasing current density at peak EQE with increasing QW width. However, increasing active region volume is in this case convoluted with decreasing wavefunction overlap, and a case can be made that the decreasing overlap is a dominant trend (see Fig. 5.4 overlap summary) and should result in increasing carrier density and decreasing J at peak EQE with increasing QW width. It has been shown, however, that higher order transitions from excited states play an increasingly dominant role in recombination in thicker QWs.[43] Evidence for excited state emission occurring in these unscreened SQW LEDs will be discussed in detail later. In screened QWs, the overlap remains high between ground state wavefunctions, so band-filling will not be sufficient to populate excited states. In unscreened QWs, on the other hand, ground state wavefunctions are spatially separated by the electric field and have a low overlap, so excited states will become populated at lower current densities. The

---

[i] Until an 11.3 nm QW width.

excited states are less localized and have a larger spatial extent and higher overlap; therefore, there should be a net reduction in carrier density with increasing QW width at most current densities. A similar efficiency trend to the one observed in the unscreened SQW LEDs in Fig. 5.11(b) has been seen with increasing QW thickness in (0001) SQW and MQW structures.[16,44]

The disagreement of the LED data with the wavefunction overlap argument can be explained in one of two ways: (1) if the argument itself is flawed and the *A*, *B*, and *C* coefficients are not all proportional to $|F_{cv}|^2$, and (2) if the mechanisms governing recombination vary from sample to sample independent of the wavefunction overlap. The first case is highly possible, if not likely. Consider the case mentioned briefly in Section 5.1, in which there is sequential capture electrons and holes by a non-radiative defect. It is easy to imagine that after the first capture event, a charged defect state will locally bend the potential and more effectively attract the opposite charge carrier. In this case, one carrier may dominate the effective SRH non-radiative rate: the one with the faster capture rate. The dependence of *A* on F_{cv} would then be of order less than 2. This could not explain the difference in peak EQE between the screened SQW LEDs in Fig. 5.11, but it may help explain the much lower efficiencies at low and mid current densities in the unscreened SQW LEDs.

In the second case, the A_0, B_0, and C_0 recombination coefficients from Eq. 5.1 with F_{cv} factored out are not identical between the devices. The differences in EQE are much more pronounced at low current densities, so a likely source of the discrepancies is the A_0 coefficient. Specifically, A_0 would be decreasing with increasing QW thickness in the screened SQW LEDs, leading to higher peak EQE. In the unscreened SQW LEDs, the drop
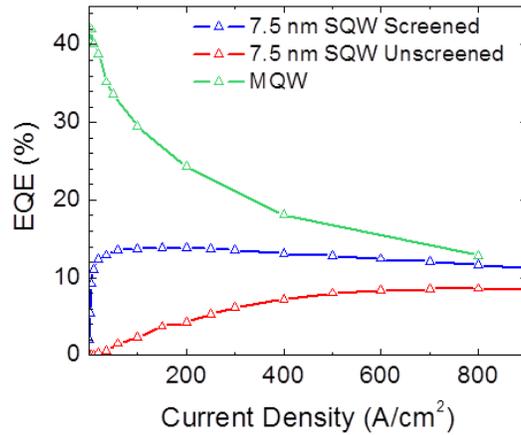
Figure 5.12: Comparison of EQE as a function of current density of screened and unscreened 7.5 nm SQW LEDs with a MQW LED (3 nm QWs).

in peak EQE relative to the screened devices could be attributed to a relatively higher A_0, but an additional effect and explanation for the delayed efficiency "turn-on" could come from the population of excited states leading to a smaller effective carrier density.

Additional evidence for an elevated A_0 coefficient can be seen in Fig. 5.12, which shows an EQE comparison of the high performance blue MQW LED with the screened and unscreened 7.5 nm SQW LEDs. The measured EQE for the MQW LED was derated by 12% (relative), which is the demonstrated difference in extraction efficiency between the transparent ZnO vertical stand package used for the MQW LED and the conventional silver header package used for the SQW LEDs.[42] The efficiency droop is much larger in the MQW LED than the screened SQW LED, but even with derating, the MQW LED has higher EQE out to 800 A/cm^2. Again following the wavefunction overlap argument, it is expected that the peak EQE for these devices would be close to the same value, but clearly, that is not the case here. The most likely explanation is that the A_0 coefficient is much higher in the SQW LED. A theory for the cause of this effect will be presented in Section 5.4.3.
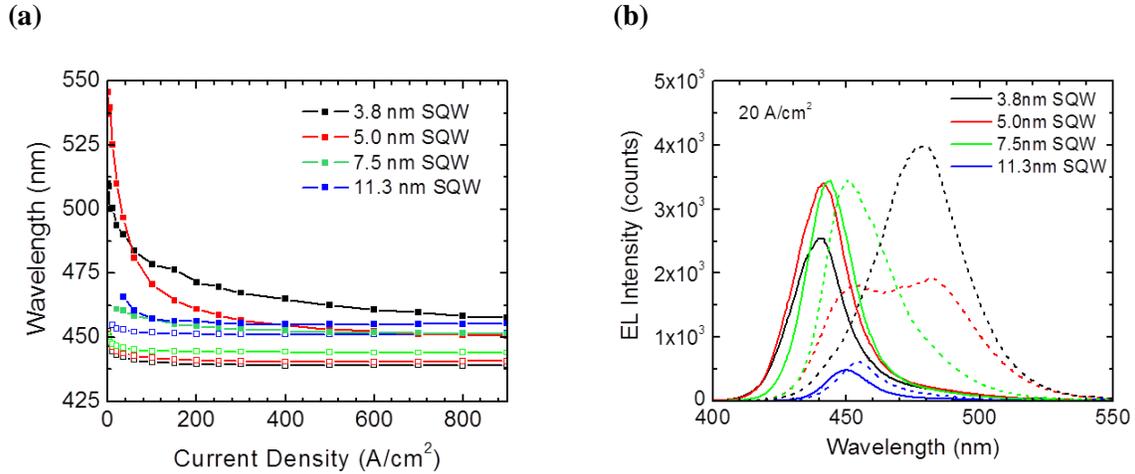
147

Figure 5.13: (a) EL centroid wavelength as a function of current density for screened and unscreened SQW LEDs with QW thickness ranging from 3.8 nm to 11.3 nm at operating current densities up to 900 A/cm^2. Open square symbols represent the screened devices and closed symbols the unscreened devices. (b) EL spectra at 20 A/cm^2 for the devices in (a). Solid lines represent the screened devices and dotted lines the unscreened devices.

Power and efficiency are not the only data that can yield important information about the recombination dynamics in SQW LEDs with different widths and electric fields. For instance, EL wavelength shift as a function of current density will reveal the effects of QCSE on emission (Fig. 5.13). Figur 5.13(a) shows the centroid wavelength of the EL emission spectrum for each measured current density for the screened (open squares) and unscreened (solid squares) SQW LEDs. The wavelength of the unscreened devices is redshifted from their screened counterparts at small current densities due to the internal field causing QCSE. With increasing J, the unscreened emission blue-shifts considerably, while the screened emission blue-shifts only slightly. This is expected because injected carriers help screen the internal field in the unscreened QWs. The lack of blue-shift in the screened wells is evidence that there is nearly zero net internal field.

The wavelength of emission from screened QWs increases monotonically with increasing well width as expected due to the decrease in quantization, but more interesting
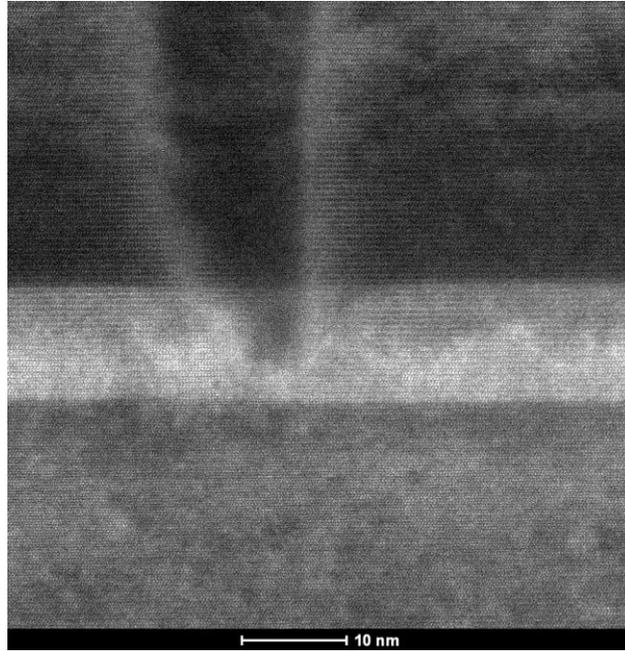
Figure 5.14: HAADF-STEM image of a dislocation generated within the InGaN QW region of the 11.3 nm screened SQW LED.

phenomena occur in the unscreened wells. The largest blue-shift from low to high current density is actually seen in the 5.0 nm QW, even though a simple model would assume that the blue-shift would keep increasing with wider wells. Furthermore, there is a cross-over in emission wavelength between the 3.8 nm and 5.0 nm SQWs at around 50 A/cm^2. The ground-state transition is still at a lower energy in the 5.0 nm QW, but its emission becomes higher in energy than from the 3.8 nm QW. The answer can be seen by looking at the emission spectra for each device at 20 A/cm^2 (Fig. 5.13(b)). The unscreened 5.0 nm QW device has two peaks evident in its emission that nearly match in wavelength the peaks of the 3.8 nm and 7.5 nm QW devices. The double-peaked emission is not an artifact caused by InGaN decomposition, and it has been confirmed by SiLENSe-simulated emission spectra not shown here. This is evidence of a transition from ground state emission to excited state emission as QW thickness increases, but only in the unscreened QWs, a phenomena that has

149

been observed and explained previously.[43] Even as injected current density partially screens the polarization field and flattens the bands in most of the QW, there are regions of much higher field at the edges of the QW where the grounds states are confined (see Fig. 5.3). The ground state separation increases with QW width and their overlap is small. Their recombination lifetime is long, so they fill up quickly, leading to a population of excited states, which are not localized at the edges of the QW, have much better overlap, and thus are not as affected by QCSE. The transition to emission from excited states will occur at a lower injected current density for wider unscreened QWs. In the 5.0 nm QW, the transition to excited state emission is occurring between zero and 100 A/cm^2, causing a much larger blue-shift and a cross-over to higher energy emission. The 3.8 nm QW is too thin for the transition to occur at all – its ground state wavefunctions have relatively high overlap. The thicker QWs emit from excited states over the entire measured range, so their emission wavelength is higher in energy shifts less.

The decrease in output power and efficiency of the screened 11.3 nm SQW LED has not yet been touched on, but can be explained by strain-related defect generation in the thick InGaN layer. 11.3 nm very close to the predicted critical thickness of dislocation generation for an In$_{0.17}$Ga$_{0.83}$N layer on (0001) GaN.[45] The presence of dislocations generated in the InGaN layer is confirmed by HAADF-STEM (Fig. 5.14). While carefully designed doping profiles can screen polarization fields and allow for arbitrarily thick active regions without suffering from QCSE, the QW thickness is, in practice, still limited by strain relaxation.

5.4.2 Biased Photoluminescence

The full screening of QW polarization fields by doping can be verified by examining photoluminescence (PL) as a function of applied bias. Typical biased PL experiments on *c*-plane QW structures reverse bias the device past the point where flat band conditions exist in the QW, and then can calculate the magnitude of the polarization-induced electric field based on the flat-well bias point.[46] Other methods of measuring the internal electric field in a nitride QW include: PL decay time as a function of bias,[47] PL peak shift with changing well width and illumination intensity,[9,48] and electroabsorption (see Chapter 3 for more details).[49] Previous experiments have examined wavelength shift of the PL centroid wavelength as function of bias for different polarization fields and QW widths.[13,14] They saw significant wavelength shift of PL at biases below device turn-on on *c*-plane, but negligible shift in nonpolar and semipolar devices where the field is zero or very small. Others have studied the extent to which polarization fields can be screened by doping by examining PL blue-shift and decay time reduction as the field is screened.[27,28]

In this experiment, illumination was provided by a resonantly exciting 405 nm laser diode operated at ~100mW with an approximately 100 μm diameter spot size. Bias was applied and photocurrent measured with a Keithley 2420 sourcemeter. PL spectra were measured using an optical fiber perpendicular to the path of the incident beam that then fed into an Ocean Optics USB2000+ spectrometer. The saturated photocurrent at short circuit of the screened 5.0 nm SQW LED was measured to be 1.11 mA, corresponding to a photocurrent density of approximately 14 A/cm^2. Assuming that the collection efficiency at photocurrent saturation is 100%, the generation rate in the QW can be calculated: 1.75 x 10^{26} cm^{-3}.
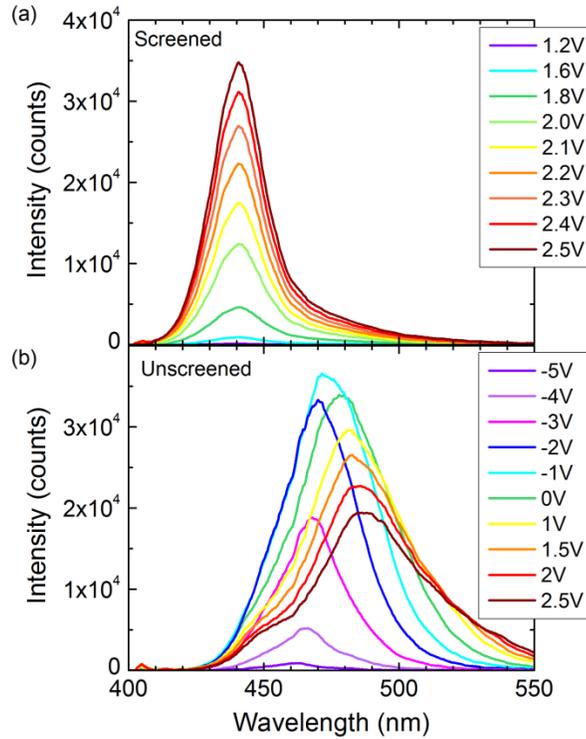
Figure 5.15: Biased photoluminescence spectra over the full range of voltage between complete carrier sweep-out (reverse bias) and EL turn-on (forward bias) for a screened (a) and unscreened (b) 5.0 nm SQW LED.

Figure 5.15 shows the PL spectra of the screened and unscreened 5.0 nm QW LEDs over a range of doping, spectrally color coded with the violet end of the spectrum. The doping range for each device extended from the extinction of the PL signal at reverse bias to the onset of electroluminescence (EL) at forward bias. PL extinction at reverse bias is caused by the carrier sweep-out rate being higher than the radiative recombination rate. In this regime, the LED operates like a solar cell or photodetector. The extinction bias for PL is determined by the size of the potential barriers for electrons and holes to escape the QW. Thinner and lower barriers will cause faster escape through increased rates of tunneling and thermionic emission, respectively.
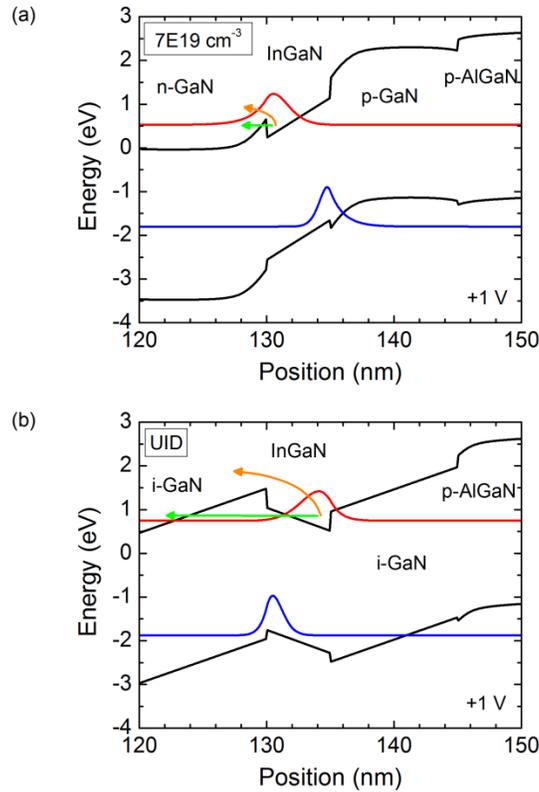
Figure 5.16: Simulated energy band diagrams and ground state electron and hole wavefunctions under forward bias (+1 V) for 5 nm SQW LEDs with barrier regions on either side of the QW (a) doped at 7×10^{19} cm^{-3}, and (b) left undoped. These diagrams correspond to the devices used in the biased PL experiment shown in Fig. 5.15. The green and orange arrows represent extraction of photogenerated electrons by tunneling and thermionic emission processes, respectively.

Figure 5.16 shows the contrast between band diagrams of the screened and unscreened SQW LEDs at low forward bias (+1 V), where there is no PL signal from the screened device, but a large PL signal form the unscreened device. In the screened case where heavy doping extends up to the edge of the QW (Fig. 5.16(a)), the potential barrier is very thin and low because the lack of polarization field means that the built in voltage can drop across the QW and not in the barrier regions. This barrier can be easily tunneled though, as shown by the short green arrow going through the barrier, and easily thermally emitted over, as shown by the orange arrow curving over the barrier. These factors explain

153
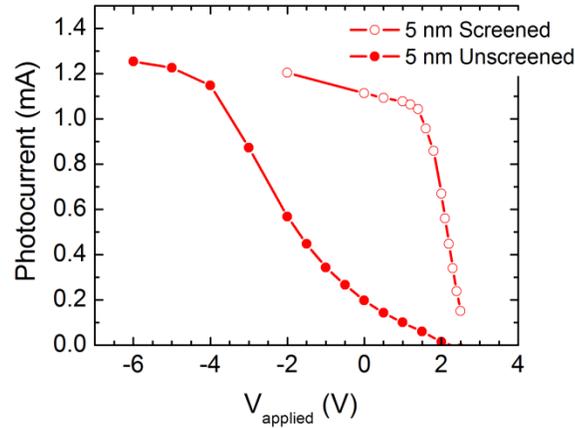
Figure 5.17: Photocurrent measured during biased PL measurements on screened and unscreened 5 nm SQW LEDs.

why carrier sweep-out is complete and photocurrent saturates (Fig. 5.17) at positive bias (+1.2 V) in the screened device.

In the unscreened well case on the other hand (Fig. 5.16(b)), the 10 nm undoped regions on either side of the QW support a large voltage drop due to both the built-in voltage of the junction and the unscreened polarization charges at the InGaN/GaN interfaces. The polarization field also localizes carriers on the opposite side of the QW from where they would escape to contribute to the photocurrent, causing the QW itself to contribute to the barrier for carrier escape. The green and orange arrows in Fig. 5.16(b) clearly show how the tunneling distance and barrier height have increased relative to the screened case in Fig. 5.16(a). These large potential barriers for carrier escape decrease the sweep-out rate, explaining why the PL signal at +1 V is so much larger in the unscreened case. To effectively thin these barriers and achieve the same sweep-out rate as in the screened case, a large reverse bias must be applied to promote field-assisted barrier lowering and tunneling. This explains why significant reverse bias (less than -5 V) is necessary for photocurrent saturation in the unscreened case (Fig. 5.17).

Over the full range of biases where only PL is visible (before EL), there is no noticeable wavelength shift in the screened SQW LED, but a large wavelength shift in the unscreened SQW LED (Fig. 5.15). The peak wavelength from the unscreened QW redshifts 24 nm from -5 V to +2.5 V, and even looking over only the same bias range as in the screened case, it still redshifts by 5 nm. The dramatic difference in wavelength shift between the screened and unscreened QWs is evidence of a significant reduction in internal electric field in the screened QW compared to the unscreened QW. Additionally, the peak PL intensity increases monotonically with increasing bias in the screened SQW LED, but reaches a maximum at -1 V in the unscreened SQW LED (Fig. 5.15(b)). The decrease in intensity going toward negative bias can be explained by the increase rate of carrier sweep-out, and the decrease in intensity going toward forward bias can be explained by QCSE.

In an unscreened c-plane InGaN QW the built-in field of the junction acts against the polarization-induced field, so with increasing forward bias the net field in the QW should increase. This will increase the impact of QCSE, leading to a redshift of emission and a reduction in radiative efficiency, which is exactly what is seen in the unscreened SQW LED (Fig. 5.15(b)). A fully screened c-plane QW should behave like an m-plane QW and should not exhibit a significant wavelength shift as a function of bias.[13] The lack of wavelength shift in the SQW LED with doped barriers, coupled with the clear evidence of QCSE in the SQW LED with undoped barriers, is a strong indication that the polarization field has been fully screened by doping.

5.4.3 Barrier Modal Overlap

Even though complete polarization screening was confirmed by biased PL, there are still trends in the LED data from Fig. 5.11 that cannot be explained by wavefunction overlap arguments alone. There needs to be another explanation for why the peak efficiency improves going from 3.8 nm to 7.5 nm screened SQW LEDs, and why the peak efficiencies in the screened SQW LEDs occur at lower J than in the unscreened SQW LEDs for a given QW thickness. As described in Section 5.4.1, a likely culprit is a difference in the wavefunction overlap-independent SRH recombination coefficient, A_0. An unchanging A_0 between devices with difference active region geometries and electrostatics assumes that A_0 is spatially constant throughout the active region: that is it the same across the well and barrier. This is probably not the case, however. The GaN barrier layers in the screened devices are extremely highly doped, which could easily cause an increase in non-radiative sites in the barrier compared to the InGaN well. Additionally, the n^+ GaN layer is rough compared to high quality UID GaN, which could cause additional recombination sites near the GaN/InGaN interface. There may also be some as-yet unexplained reason for increased levels of non-radiative defects in GaN compared to InGaN, regardless of doping. In any case, carriers with significant probability of existing outside the QW will have less chance of recombining radiatively in the QW, and any other outcome is considered loss.

If A_0 is locally different in the GaN barrier regions and the InGaN QW, then the modal overlap of the electron and hole wavefunctions with the barrier regions of either side of the SQW will determine the overall effective A_0 for the device. Band structures and electron and hole envelope wavefunctions for all states localized in the QW were calculated using SiLENSe version 5.4 software for each device in the SQW thickness series (screened

156
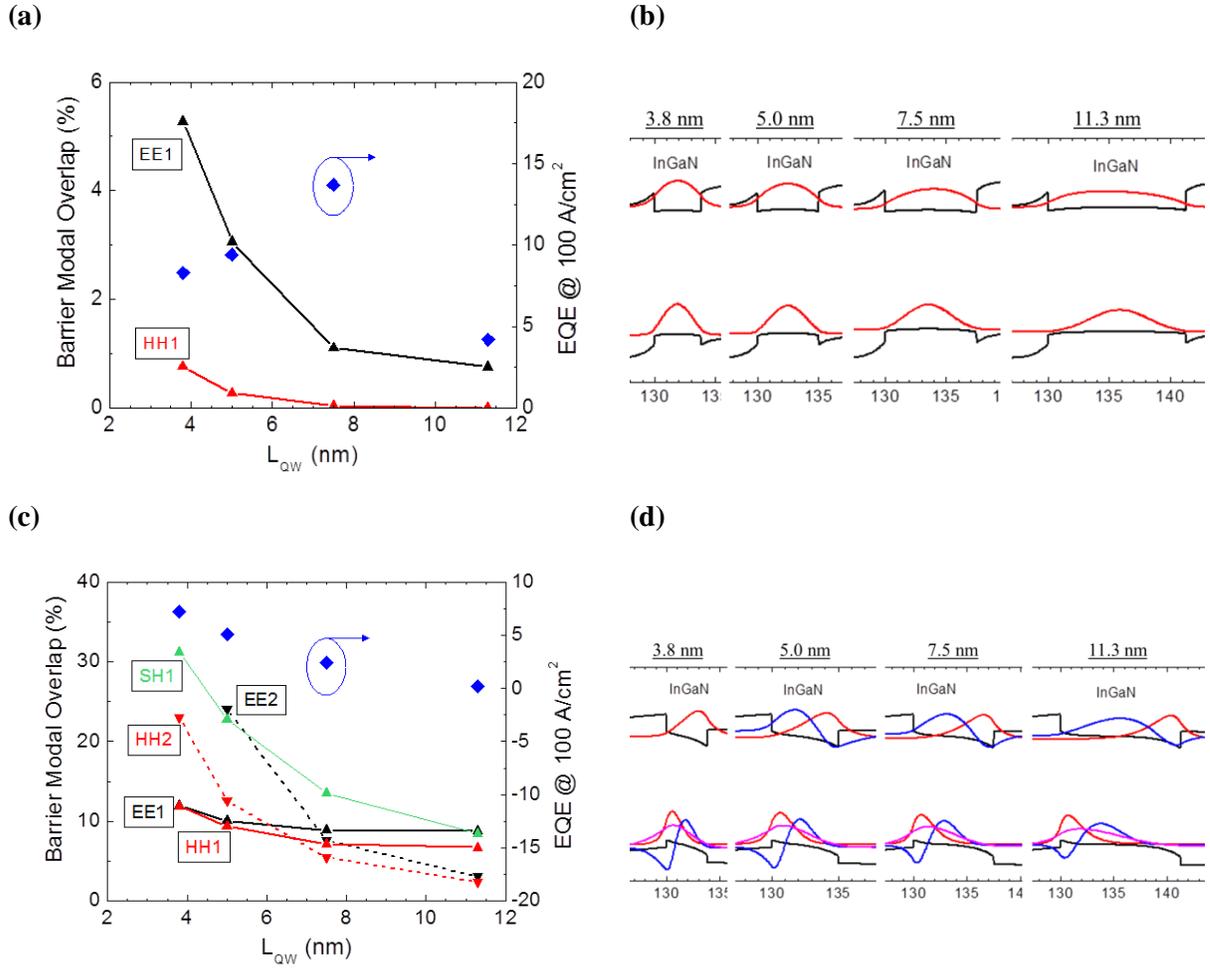
Figure 5.18: (a) Simulated barrier overlap percentage of the square of the electron and heavy hole ground state wavefunctions plotted alongside measure device EQE as a function of *screened* SQW width. (b) Simulated energy band diagrams of electron and heavy hole ground state envelope wavefunctions at each QW width showing decreasing barrier modal overlap with increasing width. (c) Simulated barrier overlap percentage of the square of the electron and hole ground state and first excited state wavefunctions, as well as the first split hole wavefunction, plotted alongside measure device EQE as a function of *unscreened* SQW width. (d) Simulated energy band diagrams of electron and heavy hole ground state, first excited state, and split hole envelope wavefunctions at each QW width showing increased barrier modal overlap for excited states. Simulations and measurements performed at 100 A/cm^2.

and unscreened), with thicknesses and composition as measured (see Section 5.4.1), and at an operating current density of 100 A/cm^2. Barrier modal overlap (F_{iB}) was calculated for electrons and holes in all supported states using the following relation:

$$F_{iB} = 1 - \frac{\int^{QW} \psi_i^*(z)\psi_i(z)dz}{\int_{-\infty}^{\infty} \psi_i^*(z)\psi_i(z)dz},\qquad (5.2)$$

where ψ_i is the normalized envelope wavefunction for either carrier in any state.

Values of F_{iB}, which corresponds to the probability that a given carrier in a given state is located in the barrier region, are plotted in Fig. 5.18(a) for the screened SQWs and in Fig. 5.18(c) for the unscreened SQWs as a function of QW thickness, along with the EQE values for those devices, all at an injected current density of 100 A/cm^2. Additionally, the calculated envelope wavefunctions for electrons and holes are plotted on the simulated energy band diagram in the vicinity of the QW for each thickness of screened QW (Fig. 5.18(c)) and unscreened QW (Fig. 5.18(d)), also at 100 A/cm^2. In Fig. 5.18(a,b) only the ground state electron and heavy hole wavefunctions are plotted, as these are the only states in which significant carrier population should exist due to the high overlap and corresponding high recombination of the ground states. In Fig. 5.18(c,d), first excited states of electrons and holes, as well as the ground state split-off hole wavefunction, are plotted in addition to the ground states because the poor overlap of the ground states makes it much more likely that higher level states will be populated and contribute to recombination, as discussed in Section 5.4.1.[43,50] It is assumed that carriers will have time to relax to the lowest available energy state in the QW before recombining.

First focusing on the trend of improved EQE between screened and unscreened SQW LEDs of the same QW thickness, it is clear from comparing values in Figs. 5.18(a) and (c) that carriers confined in the screened QWs overlap much less with the barrier regions. This is visually confirmed in the band diagrams of Figs. 5.18(b), where the wavefunctions are centered in screened QWs with flat energy bands and overlap minimally and equally with barrier regions above and below the well. In Fig. 5.18(d), on the other
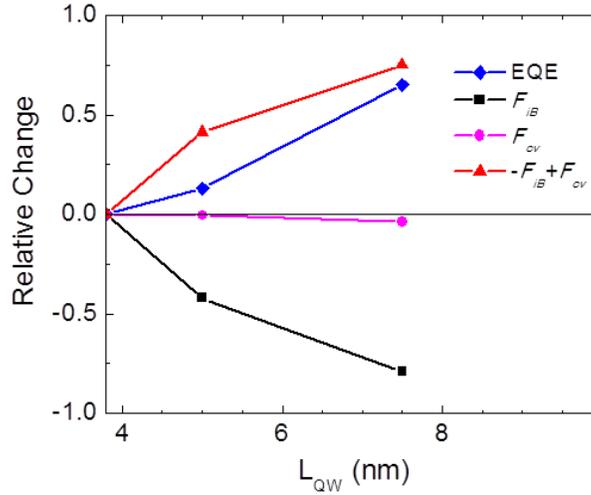
Figure 5.19: The combination of the relative changes in simulated barrier modal overlap and electron-hole wavefunction overlap match well to the relative change in measured EQE with increasing QW width, all at 100 A/cm^2.

hand, tilted energy bands in the unscreened QWs confine the ground state wavefunctions to opposite sides of the well where they overlap more with the barrier region on the side where they are confined. The higher order transitions in the unscreened QWs are more centered, but also have a larger spatial extent and are less confined to the QW region. Interestingly, the unscreened 3.8 nm QW only supports a single electron state at 100 A/cm^2 according to simulation, while the others support at least two. That may explain why its EQE peaks so much earlier than the thicker QW LEDs: it can only emit from a highly localized state and so maintains a higher carrier density. If A_0 is indeed higher in the barrier regions, we would expect the efficiency of the unscreened SQW LED to be much lower at low current density, but to increase relative to the screened SQW LED as current density increases. This is exactly what we see in the EQE curves of Fig. 5.11(b). Higher order transitions in the unscreened wells have a greater F_{cv} but also a greater F_{iB}, so they may not gain anything in

terms of radiative efficiency, which could explain the relatively lower peak EQE values in the unscreened devices.

Next, we focus on the trend of increasing peak EQE with increasing QW width in the screened QW LEDs. There is a stark decrease of barrier modal overlap with increasing QW width in these devices (Fig. 5.18(a)); because, without electric field, the ground state wavefunctions remain centered in the QW and don't significantly increase their spatial extent, so the tails of the wavefunctions interact less with the barrier regions (Fig. 5.18(b)). The relative decrease in barrier overlap as QW thickness increases, coupled with the relative change in wavefunction overlap,[i] matches reasonably well to the relative increase in EQE, as shown in Fig. 5.19. This correlation shows that there is a high probability that the extent to which the wavefunctions overlap the barriers affects LED efficiency.

It is likely that A_0 is not the only changing recombination coefficient causing differences in device efficiency. EQE in the SQW devices is depressed over a wide range of current densities, not just at low current where SRH recombination dominates. There is the possibility of a so far unidentified non-radiative process with a higher order dependence on carrier density limiting radiative efficiency in the mid-range of current density, but we cannot speculate on its nature or origin.

5.5 Conclusion

There are large polarization discontinuities at (0001) InGaN/GaN interfaces that induce large electric fields in InGaN quantum wells. These polarization fields spatially separate electron and hole wavefunctions causing a reduction in the electron-hole

---

[i] A small effect, but included for completeness

160

wavefunction overlap. SRH non-radiative, bimolecular radiative, and Auger non-radiative recombination have been proposed to each proportional to the square of the wavefunction overlap, $|F_{cv}|^2$. An increase in overlap causes an increase in the rate of all types of recombination, which lowers the carrier density for a given injection current density. That leads to the wavefunction overlap argument for LEDs, which says that if LED structures are identical except for their wavefunction overlap, then they should have the same peak efficiency and that the peak efficiency will occur at larger injection current densities for larger overlaps. The consequence, then, of increasing F_{cv} is to decrease efficiency droop at high current density. One way to increase the overlap is to screen polarization fields in InGaN QWs by doping.

Simulations of blue-emitting InGaN single quantum well LED structures reveal that increasing the width of an unscreened increases the separation of electron and hole wavefunctions and decreases their overlap. There is only a moderate overlap for thin QWs, and almost none for QWs thicker than 5 nm. When the doping immediately adjacent to the active region is increased equally on either side (n-type below and p-type above to screen the negative and positive sheet charges, respectively), the polarization field can be completely screened and the energy bands in the QW flatten, maximizing wavefunction overlap over a wide range of injected current density. In the simulation, this occurs at a doping level near 7×10^{19} cm^{-3}. Doping at that level in real LED structures should be able to screen polarization and improve droop by allowing for growth of wider QWs without a damaging loss of wavefunction overlap.

Growth of polarization screened SQW LEDs was approached systematically by first decreasing the number of QWs in the active region while maintaining the same total InGaN

thickness. The result was a decreasing in L_{op} at low current densities and droop onset at higher current density for increasing QW width and decreasing QW number, consistent with the wavefunction overlap argument presented in Section 5.4.1. Going from a MQW to a SQW with the same QW thickness resulted in a significant drop of L_{op}, probably due to increased non-radiative recombination from point defects. A separate series was grown to investigate the effect of increasing Si-doping adjacent to a SQW. L_{op} decreased with increasing [Si], probably again due to increased SRH recombination caused by high impurity concentration close to the QW, but the power remained high enough for at doping levels that would screen polarization for further studies to be done.

To test the theory and the simulations that say proper doping can completely screen polarization fields, allowing for wider QWs and less droop, a series of 4 screened and 4 unscreened SQW LEDs with QW widths ranging from 3.8 nm to 11.3 nm was grown, packaged, and tested. The widest QW suffered from strain-related defect formation in the InGaN layer. The other screened LEDs showed an increase in peak EQE and low droop with increasing QW thickness. Each screened LED had higher EQE and peak EQE at lower wavelength than its unscreened counterpart with identical QW thickness. The results don't completely agree with the wavefunction overlap argument. It was clear that overlap-independent recombination coefficients must not be consistent between samples. A potential explanation was presented: the A_0 coefficient may be higher in the barrier region or at the interface between the barrier and well. This explanation would explain the increase in peak EQE of the screened LEDs, and in fact, the trend in decreasing simulated barrier modal overlap matched the trend in increasing EQE. In the unscreened wells, it was argued that the transition from ground state to excited state recombination could explain the apparent drop

162

in carrier density between screened and unscreened SQWs, especially at larger QW thicknesses.

Finally, biased PL measurements were carried out on the 5.0 nm screened and unscreened SQW LEDs. No wavelength shift or other evidence of QCSE was observed in the screened QW as a function of bias. On the other hand, a significant red-shift and decreasing intensity of emission was observed with increasing forward bias in the unscreened QW. The biased PL results present strong evidence of full polarization screening by doping. There is hope that with more optimized growth conditions, a screened SQW LED will be able to match the peak efficiency of a MQW LED, but with much less efficiency droop at high current density.

References

1. Kioupakis, E., Yan, Q., Walle, C. G. Van De & Van de Walle, C. G. Interplay of polarization fields and Auger recombination in the efficiency droop of nitride light-emitting diodes. *Appl. Phys. Lett.* **101,** 231107 (2012).

2. Kioupakis, E., Rinke, P., Delaney, K. T. & Van De Walle, C. G. Indirect Auger recombination as a cause of efficiency droop in nitride light-emitting diodes. *Appl. Phys. Lett.* **98,** (2011).

3. Iveland, J., Martinelli, L., Peretti, J., Speck, J. S. & Weisbuch, C. Direct Measurement of Auger Electrons Emitted from a Semiconductor Light-Emitting Diode under Electrical Injection: Identification of the Dominant Mechanism for Efficiency Droop. *Phys. Rev. Lett.* **110,** 177406 (2013).

4. Iveland, J. *et al.* Origin of electrons emitted into vacuum from InGaN light emitting diodes. *Appl. Phys. Lett.* **105,** 052103 (2014).

5. Binder, M. *et al.* Identification of nnp and npp Auger recombination as significant contributor to the efficiency droop in (GaIn)N quantum wells by visualization of hot carriers in photoluminescence. *Appl. Phys. Lett.* **103,** 071108 (2013).

6. Sadi, T., Kivisaari, P., Oksanen, J. & Tulkki, J. On the correlation of the Auger generated hot electron emission and efficiency droop in III-N light-emitting diodes. *Appl. Phys. Lett.* **105,** 091106 (2014).

7. Shen, Y. C. *et al.* Auger recombination in InGaN measured by photoluminescence. *Appl. Phys. Lett.* **91,** 141101 (2007).

8. David, A. & Grundmann, M. J. Influence of polarization fields on carrier lifetime and recombination rates in InGaN-based light-emitting diodes. *Appl. Phys. Lett.* **97,** 033501 (2010).

9. Takeuchi, T., Sota, S., Katsuragawa, M. & Komori, M. Quantum-confined Stark effect due to piezoelectric fields in GaInN strained quantum wells. *Jpn. J. Appl.* (1997). at <http://jjap.jsap.jp/link?JJAP/36/L382/>

10. Lefebvre, P. *et al.* High internal electric field in a graded-width InGaN/GaN quantum well: Accurate determination by time-resolved photoluminescence spectroscopy. *Appl. Phys. Lett.* **78,** 1252 (2001).

11. Grandjean, N. *et al.* Built-in electric-field effects in wurtzite AlGaN/GaN quantum wells. *J. Appl. Phys.* **86,** 3714 (1999).

12. Im, J. J. S. *et al.* Reduction of oscillator strength due to piezoelectric fields in GaN/AlxGa1-xN quantum wells. *Phys. Rev. B* **57,** 9435–9438 (1998).

13. Masui, H. *et al.* Effects of piezoelectric fields on optoelectronic properties of InGaN/GaN quantum-well light-emitting diodes prepared on nonpolar (10-10) and semipolar (11-22) orientations. *J. Phys. D. Appl. Phys.* **42,** 135106 (2009).

14. Masui, H. *et al.* Quantum-confined Stark effect on photoluminescence and electroluminescence characteristics of InGaN-based light-emitting diodes. *J. Phys. D. Appl. Phys.* **41,** 165105 (2008).

15. Della Sala, F. *et al.* Free-carrier screening of polarization fields in wurtzite GaN/InGaN laser structures. *Appl. Phys. Lett.* **74,** 2002 (1999).

16. Li, Y. L., Huang, Y. R. & Lai, Y. H. Efficiency droop behaviors of InGaNGaN multiple-quantum-well light-emitting diodes with varying quantum well thickness. *Appl. Phys. Lett.* **91,** 10–13 (2007).

17. Becerra, D. L. *et al.* High-power low-droop violet semipolar ($30\bar{3}\bar{1}$) InGaN/GaN light-emitting diodes with thick active layer design. *Appl. Phys. Lett.* **105,** 171106 (2014).

18. Zhao, Y. *et al.* High-Power Blue-Violet Semipolar ($20\bar{2}\bar{1}$) InGaN/GaN Light-Emitting Diodes with Low Efficiency Droop at 200 A/cm^{2}. *Appl. Phys. Express* **4,** 082104 (2011).

19. Zhao, Y. *et al.* Indium incorporation and emission properties of nonpolar and semipolar InGaN quantum wells. *Appl. Phys. Lett.* **100,** 201108 (2012).

20. Pan, C. C. *et al.* High-power, low-efficiency-droop semipolar ($20\bar{2}\bar{1}$) single-quantum-well blue light-emitting diodes. *Appl. Phys. Express* **5,** (2012).

21. Waltereit, P. *et al.* Nitride semiconductors free of electrostatic fields for efficient white light-emitting diodes. *Nature* **406,** 865–8 (2000).

22. Jena, D. *et al.* Polarization-engineering in group III-nitride heterostructures: New opportunities for device design. *Phys. Status Solidi* **208,** 1511–1516 (2011).

23. Kozlowski, G., Schulz, S. & Corbett, B. Polarization matching design of InGaN-based semi-polar quantum wells—A case study of ($11\bar{2}2$) orientation. *Appl. Phys. Lett.* **104,** 051128 (2014).

24. Fiorentini, V., Bernardini, F., Della Sala, F., Di Carlo, a. & Lugli, P. Effects of macroscopic polarization in III-V nitride multi-quantum-wells. **60,** 11 (1999).

25. Davies, M. J. *et al.* The effects of Si-doped prelayers on the optical properties of InGaN/GaN single quantum well structures. *Appl. Phys. Lett.* **105,** 092106 (2014).

26. Chichibu, S. *et al.* Optical properties of InGaN quantum wells. *Mater. Sci. Eng. B* **59,** 298–306 (1999).

27. Deguchi, T. *et al.* Luminescence spectra from InGaN multiquantum wells heavily doped with Si. *Appl. Phys. Lett.* **72,** 3329 (1998).

28. Dalfors, J. *et al.* Optical properties of doped InGaN/GaN multiquantum-well structures. *Appl. Phys. Lett.* **74,** 3299 (1999).

29. Neufeld, C. J. *et al.* Effect of doping and polarization on carrier collection in InGaN quantum well solar cells. *Appl. Phys. Lett.* **98,** 243507 (2011).

30. Nakamura, S., Senoh, M., Iwasa, N. & Nagahama, S. C. High-power InGaN single-quantum-well-structure blue and violet light-emitting diodes. *Appl. Phys. Lett.* **67,** 1868–1870 (1995).

31. Mukai, T., Takekawa, K. & Nakamura, S. InGaN-based blue light-emitting diodes grown on epitaxially laterally overgrown GaN substrates. *Japanese J. Appl. Physics, Part 2 Lett.* **37,** 35–38 (1998).

32. Mukai, T., Narimatsu, H. & Nakamura, S. Amber InGaN-based light-emitting diodes operable at high ambient temperatures. *Japanese J. Appl. Physics, Part 2 Lett.* **37,** (1998).

33. Nakamura, S. The Roles of Structural Imperfections in InGaN-Based Blue Light-Emitting Diodes and Laser Diodes. *Science (80-.).* **281,** 956–961 (1998).

34. Nakamura, S. III–V nitride based light-emitting devices. *Solid State Commun.* **102,** 237–248 (1997).

35. David, A. *et al.* Carrier distribution in (0001) InGaN∕GaN multiple quantum well light-emitting diodes. *Appl. Phys. Lett.* **92,** 053502 (2008).

36. Armstrong, A. M. *et al.* Defect-reduction mechanism for improving radiative efficiency in InGaN/GaN light-emitting diodes using InGaN underlayers. *J. Appl. Phys.* **117,** 134501 (2015).

37. Fritze, S. *et al.* High Si and Ge n-type doping of GaN doping - Limits and impact on stress. *Appl. Phys. Lett.* **100,** 122104 (2012).

38. Huang, C. F. *et al.* Prestrained effect on the emission properties of InGaN/GaN quantum-well structures. *Appl. Phys. Lett.* **89,** (2006).

39.   Huang, C. F. *et al.* Enhanced efficiency and reduced spectral shift of green light-emitting-diode epitaxial structure with prestrained growth. *J. Appl. Phys.* **104,** (2008).

40.   Liu, L. *et al.* Influence of indium composition in the prestrained InGaN interlayer on the strain relaxation of InGaN/GaN multiple quantum wells in laser diode structures. *J. Appl. Phys.* **109,** (2011).

41.   Leonard, J. T. *et al.* Highly smooth e-beam deposited tin-doped indium oxide (ITO) for III-nitride vertical- cavity surface-emitting lasers. *J. Appl. Phys.* **XX,** Under Review (2015).

42.   Pan, C. C. *et al.* Vertical stand transparent light-emitting diode architecture for high-efficiency and high-power light-emitting diodes. *Jpn. J. Appl. Phys.* **49,** (2010).

43.   Laubsch, A. *et al.* Luminescence properties of thick InGaN quantum-wells. *Phys. Status Solidi Curr. Top. Solid State Phys.* **6,** 885–888 (2009).

44.   Gardner, N. F. *et al.* Blue-emitting InGaN-GaN double-heterostructure light-emitting diodes reaching maximum quantum efficiency above 200 A cm2. *Appl. Phys. Lett.* **91,** 243506 (2007).

45.   Zhao, W., Wang, L., Wang, J., Hao, Z. & Luo, Y. Theoretical study on critical thicknesses of InGaN grown on (0001) GaN. *J. Cryst. Growth* **327,** 202–204 (2011).

46.   Park, Y. M., Son, J. K., Chung, H. J., Sone, C. & Park, Y. InGaN multiquantum well structure with a reduced internal electric field and carrier decay process by tunneling. *Appl. Phys. Lett.* **95,** 231917 (2009).

47.   Jho, Y., Yahng, J. & Oh, E. Field-dependent carrier decay dynamics in strained InGaN/GaN quantum wells. *Phys. Rev. B* 1–11 (2002). doi:10.1103/PhysRevB.66.035334

48.   Im, J., Kollmer, H. & Off, J. Piezoelectric Field Effect on Optical Properties of GaN/GaInN/AlGaN Quantum Wells. *MRS* **537,** 2–7 (1998).

49.   Renner, F. *et al.* Quantitative analysis of the polarization fields and absorption changes in InGaN/GaN quantum wells with electroabsorption spectroscopy. *Appl. Phys. Lett.* **81,** 490 (2002).

50.   Schulz, T. *et al.* Recombination dynamics in InxGa1−xN quantum wells— Contribution of excited subband recombination to carrier leakage. *Appl. Phys. Lett.* **105,** 181109 (2014).

6

Germanium Doping of GaN

6.1 Motivation and Background for Germanium Doping

6.1.1 Motivation for Heavy Doping

Efficiency droop significantly limits the performance of nitride LED devices (see Section 1.3.3 for more details on droop). The phenomenon is defined as a reduction in IQE with increasing drive current. Droop worsens as the InN fraction of the InGaN QWs in the active region of the LED increases, but higher indium content is necessary for decreasing the bandgap of the QW and emitting longer wavelength light.[1] High power LED operation and efficient green LEDs for white lighting applications are significantly hampered by droop.

Nitride LEDs grown on the (0001) plane of GaN suffer from large polarization discontinuities at heterojunction interfaces between InGaN QWs and GaN barriers (see Chapter 1, Section 1.1.3). Polarization sheet charges lead to large electric fields in the QWs, where they spatially separate the electron and hole wavefunctions, reducing wavefunction overlap and consequently reducing the rate of recombination (radiative and non-radiative)

(see Section 5.1).[2] A reduction of recombination rate results in a higher carrier density in the QWs for a given drive current density. According to the ABC model of carrier recombination, $J = An + Bn^2 + Cn^3$, an increase in carrier density will increase the Auger recombination rate (Cn^3) by a factor of n more than the radiative recombination rate (Bn^2). If you are operating in the droop regime, at current densities above the maximum efficiency of the LED, the fraction of nonradiative recombination will increase, and IQE will decrease. This is the process by which polarization-induced electric fields in InGaN QWs cause LED droop. Higher indium content QWs (longer wavelength emission) have higher electric fields and will experience more droop. To reduce efficiency droop and enable longer wavelength, higher power LEDs for efficient lighting applications, these polarization fields must be eliminated.

Rather than reducing QW polarization fields by growing on nonpolar or semipolar planes of GaN,[3–7] which involve using much smaller and more expensive substrates, or by using AlInN /InGaN QWs in a "polarization-matched" active region,[8,9] which would add significant growth complications, it would be preferable to grow InGaN/GaN QW LEDs on c-plane. Since the net polarization field in blue c-plane InGaN QWs is in the opposite direction of the built-in electric field of the p-n junction, doping profiles can be designed to effectively screen the polarization field. Polarization field screening through heavy doping was first proposed by Fiorentini and Bernardini,[10] and it has been demonstrated experimentally in nitride LEDs and solar cells.[11–15] A diminished electric field allows for the growth of a thicker single QW active region without a loss of wavefunction overlap, which would further reduce carrier density and decrease droop. It was shown through extensive simulation that high doping density in excess of 7E19 cm^{-3} is necessary to fully screen the

polarization field in a blue-emitting SQW LED (see Section 5.2). These very high n-type dopant densities may present new growth challenges, which will be described below.

6.1.2 Germanium vs. Silicon for n-Type Doping of GaN

Effective n-type dopants must have low enough ionization energy for full ionization at room temperature. The only impurity elements that act as shallow donors in GaN are silicon, germanium, oxygen, and selenium.[16] The donor ionization energies of Si and Ge in GaN are both 19 meV, shallow enough to be fully ionized at room temperature regardless of dopant concentration.[17] Silicon has been the n-type dopant of choice in III-N devices since their first development in the early 1990s. Silicon and germanium doping of high quality MOCVD-grown GaN layers were first demonstrated by Nakamura *et al*. in 1992.[18] It was found that the incorporation efficiency of germanium was ten times less than that of silicon with those particular growth conditions. Until recently there have been few additional reports of Ge-doping of III-nitrides, by either MBE or MOCVD,[19,20] but no advantage over Si-doping was reported.

The extremely high doping densities required to fully screen piezoelectric polarization related electric fields on *c*-plane may require a different n-type dopant than Si, which has been shown to add tensile stress to the III-N film during growth.[21–27] There is some disagreement over the exact mechanism, but it is generally accepted that edge-type dislocation climb is responsible for the increase in tensile stress. Some claim the climb is driven by surface roughness,[24–26] others that it is due to SiN masking of the dislocation core.[27] It has been shown that Ge-doped GaN does not develop additional stress during growth, due to its negligible effect on dislocation climb compared to Si-doping.[28,29] There is
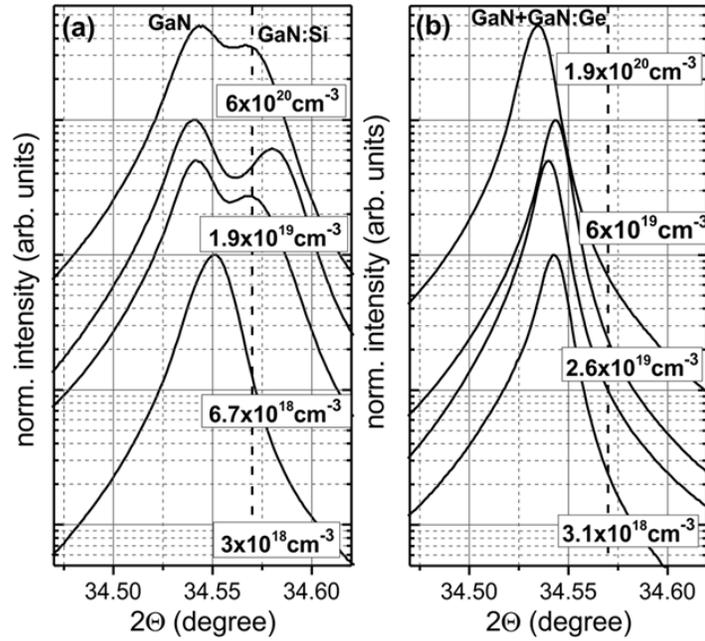
Figure 6.1: GaN (0002) XRD peaks in ω/2Θ scans for layers with (a) Si-doping with carrier concentrations ranging from 3 x 10^{18} cm^{-3} to 6 x 10^{20} cm^{-3}, and (b) G-doping with carrier concentrations ranging from 3 x 10^{18} cm^{-3} to 6 x 10^{20} cm^{-3}. The dashed vertical line marks the 2Θ angle for relaxed GaN. Figure from Fritz *et al.*[29]

also an opposing view that Ge-doping does increase GaN layer tensile stress due to vacancy generation triggered by the Fermi level and leading to dislocation climb, but this result has not been duplicated.[30]

Fritz *et al.* demonstrated that high concentrations of Si will add significant strain, but that similar concentrations of Ge will not, by performing XRD scans of the (0002) GaN peak for MOCVD grown 1 μm layers doped with Si and Ge up to concentrations of 6E20 cm^{-3} and 1.9E20 cm^{-3} respectively (Fig. 6.1).[29] The GaN:Si peaks broaden and develop a second peak above a concentration of [Si] = 3E18 cm^{-3}, indicative of two GaN layers with different strain: the undoped GaN template and the Si-doped layer. On the other hand, the GaN:Ge peaks do not broaden, maintaining a coherent, compressively stressed surface for all doping levels. GaN:Si layers with a concentration above 6.7E18 cm^{-3} were also found to be relaxed, causing significant morphological breakdown, as seen in Fig. 6.2, which shows
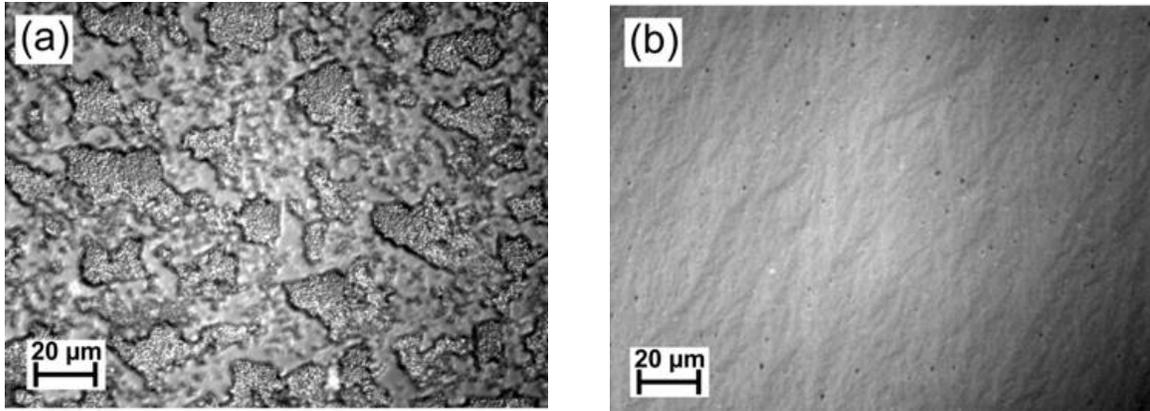
171

Figure 6.2: Nomarski microscope images of (a) a Si-doped GaN surface, and (b) a Ge-doped GaN surface with a carrier concentration of ~6 x 10^{19} cm^{-3}. Figure adapted from Fritz *et al.*[29]

optical micrographs of GaN:Si and GaN:Ge surfaces with a carrier concentration of 6E19 cm^{-3}. The Ge-doped GaN surface is much smoother at a carrier concentration close to the 7E19 cm^{-3} level that should achieve polarization field screening in blue SQW LEDs (see Chapter 5). Controllable high levels of Ge-doping have been demonstrated for plasmonic applications[31] as well as polarization field screening in AlN/GaN nanowire superlattices grown by MBE.[32,33] They found no solubility limits for Ge in GaN up to a concentration of 3.3 x 10^{20} cm^{-3}.

6.2 MOCVD Growth of GaN:Ge

The well-behaved precursor gas disilane (Si$_2$H$_6$) has traditionally been used as a silicon source for n-type doping of GaN during MOCVD growth.[34] It incorporates linearly with mole fraction ratio of Si$_2$H$_6$ to the Ga source TMGa, and, unlike SiH$_4$, its incorporation is not temperature dependent at reduced temperatures typical of active region growth (~800°C). For effective n-type doping with germanium, a Ge source with similar characteristics should be used. Germanium doping has been previously demonstrated by

MOCVD using germane (GeH$_4$) as the Ge source.[18,31] Also, Ge doping of bulk GaN films

has been demonstrated by HVPE using GeCl$_4$ as the dopant source.[35]

For MOCVD growth of all GaN:Ge films described in this chapter, a new source

bubbler was installed on a custom Nippon-Sanso two flow MOCVD system: isobutyl

germane (IBGe). IBGe is a liquid metalorganic compound with a high vapor pressure (155

torr at 25°C) and low cracking temperature (350°C), making it well suited to nitride growth

on this system.[36,37] It is not pyrophoric, much less toxic and expensive than GeH$_4$, does not

have problems with premature decomposition like GeH$_4$, and readily cracks at nitride

growth temperatures unlike other Ge-containing metalorganic compounds such as trimethyl

and monomethyl GeH$_4$. IBGe has also been used for MOCVD growth of germanium

films.[38,39] It has more importantly been demonstrated to achieve Ge incorporation in GaN

above 1E20 cm^{-3}.[29] Vapor pressure curves of IBGe have not been published, but with two

published data points of vapor pressure and bubbler temperature, a relationship can be fit:

$$\log P_{vap} = A - \frac{B}{T},$$ (6.1)

where A and B are fitting parameters, T is the bubbler temperature, and P_{vap} is the vapor

pressure of the metalorganic gas in the bubbler. The two published data points that were

used to determine A and B were (P_{vap}, T) = (155 torr, 25°C) and (45 torr, 0°C).[36] Once the

vapor pressure is known at the particular bubbler temperature (3°C in this case), the molar

flow rate of the source gas can be calculated as follows (assuming the ideal gas law):

$$\dot{N} = \dot{V}\left(\frac{P_{vap}}{P_{bub}}\right)\left(\frac{P_{bub}}{RT}\right),$$ (6.2)

where $\dot{V}$ is the volumetric flow rate usually given in standard cubic centimeters per minute

(sccm), P_{bub} is the total pressure of gas in the bubbler, R is the ideal gas constant, and T is

IBGe flow (sccm)	RMS Roughness (nm)	Carrier Density (cm^{-3})	Mobility (cm^2/Vs)
0.06	0.35	8.77 x 10^{17}	337
0.2	0.34	5.32 x 10^{18}	215
0.4	2.85	1.24 x 10^{19}	163
2.0	1.73	4.18 x 10^{19}	135
10.0	14.8	1.29 x 10^{20}	109

Table 6.1: Summary of continuously doped 300 nm GaN:Ge layer characteristics for different IBGe flow rates: RMS surface roughness measured by AFM, carrier density and mobility measured by Hall Effect measurement. Layers were grown on top of 4 μm of insulating GaN at 1180°C, with a TMGa flow of 15 sccm, a growth rate of 8 Å/s, and with H$_2$/N$_2$ mixed carrier gas.

the temperature of the bubbler. In this case, the IBGe source is kept at 3°C, with a vapor pressure of 52.8 torr.

During MOCVD growth of GaN:Ge layers, a precursor containing Ga (TMGa or TEGa), a precursor containing N (NH3), and a precursor containing Ge (IBGe) are injected into the reactor chamber (see Chapter 2). These precursor gasses are mixed with H$_2$ and/or N$_2$ carrier gas and directed to flow over the substrate material, which is heated to between 500°C and 1200°C during growth. Over most of the relevant range of growth rates and temperatures, the concentration of Ge in the GaN:Ge film is proportional to the molar flow ratio of IBGe to TMGa over the full range of bubbler flow rates (Fig. 6.4). In this case, when IBGe flow rates were varied over the full range of the mass flow controller from 0.06 sccm to 10 sccm (0.14 to 23.8 μmole/min) with a TMGa flow rate of 15 sccm (54.1 μmole/min) (molar flow ratios of Ge to Ga ranging between 0.0026 and 0.44), resulting carrier concentrations[i] from Hall Effect measurements (Section 6.3) ranged between 8.8E17 cm^{-3} to 1.3E20 cm^{-3}, respectively. Table 6.1 summarizes the carrier concentration, mobility,

---

[i] It is assumed that carrier concentration is equal to dopant incorporation because Ge is a shallow donor and should be fully ionized.

and surface roughness of the continuously doped 300 nm GaN:Ge layers for different IBGe flows.

Additionally, Ge incorporation was not affected strongly by temperature between 800°C and 1200°C, as long as the layer growth remained in the mass flow limited regime.[i] There was only a slight decrease in [Ge] from 1.24E19 cm^{-3} to 9.47E18 cm^{-3} when going from 1180°C to 870°C. There was also negligible effect on incorporation from changes in NH$_3$ flow between 3.2 and 7.0 standard liters per minute (slm) or growth rate between 1 Å/s and 8 Å/s with a constant molar flow ratio.

Ge can also be introduced via a pulsed flow of IBGe, where the Ga containing carrier gas flow remains uninterrupted. A pulsed doping scheme allows the incorporation of high concentrations of dopant while maintaining a relatively smooth surface morphology. Delta doping of Si in GaN was first demonstrated in 1999 as an extension of Si delta doping in GaAs to improve field effect transistor mobility.[40,41] Periodic delta doping of Si in GaN layers have been shown to reduce dislocation density by causing bending and annihilation of screw dislocations of opposite Burgers vectors.[42] Also, periodic delta doping of Si has resulted in a reduction of tensile stress and surface roughness,[43] as well as a reduction in yellow luminescence and no variation of film stress with increasing electron concentration.[44] Pulsed doping of Mg in p-GaN layers improved doping efficiency and p-GaN mobility.[45] Incorporating both n- and p-type delta doped layers above and below a UV LED active region led to improved surface morphology, dislocation density, and device performance.[46]

All pulse-doped layer were grown at 1000°C with a constant flow of NH$_3$ and a TEGa flow of 35 sccm (8.05 μmole/min, growth rate of 1.1 Å/s) while modulating the flow

---

[i] As opposed to the kinetically limited regime at low temperatures/high growth rates, or the desorption limited regime at high temperatures/low growth rates.

Pulse Periods	Pulse Time (sec)	Duty Cycle	Layer thickness (nm)	Substrate	RMS Roughness (nm)	Carrier Density (cm^{-3})	Mobility (cm^2/Vs)
50	10	50%	110	Sapp	18.1	1.05×10^{20}	81
50	10	50%	110	PSS	5.48	1.03×10^{20}	117
40	5	50%	45	PSS	3.18	1.04×10^{20}	106
20	10	50%	45	PSS	2.58	1.00×10^{20}	103
10	10	25%	45	PSS	2.76	8.43×10^{19}	113

Table 6.2: Summary of pulse-doped GaN:Ge layer characteristics with different number of IBGe pulse periods, pulse lengths, and duty cycles: RMS surface roughness measured by AFM, carrier density and mobility measured by Hall Effect measurement. Samples were grown on either unpatterned sapphire substrates or PSS. GaN:Ge layers were grown on top of 4 um of insulating GaN at 1000°C, with a modulated IBGe flow rate of 0.1 sccm, a continuous TEGa flow rate of 35 sccm, a constant growth rate of 1.1 Å/s, and with N_2 only carrier gas.

of IBGe, either by opening and closing the line valve to the gas manifold, or by turning on and off the mass flow controller (MFC). Cycling of the MFC would preserve the life of the valve over a large number of iterations, but it was found to adversely affect surface morphology, likely due to slower ramping affecting the interfaces between doped and undoped layers (see Section 6.4.2). IBGe flow was either 0.05 sccm (0.12 µmole/min) or 0.1 sccm (0.24 µmole/min), and each cycle consisted of 10 or 20 seconds with the IBGe flow open followed by 10-30 seconds with the IBGe flow closed. The number of periods varied from 50 x [10 sec on, 10 sec off] for a total thickness of 110 nm, to 10 x [10 sec on, 30 sec off] for a total thickness of 45 nm. Growth in the presence of H_2 improved surface roughness but also decreased Ge incorporation significantly, canceling out the morphology benefit. This was likely the result of H_2 induced dynamic GaN etching.[47]

Table 6.2 summarizes the carrier concentration, mobility, and surface roughness of the pulse-doped GaN:Ge layers for different number of periods, IBGe flow time, and duty cycle. The expected trend would probably be Ge incorporation proportional to duty cycle, but when the duty cycle doubles, the carrier concentration only increases by a factor of 1.2.

In fact, when comparing 50 x [10 sec on, 10 sec off] 110 nm layer with an IBGe flow of 0.1 sccm and an *average* molar flow ratio over the entire layer of 0.015, to a continuously doped layer from Table 6.1 with the same *average* molar flow ratio, the expected carrier concentration would be 2-3E19 cm^{-3} instead of 1E20 cm^{-3}. It is difficult without additional high resolution TEM or atom probe tomography analysis to assess what the actual average Ge concentration is, and how the correlation between carrier concentration and [Ge] might differ between continuously doped and periodically doped layers.

There are other ways to arrange the pulsed doping scheme that might have different effects but have not been tried. In the continuous growth scheme described above, there is a broad range of conditions that remain unexplored. With a 50% doping duty cycle and the IBGe MFC being operated near its minimum controllable flow rate, which is ~2% of the maximum flow rate of 3 sccm, the measured carrier concentration was still above 1E20 cm^{-3}. Increasing the IBGe flow rate and decreasing the duty cycle substantially may be an improvement, though little effect was seen, on Ge incorporation, morphology, or mobility when keeping the same IBGe flow and going from 50% to 25% duty cycle. One could also modulate both the Ga source and IBGe flows, either on the same schedule or on alternating schedules. In this case, growth would only occur while the Ga source is flowing. If IBGe flows without Ga, it will likely form a wetting layer of Ge on the growth surface that will be incorporated in the GaN film during the subsequent Ga flow step.

6.3 GaN:Ge Electrical Characteristics

Figure 6.3 shows the epitaxial structure grown by MOCVD that was used to characterize GaN:Ge layers electrically and morphologically via Hall Effect measurements,
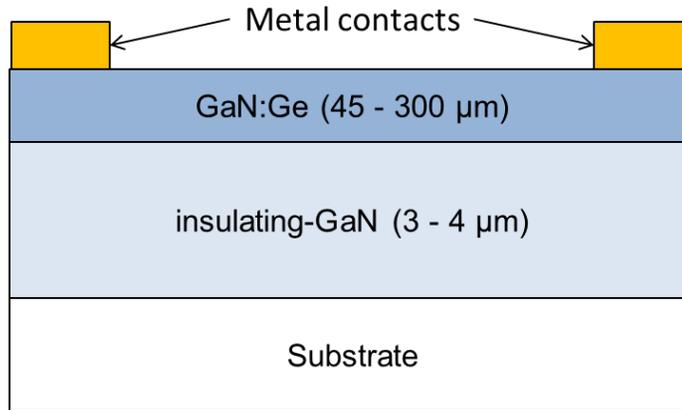
Figure 6.3: Schematic of the epitaxial structure used for characterization of GaN:Ge layers by Hall Effect measurement, AFM, and c-TLM.

circular transmission line measurements (c-TLM), and AFM. The first micron of the GaN template was doped with Mg, but left unactivated, to ensure a completely insulating buffer, which was verified. Hall Effect measurements were performed using indium contacts in a van-der-Pauw geometry. Indium dots were placed in the corners of a ~1 cm^2 sample scribed out from the original 2" wafer after growth. For c-TLM measurements, metal contact was made with e-beam-deposited Ti/Au, 30/300 nm in thickness, respectively. Spacings between the inner and outer rings (r) of the c-TLM patterns were 5, 10, 15, 25, 50, and 75 μm, and the radius of the inner ring (g) was 40 μm. Resistances were extracted from I-V characteristics that were measured by the four-point-probe method. They were linear with TLM spacing, and the contacts were ohmic for average dopant concentrations above 4E19 cm^{-3}. Resistances for non-ohmic I-V characteristics were taken at a reasonable operating condition of 100A/cm^2. The linear approximation with correction factors was used to calculate contact resistivity (R_c) and sheet resistance (R_{sh}).[48–50] Even though the necessary assumption for simplification that $r \gg g$ is not met in this case, the linear fit after correction factors were applied was highly linear, and the expected error is less than 10%.
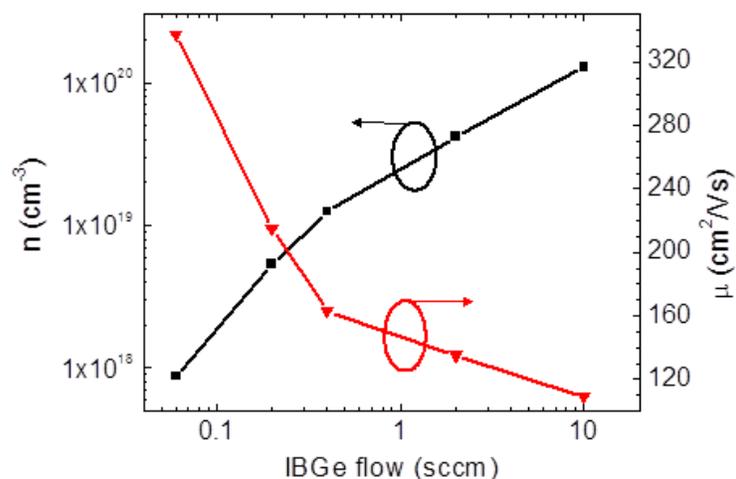
Figure 6.4: Hall Effect measurement results of carrier concentration (n) and mobility (μ) as a function of IBGe volumetric flow rate for MOCVD-grown GaN:Ge layers. Layers were 300 nm thick, continuously doped, and grown at 1180°C and at a growth rate of 8 Å/s with TMGa as the Ga source (15 sccm). Sample details can be found in Table 6.1.

In addition to achieving high carrier concentrations in excess of 1E20 cm^{-3}, the GaN:Ge layers also maintained relatively high mobility. Figure 6.4 shows the carrier concentration (n) and mobility (μ) derived from Hall effect measurements on 300 nm thick layers of GaN:Ge on top of an insulting GaN template as a function of IBGe flow (values and growth parameters in Table 6.1). Once again, the carrier concentration is assumed to be equal to the Ge concentration. IBGe flow rates were varied in the study from 0.06 sccm to 10 sccm. Molar flow ratios of Ge to Ga ranged between 0.0026 and 0.44, and resulting carrier concentrations (Ge concentrations) ranged between 8.8E17 cm^{-3} to 1.3E20 cm^{-3}, respectively. Over that range of carrier concentrations, the mobility ranged from 337 to 109 cm^2/Vs. A pulse-doped sample grown on PSS had a mobility of 117 cm^2/Vs (Table 6.2).
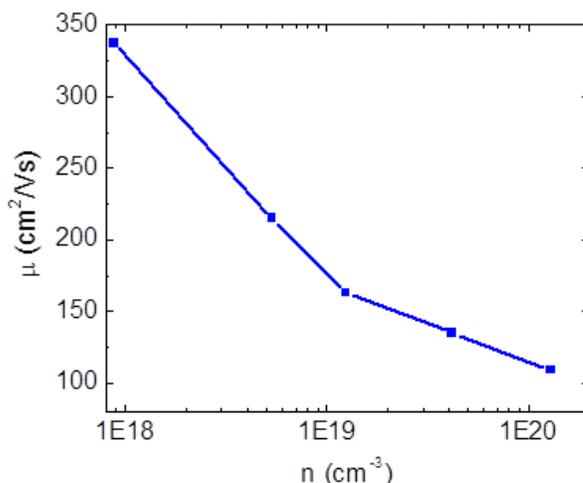
179

Figure 6.5: Hall mobility (μ) vs. carrier concentration (n) for continuously doped 300 nm GaN:Ge layers with different IBGe flows. Samples details can be found in Table 6.1.

Figure 6.5 shows the product of n and μ. The point at the bottom right of this plot represents a record $n*\mu$ product,[i] higher that the best demonstrated by MOCVD Si-doped GaN, although there have not been many attempts to grow highly Si-doped GaN layers by MOCVD.[34] It is possible that the greater similarity in size of Ga to Ge atoms, compared to Si atoms, results in less lattice scattering, hence the slight increase in mobility. It's also worth noting that highly Si-doped MBE grown GaN has achieved slightly higher μ above n = 1E20 cm^{-3}.[51] Regardless, Ge-doping could present an avenue toward increased performance in MOCVD-grown high speed/high power III-N electronics.

Figure 6.6(a) shows the measured bulk resistivity (ρ) from Hall measurements and TLM for GaN:Ge layers of varying thickness and dopant concentration grown with both continuous and pulsed doping. Values from Hall and TLM measurements agree closely. Resistivity decreases with increased Ge doping as expected, down to a minimum value (measured by Hall) of 4.4E-4 Ωcm at a carrier concentration of 1.3E20 cm^{-3}, corresponding
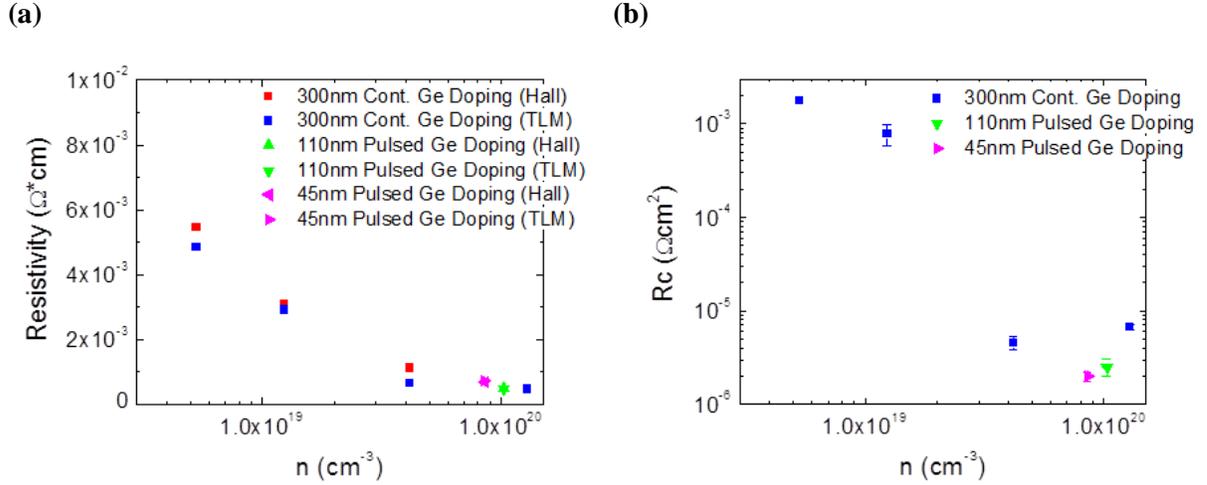
---

[i] Equivalent to conductivity

Figure 6.6: (a) Bulk resistivity as a function of carrier concentration measured by both Hall Effect and c-TLM and (b) contact resistance measured by c-TLM for 300 nm continuously doped GaN:Ge layers and pulse-doped GaN:Ge layers of 110 and 45 nm thickness. All layers were grown on sapphire substrates and 4 μm of insulating GaN. The 110 nm pulse-doped layer had 10 second pulses of IBGe flow and a 50% duty cycle, while the 45 nm pulse-doped layer had 10 second IBGe pulses and a 25% duty cycle. Sample details can be found in Tables 6.1 and 6.2.

to a R_{sh} of 14.8 Ω/□ for the 300 nm layer. Bulk resistivity values for the pulsed-doped samples are nearly identical. Sheet resistances measured in typical Si-doped layers 2-4 μm thick are usually near or slightly below 20 Ω/□, which corresponds to ρ in the mid 10^{-3} Ωcm. Highly Ge-doped films have bulk resistivities an order of magnitude lower. It stands to reason that a several micron thick Ge-doped layer would achieve much lower sheet resistance and hence better current spreading than the Si-doped n-GaN in typical LEDs, as long as good material quality could be maintained.

Figure 6.6(b) shows the measured R_c from c-TLM measurements for GaN:Ge layers of varying thickness and dopant concentration grown with both continuous and pulsed doping. The samples showed the expected trend of lower R_c with higher n-doping. At high doping near 1E20 cm^{-3}, continuously doped samples had higher R_c than pulse-doped samples due to a large increase in surface roughness (see Table 6.1). The pulse-doped samples had much smoother surfaces with similarly high carrier concentrations (see Table

6.2), leading to superior contact resistance, as low as 2E-6 Ωcm^2. This result is near the range of the lowest reported contact resistances to n-GaN.[52]

6.4 GaN:Ge Structural Characteristics

6.4.1 Continuously Doped Layer Morphology

The surface morphologies of the 300 nm GaN:Ge films grown for Hall measurements (see Section 6.3) were also characterized by AFM. The AFM micrographs for the IBGe flow series are shown in Fig. 6.7, and the electrical characteristics and growth parameters can be found in Table 6.1. There is a marked increase in root mean square (RMS) surface roughness from 0.34 nm to 14.8 nm as the Ge concentration increases from 5.3E18 cm^{-3} to 1.3E20 cm^{-3}. The surface in Fig. 6.7(a) is indicative of a typical undoped or moderately Si-doped high temperature GaN template. Pits begin to form when [Ge] goes above 1E19 cm^{-3}, and then step-bunching is evident at above [Ge] = 4E19 cm^{-3}. Finally, above [Ge] = 1E20 cm^{-3}, the growth is totally three dimensional, with a network of relatively flat plateaus and valleys.

The GaN:Ge layer in an LED device for the purpose of polarization screening does not need to be 300 nm thick; it only needs to be 10 nm thick. Another series of GaN:Ge layers was grown and investigated by AFM with thicknesses decreasing from 300 nm to 10 nm and growth conditions identical to the sample in Fig. 6.7(d) and Ge concentration measured by Hall of [Ge] = 1.6E20 cm^{-3}. Figure 6.8 shows the AFM micrographs for samples in the GaN:Ge layer thickness series. The same plateau/trench morphology that was seen in Fig. 6.7(d) is evident for all thicknesses in Fig. 6.8, even as the RMS roughness decreases from 14.6 nm to 3.3 nm as the nominal layer thickness decreases from 300 nm to
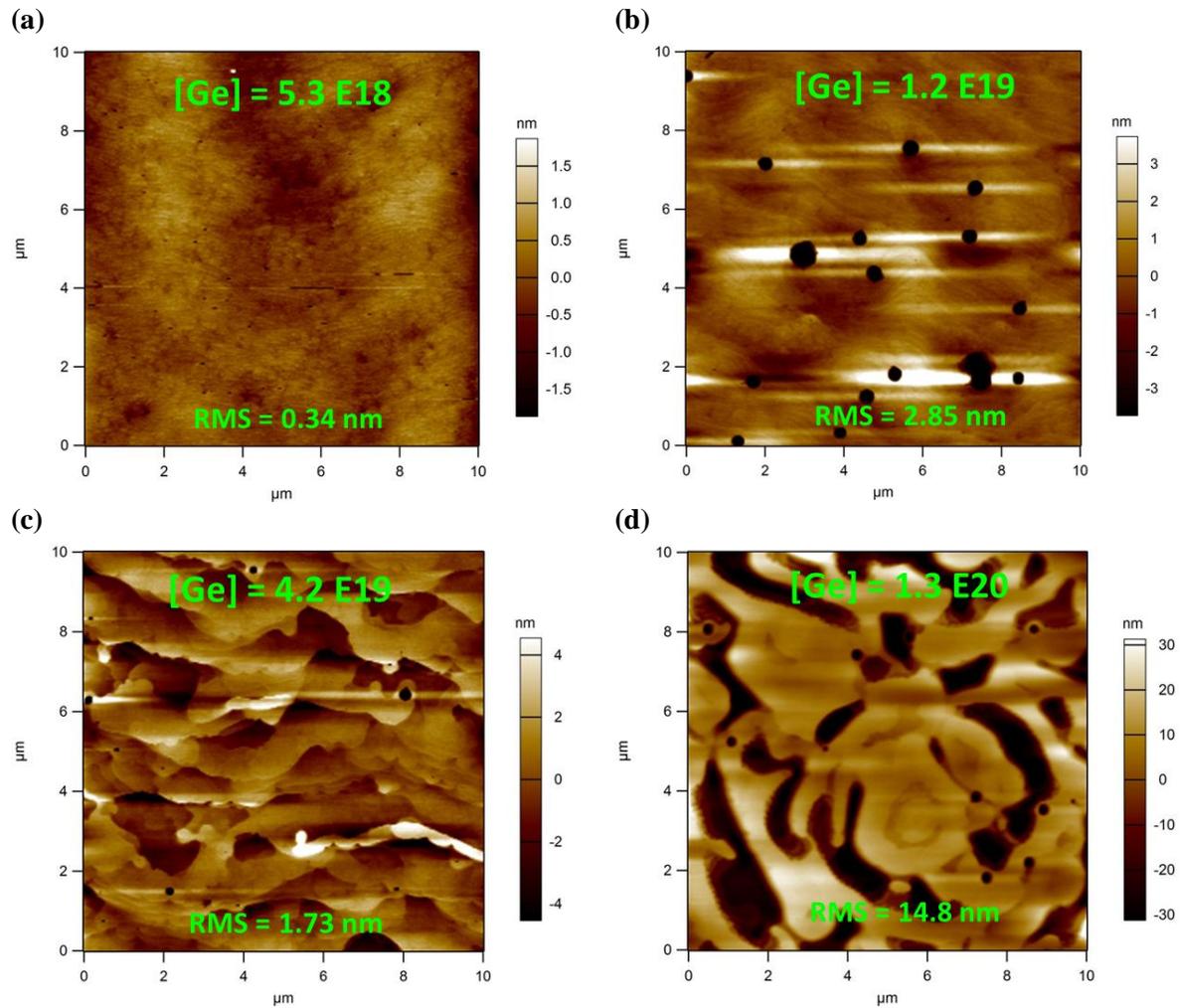
Figure 6.7: AFM micrographs of 300 nm continuously doped GaN:Ge layers with Ge concentrations of (a) 5.3×10^{18} (b) 1.2×10^{19} (c) 4.2×10^{19} (d) 1.3×10^{20}. RMS stands for root-mean-square roughness. Sample details can be found in Table 6.1.

10 nm. The size of the plateaus and the spacing between them decreases as layer thickness decreases, and the peak-to-trough difference is always on the order of the nominal layer thickness. This rules out an explanation of a buildup of stress because the three dimensional morphology begins right from the start of GaN:Ge layer growth when the concentration is near 1E20 cm^{-3}. Wide range XRD scans have not identified a different phase or material that might be present in these plateau regions. The nature of the plateau regions and the growth mechanics that lead to their formation are at this point still not understood.

183

Figure 6.8: AFM micrographs of continuously doped GaN:Ge layers with Ge concentration of 1.6 x 10^{20} with thicknesses of (a) 10 nm (b) 40 nm (c) 100 nm (d) 300 nm. Layers were grown at 1180°C with an IBGe flow of 5 sccm, a TMGa flow of 15 sccm, a growth rate of 8 Å/s, and in H_2/N_2 carrier gas. RMS stands for root-mean-square roughness.

Additionally, surface morphology was not affected strongly by temperature between 800°C and 1200°C, though there are a few more pits and consequently larger RMS roughness when going from 1180°C (Fig 6.7(b)) to 870°C (Fig 6.9(a)). The morphology actually got worse going from H_2/N_2 mixed carrier gas (Fig 6.8(a)) to N_2 only (Fig 6.9(b)). The negative morphological effects going to lower temperature and N_2 carrier gas could be explained by the resulting lower surface atom mobility making it more likely that pits or

(a)

(b)

(c)
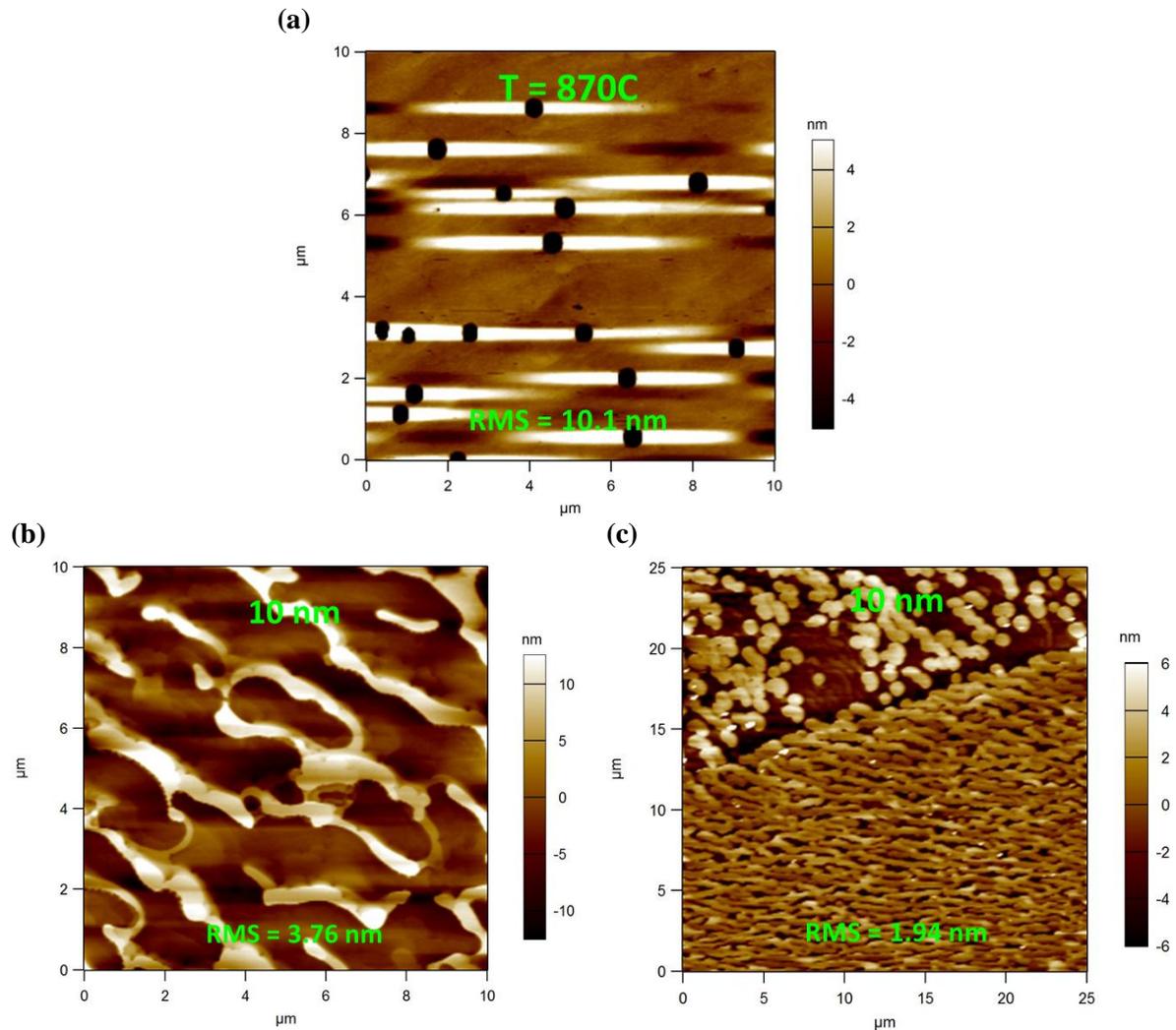
Figure 6.9: AFM micrographs of continuously doped GaN:Ge layers: (a) a 300 nm layer with Ge concentration of 9.5 x 10^{18}, grown at 870°C with an IBGe flow of 0.4 sccm, a TMGa flow of 15 sccm, and a growth rate of 8 Å/s; (b) a 10 nm layer with Ge concentration of ~1.5 x 10^{20}, grown at 1180°C with an IBGe flow of 5.0 sccm, a TMGa flow of 15 sccm, a growth rate of 8 Å/s, and grown with only N_2 carrier gas; (c) a 10 nm layer grown on a free standing GaN substrate with Ge concentration of ~1 x 10^{20}, grown at 1000°C with an IBGe flow of 0.4 sccm, a TMGa flow of 1.5 sccm growth rate of 1 Å/s. RMS stands for root-mean-square roughness.

plateaus will form. Changing substrate dislocation density (on free standing GaN with 3 x 10^6 cm^{-2} TDD and on sapphire with more than 5 x 10^8 cm^{-2} TDD) changed the character of the morphology, but not the scale of the roughness, though it is likely that the TDD has no

185

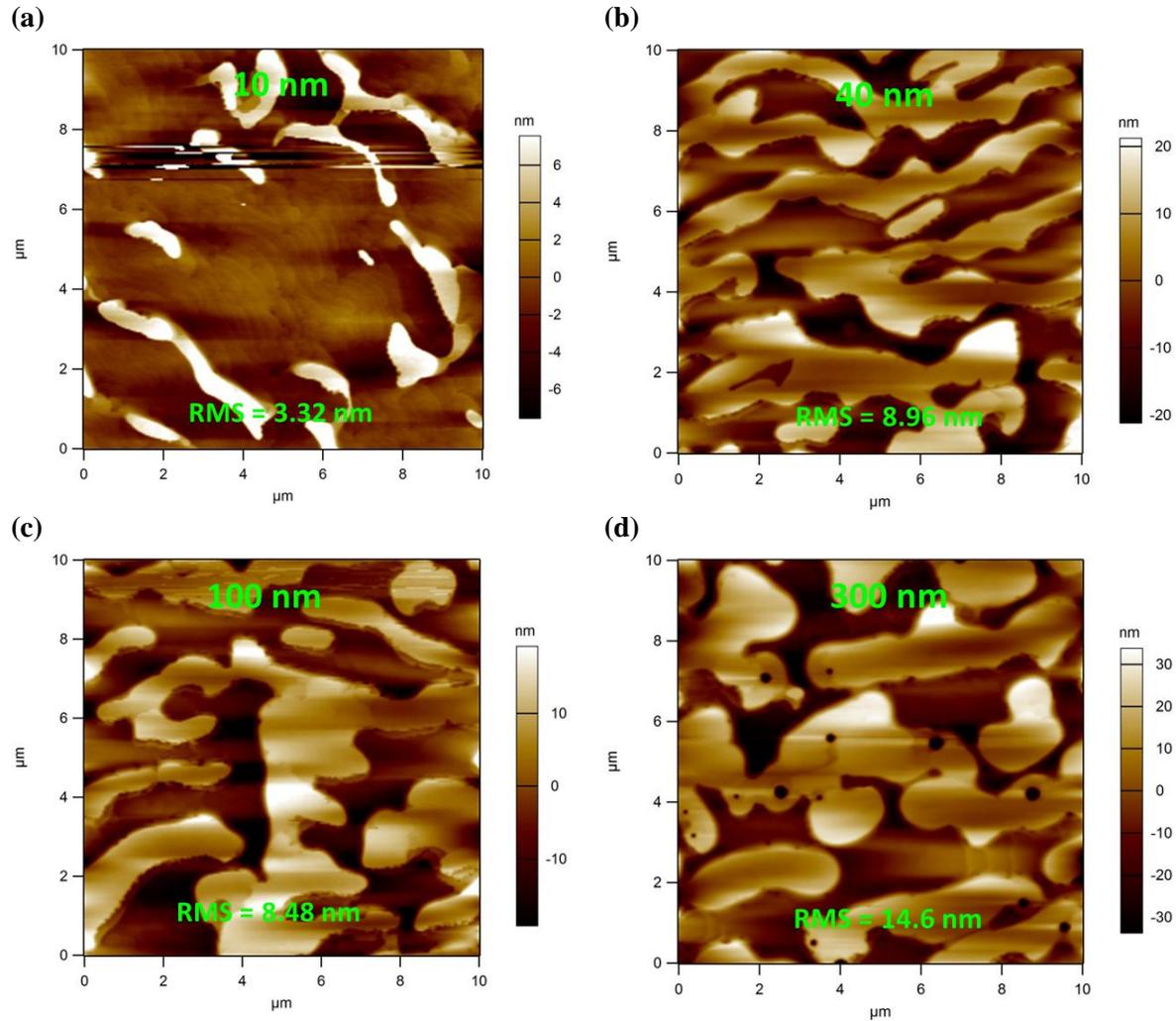**(a)**

(b)

(c)

(d)
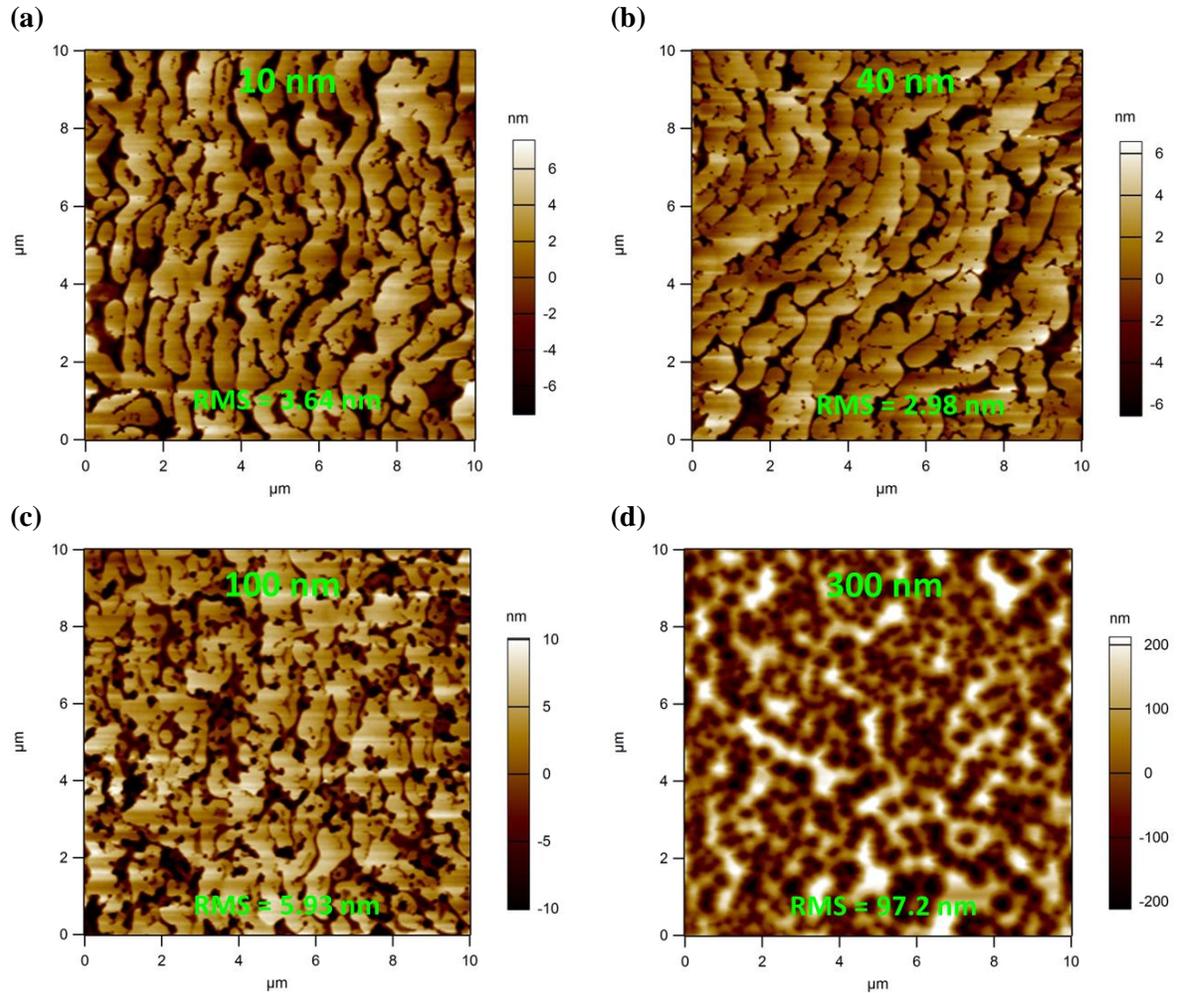
Figure 6.10: AFM micrographs of continuously doped GaN:Ge layers with Ge concentration of ~1 x 10^{20} with thicknesses of (a) 10 nm (b) 40 nm (c) 100 nm (d) 300 nm. Layers were grown at 1000°C with an IBGe flow of 0.4 sccm, a TMGa flow of 1.5 sccm, a growth rate of 1 Å/s, and in H_2/N_2 carrier gas. RMS stands for root-mean-square roughness.

affect (Fig. 6.9(c)). The change in surface step density between growth of bulk and sapphire substrates is likely responsible for what difference there is, and step-bunching and islanding are still evident.

Finally another GaN:Ge layer thickness series (10 nm to 300 nm) was grown at lower temperature (1000°C) and lower growth rate (1 Å/s) using TMGa as the Ga source (flow rate of 1.5 sccm, 5.4 μmole/min) and H_2/N_2 carrier gas. The temperature had to be reduced below 1100°C when lowering the TMGa flow to 1.5 sccm, or else desorption would

dominate and the growth rate would be essentially zero. The AFM scans from this series are shown in Fig. 6.10. Comparing to Fig 6.8, there are some differences although the roughness remains high even for thin layers. The plateaus appear to be smaller and spaced closer together. The roughness for the 40 nm and 100 nm layers is smaller than their counterparts in Fig. 6.8, but the 300 nm layer is far rougher. The lower growth rate does appear to be promoting a "spreading out" of the highly localized plateau regions, possibly because the atoms have more time to migrate on the surface. It is still far too rough for good device growth, however, and it is difficult to grow much slower than 1 Å/s without losing control of Ge incorporation because of the high vapor pressure of the IBGe bubbler and the unavailability of lower flow MFCs. The IBGe bubbler is already kept at 3°C and would have to be cooled far below freezing to make a significant difference in the vapor pressure and Ge incorporation, requiring reactor modifications.

6.4.2 X-Ray Diffraction

The continuously doped samples with varying IBGe flow rates shown in Table 6.1 were further characterized by high resolution XRD of the (0002) GaN reflection in an ω-2Θ configuration using a PANalytic MRD Pro diffractometer. Figure 6.11 shows the peaks of the GaN:Ge layers as well as that of a reference Si-doped GaN layer with the same doping concentration (~6 x 10^{18} cm^{-3}) used in standard n-GaN template layers. The reflections have been plotted on a relative 2Θ axis centered on the peak position of each scan so that they may be more easily compared. Whereas the scans of Fritz *et al.* over a similar range of Ge concentration show no peak splitting or appreciable broadening (Fig. 6.1(b)),[29] here a shoulder to the left of the main GaN peak, along with thickness fringes, appears at
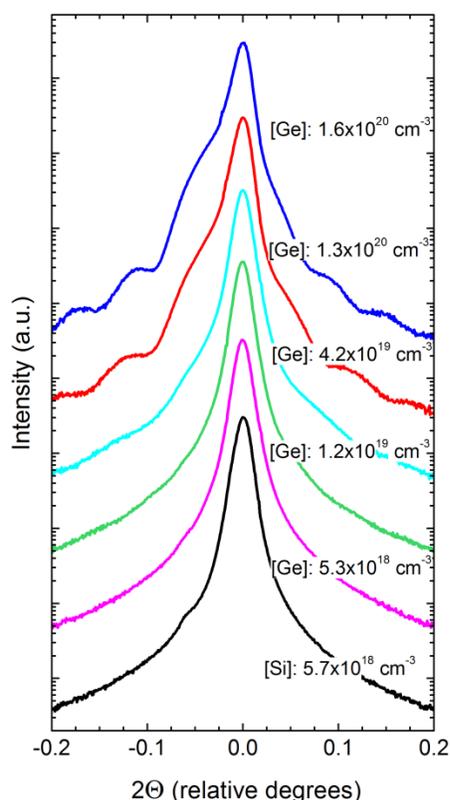
Figure 6.11: GaN (0002) XRD peaks in ω/2Θ scans for 300 nm GaN:Ge layers with Ge-doping concentrations ranging from 5.3 x 10^{18} cm^{-3} to 1.6 x 10^{20} cm^{-3}, and one GaN:Si layer with a Si-doping concentration of 5.7 x 10^{18} cm^{-3}. The dashed vertical line marks the 2Θ angle for relaxed GaN.

concentrations exceeding 4 x 10^{19} cm^{-3}. The shoulder appearing on the left of the main reflection peak indicates compressive strain in the GaN:Ge layer. There is no well-defined second peak, however, so the absolute amount of strain in the layer is clearly less than in the GaN:Si layers shown in Fig. 6.1(a). As discussed in Section 6.1.2, the mechanism for tensile strain evolution in GaN:Si layers is reasonably well understood. There is no existing theory for why the incorporation of Ge would add compressive strain to the layer. Evidence of compressive strain in the symmetric XRD scans of GaN:Ge layers corresponds with the onset of severe step bunching and three dimensional growth seen in the AFM scans in Fig. 6.7. Again, Fritz et al. saw no evidence of changing strain with increasing Ge concentration

and they observed smooth surfaces by optical micrograph (Fig. 6.2(b)). The surface quality of the highly strained GaN:Si layer they observed, on the other hand, was very poor (Fig. 6.2(a)). Clearly there is a correlation between strain buildup and morphological breakdown in highly doped films, whether the dopant is Si or Ge, and whether the strain is tensile or compressive. Further investigation will need to be done to determine the mechanism behind compressive strain evolution in GaN:Ge films.

6.4.3 Pulsed Doping Morphology

Pulsed doping can be used to achieve high doping concentrations with relatively smooth surfaces as described in Section 6.2. In an attempt to improve on the morphology of the continuous doped GaN:Ge layers, a pulsed Ge-doping scheme was developed with constant layer growth and IBGe flow modulation. Table 6.2 lists growth parameters, electrical characteristics, and RMS surface roughness for pulse-doped layers. Figure 6.12 shows AFM micrographs of 50 alternating doped and undoped 1.1 nm layers with an IBGe flow of 0.24 μmole/min and a TEGa flow of 8.05 μmole/min (molar flow ratio of 0.03) for 110 nm total thickness on co-loaded PSS and unpatterned sapphire substrates. The carrier concentration in the layers on each substrate was 1.0E20 cm^{-3}. The surface was much smoother on PSS, with an RMS roughness of only 5.5 nm compared to 18.1 nm on unpatterned sapphire. Most notably, the plateau morphology seen in the continuously doped layers is no longer evident. The plateaus have been replaced by a high pit density on the unpatterned sapphire, and some step bunching with a lower pit density on PSS. The difference between the co-loaded substrates is most likely due to the lower step edge density
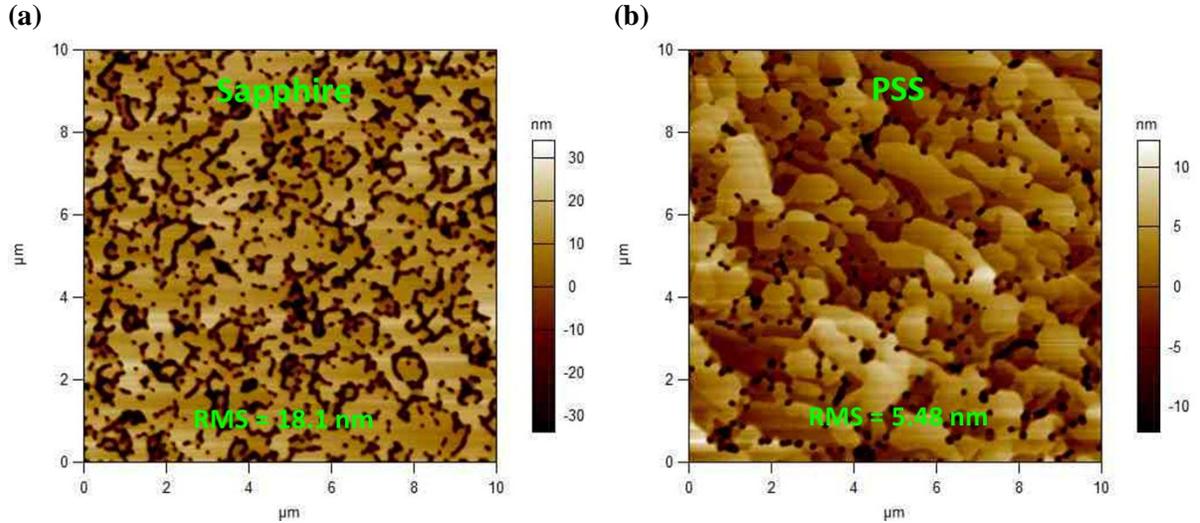
189

Figure 6.12: AFM micrographs of 110 nm pulse-doped GaN:Ge layers with carrier concentration of ~1 x 10^{20} measured by Hall Effect, grown on co-loaded (a) unpatterned sapphire and (b) PSS. RMS stands for root-mean-square roughness. Sample details can be found in Table 6.2.

seen in GaN on PSS. The lower roughness also led to better mobility and contact resistance in the pulse-doped layer.

Figure 6.13 shows AFM micrographs for a series of pulse-doped GaN:Ge layers with different IBGe flow times and duty cycles grown on PSS (see Table 6.2 for sample details). Each exhibited a "cauliflower-like" morphology indicative of step bunching, and with a few small pits. There was little difference in roughness between the samples with 10 sec/10 sec, 5 sec/5 sec, and 10 sec/30 sec IBGe flow on/off times in each pulse iteration. The sample in Fig. 6.13(a) had an identical pulse scheme to the sample in Fig. 6.12(b), but with 20 periods instead of 50 (45 nm total thickness). Decreasing the duty cycle to 25% by alternating 1.1 nm doped and 3.3 nm undoped layers for 45 nm total thickness resulted in a carrier concentration of 8.4E19 cm^{-3} and an RMS surface roughness of only 2.8 nm (Fig. 6.13(c)). Smoother surfaces with similar carrier concentrations should result in better performance for LEDs with GaN:Ge layers.

190
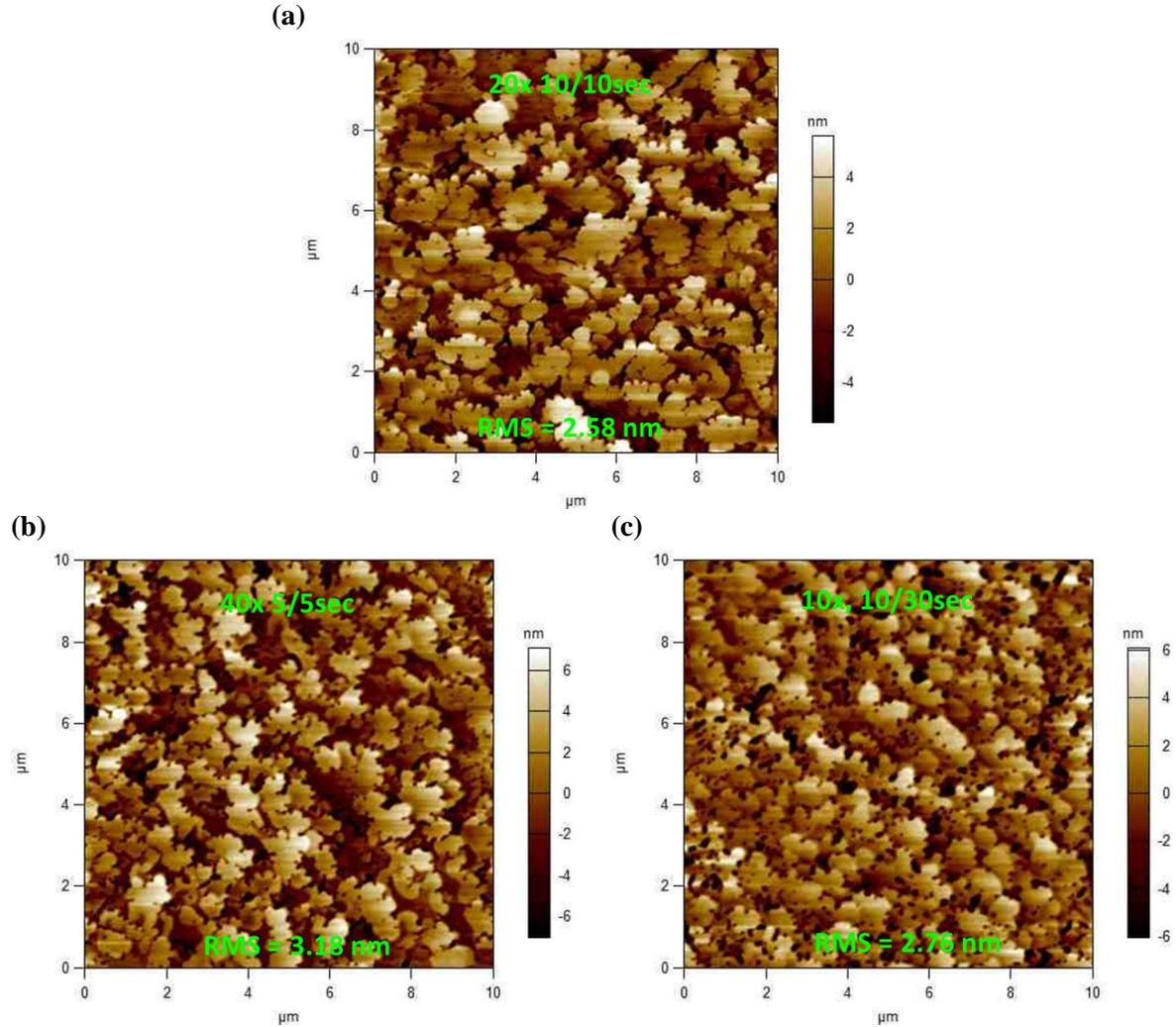
Figure 6.13: AFM micrographs of 45 nm pulse-doped GaN:Ge layers with carrier concentration of ~1 x 10^{20} measured by Hall Effect with different pulse schemes: (a) 20 x (10 sec. IBGe on/10 sec. IBGe off) (b) 40 x (5 sec. IBGe on/5 sec. IBGe off) (c) 10 x (10 sec. IBGe on/30 sec. IBGe off). RMS stands for root-mean-square roughness. Sample details can be found in Table 6.2.

Unfortunately, pulse-doped layers were not able to achieve good results in a polarization screened SQW LED device (Section 6.5.2). Figure 6.14 shows the unexpected result that a 10 nm pulse-doped GaN:Ge layer on PSS is actually rougher than a 10 nm GaN:Si layer with the same carrier concentration (nominally 7E19 cm^{-3}). Interestingly, the morphologies were completely different, with the Ge-doped layer exhibiting step-bunching and the Si-doped layer exhibiting dendritic step growth with a much larger total step area.

(a)   **(b)**
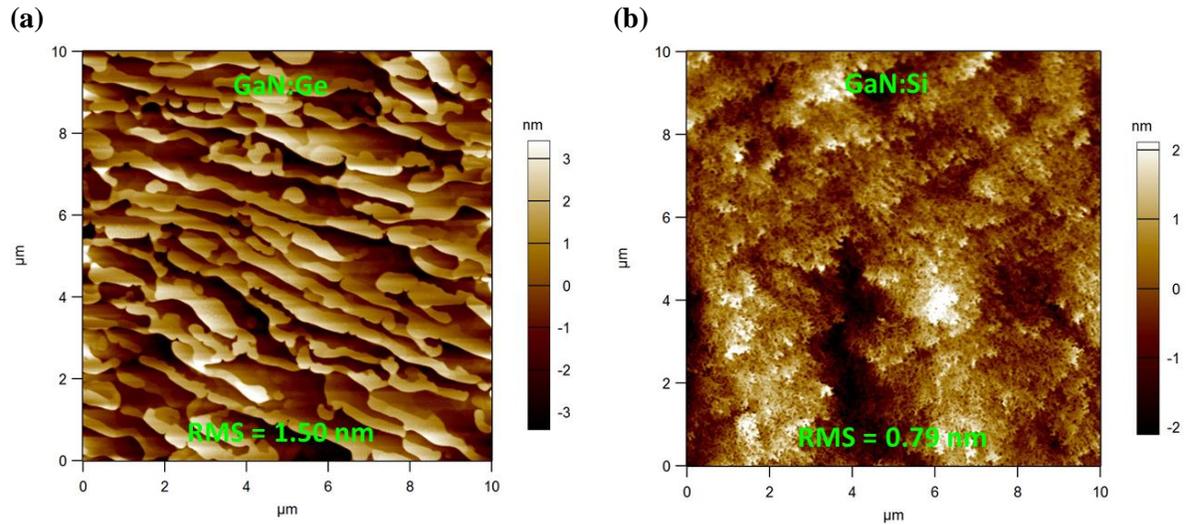
Figure 6.14: AFM micrographs of (a) a 10 nm pulse-doped GaN:Ge layer and (b) a 10 nm GaN:Si continuously doped layer, both with a carrier concentration of ~7 x 10^{19}. RMS stands for root-mean-square roughness.

6.5 Germanium Doping in LED Structures

6.5.1 GaN:Ge Layer Incorporated in a Standard LED Structure

The feasibility of Ge-doping in an LED structure was tested by including a Ge-doped layer 10 nm thick below a standard MQW blue-emitting active region. Figure 6.15 shows the results of a packaged LED with and without a layer with 1E20 cm^{-3} Ge concentration. Aside from the GaN:Ge layer, the structure of the blue-emitting MQW LED was identical to the one described in Section 5.3. This is the first demonstration of Ge doping in an LED. The *LIV* curve in Fig. 6.15(a) shows a significant improvement in both voltage and output power in the LED with the Ge-doped layer. Since the active region in this case is a MQW, we do not attribute the improved performance to field screening in the QWs, but instead to improved carrier injection and lateral current spreading on the n-side.

(a)   **(b)**

Figure 6.15: Packaged LED results comparing devices with a 10 nm GaN:Ge layer (doped ~1E20 cm^{-3}) beneath the MQW active region (6 periods of 3 nm $In_{0.15}Ga_{0.85}N$ QW/20 nm GaN barrier) and an identical device without the GaN:Ge layer: (a) *LIV* plot and (b) EQE vs. current density. Measurements were taken with continuous current injection, so heating effects are included. The dotted line in (b) represents EQE droop.
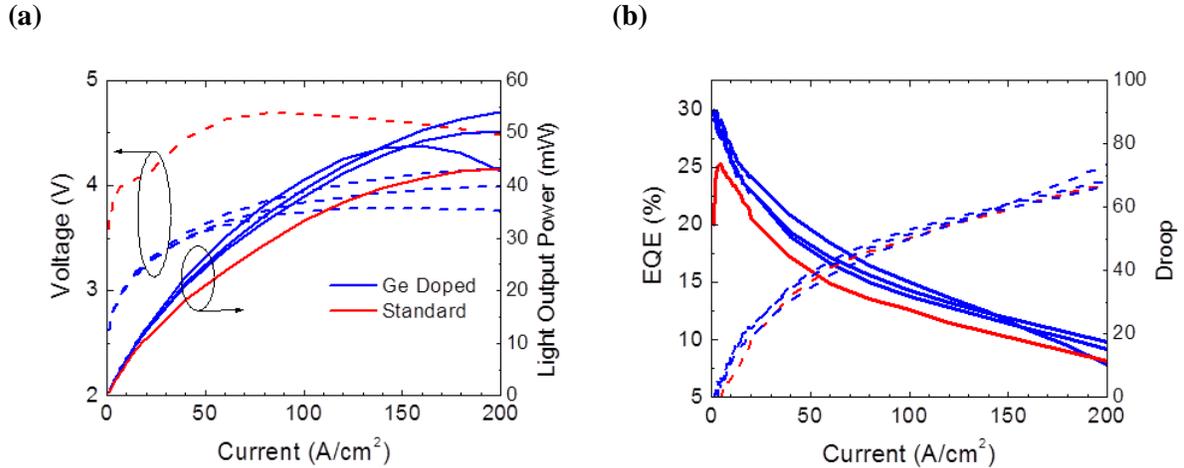
The EQE curves in Fig. 6.15(b) show a higher EQE for the Ge-doped LED, but the efficiency droop is similar. This is expected since there is no reason to believe that the polarization field in every QW has been screened in this case.

Figure 6.16 shows simulated band diagrams for a 3 QW LED at a current density of 100 mA/cm^2. In Fig. 6.16(a), the doping on the n-side is 1E18 cm^{-3} extending up to the first QW interface. In Fig. 6.16(b), the doping on the n-side is 1E20 cm^{-3} extending up to the first QW interface. The size of the barrier that electrons see when injecting from the n-GaN into the active region is significantly reduced with higher doping. This level of doping would be obtainable with Ge. Lowering the barrier for current injection would improve carrier injection efficiency, improving external quantum efficiency and decreasing operating voltage. Indeed in the simulations in Fig. 6.16, the applied voltage in Fig 6.16(a) is 4.15 V, while in Fig 6.16(b) it is 3.29 V. Significant performance improvements can be expected when utilizing Ge in high concentrations on the n-side of nitride LEDs.

(a)

(b)
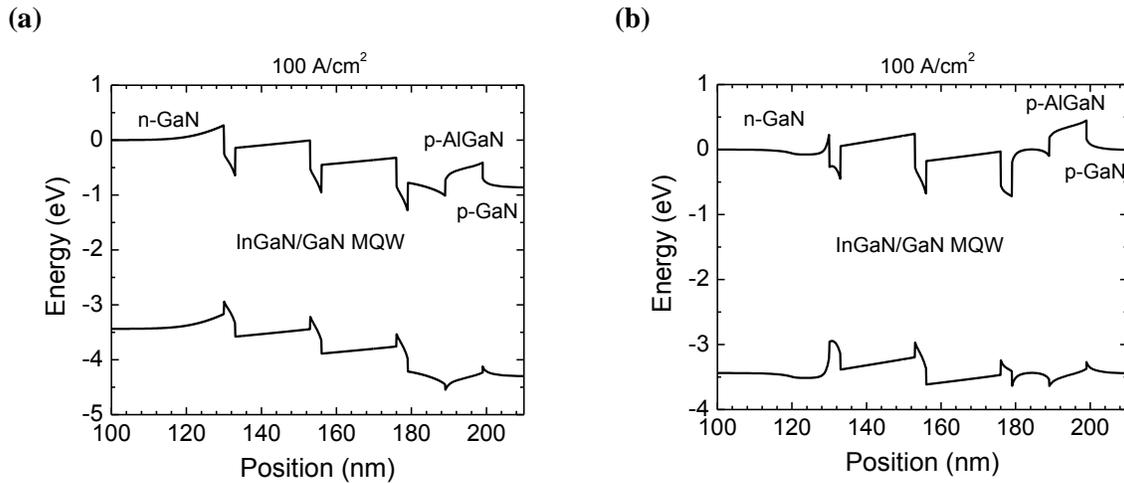
Figure 6.16: Simulated band diagrams at an injection current of 100 mA/cm^2 of, in Figure 5(a), a 3 QW LED with n-side doping of 1e18 cm^{-3} extending up to the first QW and, in Figure 5(b), a 3 QW LED with n-side doping of 1e20 cm^{-3} extending up to the first QW.

6.5.2 Single Quantum Well Spacer Series with Germanium Doping

In order to test the viability of highly Ge-doped layers for polarization screening in a SQW LED, a 10 nm pulse-doped GaN:Ge layer was placed underneath a SQW with a spacer layer of UID GaN in between. The GaN:Ge layer was identical to the layers described in Section 6.4.3, but with 4 periods of 10sec on/20sec of IBGe flow of 0.1 sccm (0.24 µmole/min) during continuous TEGa flow of 35 sccm (8.05 µmole/min, 1.1 Å/s). The nominal carrier concentration in the layer was ~1E20 cm^{-3}. The GaN spacer thickness varied from 0 nm (the condition for a polarization screened design) to 100 nm, where the layer is

194
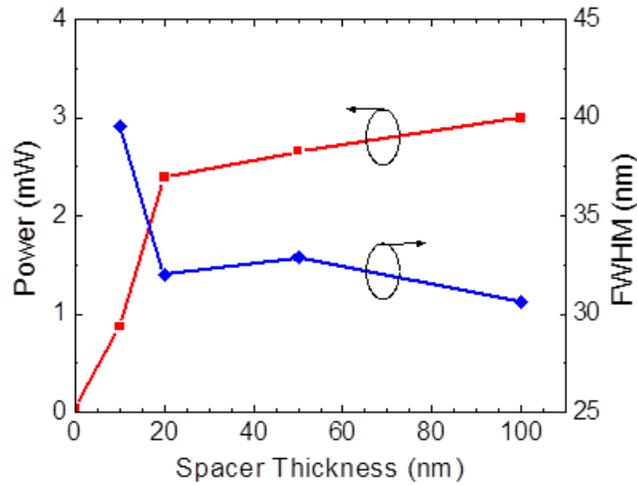
Figure 6.17: Quick test output power at 20 A/cm^2 and FWHM as a function of UID GaN spacer thickness between a 10 nm GaN:Ge layer with Ge concentration ~7E19 cm^{-3} and a 3 nm QW in a blue SQW LED structure.

much too far away from the InGaN/GaN interface to actually screen the polarization sheet charge.

The expectation was that moving the doped layer closer to the SQW would improve the output power at 20 A/cm^2 due to polarization field screening and greater wavefunction overlap, but the opposite trend was observed (Fig. 6.17). As the heavily doped GaN:Ge layer came within 20 nm of the SQW, the output power declined sharply. At zero separation, the device did not light up at all. The drop in power at 10 nm spacer thickness was accompanied by an increase in FWHM of the EL spectrum from 32 to 39 nm and a decrease in the EL peak wavelength from 493 to 450 nm. The wavelength blue-shift is likely due to a decrease in the internal electric field in the QW. The increase in FWHM could be caused by the roughness GaN:Ge in closer proximity to the QW. It is not just the roughness of the layer that causes the power to drop to zero, however. Previously results of LEDs grown on underlying InGaN layers or superlattices with high roughness due to V-defects

show no sign of a negative correlation between output power and roughness beneath the QW. More likely in this case is the possibility that the Ge doping has brought a much higher density of non-radiative defects into the QW, with an effective tail of 10-20 nm from the edge of the doped layer. These could be point defects related to energetics of Ge incorporation at such high levels, or impurities such as carbon brought in by the IBGe source. This would explain why power recovers when the Ge-doped layer is further from the QW, and why a MQW device performs well. The same effect is not seen with Si-doping, which achieves good SQW output power when the doped layer is immediately adjacent to the QW (see Chapter 5).

6.6 Conclusion

There are large internal electric fields in (0001) InGaN/GaN QWs due to polarization discontinuities at the heterointerfaces. These fields spatially separate electron and hole wavefunctions and cause a reduction in the electron-hole wavefunction overlap. A decrease in overlap leads to reduced recombination rate and higher carrier density in the active region of an LED. Higher carrier density leads to an increase in Auger recombination rate and a subsequent increase in efficiency droop at moderate to high injection current densities. Eliminating the polarization fields in InGaN QWs would decrease droop on its own, and additionally allow for new active region designs with thick SQWs to further reduce carrier density and droop. The polarization fields in InGaN/GaN QWs on the (0001) plane can be screened by heavy doping adjacent to the InGaN/GaN interfaces, but the level of doping needed, at least 7E19 cm^{-3}, presents difficulties for layer growth.

Silicon is the traditional n-type dopant used in GaN, but germanium is another option with equally small ionization energy. Silicon doping at densities above 1E19 cm^{-3} has been shown to cause an increase in tensile stress through edge dislocation climb, along with a breakdown in surface morphology. Recently, it was discovered that Ge doping up to levels in excess of 1e20 cm^{-3} did not add stress to the film and maintained a relatively smooth surface. These characteristics make Ge a more attractive n-type dopant for polarization screening in (0001) SQWs.

In order to test Ge as a dopant, an IBGe source was installed on our MOCVD reactor. IBGe is a well-behaved metalorganic source with a high vapor pressure, low cracking temperature, and linear incorporation with flow rate over a broad range of III-N growth conditions. It is also not pyrophoric and much less toxic than GeH$_4$. Ge incorporation in excess of 1E20 cm^{-3} was easily achieved. Pulsed doping was also employed in an attempt to improve surface morphology while maintaining high carrier concentration.

Electrical characteristics of GaN:Ge layers were measured by Hall Effect measurements and circular TLMs. The mobility decreased as doping density increased, but the $n*\mu$ product of the heavily doped layers was higher than anything previously reported for MOCVD grown n-GaN. Sheet resistance and bulk resistivity decreased with increasing Ge concentration as expected. Contact resistance decreases with increasing doping, and pulsed doping improves contact resistance at very high doping because of its lower roughness.

GaN:Ge layer morphology was characterized extensively by AFM. For continuously doped layers, there was a dramatic increase in roughness going over the full range of possible IBGe flows. Near [Ge] = 1E20 cm^{-3}, the morphology became three dimensional,

with plateau regions and trenches in between. The plateaus remained as the layer thickness decreased down to only 10 nm, and the height of the plateaus was on the order of the nominal layer thickness. There was no improvement on the morphology with changes in growth temperature, substrate TDD, carrier gas, or growth rate. XRD scans of the (0002) peak indicated compressive strain evolution corresponding to the breakdown of surface morphology. Pulsed doping was employed as a way to improve morphology with some success. Pulse-doped GaN:Ge layers eliminated the plateaus and were relatively smoother but still suffered from step bunching and has RMS surface roughness well over 1 nm.

Incorporating a GaN:Ge heavily doped layer in a standard blue MQW LED structure led to improvements forward voltage and output power. The likely explanation is improved spreading resistance in the n-GaN and lowering of the injection barrier. When a heavily doped GaN:Ge layer was placed near a SQW for the purpose of polarization field screening, however, the output power decreased dramatically. The reason for this behavior is unknown, but it is suspected to involve a non-radiative defect associated with the Ge doping or IBGe source specially, because the same trend is not seen with Si doping as the same densities in the same structures. There is still much work left to be done in growing and characterizing GaN:Ge films. Secondary ion mass spectroscopy, atom probe tomography, and other techniques could be used to investigate the nature of plateau regions in extremely rough films, and to discover the mechanism that causes LED failure when the GaN:Ge layer is too near the QW. Pulsed doping needs to be explored over a much wider range of conditions and pulse schemes.

References

1.   David, A. & Grundmann, M. J. Influence of polarization fields on carrier lifetime and recombination rates in InGaN-based light-emitting diodes. *Appl. Phys. Lett.* **97,** 033501 (2010).

2.   Kioupakis, E., Yan, Q., Walle, C. G. Van De & Van de Walle, C. G. Interplay of polarization fields and Auger recombination in the efficiency droop of nitride light-emitting diodes. *Appl. Phys. Lett.* **101,** 231107 (2012).

3.   Becerra, D. L. *et al.* High-power low-droop violet semipolar (303̄1̄) InGaN/GaN light-emitting diodes with thick active layer design. *Appl. Phys. Lett.* **105,** 171106 (2014).

4.   Zhao, Y. *et al.* High-Power Blue-Violet Semipolar ($20\bar{2}\bar{1}$) InGaN/GaN Light-Emitting Diodes with Low Efficiency Droop at 200 A/cm^{2}. *Appl. Phys. Express* **4,** 082104 (2011).

5.   Zhao, Y. *et al.* Indium incorporation and emission properties of nonpolar and semipolar InGaN quantum wells. *Appl. Phys. Lett.* **100,** 201108 (2012).

6.   Pan, C. C. *et al.* High-power, low-efficiency-droop semipolar (202̄1̄) single-quantum-well blue light-emitting diodes. *Appl. Phys. Express* **5,** (2012).

7.   Waltereit, P. *et al.* Nitride semiconductors free of electrostatic fields for efficient white light-emitting diodes. *Nature* **406,** 865–8 (2000).

8.   Jena, D. *et al.* Polarization-engineering in group III-nitride heterostructures: New opportunities for device design. *Phys. Status Solidi* **208,** 1511–1516 (2011).

9.   Kozlowski, G., Schulz, S. & Corbett, B. Polarization matching design of InGaN-based semi-polar quantum wells—A case study of (112̄2) orientation. *Appl. Phys. Lett.* **104,** 051128 (2014).

10.   Fiorentini, V., Bernardini, F., Della Sala, F., Di Carlo, a. & Lugli, P. Effects of macroscopic polarization in III-V nitride multi-quantum-wells. **60,** 11 (1999).

11.   Dalfors, J. *et al.* Optical properties of doped InGaN/GaN multiquantum-well structures. *Appl. Phys. Lett.* **74,** 3299 (1999).

12.   Deguchi, T. *et al.* Luminescence spectra from InGaN multiquantum wells heavily doped with Si. *Appl. Phys. Lett.* **72,** 3329 (1998).

13. Chichibu, S. *et al.* Optical properties of InGaN quantum wells. *Mater. Sci. Eng. B* **59,** 298–306 (1999).

14. Davies, M. J. *et al.* The effects of Si-doped prelayers on the optical properties of InGaN/GaN single quantum well structures. *Appl. Phys. Lett.* **105,** 092106 (2014).

15. Neufeld, C. J. *et al.* Effect of doping and polarization on carrier collection in InGaN quantum well solar cells. *Appl. Phys. Lett.* **98,** 243507 (2011).

16. Sheu, J. *et al.* The doping process and dopant characteristics of GaN. *J. Phys. Condens. Matter* **657,** (2002).

17. Götz, W. *et al.* Hall-effect characterization of III-V nitride semiconductors for high efficiency light emitting diodes. *Mater. Sci. Eng. B Solid-State Mater. Adv. Technol.* **59,** 211–217 (1999).

18. Nakamura, S., Mukai, T. & Senoh, M. Si-and Ge-doped GaN films grown with GaN buffer layers. *Jpn. J. Appl. Phys.* **31,** 2883–2888 (1992).

19. Hageman, P. R., Schaff, W. J., Janinski, J. & Liliental-Weber, Z. n-type doping of wurtzite GaN with germanium grown with plasma-assisted molecular beam epitaxy. *J. Cryst. Growth* **267,** 123–128 (2004).

20. Zhang, X. *et al.* Growth of AlxGa1-xN:Ge on sapphire and silicon substrates. *Appl. Phys. Lett.* **67,** 1745–1747 (1995).

21. Xie, J. *et al.* Strain in Si doped GaN and the Fermi level effect. *Appl. Phys. Lett.* **98,** 96–99 (2011).

22. Romano, L. T., Van de Walle, C. G., Ager, J. W., Götz, W. & Kern, R. S. Effect of Si doping on strain, cracking, and microstructure in GaN thin films grown by metalorganic chemical vapor deposition. *J. Appl. Phys.* **87,** 7745 (2000).

23. Romano, L. T. *et al.* Effect of Si doping on the strain and defect structure of GaN thin films. *Phys. B Condens. Matter* **273-274,** 50–53 (1999).

24. Romanov, A. E. & Speck, J. S. Stress relaxation in mismatched layers due to threading dislocation inclination. *Appl. Phys. Lett.* **83,** 2569–2571 (2003).

25. Cantu, P. *et al.* Si doping effect on strain reduction in compressively strained Al 0.49Ga0.51N thin films. *Appl. Phys. Lett.* **83,** 674–676 (2003).

26. Follstaedt, D. M., Lee, S. R., Allerman, a. a. & Floro, J. a. Strain relaxation in AlGaN multilayer structures by inclined dislocations. *J. Appl. Phys.* **105,** (2009).

27.   Dadgar, A. *et al.* MOVPE growth of GaN on Si - Substrates and strain. *Thin Solid Films* **515,** 4356–4361 (2007).

28.   Dadgar, A., Bläsing, J., Diez, A. & Krost, A. Crack-Free, Highly Conducting GaN Layers on Si Substrates by Ge Doping. *Appl. Phys. Express* **4,** 011001 (2011).

29.   Fritze, S. *et al.* High Si and Ge n-type doping of GaN doping - Limits and impact on stress. *Appl. Phys. Lett.* **100,** 122104 (2012).

30.   Xie, J. *et al.* On the strain in n-type GaN. *Appl. Phys. Lett.* **99,** 141916 (2011).

31.   Kirste, R. *et al.* Ge doped GaN with controllable high carrier concentration for plasmonic applications. *Appl. Phys. Lett.* **103,** 242107 (2013).

32.   Hille, P. *et al.* Screening of the quantum-confined Stark effect in AlN/GaN nanowire superlattices by germanium doping. *Appl. Phys. Lett.* **104,** 102104 (2014).

33.   Schörmann, J. *et al.* Germanium doping of self-assembled GaN nanowires grown by plasma-assisted molecular beam epitaxy. *J. Appl. Phys.* **114,** 103505 (2013).

34.   Rowland, L. B., Doverspike, K. & Gaskill, D. K. Silicon doping of GaN using disilane. *Appl. Phys. Lett.* **66,** 1495 (1995).

35.   Oshima, Y., Yoshida, T., Watanabe, K. & Mishima, T. Properties of Ge-doped, high-quality bulk GaN crystals fabricated by hydride vapor phase epitaxy. *J. Cryst. Growth* **312,** 3569–3573 (2010).

36.   Shenai, D. V. *et al.* Safer alternative liquid germanium precursors for relaxed graded SiGe layers and strained silicon by MOVPE. *J. Cryst. Growth* **298,** 172–175 (2007).

37.   Woelk, E. *et al.* Designing novel organogermanium OMVPE precursors for high-purity germanium films. *J. Cryst. Growth* **287,** 684–687 (2006).

38.   Bosi, M. *et al.* MOVPE growth of homoepitaxial germanium. *J. Cryst. Growth* **310,** 3282–3286 (2008).

39.   Attolini, G. *et al.* Homo and hetero epitaxy of Germanium using isobutylgermane. *Thin Solid Films* **517,** 404–406 (2008).

40.   Kim, J. H. *et al.* Delta-doping of Si in GaN by metalorganic chemical vapor deposition. *Japanese J. Appl. Physics, Part 1 Regul. Pap. Short Notes Rev. Pap.* **38,** 681–682 (1999).

41.   Zhao, G. Y. *et al.* Growth of Si delta-doped GaN by metalorganic chemical-vapor deposition. *Appl. Phys. Lett.* **77,** 2195 (2000).

42. Contreras, O., Ponce, F. a., Christen, J., Dadgar, a. & Krost, A. Dislocation annihilation by silicon delta-doping in GaN epitaxy on Si. *Appl. Phys. Lett.* **81,** 4712–4714 (2003).

43. Wang, L. S., Zang, K. Y., Tripathy, S. & Chua, S. J. Effects of periodic delta-doping on the properties of GaN:Si films grown on Si (111) substrates. *Appl. Phys. Lett.* **85,** 5881–5883 (2004).

44. Zheng, Z. *et al.* Effect of periodic Si-delta-doping on the evolution of yellow luminescence and stress in n-type GaN epilayers. *J. Cryst. Growth* **387,** 52–56 (2014).

45. Aoyagi, Y., Takeuchi, M., Iwai, S. & Hirayama, H. Formation of AlGaN and GaN epitaxial layer with high p-carrier concentration by pulse supply of source gases. *AIP Adv.* **2,** 012177 (2012).

46. Kim, K. H., Li, J., Jin, S. X., Lin, J. Y. & Jiang, H. X. III-nitride ultraviolet light-emitting diodes with delta doping. *Appl. Phys. Lett.* **83,** 566–568 (2003).

47. Hu, Y.-L. *et al.* Effect of quantum well cap layer thickness on the microstructure and performance of InGaN/GaN solar cells. *Appl. Phys. Lett.* **100,** 161101 (2012).

48. Marlow, G. S. & Das, M. B. The effects of contact size and non-zero metal resistance on the determination of specific contact resistance. *Solid. State. Electron.* **25,** 91–94 (1982).

49. Lester, L. F. *et al.* Nonalloyed Ti/Al Ohmic contacts to n-type GaN using high-temperature premetallization anneal. *Appl. Phys. Lett.* **69,** 2737 (1996).

50. Klootwijk, J. H. & Timmering, C. E. Merits and Limitations of Circular TLM structures for contact resistance determination for novel III-V HBTs. in *IEEE Int. Conf. Microelectron. Test Struct.* **17,** 247–252 (2004).

51. Kyle, E. C. H. *et al.* High-electron-mobility GaN grown on free-standing GaN templates by ammonia-based molecular beam epitaxy. *J. Appl. Phys.* **115,** 193702 (2014).

52. Wang, D.-F. *et al.* Low-resistance Ti/Al/Ti/Au multilayer ohmic contact to n-GaN. *J. Appl. Phys.* **89,** 6214 (2001).

7

Conclusions and Future Work

7.1 Conclusions

The III-nitrides offer a rich set of both device and growth physics that provided a fruitful platform for tackling the many challenges involved in developing efficient optoelectronic devices. The limits of MOCVD growth were tested in trying to balance the sometimes competing demands of high structural quality and high device efficiency. The InGaN alloy itself presented significant challenges when aiming for higher indium content and lower bandgap that would allow conversion of more incident photons and enable multijunction integration of an InGaN solar cell: large lattice mismatch to GaN limits the thickness (and therefore absorbing volume) that can be grown before relaxation, and low growth temperatures lead to the formation and propagation of deleterious V-defects. Another challenge that the wurtzite III-N material system presented was the large piezoelectric polarization present in strained InGaN layers. Polarization-induced electric fields cause the Quantum-Confined Stark Effect, which has negative effects for InGaN QW based optoelectronic devices: it decreases the absorption strength near the band edge of a solar cell, and it red-shifts and decreases the efficiency of radiative transitions in an LED.

203

The key tradeoff in the development of InGaN solar cells was growing enough InGaN absorber layer thickness to absorb most of the incident above-bandgap photons while also incorporating enough indium to reduce the bandgap to a reasonable level for solar conversion. A MQW design allowed the strain from the InGaN layers to be spread over a larger distance so that more total InGaN thickness could be incorporated in the device active region. The MQW structure brought up the problem of carrier transport out of the active region. It was found through temperature dependent measurements of InGaN MQW solar cells that thinner quantum barriers improved collection efficiency by promoting tunneling escape of electrons and holes from QWs in favor of thermionic emission. A two dimensional carrier escape model confirmed these results.

MOCVD growth of thick MQW active regions with thin barriers proved to be a delicate balance. On one hand, higher growth temperature and the presence of H_2 in the barriers could mitigate the formation of V-defects. On the other hand, those same conditions attacked the integrity of the InGaN QWs. The solution was a two-step barrier growth with a low temperature capping layer followed by a +100°C ramp and a GaN layer grown in H_2. After optimization, a 4 nm total barrier thickness provided maximum solar cell performance while maintaining smooth interfaces. With the optimized MQW structure, solar cell performance increased up to 30 QW periods, after which point strain relaxation related defect formation degraded efficiency. These devices exhibited record high V_{oc} and FF due to the thin barrier design. Dielectric optical coatings were deposited on the best device (30 QWs) in order to boost efficiency and demonstrate feasibility for multijunction integration. The front surface anti-reflective coating and rear surface dichroic mirror were composed of alternating layers of SiO_2 and Ta_2O_5 deposited by ion beam deposition. Eliminating surface

reflections and providing a second pass of light, while allowing light not absorbed by the InGaN layers to pass through for potential underlying solar junctions, boosted conversion efficiency by 37.5%. The resulting efficiency of 3.33% at AM0 was a record for a stand-alone nitride solar cell.

III-N LEDs are based on InGaN QWs, which, when grown on c-plane, contain large piezoelectric polarization-induced electric fields. These fields spatially separate electron and hole wavefunctions, reducing the transitions rate for all types of recombination. If SRH, radiative, and Auger recombination each depend on the square of the wavefunction overlap, as has been postulated in theory and experiment, then an argument can be constructed about the relationship between wavefunction overlap and LED efficiency: increased overlap will decrease the carrier density at a given current density; the peak IQE will not change, but will push to larger current densities; the efficiency droop will therefore decrease.

Simulations of blue LEDs with a single QW active region showed that increasing the width of the QW decreases the wavefunction overlap because of the polarization field. By doping n- and p-type immediately adjacent to the QW, the polarization field could be screened. Complete screening was predicted at a very high doping level of $7\text{x}10^{19}$ cm^{-3}. To test the screening of polarization fields, blue c-plane SQW LEDs were grown with and without screening doping at QW thicknesses of 3.8 to 11.3 nm. The widest QW samples showed degradation due to defect formation in the InGaN layer. The other screened LEDs showed increasing peak EQE with increasing QW thickness, which went against the wavefunction overlap argument. The unscreened LEDs had lower peak EQEs than their screened counterparts and a very delayed turn-ons except for the thinnest QW device. There must have been a difference in the SRH nonradiative coefficient between these devices. A

possible explanation is that the extent to which electron and hole wavefunctions overlap barrier regions could change the degree of nonradiative recombination in these devices. Finally, biased PL measurements proved complete polarization screening in the doped SQWs. No wavelength shift was observed in devices with doping, but significant shifts were observed in devices without doping.

The high levels of doping necessary to screening polarization fields in blue InGaN QWs can present problems with n-type doping. The traditional donor impurity, Si, has been shown to, at large concentrations, cause dislocation climb, resulting in the development of tensile stress in the film. Germanium also acts as a donor in GaN, and has been shown to not increase tensile strain. The Ge source IBGe was installed on the MOCVD reactor and showed linear incorporation with flow rate. Hall Effect measurements showed relatively high mobility at Ge concentrations exceeding 1E20 cm^{-3}. The layer conductivities were the highest reported in an MOCVD grown GaN film. TLM measurements showed decreasing sheet resistivity with increasing doping and low contact resistance.

However, above a concentration of 1E19 cm^{-3}, the morphology of GaN:Ge layers degraded significantly. A plateau-like morphology developed with heights on the order of the nominal layer thickness. XRD scans of the (0002) peak indicated compressive strain in these layers. A pulsed doping scheme improved surface morphology and contact resistance, but the morphology was still rougher than ideal for a layer immediately adjacent to a QW. A MQW LED with a highly Ge doped layer beneath the active region performed slightly better than a control sample, likely due to improved carrier injection and lateral current spreading. When the highly Ge doped layer was grown immediately adjacent to an InGaN SQW, there

was no EL output power. Light output recovered as the Ge doped layer was moved away from the QW by at least 20 nm.

The methods and results described in this thesis illustrate the value of a combined focus on materials growth and device physics. The field of III-N optoelectronic devices in particular straddles a line between those two disciplines. Significant challenges to progress in device efficiency lie both in overcoming difficult material growth problems, and in designing novel active regions within the growth constraints that either harness or minimize the unique properties of the material system, such as polarization. Device design simply cannot be effective without considering the interplay between materials and physics.

7.2 Future Work

7.2.1 Solar Cells

The work on InGaN MQW solar cells in this dissertation represents a nearly complete optimization of the device structure and materials growth strategies. Further improvements on this structure would need to take a truly novel path, not just one of incremental improvement. Future work in nitride solar should focus on the following areas: integrating with an existing multijunction solar cell, expanding the wavelength range of absorption and enabling thicker active region growth, and improving IQE.

A scheme for integrating a nitride solar cell junction into a MJSC is described in detail in section 4.4.2. The underlying III-V 4-junction solar cell has already been highly developed and is not a concern in this design. The top junction of that device is normally thinner than necessary for full absorption for the sake of current matching, so adding a nitride junction on top would not scavenge many photons from that junction. Also, the

207

nitride device would be electrically decoupled, so current matching would not be an issue. The efficiencies of the nitride solar cell and the underlying MJSC are nearly additive as long as the most important layers of design can be engineered properly: the optical coatings and the bonding interlayer. Antireflection coating and dichroic mirror design is discussed in detail in section 4.4. One strategy to improve upon the design of alternating planar dielectric layers is to implement a nanostructured coating known as a moth eye design.[1] The bonding interlayer between the nitride cell and the underlying MJSC is a key and difficult part of the overall design. Optically, it must be low loss over a very wide wavelength range, and structurally it must provide a strong and flexible bond that will not delaminate during the large temperature swings common in CPV operation. The combination of BCB as a bonding layer and well-designed coatings shows promise as a theoretical design.[2] An actual integrated device has yet to be built and tested, however.

An aspect of the InGaN solar cell performance that is important for integration is the steepness of the EQE spectrum. Any slope of the absorption edge of the EQE spectrum will both reduce the potential efficiency of that junction and scavenge photons from the next junction. As discussed in Chapter 3, polarization fields in c-plane InGaN layers cause a smearing of the absorption edge, which would be detrimental to both the InGaN cell efficiency and the underlying cell efficiency in an integrated MJSC. Eliminating polarization fields would also be important for improving IQE and pushing to longer wavelength absorption by increasing the In content of InGaN. Polarization fields get larger and more detrimental with higher indium content. Without polarization field, and making the bad assumption that there is no strain limitation, InGaN layers could be grown arbitrarily thick without developing a field that acts counter to the normal junction field, which is

responsible for carrier collection. The MQW design could be replaced by a simple DH, which would improve carrier collection efficiency.

One potential strategy for reducing polarization fields is to grow on nonpolar or semipolar planes of GaN. There are little in the literature on this approach, but it has been attempted at UCSB. Reduction of field in the InGaN QWs is achievable,[3] but InGaN layers on these planes relax much more easily than on c-plane because of the presence of dislocation glide plane with resolved shear stress. Even at modest compositions (absorbing near 450 nm), the total thickness of InGaN that can be grown before degradation from relaxation is not enough to compete with the best *c*-plane devices. Another strategy would be to surround InGaN layers with polarization-matched AlInN or AlInGaN layers so that there is no net polarization sheet charge at the interface.[4–7] Polarization matching with these layers has been predicted and demonstrated, but their growth is particularly complicated by the presence of both Al, which prefers higher growth temperatures, and In, which does not incorporated effectively except at lower growth temperatures. More importantly, the strain in ternary and quarternary layers polarization matched to InGaN is also compressive; meaning that even less InGaN could be grown before relaxation. This approach may work in an LED, but it seems doomed in a solar cell that requires thick active regions, unless a reduced strain structure can be implemented.

Strain is the main limiting factor in increasing the total InGaN thickness and in going to lower bandgap absorbing layers by increasing the indium content. The holy grail of strain reduction in the nitrides would be a relaxed InGaN buffer. The idea of a relaxed buffer is to grade the lattice constant though misfit dislocation glide while containing the defects to the buffer region. Layers above the buffer would be grown coherently to the lattice constant of

the relaxed InGaN. In this case, the active region could be grown as an InGaN homojunction of arbitrary thickness. Relaxed buffers are common in arsenide-based MJSCs, grading the lattice constant between material junctions without introducing new defects.[8] Because dislocation glide is necessary for this kind of relaxation, semipolar planes of GaN should allow much easier growth of relaxed buffers.[9] However, two dimension relaxation onset creates new threading dislocations which are catastrophic to device performance. Graded buffers on c-plane are possible by MBE and have been used to increase the performance of MOCVD-grown long wavelength LEDs.[10] That approach is complicated by the use of both MBE and MOCVD growth, but an acceptable MOCVD-only approach has yet to be demonstrated.

In a standard MQW design, strain in the InGaN well can be compensated by using tensile strained barriers. On a GaN template, the barrier would have to be AlGaN, AlInN, or AlInGaN. On an InGaN template, the barrier could be GaN, which would reduce the growth complication in the MQW. Strain balanced MQWs have been used successfully in GaAs-based solar cells,[11] and have also been demonstrated with InGaN quantum wells.[12] Incorporation of AlGaN capping layers in a green InGaN MQW have also been shown to improve device performance, though the effect is not thought to be strain related.[13,14] Replacing the GaN cap with AlGaN in the two-step barrier growth method described in Chapter 4 could allow improved efficiencies of InGaN MQW solar cells absorbing at green wavelengths and beyond.

7.2.2 SQW LEDs

The SQW LED effort presented in this dissertation has been successful with regards to effectively screening the polarization field in an InGaN QW with doping. What remains incomplete, however, is a full understanding of the factors influencing the efficiency of these devices. The next steps along this line of research will be to characterize the nature of recombination occurring in the SQW active regions. The speculation in Chapter 5 is that the highly doped barrier layers may contribute to a much higher than normal SRH coefficient. That would explain why thicker wells, with less wavefunction-barrier interaction, have higher peak EQE. The other possibility is that the dependence of A, B and C coefficients on wavefunction overlap is not the same. It is entirely possible that A and C do not depend on the square of the overlap like B does, and that could itself explain the observed efficiency dependence on screening and well thickness, as discussed in Chapter 5. Choosing the right experiments to differentiate between these possible explanations, or to find another un-thought-of explanation, will be essential going forward.

Time-resolved measurements are generally the best way to observe recombination characteristics. TRPL and TREL show how the luminescence of a sample decays as a function of time after an input pulse of light or current. The characteristic decay time of the luminescence is a measure of the total recombination lifetime. At very low temperature (7K for instance) SRH recombination should be frozen out, and assuming that the injected carrier density is low enough so that the radiative process dominates over Auger, the decay time will represent the radiative recombination lifetime.[15] Comparing low temperature and high temperature lifetimes gives information about the SRH coefficient. Differential lifetime measurements coupled with IQE measurements can also give valuable information about the

relative contributions of radiative and nonradiative processes to the total lifetime.[16] Another technique that could be very useful is electron emission spectroscopy, which can detect the Auger signature of electrons excited to high energies in the conduction band.[17–19] These measurements would determine if Auger recombination is happening at all in the screened SQW structures, even at very high current density, or if another recombination process is dominant, which could explain why the EQE is low and relatively flat.

In addition to the SQW structures described in Chapter 5, further structures could be grown for recombination investigations. The highly doped layers can be moved away from the SQW on the n-side and p-side separately in order to see if either has a strong proximity effect on *A*. The EBL can be removed and then a hole blocking AlGaN layer can be added underneath the SQW to see if electron or hole overflow is causing significant efficiency loss. These measurements should also be done on structures grown on other planes of GaN to compare similar different QW fields without the presence of highly doped layers.

7.2.3 Germanium Doping

The work on Ge doping of GaN in this dissertation only represents the first small step toward an understanding of how to effectively incorporate large concentrations of Ge and how to integrate such highly doped layers into a device. Many challenges have presented themselves during the short time this project has been active, and continuing research should prove fruitful. There are two broad areas where work remains to be done: GaN:Ge layer growth and the incorporation of GaN:Ge layers into new device structures.

Throughout the investigations in this dissertation, the morphology of highly doped GaN:Ge layers remained relatively poor. Pulsed doping via a modulated IBGe flow made

some headway toward improving the morphology, but significant further improvement will be necessary before heavily doped GaN:Ge layers can be reliably incorporated into device structures. Only a small amount of the potential growth space for pulsed doping has thus far been explored. There are several ways to adjust the scheme in order to attempt to change the growth mode while maintaining a high effective doping density. Instead of a 50% duty cycle of IBGe flow, that ratio can be dropped. This would give more time to UID GaN growth in order to more effectively recover the surface morphology in between GaN:Ge spikes. The time of the GaN:Ge layer can also be decreased, irrespective of duty cycle. Alternating 10 nm layers, which have been grown so far, are relatively thick. More spike-like layers of 1-2 nm could maintain both high structural quality and high carrier density.[20,21] Another strategy that should be explored is the addition of growth interrupts between the doped layer and undoped GaN in the periodic sequence. The interrupt should remove excess dopant atoms from the surface, making sharper spikes of doping and possibly allowing for better morphology throughout the stack. Digital GaN:Ge doping could also be attempted. In this scheme, flows of TMG (TEG) and IBGe alternate. The hope is that with a high enough IBGe flow, Ge will accumulate on the surface and introduce very sharp spikes of dopants into the GaN layer. Finally, perhaps the most promising avenue toward high n-type doping concentrations using Ge is to combine it with Si doping. Figure 6.14 showed the very different morphologies of GaN:Ge and GaN:Si, with the former preferring step bunching and the latter preferring very large step area. If one can find the right combination of Ge and Si incorporation, it is likely that these morphological effects will offset, and the layer will grow smoothly in step-flow. Additionally, the strain introduced by high Si and Ge

213

incorporation in the GaN lattice is opposite – GaN:Ge develops compressive stress and GaN:Si develops tensile stress – so a GaN:Ge+Si layer could be grown largely unstrained.

An initial attempt was made (see Chapter 6) to use a GaN:Ge layer for polarization screening in a SQW LED, but that device suffered a catastrophic loss of output power. When the GaN:Ge layer was moved away from the SQW by 20 nm, the power recovered. It will need to be determined what effect the GaN:Ge layer had to cause this sharp drop in efficiency when in close proximity to a QW. SIMS or atom probe measurements could show whether there is a short tail of Ge atom or other impurity atoms into the QW that could act as nonradiative recombination centers. TRPL and TREL can be performed on structures with varying placement and concentration of Ge doping to extract rates of recombination. Iterating these measurements with changes in architecture or growth mode may lead to a solution with complete field screening and high radiative efficiency.

Beyond use in SQW LEDs, Ge doping could be used in other devices that need highly doped layers or high mobility layers. Tunnel junctions (TJs) require a p-n junction with thin degenerately doped layers. Electron states in conduction band of the n-side of the junction line up in energy with hole states in the valence band on the p-side of the junction, and if the junction field is strong enough and the tunneling distance through the bandgap is short enough, then a low resistance TJ can be formed. This is difficult in GaN because of its large bandgap, so especially high levels of doping must be used, along with other strategies such as polarization engineering[22] and rare-earth nanoparticles.[23] Ge could provide an advantage over Si on the n-side of the TJ since it does not develop large tensile strains. GaN TJs could enable the elimination of troublesome p-contacts and deposited current spreading layers.[24] They could also allow stacking of multiple active regions of LEDs, for lower

carrier density or multiple colors, or multiple junctions in a nitride solar cell.[25–27] Highly Ge doped layers can also be used as low resistance contact and current spreading layers in GaN electronic devices and top contact LEDs. Since GaN:Ge seems to have slightly higher mobility than GaN:Si, very low doping could be used in n-channel transistors.

References

1. Perl, E. E., McMahon, W. E., Friedman, D. J. & Bowers, J. E. Ultrabroadband and Wide-Angle Hybrid Antireflection Coatings With Nanostructures. *IEEE J. Photovoltaics* **4,** 962–967 (2014).

2. Toledo, N. G. *et al.* Design of integrated III-nitride/non-III-nitride tandem photovoltaic devices. *J. Appl. Phys.* **111,** 054503 (2012).

3. Zhao, Y. *et al.* Indium incorporation and emission properties of nonpolar and semipolar InGaN quantum wells. *Appl. Phys. Lett.* **100,** 201108 (2012).

4. Fiorentini, V., Bernardini, F., Della Sala, F., Di Carlo, a. & Lugli, P. Effects of macroscopic polarization in III-V nitride multi-quantum-wells. **60,** 11 (1999).

5. Dadgar, a. *et al.* Green to blue polarization compensated c-axis oriented multi-quantum wells by AlGaInN barrier layers. *Appl. Phys. Lett.* **102,** (2013).

6. Jena, D. *et al.* Polarization-engineering in group III-nitride heterostructures: New opportunities for device design. *Phys. Status Solidi* **208,** 1511–1516 (2011).

7. Schubert, M. F. *et al.* Polarization-matched GaInNAlGaInN multi-quantum-well light-emitting diodes with reduced efficiency droop. *Appl. Phys. Lett.* **93,** 2006–2009 (2008).

8. Geisz, J. F. *et al.* 40.8% Efficient Inverted Triple-Junction Solar Cell With Two Independently Metamorphic Junctions. *Appl. Phys. Lett.* **93,** 123505 (2008).

9. Koslow, I. L. *et al.* Onset of plastic relaxation in semipolar () InxGa1−xN/GaN heterostructures. *J. Cryst. Growth* **388,** 48–53 (2014).

10. Däubler, J. *et al.* Long wavelength emitting GaInN quantum wells on metamorphic GaInN buffer layers with enlarged in-plane lattice parameter. *Appl. Phys. Lett.* **105,** 111111 (2014).

11. Mazzer, M. *et al.* Progress in quantum well solar cells. *Thin Solid Films* **511-512,** 76–83 (2006).

12. Van Den Broeck, D. M., Bharrat, D., Hosalli, a. M., El-Masry, N. a. & Bedair, S. M. Strain-balanced InGaN/GaN multiple quantum wells. *Appl. Phys. Lett.* **105,** 031107 (2014).

13. Shioda, T., Yoshida, H., Tachibana, K., Sugiyama, N. & Nunoue, S. Enhanced light output power of green LEDs employing AlGaN interlayer in InGaN/GaN MQW structure on sapphire (0001) substrate. *Phys. Status Solidi* **209,** 473–476 (2012).

14. Koleske, D. D., Fischer, A., Bryant, B. N., Kotula, P. G. & Wierer, J. J. On the increased efficiency in InGaN-based multiple quantum wells emitting at 530–590nm with AlGaN interlayers. *J. Cryst. Growth* **415,** 57–64 (2015).

15. Sun, C.-K. *et al.* Radiative recombination lifetime measurements of InGaN single quantum well. *Appl. Phys. Lett.* **69,** 1936 (1996).

16. David, A. & Grundmann, M. J. Droop in InGaN light-emitting diodes: A differential carrier lifetime analysis. *Appl. Phys. Lett.* **96,** 1–4 (2010).

17. Iveland, J., Martinelli, L., Peretti, J., Speck, J. S. & Weisbuch, C. Direct Measurement of Auger Electrons Emitted from a Semiconductor Light-Emitting Diode under Electrical Injection: Identification of the Dominant Mechanism for Efficiency Droop. *Phys. Rev. Lett.* **110,** 177406 (2013).

18. Iveland, J. *et al.* Origin of electrons emitted into vacuum from InGaN light emitting diodes. *Appl. Phys. Lett.* **105,** 052103 (2014).

19. Piccardo, M. *et al.* Determination of the first satellite valley energy in the conduction band of wurtzite GaN by near-band-gap photoemission spectroscopy. *Phys. Rev. B* **89,** 235124 (2014).

20. Wang, L. S., Zang, K. Y., Tripathy, S. & Chua, S. J. Effects of periodic delta-doping on the properties of GaN:Si films grown on Si (111) substrates. *Appl. Phys. Lett.* **85,** 5881–5883 (2004).

21. Aoyagi, Y., Takeuchi, M., Iwai, S. & Hirayama, H. Formation of AlGaN and GaN epitaxial layer with high p-carrier concentration by pulse supply of source gases. *AIP Adv.* **2,** 012177 (2012).

22. Krishnamoorthy, S., Akyol, F., Park, P. S. & Rajan, S. Low resistance GaN/InGaN/GaN tunnel junctions. *Appl. Phys. Lett.* **102,** 113503 (2013).

23. Krishnamoorthy, S. *et al.* GdN nanoisland-based GaN tunnel junctions. *Nano Lett.* **13,** 2570–5 (2013).

24. Jeon, S.-R. *et al.* Lateral current spreading in GaN-based light-emitting diodes utilizing tunnel contact junctions. *Appl. Phys. Lett.* **78,** 3265 (2001).

25. Akyol, F., Krishnamoorthy, S. & Rajan, S. Tunneling-based carrier regeneration in cascaded GaN light emitting diodes to overcome efficiency droop. *Appl. Phys. Lett.* **103,** 081107 (2013).

26. Chang, S.-J., Lin, W.-H. & Yu, C.-T. GaN-based multiquantum well light-emitting diodes with tunnel-junction-cascaded active regions. *IEEE Electron Device Lett.* **3106,** 1–1 (2015).

27. Grundmann, M. & Mishra, U. Multi-color light emitting diode using polarization-induced tunnel junctions. *Phys. status solidi* **4,** 2830–2833 (2007).